Università degli Studi di Padova
Dipartimento di Scienze Chimiche
Scuola di Dottorato in Scienze Molecolari
CICLO XXXII

$Au_{25}(SR)_{18}$: Metal Doping, Ligand Exchange, and Fusion Reactions

Direttore della Scuola: Ch.mo Prof. Leonard Prins
Supervisore: Ch.mo. Prof. Flavio Maran

Dottoressa: Wenwen Fei

Abstract

In the past few years, the interest in the study of atomically precise metal nanoclusters has grown very significantly. Main reasons are the refined techniques nowadays available for controlling their structure and composition, their often-intriguing properties, and the possibility to tailor them for specific applications. This Thesis aims at providing new tools to synthesize, control, modify, and characterize thiolate-protected gold nanoclusters. The focus of the research is on the thiolate-protected $Au_{25}(SR)_{18}$ cluster, which is considered by many the true benchmark system for the study of atomically precise nanoclusters. Due to quantum-confinement effects, these nanoclusters have discrete electron-energy states, and this causes the emergence of molecular properties, such as a HOMO-LUMO gap, distinct optical and redox behavior, and magnetism. Additionally, the composition of the metal part and/or the capping monolayer can be modified to make the cluster exhibit specific, sometimes unexpected properties.

The goal of this research is to show that by performing controlled modifications of the cluster core and protecting monolayer, one can indeed introduce new properties, and thereby, explore new frontiers for possible applications of these nanosystems. From the viewpoint of the metal, $Au_{25}(SR)_{18}$ was modified by introducing one-single foreign metal atom. The synthetic, purification, modification, and characterization procedures were refined to explore new ways for achieving proper understanding of the structure of the doped molecular cluster. Particular emphasis has been put on the NMR characterization of the products, a still unexplored yet very powerful tool to localize the position of the doping metal. It is shown that the actual position of the doping metal changes depending on the element.

The effect of Au_{25} doping is then explored from the viewpoint of the generation and detection of singlet oxygen, which is an area of tremendous interest for the treatment of cancer via photodynamic therapy. Metal nanoclusters exhibit discrete optical transitions and have sufficiently long-lived triplet excited states.

This makes them react quite efficiently with triplet ground-state oxygen to form singlet excited-state oxygen. Here we show that by proper tuning of the cluster composition (doping metals and ligands), these nanosystems can be made to exhibit the same singlet-oxygen photosensitization performance of systems currently used in the medical practice.

We discovered an intriguing transformation of Au_{25} core. This can be considered as a fusion reaction that consists in the spontaneous transformation of two $Au_{25}(SR)_{18}$ clusters to form $Au_{38}(SR)_{24}$, which is another benchmark gold nanocluster. The radical nature of $Au_{25}(SR)_{18}^{0}$ appears to play an important role in this bimolecular reaction that, importantly, does not require addition of exogenous thiols or other co-reactants. This is indeed a very unexpected result that could modify our view about the relative stability of molecular gold nanoclusters.

After exploring core modifications, we also investigated strategies to carry out chemical reactions, namely polymerization, directly on the cluster monolayer. Proper functionalization of the nanocluster, that is, capping the cluster with different thiolates, relies on the possibility of either preparing the cluster directly, starting from a mixture of appropriate thiols, or taking advantage of ligand-place exchange reactions, in which the native thiolates present in preformed clusters are partially exchanged with other thiols. In this Thesis, we have implemented experimental conditions for controlling ligand-place exchange reactions on $Au_{25}(SR)_{18}$ with the goal of introducing functional groups suitable to react with a specific monomer. After polymerization, a polylysine protected Au_{25} cluster could be prepared.

Table of Contents

Chapter 1. Introduction

1.1 From Gold Nanoparticles to Gold Nanoclusters

Research on colloidal gold nanoparticles dates back to the work by Michael Faraday who published a paper about the study of a gold colloid prepared by the reaction of aqueous $HAuCl_4$ and phosphorus (in ether).[1]

$$HAuCl_4 + P \rightarrow Au(sol)$$

In the following years, there were many efforts both from a synthetic viewpoint, particularly to achieve a precise dimensional control of the colloidal particles, and a theoretical perspective, to understand their outstanding stability, peculiar optical properties, structure, etc. In 1908, Mie published an important work[2] in which he successfully modeled the optical behavior of colloidal gold nanoparticles by solving the Maxwell equations. Among synthetic achievements, the method described by Zsigmondy for hydrosol formation by reduction of $HAuCl_4$ with formaldehyde is worth mentioning.[3] During the following decades, a large amount of new physicochemical properties and applications of fine gold particles were described, such as the huge enhancement of the Raman effect produced by colloidal gold nanoparticles,[4-8] which subsequently gave birth to the surface enhanced Raman spectroscopy technique.[9] The most significant advances took place in the late 1990s. New synthetic routes and advanced analytical methods allowed achieving better control over the preparation of nanoparticles and a deeper understating of their structures and properties. The amount of research carried out over the last two decades is enormous. Nonetheless, there is still a lot to be done from the viewpoint of synthetic control, analytical characterization, study of the fundamental properties, and theoretical modeling. One of the major issues the researchers always had to deal with is the dimensional control of gold nanoparticles. Before the '30s, the particles dimensions were commonly determined by methods such as ultramicroscopy,[3] X-ray diffraction (by means of the Scherrer method),[10] and ultracentrifugation (using the Stokes' law of sedimentation).[11] The latter two methods are still used for some applications. These methods, however, were largely substituted when transmission electron microscopy (TEM) was introduced.[12-14] In addition to accurately measuring the particles dimensions, TEM microscopy also provides detailed information on their shape and, in some cases, crystalline structure.[15]

The ultimate goal was to obtain truly "monodisperse" nanoparticles, in which the dimensions could be controlled at the atomic level and where all particles have exactly the same dimension, shape, and structure. However, until recently, the researchers managed to obtain only more or less polydisperse systems, characterized by average dimensions, with a certain standard deviation always present. The issue was at least partially overcome in the 2000s, for ultrasmall gold nanoparticles with dimensions ranging from a fraction of nanometer to about 2 nm.[16,17] Due to their tiny dimensions, atomically determined composition and often molecular behavior (this issue will be addressed below in detail), these systems are usually called gold nanoclusters to distinguish them from the larger and less well defined gold nanoparticles.[18] The term “cluster” indicates the presence of metal-metal bonds and structures different from the usual structure of bulk gold, and usually applies to objects smaller than the common nanoparticles.

Because of their molecular or nearly molecular characteristics, gold nanoclusters can be analyzed by typical molecular techniques. As a matter of fact, the dimensions and monodespersity of gold nanoclusters can be precisely evaluated by mass spectrometry, while their crystal structure can be accurately determined by single crystal X-ray crystallography with additional information provided by nuclear magnetic resonance (NMR) spectroscopy. Electrochemistry and UV-visible spectroscopy provide information on the energy levels of these systems.[18-21] To be stable, the gold clusters must be protected by a molecular monolayer.[18,19] These clusters are indeed often referred to as monolayer-protected clusters (MPCs). The most commonly used protecting ligands are thiolates, mainly because of the remarkable strength of the gold-sulfur bond.

Au MPCs are of paramount importance from the viewpoint of both applications and fundamental science. Regarding the latter, they help to increase our understanding of the properties of gold nanoparticles, including the larger ones.

In this field, some peculiar features are indeed still poorly understood and important questions remain unanswered. First, the structure of the dynamic protecting monolayer is not completely clear. Particularly, it is still not clearly established what exactly protects the nanoparticles surface, how the ligands are bonded to the Au core and, most importantly, what determines the stability of the monolayer-protected nanoparticles. Second, the structure and the properties of small nanoparticles (diameters of <3 nm) are not fully understood. In particular, a full comprehension of the transition from the metallic behavior of larger nanoparticles to the molecular behavior peculiar of small clusters is still missing, though research in this field is very active.[22-25] An approach for describing the properties of the clusters/particles in the intermediate dimensional range is still to be found. Finally, many aspects of the shape-controlled self-assembly of the particles are still unclear: questions arise regarding the formation of anisotropic nanoparticles, on how the ligands bond to the metal core, and whether this process is kinetically or thermodynamically driven.

As aforementioned, Au MPCs, especially ultrasmall MPCs, could potentially contribute to answering all these important questions. The first atomically defined monolayer-protected cluster dates back to as far as 1969. It was a Au_{11} cluster protected with phosphine and thiocyanate ligands, specifically $Au_{11}(PPh_3)_7(SCN)_3$, prepared by Mason and his coworkers.[26] In the following decades, several other gold clusters were described, such as $Au_{55}\{P(C_6H_5)_3\}_{12}Cl_6$, synthesized in 1981 by the Schmid group.[27] An important step for the development and understanding of this field was the publication by Nuzzo and Allara of a study in which they described the formation of a self-assembled monolayer on a gold surface.[28,29] In 1994, Brust et al. developed an innovative method for the synthesis of thiolate-protected Au nanoparticles,[30] which became a real breakthrough in the field. It was now clear that the capping thiols are very efficient in stabilizing the small gold cores and preventing their aggregation. In the following years, the field of thiol protected MPCs developed very quickly, with a large amount of structures and properties being continuously discovered.[18-20,30]

Concerning the theoretical aspects, a turning point in the understanding of the properties of Au MPCs was the groundbreaking study by Walter et al.[31] that showed that the electronic properties of many MPCs can be successfully described by the superatom concept. Using this model, the authors were able to rationalize the stability and some properties of several already isolated and experimentally characterized clusters, but they also managed to predict some stable structures, which were later synthesized.

1.2 The Benchmark Gold Nanocluster: $Au_{25}(SR)_{18}$

Since the structure of the first atomically precise Au nanocluster entirely protected by thiolates, $Au_{102}(SR)_{44}$, was reported,[32] the quest for preparing and characterizing new nanoclusters underwent spread rapidly worldwide. Up to now, more than 40 monothiolated Au nanoclusters with an atomically precise structure have been reported, such as Au_{18}, Au_{20}, Au_{21}, Au_{23}, Au_{24}, Au_{25}, Au_{28}, Au_{30}, Au_{34}, Au_{36}, Au_{38}, Au_{40}, Au_{42}, Au_{43}, Au_{44}, Au_{49}, Au_{52}, Au_{60}, Au_{92}, Au_{102}, Au_{103}, Au_{130}, Au_{133}, Au_{144}[25,33] Au_{146}, Au_{246}, and Au_{279}.[34-67] In addition, several other monodispersed Au nanoclusters were also synthesized, though their crystal structures could not be solved.[41,68-72] Among these atomically precise nanoclusters of well-defined structure, $Au_{25}(SR)_{18}$ and its several derivatives hold a very special place in the nanocluster field (Scheme 1.1). The reasons for this are the early discovery, the ease by which they can be prepared, their general high stability and ease of functionalization, and their interesting applications.[73-75] Through many years of efforts and developments, the physicochemical properties of $Au_{25}(SR)_{18}$ have been investigated, including catalytic, optical, electrochemical, chiral, and magnetic properties.[18,21,23,76-80]

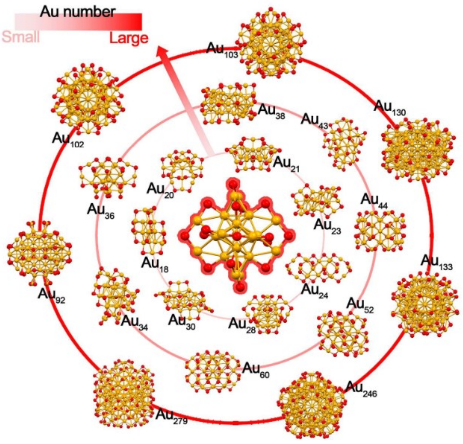

Scheme 1.1. Summary of the Au nanoclusters (protected by thiolates) with atomically precise structures. (From ref. 32, 35, 37-49, 55, 57, 64-67, 169, 189)

Moreover, as depicted in Scheme 1.2, $Au_{25}(SR)_{18}$ and its several functionalized derivatives simulate great interest not only in theoretical research, but also for practical applications. For instance, the available crystal structure of the $Au_{25}(SR)_{18}$ permits the correlation of its catalytic activity with the atomically precise structure.[81] Furthermore, due to the high biocompatibility, good photostability, and low toxicity, hydrophilic $Au_{25}(SR)_{18}$ nanoclusters are highly promising candidates for applications in the biological field, such as cell labeling, phototherapy, and biosensing.[82-86]

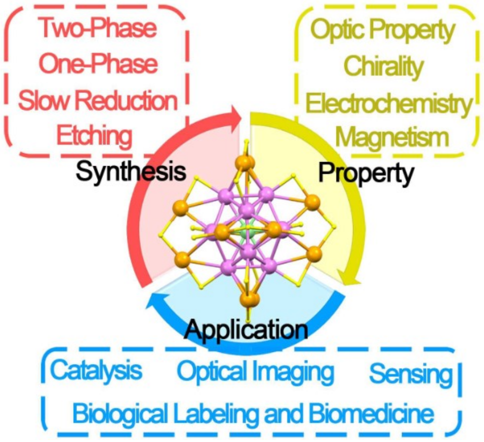

Scheme 1.2. Syntheses, properties, and applications of the $Au_{25}(SR)_{18}$ nanocluster. (From ref. 189)

1.2.1 Synthetic Methods

Despite the remarkably aforementioned progresses that have been made in the syntheses of $Au_{25}(SR)_{18}$, the synthetic procedures often suffer from the formation of other nanocluster sizes, and thus the yield of $Au_{25}(SR)_{18}$ can be quite low;[87-90] $Au_{25}(SR)_{18}$ can be separated from these mixtures by using several techniques, such as liquid-phase extraction and high performance liquid chromatography.[91-93] In this context, the possibility of achieving a high-yield and high-purity in the synthesis of $Au_{25}(SR)_{18}$ has been an important target. In 2008, the Jin group devised a kinetically controlled, thermodynamically selective strategy (Scheme 3a.),[83] which was mainly related to the Brust-Schiffrin two-phase method.[34] Not long after, in 2010, the Murray group presented a one-phase (tetrahydrofuran, THF) synthetic method for preparing the monodisperse $[TOA]^+[Au_{25}(SR)_{18}]^-$ in high yield (~ 50 % yield, based on Au source in $HAuCl_4$) (Scheme 3b.).[84] They synthesized Au_{25} nanoclusters protected by various thiols. The successful preparations of these $Au_{25}(SR)_{18}^-$ nanoclusters highlighted the benefits of this synthetic procedure.

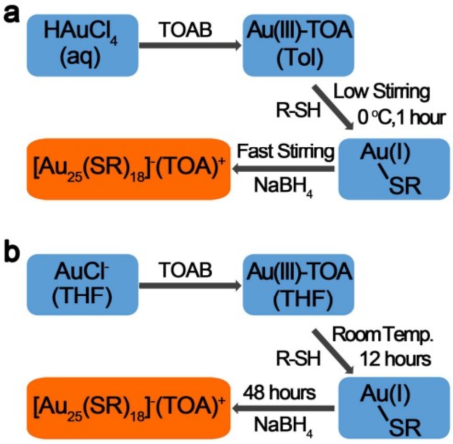

Scheme 1.3. Schematic illustration for the formation of $Au_{25}(SC_2H_4Ph)_{18}$ nanocluster by (a) kinetically controlled, thermodynamically selective two-phase strategy (Jin Group) and (b) one-phase and in-situ synthetic method (Murray Group). (From ref. 74 and 75)

1.2.2 Different Charge State of $Au_{25}(SR)_{18}$

The $Au_{25}(SR)_{18}^{-}$ nanocluster, which contains 25 gold atoms and 18 capping ligands, is an $8e^{-}$ system that corresponds to a noble gas-like $^{1}S_{2}{}^{1}P_{6}$ superatom electron configuration.[100] The electron configuration of $Au_{25}(SR)_{18}$ can be modified from the $^{1}S_{2}{}^{1}P_{6}$, to the $^{1}S_{2}{}^{1}P_{5}$ and $^{1}S_{2}{}^{1}P_{4}$ configuration as one goes from $Au_{25}(SR)_{18}^{-}$ to $Au_{25}(SR)_{18}^{0}$ and $Au_{25}(SR)_{18}^{+}$, respectively. It should be noted that in the aforementioned preparations $Au_{25}(SR)_{18}$ is obtained as an anion; TOABr (tetraoctylammonium bromide) is added as a phase transfer agent (two-phase method) and, notably, provides the countercation.[102] The Maran group synthesized $Au_{25}(SC_{2}H_{4}Ph)_{18}$ (hereafter, we will indicate the number of carbon atoms of the alkyl chain simply as Cn: e.g., $SC_{2}H_{4}Ph$ will be denoted as SC2Ph) in its -1 and 0 charge states and oxidized them with bis(pentafluorobenzoyl) peroxide to form the corresponding cation.[94] NMR results of these three nanoclusters nicely match the corresponding structures, which shows the presence of two different ligand populations in the capping monolayer. In addition, the similar NMR patterns of Au_{25} nanoclusters with +1 and -1 charge states showed that also $Au_{25}(SC2Ph)_{18}^{+}$ is a diamagnetic species. In 2013, the Maran group synthesized $Au_{25}(SC2Ph)_{18}^{0}$ and studied its reduction or oxidation, in dichloromethane (DCM) containing 0.1 M tetrabutylammonium hexafluorophosphate (TBAH), to a series of charge states, -2, -1, +1, +2, and +3, under cyclic voltammetry (CV) or differential pulse voltammetry (DPV) conditions (Fig. 12).[95] Concerning the lifetime of the various oxidation states, the order is $Au_{25}(SR)_{18}^{2-}$ (4 ms) < $Au_{25}(SR)_{18}^{3+}$ (20 ms) < $Au_{25}(SR)_{18}^{2+}$ (0.33 s) (Figure 1.1).

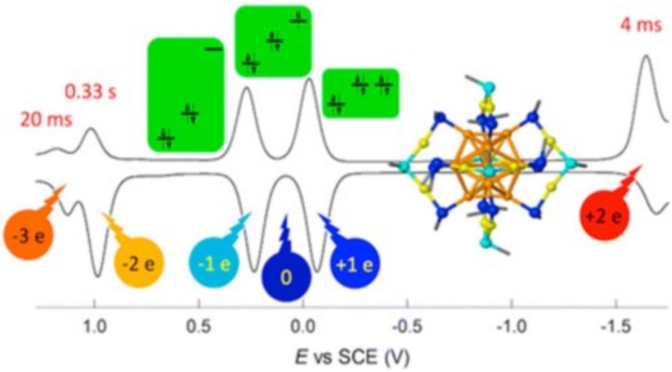

Figure 1.1. DPV evidencing the different charge states (-2, -1, 0, +1, +2, +3 charge states) and lifetimes of $Au_{25}(SR)_{18}$ nanocluster in DCM/0.1 M TBAH. (From ref. 95)

The physicochemical properties are determined by the structures of the nanoclusters. Accordingly, the Au_{25} nanoclusters with different charge states should have differently electronic structure and show slightly different properties. Tofanelli et al. reported the crystal structures of $Au_{25}(SR)_{18}$ in its -1, 0, and +1 charge states, in which the differences between oxidation state, structure, and magnetism were described in terms of first-order Jahn-Teller distortions.[96, 97] The noble gas-like configuration ($^1S_2{}^1P_6$) is at the basis of the $Au_{25}(SR)_{18}^-$ diamagnetism and comparatively high thermal stability. As to $Au_{25}(SR)_{18}^0$, which has a $^1S_2{}^1P_5$ superatom electron configuration, the unpaired 1p electron is the origin of its paramagnetism. Larger distortions are observed in $Au_{25}(SR)_{18}^+$ compared with Au_{25} nanoclusters with 0 or -1 charge states, which is caused by the unoccupied P orbital. It should be noted, however, that similar conclusions were previously described by the Maran group as a consequence of in-depth studies on the reorganization energies affecting the relevant electrochemical processes.[98, 111]

1.2.3 Crystallography of $Au_{25}(SR)_{18}$

$Au_{25}(SR)_{18}$ nanocluster has an icosahedral Au_{13} core (the Au_{12} icosahedron contains a central Au atom) and this core is capped by six pairs of $Au_2(SR)_3$ staple motifs to form a core-shell system (Figure 1.2a.-c. and Figure 1.3). These six $Au_2(SR)_3$ staple motifs are all in the "V-shape" semi-ring configuration (Figure 1.2b.). It should be noted that the icosahedron possesses 20 triangular faces. Except for the 12 faces on the icosahedral Au_{13} kernel capped by the staple motifs, eight Au_3 faces of the icosahedron are uncapped (Figure 1.2d.).

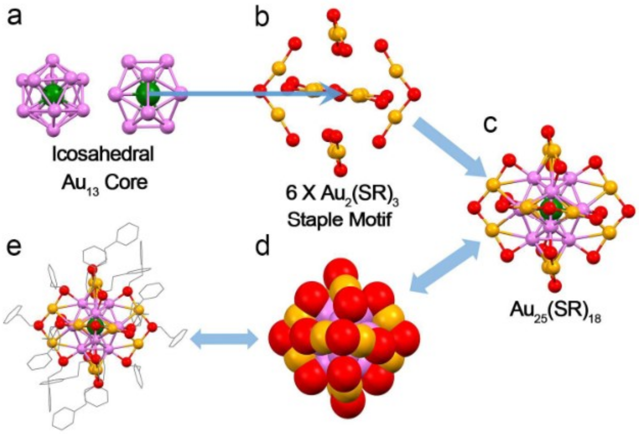

Figure 1.2. Structural anatomy of $Au_{25}(SR)_{18}$ nanocluster. (a) Icosahedral Au_{13} core. (b) Six pairs of $Au_2(SR)_3$ staple motifs. (c) Core-shell structure of $Au_{25}(SR)_{18}$, in ball-and-stick rendering. (d) Core-shell structure of $Au_{25}(SR)_{18}$, in with space-fill rendering mode. (e) Overall structure of $Au_{25}(SR)_{18}$.

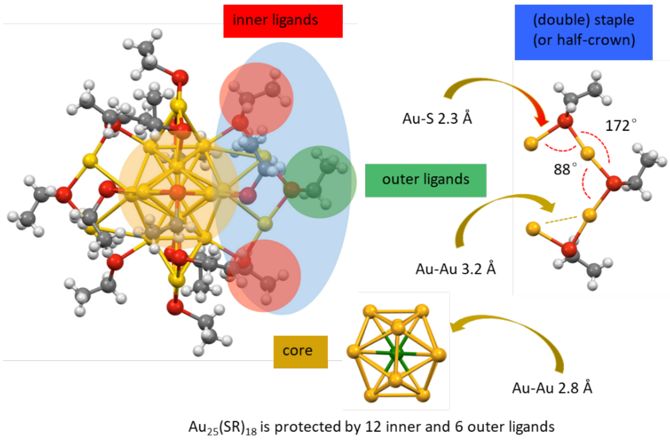

Figure 1.3. Structural anatomy of $Au_{25}(SR)_{18}$ nanocluster. (From ref. 99)

In 2014, the Maran group reported the synthesis and crystal structure of $Au_{25}(SC2)_{18}{}^0$.[99] Black crystals of this nanocluster were obtained by vapor diffusion of diisopropyl ether into a toluene solution of $Au_{25}(SC2)_{18}{}^0$. Using the same method, the crystal structure of polymeric $[Au_{25}(SC4)_{18}]_n$ has also been obtained.[111] Very recently, the Maran group also reported an electro-crystallization strategy to prepare the crystals of nanoclusters in large quantity and very high quality (Figure 4).[102] Electrocrystallization was tested to obtain the crystals of a series of $Au_{25}(SR)_{18}$ nanoclusters. With this strategy, a new polymeric structure could be evidenced for $[Au_{25}(SC5)_{18}]_n$ and unprecedentedly pure $Au_{25}(SC2Ph)_{18}^0$ crystals.

Figure 1.4. Different shapes of crystals of $Au_{25}(SC5)_{18}^0$, $Au_{25}(SC4)_{18}^0$, and $Au_{25}(SC2Ph)_{18}^0$ nanoclusters covering the electrode surface, as prepared by the electrocrystallization strategy. (From ref. 102)

Our group found that the paramagnetic $Au_{25}(SC4)_{18}^0$ could self-assemble into a linear polymer of nanoclusters connected via single Au-Au aurophilic bonds and stabilized by proper orientation of the staples and dispersion interactions between the SC4 ligands of neighboring clusters (Figure 1.5a.). The intermolecular Au-Au bond distance was found to be 3.152 Å, similar to the average Au-Au bond distances of core-shell Au-motif Au (Figure 1.5b). However, for Au_{25} capped by SC2 or SC2Ph ligands, no polymerization was observed, which implies that too short or sterically hindered ligands are not suitable for stabilizing the 1D polymer composed by a regular sequence of nanoclusters (see Figure 1.5c for the crystal packing mode of unassembled Au_{25} protected by SC2 ligands).[95]

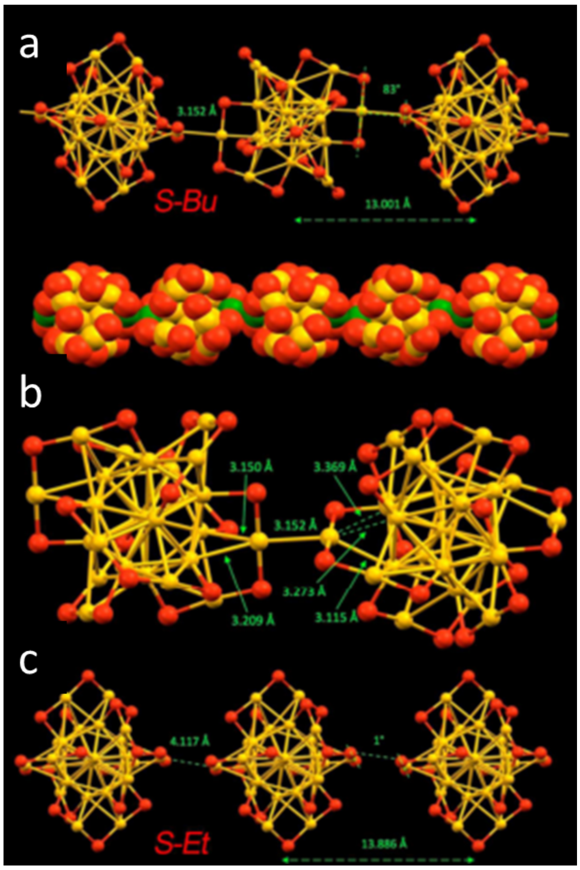

Figure 1.5. Structural/Packing-mode comparison of Au_{25} with different charge states or capped ligands. (a, b) Self-assembled $Au_{25}(SC4)_{18}^0$ nanoclusters with via single Au-Au bonds to compose a linear polymer. (c) Un-assembled $Au_{25}(SC2)_{18}^0$ nanoclusters. (From ref. 96)

1.3 Modification of Properties: Doping, Ligand Exchange and Transformation

Up to now, various strategies have been developed to modify the properties of gold nanoclusters, such as: (i) capping the metal core surface with different types of ligands to modify the protecting monolayer, such as by ligand exchange reactions;[103-105] (ii) doping the cluster with other metal atoms to modify the metallic part of the nanocluster,[106,107] and (iii) using transformation reaction aimed to modify the core size of nanoclusters.[44]

1.3.1 Doping and Alloy

Recently, research has also been focusing on the selective doping of metal nanoclusters through introduction of foreign-metal atoms. This is a very important area for both fundamental (e.g., modification of the electronic properties) and applied (e.g., catalysis) purposes. Modification of the metal composition has been studied for several clusters, but most research has focused on $Au_{25}(SR)_{18}$, which is an atomically precise cluster that has been long considered a convenient benchmark system for understanding properties and devising applications of gold nanoclusters.

Au-Ag Doping

When Ag atoms are doped into $Au_n(SR)_m$ nanoclusters, the dopant atoms tend to distribute on the metal−thiolate interface, instead of the cluster center, as demonstrated by the crystal structures of $Ag_xAu_{25-x}(SR)_{18}$ and $Ag_xAu_{38-x}(SR)_{24}$ reported by Kumara et al.[108,109] Xiang et al. recently reported the X-ray structure of $Au_{15}Ag_3(SC_6H_{11})_{14}$, in which the three Ag dopants are located in the middle layer of the nine-atom hcp three-layer structure.[110] Molina and Tlahuice-Flores[111] theoretically analyzed the structures and chiroptical properties of thiolated $Au_{18-x}Ag_x$ clusters and found that doping with more than four Ag atoms results in enhancement of the HOMO−LUMO peak’s oscillator strength. Heavy doping of $Au_{25}(SR)_{18}$ with Ag (up to ∼20 Ag atoms) was also reported by Li et al.,[112] in which the Ag dopants were located in both the icosahedron and staples.

The bimetallic Au−Ag nanoclusters in which the Ag dopants were preferentially located in the inner core were found to exhibit weaker CD signals than the nondoped gold nanoclusters.[113] This effect was explained in terms of the multiple geometrical isomers of bimetallic nanoclusters because an increased number of possible configurations gives an average in the CD response with positive and negative bands of different optical isomers being somewhat averaged out.

Doping gold nanoclusters with silver also can dramatically enhance the luminescence. One example is the rod-shaped $[Au_{25-x}Ag_x(PPh_3)_{10}(SC_2H_4Ph)_5Cl_2]^{2+}$ (quantum yield, QY = 40 − 60%).[107] This extraordinary QY was obtained by site-specific doping of $[Au_{25}(PPh_3)_{10}(SC_2H_4Ph)_5Cl_2]^{2+}$ (QY ≈ 0.1%) with 13 silver atoms, whereas doping of less than 13 atoms did not induce a high luminescence. Silver doping into $Au_{25}(SR)_{18}$ was found to exhibit largely enhanced hyperpolarizabilities since the doping eliminates the centrosymmetry.[113,114]

Au-Pt/ Pd Doping

The very first example of an atomically precise bimetallic cluster, $Au_{24}Pd(SR)_{18}$, was synthesized by the Murray group,[116] which was further examined by Tsukuda and collaborators[117] in greater detail. Negishi et al. obtained pure $Au_{24}Pd(SR)_{18}$ nanoclusters by chromatographic isolation and concluded that the dopant site is in the icosahedral center on the basis of experimental and theoretical results.[118] Qian et al. also obtained pure $Au_{24}Pd(SR)_{18}$ and observed $Au_{37}Pd(SR)_{24}$ and $Au_{36}Pd_2(SR)_{24}$ in mass spectrometry analysis.[119]

Pt doping into gold nanoclusters is particularly challenging in terms of characterization because of the very similar masses and electron-scattering capabilities of Pt and Au.[120] X-ray absorption spectroscopy was used to probe the Pt position in the mono-Pt-doped, $Au_{24}Pt(SR)_{18}$ nanocluster.[121] Kwak et al.[122] recently investigated the six-electron configurations of native neutral $Au_{24}M(SR)_{18}^0$ (M = Pd, Pt) nanoclusters and revealed an oblate shape of the $Au_{12}M$ kernel due to Jahn−Teller distortion of the 6e configuration, whereas the 8e system has no distortion. The optical absorption spectrum of $Au_{24}Pd(SR)_{18}$ is similar to that of the undoped cluster, but the corresponding spectrum of $Au_{24}Pt(SR)_{18}$ differs dramatically from that of the undoped cluster. Such a trend is also reflected in the transient spectra and ultrafast relaxation dynamics of $Au_{24}M(SR)_{18}$ (M = Pd, Pt, R= C2Ph) clusters.[123]

Negishi et al. used HPLC to isolate $Au_{24}Pd(SR)_{18}$ with high purity. Figure 1.6 shows the MALDI-MS of the isolated $Au_{24}Pd(SR)_{18}$ cluster and its monometallic analogue $Au_{25}(SR)_{18}$, which differs by mass units. From a detailed structural analysis, it was inferred that the Pd atom sits in the central position of the icosahedral core and that the alloy cluster has an enhanced stability compared to the $Au_{25}(SR)_{18}$ cluster. The position of Pd was further confirmed from the recent crystal structure of $Au_{24}Pd(SR)_{18}$ cluster (inset of Figure 1.6).[124]

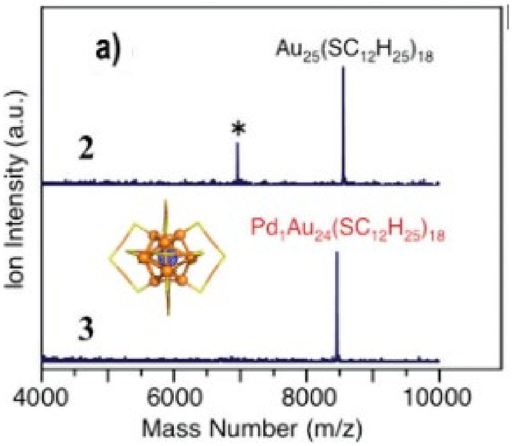

Figure 1.6. Negative-ion MALDI mass spectra of Au_{25} cluster and $PdAu_{24}$ cluster separated by HPLC. Inset shows the recent crystal structure of $Au_{24}Pd(PET)_{18}$. (From ref. 124)

The Ag_{44} structure (vide infra) was shown to be quite different from that of the same size $Au_{44}(SR)_{28}$ nanocluster. Thus, it was thought that Ag nanoclusters might follow quite different structural rules than gold nanoclusters. However, the structures of $Ag_{25}(SR)_{18}^{-}$[125] and monodoped $Ag_{24}M(SR)_{18}^{2-}$ nanoclusters (M = Pd, Pt)[126] were subsequently found to be essentially identical to that of $Au_{25}(SR)_{18}$.[41,42] Thus, the extent to which the $Ag_n(SR)_m$ and $Au_n(SR)_m$ systems behave differently still remains to be clarified.

Xie et al. developed Au_{25} and $Au_{24}Pd$ cluster-based catalysts supported on multiwalled carbon nanotubes.[127] Their study shows that single Pd atom doping can significantly improve the catalytic performance. In subsequent works, the Bürgi group systematically studied the racemization,[128] effect of Pd doping,[129] and other aspects.[80, 130, 131] The gold−thiolate interface was deemed to be flexible. The activation energy for the racemization of one enantiomer into the other was experimentally determined to be ~28 kcal/mol, which is quite low. Palladium doping in the 38-atom nanocluster was found to further reduce the activation energy to ~20 kcal/mol, but the anisotropy factor remained the same. The chirality of the Au_{38} core was also found to transfer to the achiral -SC2Ph ligand, resulting in a chiral conformation of the ligand, as evidenced by the observation of strong vibrational circular dichroism (VCD) signals of the surface ligands.

Au-Cu Doping

Cu doping is another special example. Gottlieb et al. synthesized the $Cu_xAu_{25-x}(SR)_{18}$ nanocluster in-situ and determined the Cu-doping atoms by MALDI-TOF mass spectrometry. It is suggested that no more than four Au atoms can be substituted by Cu atoms. Interestingly, a time-dependent de-alloying process was observed. In other word, the stability of $Cu_xAu_{25-x}(SR)_{18}$ is far weaker than that of the $Au_{25}(SR)_{18}$ nanoclusters.[132,133] In 2015, Hartman et al.[134] theoretically analyzed the energetics and optical spectra of $Au_{25-x}Cu_x(SH)_{18}^-$ and compared the three unique sites for the Cu dopant.

The number of Ag or Cu atoms doped into the clusters is typically a distribution that can be controlled to some degree by changing the initial ratio of gold and silver salts in the synthesis. Zhu and co-workers[135] recently reported a metal-exchange method for the synthesis of $Au_{25-x}Cu_x(SR)_{18}$, $Au_{25-x}Ag_x(SR)_{18}$, $Au_{24}Cd(SR)_{18}$, and $Au_{24}Hg(SR)_{18}$ through reactions of $Au_{25}(SR)_{18}$ with metal−thiolate complexes of Cu(II), Ag(I), Cd(II), and Hg(II), respectively, as opposed to common salt precursors such as $CuCl_2$ and $AgNO_3$. Their results indicated that the exchange between gold sites in the cluster structure and the incoming heterometal atoms does not necessarily follow the metal nobility order (i.e., galvanic sequence).

Au-Cd/ Hg/ Ir Doping

For $Au_{24}Cd(SR)_{18}$, the Cd dopant was described to be located at the center of the 13-atom icosahedral core.[135] In a related study, however, the Wu group reported that the Hg dopant in $Au_{24}Hg(SR)_{18}$ is surprisingly located in the staple, whereas Cd goes on the icosahedron.[136] Au_{25} could be transformed into alloy clusters composed of three different metals, with the general formula $Ag_xAu_{24-x}M(SR)_{18}$ (M = Cd, Hg)[137,138] Pradeep and his co-workers found that besides reacting with $Ag_{44}(SR)_{32}$ and $Ag_{25}(SR)_{18}$ nanoclusters, $Au_{25}(SR)_{18}$ nanocluster could also react with $Ir_9(SR)_6$ to generate the bi-metallic $Au_{22}Ir_3$ nanocluster. DFT calculations were performed to understand the favorable geometry of the $Au_{22}Ir_3(SR)_{18}$ nanocluster, where the first Ir atom prefers to occupy the central position of the $Au_{25}(SR)_{18}$ nanocluster, whereas the second and third Ir atoms will metal-exchange the Au atoms on the surface of the icosahedral $Au_{12}Ir$ kernel, generating the center-doped $Au_{22}Ir_3(SR)_{18}$ nanocluster.[139]

General considerations on Doping

Substituting one or more gold atoms with heteroatom(s) of other metal elements, such as Pd, Pt, Ag, and Cu, provides an exciting opportunity to tune the electronic, optical, and catalytic properties of nanoclusters and also to gain a deeper understanding of the stability and other aspects of nanoclusters.[140,141] Interesting questions include how many heteroatoms can be doped into the parent cluster and how/where these heteroatoms are distributed.[140-142]

Determining the doping sites of heterometal atoms will provide fundamental insight into the alloying and intermetallic properties of gold-based nanoclusters. Besides the aforementioned foreign-metal atoms, theoretical work suggests the compatibility of magnetic elements such as Fe, Co, and Ni in the cluster structures.[143,144] In the bulk state, gold−cobalt can indeed be made, but attempts to prepare alloy nanoclusters have not been successful. New synthetic strategies should, therefore, be devised. Magnetic-metal doping would be interesting to gain more insights into clusters' magnetism, as well as spin coupling.

The dopant position, as well as the proximity of two dopants, was found to influence the electronic structure. Fortunelli, Stener, Dass and their co-workers studied the enhancing effects of doping and ligand on the optical absorption of Au and Au-Ag nanoclusters.[145,146] Bimetallic nanostructures,[147] especially clusters, are of tremendous interest, particularly in the field of catalysis, because of their distinct properties from their corresponding monometallic counterparts.[148]

So far, the synthetic strategies for alloying $Au_{25-x}M_x(SR)_{18}$ nanoclusters can be classified into two classes: (i) in-situ synthesis through reducing the mixture of Au-SR and M-SR complexes; (ii) doping the templated $Au_{25}(SR)_{18}$ nanocluster with heteroatom complexes. The early in-situ syntheses of alloyed $Au_{25-x}M_x(SR)_{18}$ nanoclusters are almost entirely based on the synthetic method used to prepare the monometallic $Au_{25}(SR)_{18}$ nanoclusters. Different methods, such as UV-vis, MALDI-MS, ESI-MS, CV, DPV, X-ray crystallography, have been utilized to understand whether the alloy process occurred or not and how many heteroatoms were alloyed into the $Au_{25}(SR)_{18}$ nanocluster.

Up to the present, the alloying based on the template of $Au_{25}(SR)_{18}$ has been achieved for Ag, Pt, Pd, Cu, Hg, Cd, and Ir. DFT calculations have also been performed on the heteroatoms of Ge, Sn, Pb, Zn, Ni, Fe, Co, and Rh. The reaction conditions, including solvent, temperature, oxygen, reaction time, and stirring speed, are all significant in preparing the alloy nanoclusters with different composition and stability. Future work is expected to gather more insights into the alloy effect on the electronic structures and physicochemical properties. In addition, the preferential doping site of each heteroatom should be further analyzed, also to provide guidelines for improving the synthetic methods. Furthermore, alloying $Au_{25}(SR)_{18}$ with new types of metals, such as Ni, Zn and Fe, could lead to make novel functional nanoclusters for practical applications.

Controlled doping and the use of the ensuing clusters are indeed an important part of my Thesis. In Chapter 2, I describe a study focused on providing new insights and perspectives into this general problem and describing a possible experimental methodology to understand the actual doping location. The power of NMR spectroscopy and associated isotopic effects will be especially highlighted. In Chapter 3, I describe the singlet-oxygen photosensitizing behavior of a series of $Au_{25}(SR)_{18}^-$ and monodoped $Au_{25}M(SR)_{18}$ (M = Cd, Hg) clusters. The analysis was extended to monodoped clusters because the electrochemical and optical behaviors of these clusters show significant differences that are related to the relative energies of the corresponding highest occupied and lowest unoccupied molecular orbitals (HOMO and LUMO). As we will see, these aspects are crucial to determine the efficiency of photosensitization.

1.3.2 Ligand Exchange

Nanoclusters with functionalized ligands (e.g., bearing -NH_2, -COOH, polymerizable groups, or signal reporters) are particularly important for sensing and other applications. Functionalization can be achieved by carrying out the synthesis directly from a mixture of appropriate thiols[149-151] or *via* reactions of reactive groups present on the outermost part of the capping monolayer. The best method, however, is to take advantage of thiolate-ligand place-exchange reactions. In the latter, thiolates of preformed nanoclusters are exchanged with exogenous thiols, a modification path implemented several years ago by the Murray group.[152] Exchange reactions are particularly useful, *e.g.*, to introduce expensive/ less easily available thiols, when the target thiols carry groups that are unstable during the reducing conditions typical of the widely employed Brust-Schiffrin type direct synthesis approach,[30] or when solubility issues would prevent controlling the cluster size in direct syntheses, such as when hydrophilic terminated thiols are employed in organic solvents and cause precipitation of the so-formed hydrophilic transient clusters. These concepts have been discussed in good detail.[153-156] Ligand exchange is also the most suitable and convenient way to incorporate desired properties such as FRET, chirality, etc., in a given monolayer protected noble metal cluster.[157-160] The general idea of ligand exchange is to keep the cluster core intact while the shell is modified. Besides modifying the monolayer, ligand exchange also provides a platform for thoroughly analyzing the intermolecular reaction process on the nanocluster surface.

In 2005, Shichibu et al. reported the large-scale synthesis of $Au_{25}(SG)_{18}$ from phosphine stabilized Au_{11} nanocluster with ligand exchange method.[161] The Pradeep group has also shown several exchange possibilities and incorporation of diverse properties in the Au_{25} cluster.[162,163] However, ligand exchange can result in an increase of the core size, as it was demonstrated by Shichibu et al.[161]

For Au_{11} cluster; whose ligand exchange led to the formation of the most stable Au_{25} cluster. After that, the Bürgi group reported the ligand exchange on $Au_{25}(SC2Ph)_{18}$ with two chiral ligands R/ S-BINAS and NILC/ NIDC (where the R/ S-BINAS represents R/ S-1,1'-binaphthyl-2,2'-dithiol; the NILC/ NIDC represents N-isobutyryl-L-cysteine/ N-isobutyryl-D-cysteine).[158] In 2012, on the basis of the crystal structure of Au_{102}(SPh-*p*-COOH)$_{44}$, Ackerson and co-workers identified the ligand-exchange site, that is, the site that would be first to be subject to ligand exchange. Their results indicated that the incoming *p*-BBT (para-bromobenzene thiol) first attacks the top/bottom sites along the C_5 axis of the Au_{102} cluster, mapped out by the crystal structure of the exchanged nanocluster (Figure 1.7), in which two of the 22 symmetry-unique p-MBA ligand sites were found to be partially exchanged to *p*-BBT during a 5-min exchange reaction. In terms of the site-specificity mechanism, the involved surface Au atom sites were found to be accessible to solvent; hence, these sites were first attacked by the incoming thiol molecules. Based on the experimental results, further DFT calculations suggested a more detailed pathway for the thiol-for- thiol exchange mechanism.[164]

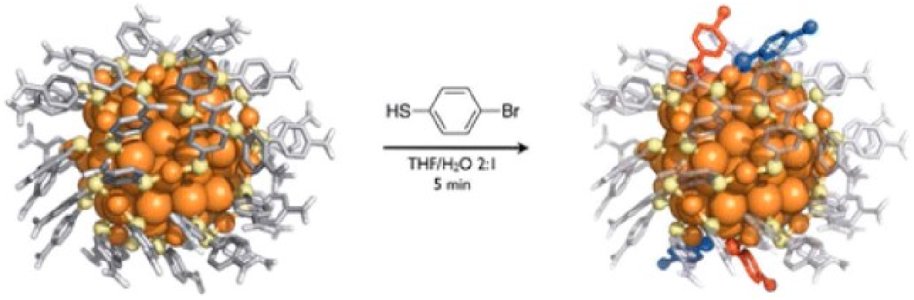

Figure 1.7. X-ray structure of a partially exchanged Au_{102}(*p*-MBA)$_{40}$(*p*-BBT)$_4$ cluster (*p*-MBA = para-mercaptobenzoic acid, *p*-BBT = para-bromobenzene thiol) with *p*-BBT as the incoming ligand. (From ref. 164)

In 2013, The Zhu group demonstrated ligand exchange of $Au_{25}(SR)_{18}$ with selenol and obtained $Au_{25}(SePh)_{18}$ and $Au_{18}(SePh)_{14}$.[165] The Negishi group has carried out extensive work on the high-resolution reverse-phase HPLC isolation of ligand- exchanged nanocluster isomers (Scheme 1.4).[153,166,167] They further isolated coordination isomers by HPLC; for example, the chromatogram of Pd@$Au_{24}(SR)_{17}(SR')_1$ showed that the major isomer corresponds to the SR′ ligand being at the inner site of the dimer staple, whereas the minor isomer shows the SR′ ligand being at the external site (Figure 1.8).

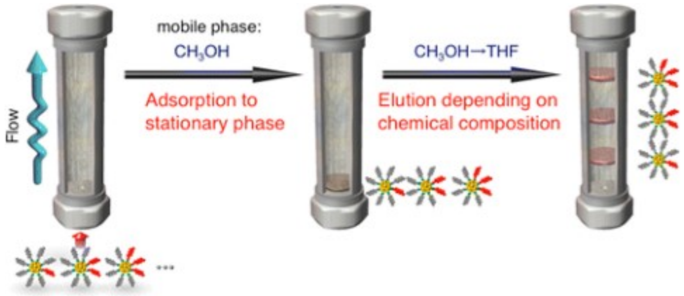

Scheme 1.4. Chromatographic Isolation of Ligand Isomers. (From ref. 153)

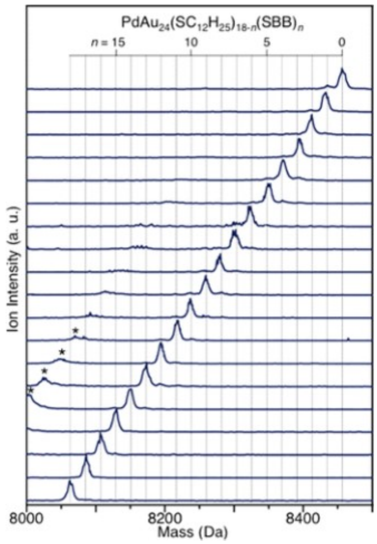

Figure 1.8. HPLC isolation of nanoclusters with different ligand compositions. MALDI mass spectra of isolated species of $Pd_1Au_{24}(SC_{12}H_{25})_{18-n}(SBB)_n$ according to n, where SBB = SCH_2Ph-^{t}Bu. (From ref. 166)

Niihori et al.[153] showed the precise isolation of ligand exchanged clusters taking $PdAu_{24}(SR)_{18}$ as an example. Each individual species of composition $PdAu_{24}(SR_1)_{18-n}(SR_2)_n$ (n = 0, 1, 2, ..., 18) was isolated using gradient HPLC. The corresponding chromatograms are displayed in Figure 1.9a. The mobile phase was systemically varied from pure MeOH to THF. The numbers 10, 20, 30, 40, and 50 in Figure 1.8a refer to the time (in minutes) taken for the mobile phase to become 100% THF, starting from pure MeOH. The corresponding mass spectral feature (Figure 1.9b) also shows an envelope similar to that of the HPLC chromatogram (Figure 1.9c). Each of these clusters was isolated and characterized using MALDI-MS. Recently, the Negishi group carried out an extensive study of the separation and isolation of alloy clusters, such as $Au_{24}Pd(SR_1)_{18-x}(SR_2)_x$ and $Au_{24}Pd(SR_1)_{18-x}(SeR_2)_x$ (SR_1, SR_2 = thiolate; SeR_2 = selenolate).[168] Precise isolation after ligand exchange reaction opens up the possibility of individual structure analysis of clusters.

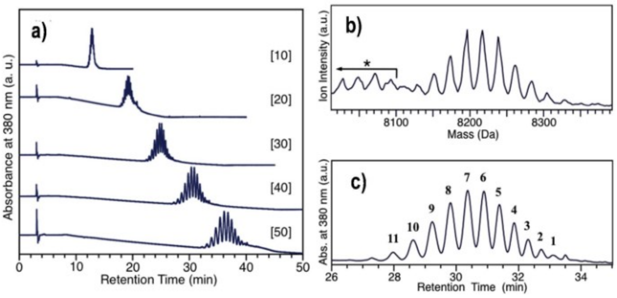

Figure 1.9. (a) Chromatograms of $PdAu_{24}(SC_{12}H_{25})_{18-n}(SBB)_n$ (n = 6−16) at different gradient programs. (b and c) Comparative MALDI mass spectra in negative mode (b) and chromatogram (c) of $PdAu_{24}(SC_{12}H_{25})_{18-n}(SBB)_n$ (n = 6-16) obtained using a gradient program, respectively. (From ref. 153)

In 2014, Ackerson and co-workers further determined the initial exchange site on the small nanocluster $Au_{25}(SR)_{18}$.[169] A pair of oppositely distributed ligands was found to be exchanged to *p*-BBT; again, these sites were the Au atoms most exposed to solvent, consistent with the Au_{102} case as well as an associative ligand-exchange mechanism. The Ackerson group reacted the $Au_{25}(SC6)_{18}$ nanocluster with 5-fold molar excess of *p*-bromobenzenethiol (*p*BBT), and the ligand-exchange process was stopped when reacted for 7 min. The crystal structure of the resulting $Au_{25}(SC)_{16}(pBBT)_2$ illustrated that the two ligand-exchange position was on the symmetric sites and bonded to the most solvent-exposed Au atom in the structure (Figure 1.10). This work was the first to describe on as a structural basis the outcome of a ligand exchange process on the $Au_{25}(SR)_{18}$ nanocluster and to show that the ligand exchange on $Au_{25}(SR)_{18}$ nanocluster is a stepwise process.[169] Of note, in 2014, Hutchison and co-workers found that the ligand-exchange from Au11 to $Au_{25}(SG)_{18}$ could be achieved by using $Au_{11}(PPh)_7Cl_3$. As to $[Au_{11}(PPh_3)_8Cl_2]Cl$, the products yielded only small nanoclusters relative to $Au_{25}(SG)_{18}$ (Figure 1.10).[170]

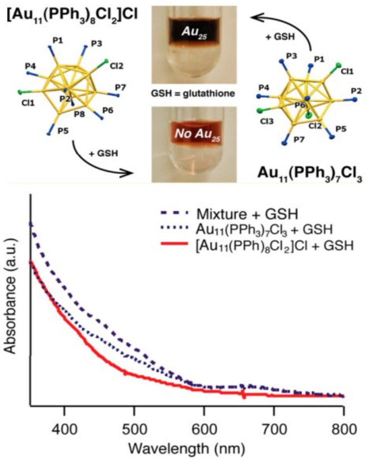

Figure 1.10. Resultants of ligand exchanging the $Au_{11}(PPh)_7Cl_3$ and $[Au_{11}(PPh_3)_8Cl_2]Cl$ with GSH. (From ref. 170)

In 2015, Theoretical work on ligand exchange by Aikens and co-workers found that the most favorable ligand exchange takes place between terminal -SH units and staple gold atoms.[171] Pengo et al. performed a kinetic analysis of the place exchange reaction on the $Au_{25}(SC2Ph)_{18}{}^0$ cluster using 4-fluorobenzylthiol and other substituted arylthiols and revealed that the selectivity for the inner and outer positions of the dimeric staples can be modulated by using incoming thiols with different structures.[172] The Aikens group theoretically investigated the kinetics of the ligand-exchange process based on the structure of $Au_{25}(SR)_{18}$ (where SR = SC1), and three possible ligand exchange sites were proposed.[173] Based on the results of ^1H NMR, the Murray group reported the second-order rate constants for associative ligand exchanges in $Au_{25}(S6)_{18}$ nanoclusters with different charge states, and concluded that the electron depletion retarded the ligand exchange.[173] In 2016, Negishi and co-workers systematically performed the ligand exchange on the $Au_{25}(SC2Ph)_{18}$ nanocluster with HSePh or $(TePh)_2$ ligands.[174] A broadening and red shift of the optical absorption bands was observed, also accompanied by the increasing substitution of the native SR ligands with SeR or TeR ligands.[174] Very recently, Bürgi and co-workers investigated the factors that influence the ligand exchange process in the reaction of $Au_{25}(SR)_{18}$ nanocluster with excess different thiol ligands and demonstrated that the thiolate monolayer of Au_{25} nanoclusters has a dynamic nature.[175]

In general, ESI-MS works well with aqueous soluble gold clusters as they are easily ionizable, whereas for organic soluble clusters this technique is not well-suited. Lately, several new methodologies have been implemented to overcome these problems. Researchers have shown that ionization efficiency can be improved by adding external ionizing agents such as cesium acetate (CsOAc).[176] Ligand exchange with an ionizable ligand is another way to obtain good mass spectral features.[89, 116] Negishi et al.[177] introduced an oxidation (by $Ce(SO_4)_2$) or a reduction (by $NaBH_4$) process to improve the ionizing capacity by enhancing the charge state of the $Au_{25}(SR)_{18}$ cluster (see Figure 1.11).

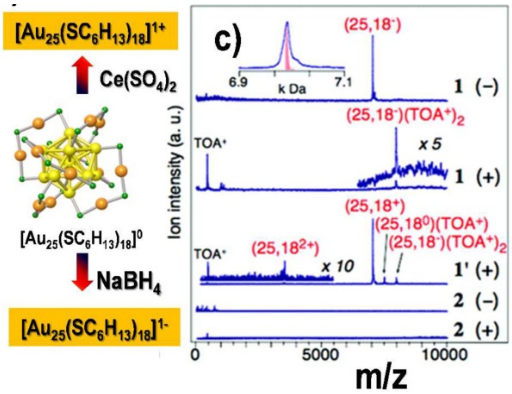

Figure 1.11. Scheme of positively and negatively charged $Au_{25}(SR)_{18}$ cluster synthesis from neutral $Au_{25}(SR)_{18}$ cluster. (From ref. 177)

Graphene, which contains carboxylic acid groups, was further functionalized to form thiolated graphene that was used in a ligand exchange reaction to generate a composite with gold clusters. The composite was purified by the phase transfer method. The optical properties of the composite exhibited the features of the cluster as well as those of graphene. Interestingly, the cluster fluorescence was only quenched when a high concentration of the thiolated graphene was used for the exchange process. A variety of nanocomposites can be generated by varying the functional groups, length, and properties of the linker molecules. Such composites can be used in several applications such as bioimaging,[178] biosensors,[31, 179] antibacterial activity,[180] etc.

Chirality can also be induced to an achiral cluster through ligand exchange with chiral ligands.[181] Yao et al.[182] achieved chirality in monolayer protected silver clusters by introducing chiral thiols. Dolamic et al. have shown that an intrinsically chiral gold cluster, $Au_{38}(2\text{-PET})_{24}$(2-PET = 2-phenylethylthiolate), can transfer its handedness to an achiral molecule (2-PET) adsorbed on its surface.[131]

In chapter 5, we will discuss the effects of ligand exchange reactions on the modification of the properties of $Au_{25}(SR)_{18}$ nanoclusters.

1.3.3 Transformation: Fusion

Recent research has revealed that nanoclusters are commonly composed of a kernel and a surface-protecting shell (or staple-like metal–ligand motifs). Understanding the kernel configuration and its evolution is one of the central topics in nanoscience research. Several basic kernel units have been observed, such as the M_4, M_{13} and M_{14} polyhedrons (where, M = metal atom). Among them, the tetrahedral M_4 and icosahedral M_{13} units are the most common ones, and as such they have been used as building blocks to construct larger kernel structures *via* various fusion or aggregation modes, including the vertex- and face-sharing mode, the double-strand and alternate single-strand growth, and cyclic fusion of units, as well as the fcc-based cubic growth pattern.[184] The identification of the kernel growth pathways has led to a deeper understanding of the evolution of electronic structure and optic properties.

Among the basic structural units of the kernel, the Au_{13} cuboctahedron, icosahedron, and decahedron are quite often observed. An important question is the growth of such building blocks into larger structures. In the following subsections, we summarize a few modes that have been observed experimentally, including the fusion, interpenetration, shell-by-shell, layer-by-layer, and Au_4 tetrahedron-based vertex-sharing growth modes. We note that the following discussion is based on structural aspects and that the growth modes might not necessarily reflect the real growth mechanisms of nanoclusters in the solution phase. Nevertheless, experimentally, fusion growth seems to occur in the conversion of Au_{11} to Au_{25} rod nanoclusters,[185] as well as the synthesis of linear triicosahedral Au_{37} nanoclusters,[186] with both being protected by mixed ligands (phosphines and thiolates).

The $Au_{38}(SR)_{24}$ nanocluster has a Au_{23} kernel, which can be viewed as two Au_{13} icosahedra fused together by sharing a common Au_3 face (Figure 1.12).[52] The fusion of the two icosahedra occurs along the C_3 axis of the icosahedron. The resultant Au_{23} rod is structurally strengthened by three monomeric staples at the waist (Figure 1.12); then, the top icosahedron is further capped by three dimeric staples that are arranged in a rotary fashion, resembling a triblade "propeller". Similarly, another three staples are arranged on the bottom icosahedron, but the bottom propeller is rotated by ~60° relative to the top one, forming a staggered dual-propeller configuration. The entire cluster is chiral because of the rotary arrangement of the dimeric staples, even though the Au_{23} kernel is achiral.

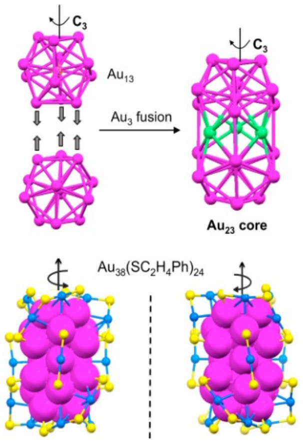

Figure 1.12. Total structure of $Au_{38}(SC2Ph)_{24}$. (Top) Au_{23} biicosahedral kernel and (bottom) positions of dimeric staple $Au_2(SR)_3$ and monomeric staple $Au(SR)_2$ on the kernel, as well as the two enantiomers. Yellow, sulfur; other colors, Au. The carbon tails (-SC2Ph) are omitted for clarity. (From ref. 52)

The $Au_{20}(SR)_{16}$ structure (R = $-Ph-^tBu$) exhibits a bitetrahedral Au_7 kernel, which can be viewed as two Au_4 building blocks fused together by vertex sharing (Figure 13).[36] Recently, a sharp transition from non-metallic $Au_{246}(SR)_{80}$ to plasmonic $Au_{279}(SR)_{84}$ has been revealed.[187] The unique properties of metal nanoclusters endow them with great potential for applications in catalysis, bioimaging, chemical sensing, and so on. Since the structures of nanoclusters exhibit certain patterns,[20] it is highly desirable to explore the structure–property correlation and thus understand the size evolution.

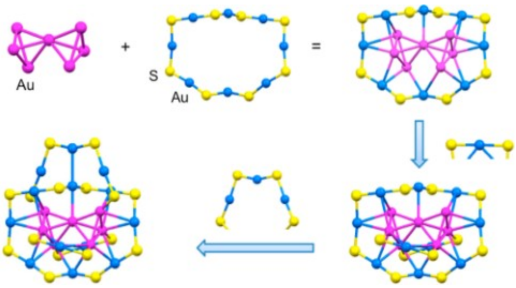

Figure 1.13. Anatomy of the structure of the $Au_{20}(SPh-^tBu)_{16}$ nanocluster. The Au_7 kernel is protected by an octameric ring motif and then by monomers (front and back of the kernel) and one trimer (top of the kernel). Carbon groups are omitted for clarity.

The 13-atom icosahedral structure (M_{13}) is a ubiquitous structural unit, which is composed of a center and a 12-atom shell of icosahedral geometry (Figure 1.14). Such a M_{13} kernel was reported in many works, *e.g.* the $Au_{13}(dppe)_5Cl_2^{3+}$ cluster (where, dppe = 1,2-bis(diphenylphosphino) ethane).[188] A rod-like bi-icosahedral $Au_{25}(PPh_3)_{10}(SR)_5Cl_2^{2+}$ nanocluster (R = C2 or C2Ph) has also been successfully synthesized and characterized.[189,204] The Au_{25} kernel structure is constructed via vertex sharing of two Au_{13} units (*i.e.*, 13+13−1=25). More interestingly, another icosahedron-based structure has recently been unveiled, with its formula being $Au_{37}(PPh_3)_{10}(SC2Ph)_{10}Cl_2^+$, in which the core comprises three Au_{13} building blocks that are linearly assembled together *via* vertex-sharing.[186]

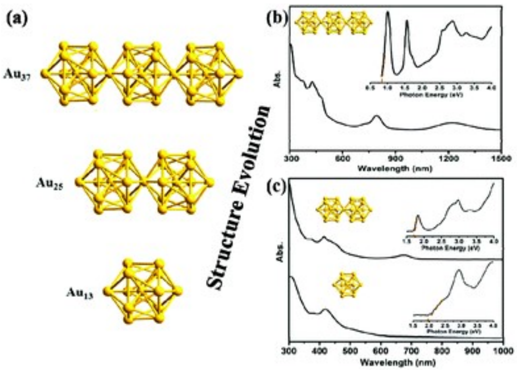

Figure 1.14. Kernel evolution in the Au_{13}-Au_{25}-Au_{37} series (a); UV-vis-NIR spectra of the Au_{37} (b) and Au_{25} and Au_{13} (c) nanoclusters (insets: spectra on the photon energy scale). (From ref. 186)

Transformation of clusters from one to the other presents new examples of chemistry at the nanometer length scale. It is likely that these reactions produce new examples of nanochemistry. The science of clusters is becoming analogous to that of molecules. Intercluster chemistry has shown several examples, and they suggest that the science of clusters is similar to that of simple molecules. Clusters with their cores and ligands act as single entities in these transformations. This new category of chemistry is distinctly different from that of the ligands and the cores which have been probed in more detail.

In chapter 4, we demonstrate that it is possible to transform $Au_{25}(SR)_{18}$ directly into $Au_{38}(SR)_{24}$ by just dissolving the former at relatively high concentration in an inert solvent.

1.4 Aims and Outline of the Thesis

In this Thesis, I focused on the modification of the external and internal structures of $Au_{25}(SR)_{18}$ with the goal of obtaining new gold nanoclusters and/or understanding the effect of these modifications on the fundamental properties of $Au_{25}(SR)_{18}$. Chapters 2-5 focus on a series of aspects.

Chapter 2. Metal Doping of $Au_{25}(SR)_{18}^{-}$: Insights and Hindsights.

The study of the structures and properties of atomically precise gold nanoclusters is the object of active research worldwide. Recently, research has been also focusing on the doping of metal nanoclusters through introduction of noble metals, such as platinum, and less noble metals, such as cadmium and mercury. Previous studies, which relied extensively on the use of mass spectrometry and single crystal X-ray crystallography, led to assign the location where each of these foreign-metal atoms go. Our study provides new insights into this topic and, particularly, compelling evidence about the actual position of the selected metal atoms M = Pt, Pd, Hg, and Cd in the structure of $Au_{24}M(SR)_{18}^{0}$. To make sure that the results were not dependent on the thiolate, for SR we used both butanethiolate and phenylethanethiolate. The clusters were prepared according to different literature procedures that were supposed to lead to different doping positions. Use of NMR spectroscopy and isotope effects, with the support of mass spectrometry, electrochemistry, and single crystal X-ray crystallography, led us to confirm that noble metals indeed dope the cluster at its central position, whereas no matter how the doping reaction is conducted and the nature of the ligand, the position of both Cd and Hg is always on the icosahedron shell, rather than at the central or staple position, as often reported. Our results not only provide a reassessment of previous conclusions, but also highlight the importance of NMR spectroscopy studies and cast doubts on drawing conclusions mostly based on single crystal X-ray crystallography.

Chapter 3. Understanding and Controlling the Efficiency of $Au_{24}M(SR)_{18}$ Nanoclusters as Singlet-Oxygen Photosensitizers.

Singlet oxygen, $^1O_2$, can be generated by suitable photosensitizers, that is, molecules that can be photoexcited and their triplet excited states used to cause the $^3O_2 \rightarrow {}^1O_2$ transition by energy transfer. These molecules, on the other hand, also act as quenchers of $^1O_2$ and thus make its lifetime shorter than allowed by the specific solvent. We studied the photosensitizer behavior of a series of molecular $Au_{24}M(SR)_{18}$ clusters, where R = n-C_3H_7 (C3), n-C_4H_9 (C4), and C_2H_4Ph (C2Ph), and M = Au, Hg, and Cd. For detection, we used time-resolved electron paramagnetic resonance (TREPR). Upon nanosecond photoexcitation of the cluster, a triplet state is eventually formed, followed by energy exchange with $^3O_2$ to generate $^1O_2$. In TREPR, the presence of $^1O_2$ is detected very sensitively with a nitroxide radical probe. $^1O_2$ induces in the latter populations of the radical spin sublevels that differ significantly from those at thermal equilibrium. This spin polarization is detected as a transient signal that depends on the effective $^1O_2$ lifetime in the given experimental conditions. For all clusters, the transients detected in toluene at 240 K obeyed a single-exponential decay law. This allowed us to determine $^1O_2$ lifetimes ranging from a minimum of 2.71 ($Au_{25}(SC4)_{18}^-$) to a maximum of 27.9 μs ($Au_{24}Cd(SC2Ph)_{18}^0$). The different activity of these clusters was also confirmed by studying the reaction of photosensitized $^1O_2$ with 9,10-diphenylanthracene. We found that: (i) the cluster's excited state responsible for the activation of triplet oxygen is a triplet state; (ii) a more positive potential for the oxidation of the cluster is matched by a longer $^1O_2$ lifetime; (iii) proper design of the cluster yields results analogous to those of tetraphenylporphirin ($^1O_2$ lifetime of 28.2 μs), which is a well-known reference photosensitizer. Kinetic analysis led to important insights into the mechanism of the quenching of $^1O_2$ by gold nanoclusters, how to control it, and why properly doped gold nanoclusters may perform very well in $^1O_2$ photosensitization.

Chapter 4. Gold Fusion: From $Au_{25}(SR)_{18}$ to $Au_{38}(SR)_{24}$, the Most Unexpected Transformation of a Very Stable Nanocluster

The study of the molecular cluster $Au_{25}(SR)_{18}$ has provided a wealth of fundamental insights into the properties of clusters protected by thiolated ligands (SR). This is also because this cluster has been particularly stable under a number of experimental conditions. Very unexpectedly, we found that paramagnetic $Au_{25}(SR)_{18}^0$ undergoes a spontaneous bimolecular fusion to form another benchmark gold nanocluster, $Au_{38}(SR)_{24}$. We tested this reaction with a series of Au_{25} clusters. The fusion was confirmed and characterized by UV−vis absorption spectroscopy, ESI mass spectrometry, ^{1}H and ^{13}C NMR spectroscopy, and electrochemistry. NMR evidences the presence of four types of ligand and, for the same proton type, double signals caused by the diastereotopicity arising from the chirality of the capping shell. This effect propagates up to the third carbon atom along the ligand chain. Electrochemistry provides a particularly convenient way to study the evolution process and determine the fusion rate constant, which decreases as the ligand length increases. No reaction is observed for the anionic clusters, whereas the radical nature of $Au_{25}(SR)_{18}^0$ appears to play an important role. This transformation of a stable cluster into a larger stable cluster without addition of any co-reagent also features the bottom-up assembly of the Au_{13} building block in solution. This very unexpected result could modify our view of the relative stability of molecular gold nanoclusters.

Chapter 5. Ligand Exchange and Polymerization Reaction on $Au_{25}(SR)_{18}$

This part of the research aims at decorating the Au_{25} monolayer with polymerizable groups to investigate the effect of this modified monolayer on the cluster's optical properties. After synthetizing the proper ligand, exchange reactions were carried out and the resulting cluster characterized. The extent of exchange was controlled by adjusting the relative concentrations of the cluster and exogenous ligand. The reaction was monitored by UV-vis absorption and MALDI-TOF mass spectroscopy. After polymerization, the resulting nanocluster exhibits an SPR-like band that grows until it reaches a maximum after a few days.

1.5 References

1. Faraday, M. X. The Bakerian Lecture. —Experimental relations of gold (and other metals) to light. *Philos. Trans. R. Soc. London* **1857**, *147*, 145-181.
2. Mie, G. Beiträge zur Optik Trüber Medien, Speziell Kolloidaler Metallö sungen. *Ann. Phys.* **1908**, *330*, 377-445.
3. Zsigmondy, R. Colloids and the Ultramicroscope: A Manual of Colloid Chem-

istry and Ultramicroscopy. Authorized Translation. *John Wiley & Sons: New York,* **1909**.

4. Fleischmann, M.; Hendra, P. J.; McQuillan, A. Raman spectra of pyridine adsorbed at a silver electrode. *Chem. Phys. Lett.* **1974**, *26*, 163-166.
5. Albrecht, M. G.; Creighton, J. A. Anomalously intense Raman spectra of pyridine at a silver electrode. *J. Am. Chem. Soc.* **1977**, *99*, 5215-5217.
6. Jeanmaire, D. L.; Van Duyne, R. P. Surface Raman spectroelectrochemistry: Part I. Heterocyclic, aromatic, and aliphatic amines adsorbed on the anodized silver electrode. *J. Electroanal. Chem. Interfacial Electrochem.* **1977**, *84*, 1-20.
7. Creighton, J. A.; Blatchford, C. G.; Albrecht, M. G. Plasma resonance enhancement of Raman scattering by pyridine adsorbed on silver or gold sol particles of size comparable to the excitation wavelength. *J. Chem. Soc., Faraday Trans*. 2 **1979**, *75*, 790-798.
8. Zou, Y.; Chen, H.; Li, Y.; Yuan, X.; Zhao, X.; Chen, W.; Cao, F.; Cai, N.; Huang, X.; Yang, F.; Liu, W. Synthesis of mesoporous-silica coated multi-branched gold nanoparticles for surface enhanced Raman scattering evaluation of 4-bromomethcathinone. *J. Saudi. Chem. Soc.* **2019**, *23*, 378-383.
9. Freeman, R. G.; Grabar, K. C.; Allison, K. J.; Bright, R. M.; Davis, J. A.; Guthrie, A. P.; Hommer, M. B.; Jackson, M. A.; Smith, P. C.; Walter, D. G.; Natan, M. J. Self-assembled metal colloid monolayers: an approach to SERS substrates. *Science* **1995**, *267*, 1629-1632.
10. Scherrer, P. N.; . Ges. Wiss. Goettingen, *Math. -Phys. Kl.* **1918**, *1918*, 98-100.
11. Svedberg, T.; Pedersen, K. O. The Ultracentrifuge. *Elsevier: Amsterdam*, **1940**.
12. Turkevich, J.; Hillier, J. Electron Microscopy of Colloidal Systems. *Anal. Chem.* **1949**, *21,* 475-485.
13. Turkevich, J.; Stevenson, P. C.; Hillier, J. A study of the nucleation and growth processes in the synthesis of colloidal gold. *Discuss. Faraday Soc.* **1951**, *11*, 55-75.

14. Turkevich. J. Colloidal Gold. Part I. *Gold Bull.* **1985**, *18*, 86-91.
15. Whetten, R. L.; Shafigullin. M. N.; Khoury. J. T.; Schaaff. T. G.; Vezmar. I.; Alvarez. M. M.; Wilkinson. Crystal structures of molecular gold nanocrystal arrays. *Acc. Chem. Res*. **1999**, *32*, 397-406.
16. Qian, H.; Zhu, M.; Wu, Z.; Jin, R. Quantum sized gold nanoclusters with atomic precision. *Acc. Chem. Res.* **2012**, *45*, 1470-1479.
17. Jin, R. Atomically precise metal nanoclusters: stable sizes and optical properties. *Nanoscale,* **2015**, *7*, 1549-1565.
18. Jin, J.; Zhu, Y.; Qian, Y. Quantum‐Sized Gold Nanoclusters: Bridging the Gap between Organometallics and Nanocrystals. *Chem. Eur. J.* **2011**, *17*, 6584-6593.
19. Jin, R.; Zeng, C.; Zhou, M.; Chen, Y. Atomically precise colloidal metal nanoclusters and nanoparticles: fundamentals and opportunities. *Chem. Rev.* **2016**, *116*, 10346-10413.
20. Antonello, S.; Maran, F. Molecular electrochemistry of monolayer-protected clusters. *Curr. Opin. Electrochem*. **2017**, *2*, 18-25.
21. Agrachev, M.; Ruzzi, M.; Venzo, A.; Maran, F. Nuclear and Electron Magnetic Resonance Spectroscopies of Atomically Precise Gold Nanoclusters. *Acc. Chem. Res*. **2019**, *52*, 44-52.
22. Malola, S.; Lehtovaara, L.; Enkovaara. J.; Häkkinen. H. Birth of the localized surface plasmon resonance in monolayer-protected gold nanoclusters. *ACS Nano*, **2013**, *7*, 10263-10270.
23. Yi, C.; Tofanelli, M. A.; Ackerson, C. J.; Knappenberger Jr, K. L. Optical Properties and Electronic Energy Relaxation of Metallic $Au_{144}(SR)_{60}$ Nanoclusters. *J. Am. Chem. Soc.*, **2013**, *135*, 18222-18228.
24. Weissker, H.-Ch.; Escobar, H. B.; Thanthirige, V. D.; Kwack, K.; Lee, D.; Ramakrishna, G.; Whetten, R. L.; Lopez-Lozano, X. Information on quantum states pervades the visible spectrum of the ubiquitous $Au_{144}(SR)_{60}$ gold nanocluster, *Nat. Comm.* **2014**, *5*: 3785.
25. Dainese, T.; Agrachev. M.; Antonello, S.; Badocco, D.; Black, D. M.; Fortunelli, A.; Gascón, J. A.; Stener, M.; Venzo, A.; Whetten. R. L.; Maran, F. Atomically precise

$Au_{144}(SR)_{60}$ nanoclusters (R = Et, Pr) are capped by 12 distinct ligand types of 5-fold equivalence and display gigantic diastereotopic effects. *Chem. Sci.*, **2018**, *9*, 8796-8805.

26. McPartlin, M.; Mason, R.; Malatesta, L. Novel Cluster Complexes of Gold(0)-Gold(I). *J. Chem. Soc. D* **1969**, 334.
27. Schmid, G.; Pfeil, R.; Boese, R.; Bandermann, F.; Meyer, S.; Calis, G. M. H.; Vandervelden, W. A. $Au_{55}[P(C_6H_5)_3]_{12}Cl_6$—ein Goldcluster ungewöhnlicher Größe. *Chem. Ber.* **1981**, *114*, 3634-3642.
28. Nuzzo, R. G.; Allara, D. L. Adsorption of bifunctional organic disulfides on gold surfaces. *J. Am. Chem. Soc.*, **1983**, *105*, 4481-4483.
29. Love, J. C.; Estroff, L. A.; Kriebel, J. K.; Nuzzo, R. G.; Whitesides, G. M. Self-assembled monolayers of thiolates on metals as a form of nanotechnology. *Chem. Rev.* **2005**, *105*, 1103-1169.
30. Brust, M.; Walker, M.; Bethell, D.; Schiffrin, D. J.; Whyman, R. Synthesis of thiol-derivatised gold nanoparticles in a two-phase liquid–liquid system. *J. Chem. Soc., Chem. Commun.* **1994**, 801-802.
31. Walter, M.; Akola, J.; Lopez-Acevedo, O.; Jadzinsky, Pablo D.; Calero, G.; Ackerson, C.J.; Whetten, R.L.; Grönbeck, H.; Häkkinen H. A unified view of ligand-protected gold clusters as superatom complexes. *Proc. Natl. Acad. Sci. U.S.A.* **2008**, *105(27)*, 9157-9162.
32. Jadzinsky, P. D.; Calero, G.; Ackerson, C. J.; Bushnell, D. A.; Kornberg, R. D. Structure of a thiol monolayer-protected gold nanoparticle at 1.1 Å resolution. *Science*, **2007**, *318*, 430-433.
33. Qian, H.; Jin, R. Controlling Nanoparticles with Atomic Precision: The Case of $Au_{144}(SCH_2CH_2Ph)_{60}$. *Nano Lett.* **2009**, *9*, 4083-4087.
34. Das, A.; Liu, C.; Byun, H. Y.; Nobusada, K.; Zhao, S.; Rosi. N.; Jin, R. Structure Determination of $[Au_{18}(SR)_{14}]$. *Angew. Chem. Int. Ed.*, **2015**, *54*, 3140-3144.
35. Chen, S.; Wang, S.; Zhong, J.; Song, Y.; Zhang, J.; Sheng, H.; Pe, Y.; Zhu, M. The Structure and Optical Properties of the $[Au_{18}(SR)_{14}]$ Nanocluster. *Angew. Chem. Int. Ed.* **2015**, *54*, 3145-3149.

36. Zeng, C.; Liu, C.; Chen, Y.; Rosi, N. L.; Jin, R. Gold–Thiolate Ring as a Protecting Motif in the $Au_{20}(SR)_{16}$ Nanocluster and Implications. *J. Am. Chem. Soc.* **2014**, *136*, 11922-11925.
37. Chen, S.; Xiong, L.; Wang, S.; Ma, Z.; Jin, S.; Sheng, H.; Pei, Y.; Zhu, M. Total Structure Determination of Au_{21}(S-Adm)$_{15}$ and Geometrical/Electronic Structure Evolution of Thiolated Gold Nanoclusters. *J. Am. Chem. Soc.* **2016**, *138*, 10754-10757.
38. Das, A.; Li, T.; Nobusada, K.; Zeng, C.; Rosi, N. L.; Jin, R. Nonsuperatomic $[Au_{23}(SC_6H_{11})_{16}]^-$ Nanocluster Featuring Bipyramidal Au_{15} Kernel and Trimeric $Au_3(SR)_4$ Motif. *J. Am. Chem. Soc.* **2013**, *135*, 18264-18267.
39. Das, A.; Li, T.; Nobusada, K.; Zeng, C.; Rosi, N. L.; Jin, R. Crystal structure and electronic properties of a thiolate-protected Au_{24} nanocluster. *Nanoscale*, **2014**, *6*, 6458-6462.
40. Gan, Z.; Lin, Y.; Luo, L.; Han, G.; Liu, W.; Liu, Z.; Yao, C.; Weng, L.; Liao, L.; Chen, J.; Liu, X.; Luo, Y.; Wang, C.; Wei S.; Wu, Z. Fluorescent Gold Nanoclusters with Interlocked Staples and a Fully Thiolate-Bound Kernel. *Angew. Chem. Int. Ed.*, **2016**, *55*, 11567-11571.
41. Heaven, M. W.; Dass, A.; White, P. S.; Holt, K. M.; Murray, R. W. Crystal Structure of the Gold Nanoparticle $[N(C_8H_{17})_4][Au_{25}(SCH_2CH_2Ph)_{18}]$. *J. Am. Chem. Soc.* **2008**, *130*, 3754-3755.
42. Zhu, M.; Aikens, C. M.; Hollander, F. J.; Schatz, G. C.; Jin, R. Correlating the Crystal Structure of A Thiol-Protected Au_{25} Cluster and Optical Properties. *J. Am. Chem. SOC.* **2008**, *130*, 5883-5885.
43. Zeng, C.; Li, T.; Das, A.; Rosi, N. L.; Jin, R. Chiral structure of thiolate-protected 28-gold-atom nanocluster determined by X-ray crystallography. *J. Am. Chem. Soc.* **2013**, *135*, 10011-10013.
44. Chen, Y.; Liu, C.; Tang, Q.; Zeng, C.; Higaki, T.; Das, A.; Jiang, D.-e.; Rosi, N. L.; Jin, R. Isomerism in $Au_{28}(SR)_{20}$ Nanocluster and Stable Structures. *J. Am. Chem. Soc.* **2016**, *138*, 1482-1485.
45. Crasto, D.; Malola, S.; Brosofsky, G.; Dass A.; Häkkinen, H. Single Crystal XRD Structure and Theoretical Analysis of the Chiral $Au_{30}S$(S-t-Bu)$_{18}$ Cluster.

J. Am. Chem. Soc., **2014**, *136*, 5000-5005.

46. Crasto, D.; Barcaro, G.; Stener, M.; Sementa, L.; Fortunelli, A.; Dass, A. $Au_{24}(SAdm)_{16}$ Nanomolecules: X-ray Crystal Structure, Theoretical Analysis, Adaptability of Adamantane Ligands to Form $Au_{23}(SAdm)_{16}$ and $Au_{25}(SAdm)_{16}$, and Its Relation to $Au_{25}(SR)_{18}$. *J. Am. Chem. Soc.* **2014**, *136*, 14933-14940.
47. Higaki, T.; Liu, C.; Zeng, C.; Jin, R.; Chen, Y.; Rosi, N. L.; Jin, R. Controlling the Atomic Structure of Au_{30} Nanoclusters by a Ligand‐Based Strategy. *Angew. Chem. Int. Ed.*, **2016**, *55*, 6694-6697.
48. Dong, H.; Liao, L.; Zhuang, S.; Yao, C.; Chen, J.; Tian, S.; Zhu, M.; Liu, X.; Li, L.; Wu, Z. A novel double-helical-kernel evolution pattern of gold nanoclusters: alternate single-stranded growth at both ends. *Nanoscale*, **2017**, *9*, 3742-3746.
49. Zhuang. S., Liao. L., Zhao. Y., Yuan. J., Yao. C., Liu. X., Li. J., Deng. H., Yang. J. and Wu. Z. Is the kernel–staples match a key–lock match? *Chem. Sci.*, **2018**, *9*, 2437-2442.
50. Zeng, C.; Qian, H.; Li, T.; Li, G.; Rosi, N. L.; Yoon, B.; Barnett, R. N.; Whetten, R. L.; Landman, U.; Jin, R. Total Structure and Electronic Properties of the Gold Nanocrystal $Au_{36}(SR)_{24}$. *Angew. Chem. Int. Ed.*, **2012**, *51*, 13114-13118.
51. Yang, S.; Chai, J.; Song, Y.; Kang, X.; Sheng, H.; Chong, H.; Zhu, M. A New Crystal Structure of Au_{36} with a Au_{14} Kernel Cocapped by Thiolate and Chloride. *J. Am. Chem. Soc.* **2015**, *137*, 10033-10035.
52. Qian, H.; Eckenhoff, W. T.; Zhu, Y.; Pintauer, T.; Jin, R. Total Structure Determination of Thiolate-Protected Au_{38} Nanoparticles. *J. Am. Chem. Soc.*, **2010**, *132*, 8280-8281.
53. Liu, C.; Li, T.; Li, G.; Nobusada, K.; Zeng, C.; Pang, G.; Rosi, N. L.; Jin, R. Observation of Body-Centered Cubic Gold Nanocluster. *Angew. Chem. Int. Ed.* **2015**, *54*, 9826-9829.
54. Tian, S.; Li, Y.; Li, M.; Yuan, J.; Yang, J.; Wu, Z.; Jin, R. Structural isomerism in gold nanoparticles revealed by X-ray crystallography. *Nat. Commun.*, **2015**, *6*: *8667*.

55. Zeng, C.; Chen, Y.; Liu, C.; Nobusada, K.; Rosi N. L.; Jin, R. Gold tetrahedra coil up: Kekulé-like and double helical superstructures. *Sci. Adv.* **2015**, *1*, e1500425.
56. Zeng, C.; Chen, Y.; Iida, K.; Nobusada, K.; Kirschbaum, K.; Lambright, K. J.; Jin, R. Gold Quantum Boxes: On the Periodicities and the Quantum Confinement in the Au_{28}, Au_{36}, Au_{44}, and Au_{52} Magic Series. *J. Am. Chem. Soc.*, **2016**, *138*, 3950-3953.
57. Liao, L.; Zhuang, S.; Yao, C.; Yan, N.; Chen, J.; Wang, C.; Xia, N.; Liu, X.; Li, M.-B.; Li, L.; Bao X.; Wu, Z. Structure of Chiral Au_{44}(2,4-DMBT)$_{26}$ Nanocluster with an 18-Electron Shell Closure. *J. Am. Chem. Soc.* **2016**, *138*, 10425-10428.
58. Liao, L.; Zhuang, S.; Wang, P.; Xu, Y.; Yan, N.; Dong, H.; Wang, C.; Zhao, Y.; Xia, N.; Li, J.; Deng, H.; Pei, Y.; Tian S.-K.; Wu, Z. Quasi-Dual-Packed-Kerneled Au_{49}(2,4-DMBT)$_{27}$ Nanoclusters and the Influence of Kernel Packing on the Electrochemical Gap. *Angew. Chem. Int. Ed.* **2017**, *56*, 12644-12648.
59. Zhuang, S.; Liao, L.; Li, M.-B.; Yao, C.; Zhao, Y.; Dong, H.; Li, J.; Deng, H.; Li, L.; Wu, Z. The fcc structure isomerization in gold nanoclusters. *Nanoscale*, **2017**, *9*, 14809-14813.
60. Gan, Z.; Chen, J.; Wang, J.; Wang, C.; Li, M.-B.; Yao, C.; Zhuang, S.; Xu, A.; Li, L.; Wu, Z. The fourth crystallographic closest packing unveiled in the gold nanocluster crystal. *Nat. Commun.* **2017**, *8*, 14739.
61. Zeng, C.; Liu, C.; Chen, Y.; Rosi, N. L.; Jin, R. Atomic Structure of Self-Assembled Monolayer of Thiolates on a Tetragonal Au_{92} Nanocrystal. *J. Am. Chem. Soc.*, **2016**, *138*, 8710-8713.
62. Liao, L.; Chen, J.; Wang, C.; Zhuang, S.; Yan, N.; Yao, C.; Xia, N.; Li, L.; Bao, X.; Wu, Z. Beyond the Golden Era of public health: charting a path from sanitarianism to ecological public health. *Chem. Commun.* **2016**, *52*, 12036-12036.
63. Higaki, T.; Liu, C.; Zhou, M.; Luo, T.-Y.; Rosi, N. L.; Jin, R. Tailoring the Structure of 58-Electron Gold Nanoclusters: $Au_{103}S_2$(S-Nap)$_{41}$ and Its

Implications. *J. Am. Chem. Soc.*, **2017**, *139*, 9994-10001.

64. Chen, Y.; Zeng, C.; Liu, C.; Kirschbaum, K.; Gayathri, C.; Gil, R. R.; Rosi, N. L.; Jin, R. Crystal Structure of Barrel-Shaped Chiral $Au_{130}(p\text{-}MBT)_{50}$ Nanocluster. *J. Am. Chem. Soc.* **2015**, *137*, 10076-10079.
65. Dass, A.; Theivendran, S.; Nimmala, P. R.; Kumara, C.; Jupally, V. R.; Fortunelli, A.; Sementa, L.; Barcaro, G.; Zuo, X.; Noll, B. C. $Au_{133}(SPh\text{-}tBu)_{52}$ Nanomolecules: X-ray Crystallography, Optical, Electrochemical, and Theoretical Analysis. *J. Am. Chem. Soc.* **2015**, *137*, 4610-4613.
66. Zeng, C.; Chen, Y.; Kirschbaum, K.; Lambright, K. J.; Jin, R. Emergence of hierarchical structural complexities in nanoparticles and their assembly. *Science*, **2016**, *354*, 1580-1584.
67. Sakthivel, N. A.; Theivendran, S.; Ganeshraj, V.; Oliver, A. G.; Dass, A. Crystal Structure of Faradaurate-279: $Au_{279}(SPh\text{-}tBu)_{84}$ Plasmonic Nano-crystal Molecules. *J. Am. Chem. Soc.* **2017**, *139*, 15450-15459.
68. Xia, N.; Gan, Z.; Liao, L.; Zhuang, S.; Wu, Z. The reactivity of phenylethane-thiolated gold nanoparticles with acetic acid. *Chem. Commun.* **2017**, *53*, 11646-11649.
69. Whetten, R. L.; Khoury, J. T.; Alvarez, M. M.; Murthy, S.; Vezmar, I.; Wang, Z. L.; Stephens, P. W.; Cleveland, C. L.; Luedtke, W. D.; Landman, U. Nanocrystal gold molecules. *Adv. Mater.*, **1996**, *8*, 428-433.
70. Qian, H.; Zhu, Y.; Jin, R. Isolation of Ubiquitous $Au_{40}(SR)_{24}$ Clusters from the 8 kDa Gold Clusters. *J. Am. Chem. Soc.*, **2010**, *132*, 4583-4585.
71. Zhu, M.; Qian, H.; Jin, R. Thiolate-Protected $Au_{24}(SC_2H_4Ph)_{20}$ Nanoclusters: Superatoms or Not? *J. Phys. Chem. Lett.*, **2010**, *1*, 1003-1007.
72. Takano, S.; Yamazoe, S.; Koyasu, K.; Tsukuda, T. Slow-reduction synthesis of a thiolate-protected one-dimensional gold cluster showing an intense near-infrared absorption. *J. Am. Chem. Soc.* **2015**, *137*, 7027-7030.
73. Donkers, R. L.; Lee, D.; Murray, R. W. Synthesis and Isolation of the Molecule-like Cluster $Au_{38}(PhCH_2CH_2S)_{24}$. *Langmuir*, **2004**, *20*, 1945-1952.
74. Zhu, M.; Lanni, E.; Garg, N.; Bier, M. E.; Jin, R. Kinetically Controlled, High-Yield Synthesis of Au_{25} Clusters. *J. Am. Chem. Soc.* **2008**, *130*, 1138-1139.

75. Parker, J. F.; Weaver, J. E. F.; McCallum, F.; Fields-Zinna, C. A.; Murray, R. W. Synthesis of Monodisperse [Oct_4N^+][$Au_{25}(SR)_{18}^-$] Nanoparticles, with Some Mechanistic Observations. *Langmuir*, **2010**, *26*, 13650-13654.
76. Parker, J. F.; Fields-Zinna, C. A.; Murray, R. W. The Story of a Monodisperse Gold Nanoparticle: $Au_{25}L_{18}$. *Acc. Chem. Rev.* **2010**, *43*, 1289-1296.
77. Murray, R. W. Nanoelectrochemistry: metal nanoparticles, nanoelectrodes, and nanopores. *Chem. Rev.*, **2008**, *108*, 2688-2720.
78. Niihori, Y.; Hossain, S.; Sharma, S.; Kumar, B.; Kurashige, W.; Negishi, Y. Understanding and practical use of ligand and metal exchange reactions in thiolate-protected metal clusters to synthesize controlled metal clusters. *Chem. Rec.* **2017**, *17*, 473-484.
79. Agrachev, M.; Antonello, S.; Dainese, T.; Ruzzi, M.; Zoleo, A.; Aprà, E.; Govind, N.; Fortunelli, A.; Sementa, L.; Maran, F. Magnetic ordering in gold nanoclusters. *ACS Omega* **2017**, *2*, 2607-2617.
80. Knoppe, S.; Bürgi, T. Chirality in thiolate-protected gold clusters. *Acc. Chem Res.* **2014**, *47*, 1318-1326.
81. Li, G.; Jin, R. Gold nanocluster-catalyzed semihydrogenation: A unique activation pathway for terminal alkynes. *J. Am. Chem. Soc.* **2014**, *136*, 11347-11354.
82. Du, B.; Jiang, X.; Das, A.; Zhou, Q.; Yu, M.; Jin, R.; Zheng, J. Glomerular barrier behaves as an atomically precise bandpass filter in a sub-nanometre regime. *Nat. Nanotech.* **2017**, *12*, 1096-1102.
83. Goswami. N., Zheng. K. and Xie. J. Bio-NCs–the marriage of ultrasmall metal nanoclusters with biomolecules. *Nanoscale*, **2014**, *6*, 13328-13347.
84. Wong, O. A.; Hansen, R. J.; Ni, T. W.; Heinecke, C. L.; Compel, W. S.; Gustafson, D. L.; Ackerson, C. J. Structure–activity relationships for biodistribution, pharmacokinetics, and excretion of atomically precise nanoclusters in a murine model. *Nanoscale*, **2013**, *5*, 10525-10533.
85. Katla, S. K.; Zhang, J.; Castro, E.; Bernal, R. A.; Li, X. Atomically Precise $Au_{25}(SG)_{18}$ Nanoclusters: Rapid Single-Step Synthesis and Application in Photothermal Therapy. *ACS Appl. Mater. Interfaces*, **2018**, *10*, 75-82.

86. Zhang, X.-D.; Chen, J.; Luo, Z.; Wu, D.; Shen, X.; Song, S.-S.; Sun, Y.-M.; Liu, P.-X.; Zhao, J.; Huo, S.; Fan, S.; Fan, F.; Liang, X.-J.; Xie, J. Enhanced Tumor Accumulation of Sub-2 nm Gold Nanoclusters for Cancer Radiation Therapy. *Adv. Healthcare Mater.* **2014**, *3*, 133-141.
87. Jimenez, V. L.; Georganopoulou, D. G.; White, R. J.; Harper, A. S.; Mills, A. J.; Lee, D.; Murray, R. W. Hexanethiolate monolayer protected 38 gold atom cluster. *Langmuir*, **2004**, *20*, 6864-6870.
88. Kim, J.; Lema, K.; Ukaigwe, M.; Lee, D. Correction to “Facile Preparative Route to Alkanethiolate-Coated Au_{38} Nanoparticles: Postsynthesis Core Size Evolution”. *Langmuir* **2007**, *23*, 7853-7858.
89. Tracy, J. B.; Kalyuzhny, G.; Crowe, M. C.; Balasubramanian, R.; Choi, J.-P.; Murray, R. W. Poly (ethylene glycol) ligands for high-resolution nanoparticle mass spectrometry. *J. Am. Chem. Soc.* **2007**, *129*, 6706-6707.
90. Reilly, S. M.; Krick, T.; Dass, A. Surfactant-free synthesis of ultrasmall gold nanoclusters. *J. Phys. Chem. C*, **2010**, *114*, 741-745.
91. Shichibu, Y.; Negishi, Y.; Tsunoyama, H.; Kanehara, M.; Teranishi, T.; Tsukuda, T. Extremely High Stability of Glutathionate-Protected Au_{25} Clusters Against Core Etching. *Small*, **2007**, *3*, 835-839.
92. Negishi, Y.; Takasugi, Y.; Sato, S.; Yao, H.; Kimura, K.; Tsukuda, T. Magic-Numbered Au_n Clusters Protected by Glutathione Monolayers (n = 18, 21, 25, 28, 32, 39): Isolation and Spectroscopic Characterization. *J. Am. Chem. Soc.* **2004**, *126*, 6518-6519.
93. Negishi, Y.; Nobusada, K.; Tsukuda, T. Glutathione-protected gold clusters revisited: Bridging the gap between gold (I)− thiolate complexes and thiolate-protected gold nanocrystals. *J. Am. Chem. Soc.* **2005**, *127*, 5261-5270.
94. Venzo, A.; Antonello, S.; Gascón, J. A.; Guryanov, I.; Leapman, R. D.; Perera, N. V.; Sousa, A.; Zamuner, M.; Zanella, A.; Maran, F. Effect of the Charge State (z = −1, 0, +1) on the Nuclear Magnetic Resonance of Monodisperse $Au_{25}[S(CH_2)_2Ph]_{18}^z$ Clusters. *Anal. Chem.* **2011**, *83*, 6355-6362.
95. Antonello, S.; Perera, N. V.; Ruzzi, M.; Gascón, J. A.; Maran, F. Interplay of Charge State, Lability, and Magnetism in the Molecule-like $Au_{25}(SR)_{18}$ Cluster.

J. Am. Chem. Soc. **2013**, *135*, 15585-15594.

96. Tofanelli, M. A.; Salorinne, K.; Ni, T. W.; Malola, S.; Newell, B.; Phillips, B.; Häkkinen, H.; Ackerson, C. J. Jahn-Teller effects in $Au_{25}(SR)_{18}$. *Chem. Sci.* **2016**, *7*, 1882-1890.
97. Jahn, H. A.; Teller, E. Stability of polyatomic molecules in degenerate electronic states-I—Orbital degeneracy. *Proc. R. Soc. London, Ser. A*, **1937**, *161*, 220-235.
98. Antonello, S.; Holm, A. H.; Instuli, E.; Maran, F. Molecular Electron-Transfer Properties of Au_{38} Clusters. *J. Am. Chem. Soc.* **2007**, *129*, 9836-9837.
99. Dainese, T.; Antonello, S.; Gascón, J. A.; Pan, F.; Perera, N. V.; Ruzzi, M.; Venzo, A.; Zoleo, A.; Rissanen, K.; Maran, F. $Au_{25}(SEt)_{18}$, a Nearly Naked Thiolate-Protected Au_{25} Cluster: Structural Analysis by Single Crystal X-ray Crystallography and Electron Nuclear Double Resonance. *ACS Nano*, **2014**, *8*, 3904-3912.
100. Walter, M.; Akola, J.; Lopez-Acevedo, O.; Jadzinsky, P. D.; Calero, G.; Ackerson, C. J.; Whetten, R. L.; Grönbeck, H.; Häkkinen, H. A unified view of ligand-protected gold clusters as superatom complexes, *PNAS*, **2008**, *105*, 9157-9162,
101. Nardi, M. D.; Antonello, S.; Jiang, D.-e.; Pan, F.; Rissanen, K.; Ruzzi, M.; Venzo, A.; Zoleo, A.; Maran, F. Gold Nanowired: A Linear $(Au_{25})_n$ Polymer from Au_{25} Molecular Clusters. *ACS Nano*, **2014**, *8*, 8505-8512.
102. Antonello, S.; Dainese, T.; Pan, F.; Rissanen, K.; Maran, F. Electrocrystallization of Monolayer-Protected Gold Clusters: Opening the Door to Quality, Quantity, and New Structures. *J. Am. Chem. Soc.* **2017**, *139*, 4168-4174.
103. Tang, Z.; Xu, B.; Wu, B.; Robinson, D. A.; Bokossa, N.; Wang, G. Monolayer reactions of protected au nanoclusters with monothiol tiopronin and 2, 3-dithiol dimercaptopropanesulfonate. *Langmuir*, **2011**, *27*, 2989-2996.
104. Zheng, J.; Petty, J. T.; Dickson, R. M. High Quantum Yield Blue Emission from Water-Soluble Au_8 Nanodots. *J. Am. Chem. Soc.* **2003**, *125*, 7780-7781.
105. Chen, W.-Y.; Lan, G.-Y.; Chang, H.-T. Use of fluorescent DNA-templated

gold/silver nanoclusters for the detection of sulfide ions. *Anal. Chem.* **2011**, *83*, 9450-9455.

106. Negishi, Y.; Iwai, T.; Ide, M. Continuous modulation of electronic structure of stable thiolate-protected Au_{25} cluster by Ag doping. *Chem. Commun.* **2010**, *46*, 4713-4715.

107. Wang, S.; Meng, X.; Das, A.; Li, T.; Song, Y.; Cao, T.; Zhu, X.; Zhu, M.; Jin, R. A 200-fold Quantum Yield Boost in the Photoluminescence of Silver-Doped Ag_xAu_{25-x} Nanoclusters: The 13th Silver Atom Matters. *Angew. Chem. Int. Ed.* **2014**, *53*, 2376-2380.

108. Kumara, C.; Aikens, C. M.; Dass, A. X-ray Crystal Structure and Theoretical Analysis of $Au_{25-x}Ag_x(SCH_2CH_2Ph)_{18}^-$ Alloy. *J. Phys. Chem. Lett.* **2014**, *5*, 461-466.

109. Kumara, C.; Gagnon, K. J.; Dass, A. X-ray Crystal Structure of $Au_{38-x}Ag_x(SCH_2CH_2Ph)_{24}$ Alloy Nanomolecules. *J. Phys. Chem. Lett.* **2015**, *6*, 1223-1228.

110. Xiang, J.; Li, P.; Song, Y.; Liu, X.; Chong, H.; Jin, S.; Pei, Y.; Yuan, X.; Zhu, M. X-Ray crystal structure, and optical and electrochemical properties of the $Au_{15}Ag_3(SC_6H_{11})_{14}$ nanocluster with a core–shell structure. *Nanoscale* **2015**, *7*, 18278-18283.

111. Molina, B.; Tlahuice-Flores, A. Thiolated Au_{18} cluster: preferred Ag sites for doping, structures, and optical and chiroptical properties. *Phys. Chem. Chem. Phys.* **2016**, *18*, 1397-1403.

112. Li, Q.; Wang, S.; Kirschbaum, K.; Lambright, K. J.; Das, A.; Jin, R. Heavily doped $Au_{25-x}Ag_x(SC_6H_{11})_{18}^-$ nanoclusters: silver goes from the core to the surface. *Chem. Commun.* **2016**, *52*, 5194-5197.

113. Kobayashi, R.; Nonoguchi, Y.; Sasaki, A.; Yao, H. Chiral monolayer-protected bimetallic Au–Ag nanoclusters: alloying effect on their electronic structure and chiroptical activity. *J. Phys. Chem. C* **2014**, *118*, 15506-15515.

114. Knoppe, S.; Vanbel, M.; van Cleuvenbergen, S.; Vanpraet, L.; Bürgi, T.; Verbiest, T. Nonlinear optical properties of thiolate-protected gold clusters. *J. Phys. Chem. C* **2015**, *119*, 6221-6226.

115. Knoppe, S.; Häkkinen, H.; Verbiest, T. Nonlinear optical properties of thiolate-protected gold clusters: a theoretical survey of the first hyperpolarizabilities. *J. Phys. Chem. C* **2015**, *119*, 27676-27682.

116. Fields-Zinna, C. A.; Crowe, M. C.; Dass, A.; Weaver, J. E. F.; Murray, R. W. Mass spectrometry of small bimetal monolayer-protected clusters. *Langmuir*, **2009**, *25*, 7704−7710.

117. Bruma, A.; Negreiros, F. R.; Xie, S.; Tsukuda, T.; Johnston, R. L.; Fortunelli, A.; Li, Z. Y. Direct atomic imaging and density functional theory study of the $Au_{24}Pd_1$ cluster catalyst. *Nanoscale*, **2013**, *5*, 9620-9625.

118. Negishi, Y.; Kurashige, W.; Niihori, Y.; Iwasa, T.; Nobusada, K. Isolation, structure, and stability of a dodecanethiolate-protected Pd_1Au_{24} cluster. *Phys. Chem. Chem. Phys.* **2010**, *12*, 6219-6225.

119. Qian, H.; Barry, E.; Zhu, Y.; Jin, R. Doping 25-atom and 38-atom gold nanoclusters with palladium. *Acta Phys.-Chim. Sin.* **2011**, *27*, 513-519.

120. Qian, H.; Jiang, D.-e.; Li, G.; Gayathri, C.; Das, A.; Gil, R. R.; Jin, R. Monoplatinum doping of gold nanoclusters and catalytic application. *J. Am. Chem. Soc.* **2012**, *134*, 16159-16162.

121. Christensen, S. L.; MacDonald, M. A.; Chatt, A.; Zhang, P.; Qian, H.; Jin, R. Dopant Location, Local Structure, and Electronic Properties of $Au_{24}Pt(SR)_{18}$ Nanoclusters. *J. Phys. Chem. C* **2012**, *116*, 26932-26937.

122. Kwak, K.; Tang, Q.; Kim, M.; Jiang, D.-e.; Lee, D. Interconversion between Superatomic 6-Electron and 8-Electron Configurations of $M@Au_{24}(SR)_{18}$ Clusters (M = Pd, Pt). *J. Am. Chem. Soc.* **2015**, *137*, 10833-10840.

123. Zhou, M.; Qian, H.; Sfeir, M. Y.; Nobusada, K.; Jin, R. Effects of single atom doping on the ultrafast electron dynamics of $M_1Au_{24}(SR)_{18}$ (M= Pd, Pt) nanoclusters. *Nanoscale*, **2016**, *8*, 7163-7171.

124. Tofanelli, M. A.; Ni, T. W.; Phillips, B. D.; Ackerson, C. J. Crystal Structure of the $PdAu_{24}(SR)_{18}^0$ Superatom. *Inorg. Chem.* **2016**, *55*, 999-1001.

125. Joshi, C. P.; Bootharaju, M. S.; Alhilaly, M. J.; Bakr, O. M. $[Ag_{25}(SR)_{18}]^-$: The “Golden” Silver Nanoparticle. *J. Am. Chem. Soc.* **2015**, *137*, 11578-11581.

126. Yan, J.; Su, H.; Yang, H.; Malola, S.; Lin, S.; Häkkinen, H.; Zheng, N. Total Structure and Electronic Structure Analysis of Doped Thiolated Silver $[MAg_{24}(SR)_{18}]^{2-}$ (M = Pd, Pt) Clusters. *J. Am. Chem. Soc.* **2015**, *137*, 11880-11883.

127. Xie, S.; Tsunoyama, H.; Kurashige, W.; Negishi, Y.; Tsukuda, T. Enhancement in Aerobic Alcohol Oxidation Catalysis of Au_{25} Clusters by Single Pd Atom Doping. *ACS Catal.* **2012**, *2*, 1519-1523.

128. Knoppe, S.; Dolamic, I.; Bürgi, T. Racemization of a chiral nanoparticle evidences the flexibility of the gold–thiolate interface. *J. Am. Chem. Soc.* **2012**, *134*, 13114-13120.

129. Barrabés, N.; Zhang, B.; Bürgi, T. Racemization of Chiral $Pd_2Au_{36}(SC_2H_4Ph)_{24}$: Doping Increases the Flexibility of the Cluster Surface. *J. Am. Chem. Soc.* **2014**, *136*, 14361-14364.

130. Varnholt, B.; Dolamic, I.; Knoppe, S.; Bürgi, T. On the flexibility of the gold–thiolate interface: racemization of the $Au_{40}(SR)_{24}$ cluster. *Nanoscale*, **2013**, *5*, 9568-9571.

131. Dolamic, I.; Varnholt, B.; Bürgi, T. Chirality transfer from gold nanocluster to adsorbate evidenced by vibrational circular dichroism. *Nat. Commun.* **2015**, *7117,* 1-6.

132. Gottlieb, E.; Qian, H.; Jin, R. Atomic-Level Alloying and De-alloying in Doped Gold Nanoparticles. *Chem. Eur. J.* **2013**, *19*, 4238-4243.

133. Negishi, Y.; Munakata, K.; Ohgake, W.; Nobusada, K. Effect of Copper Doping on Electronic Structure, Geometric Structure, and Stability of Thiolate-Protected Au_{25} Nanoclusters. *J. Phys. Chem. Lett.* **2012**, *3*, 2209-2214.

134. Hartmann, M. J.; Häkkinen, H.; Millstone, J. E.; Lambrecht, D. S. Impacts of Copper Position on the Electronic Structure of $[Au_{25-x}Cu_x(SH)_{18}]^-$ Nanoclusters. *J. Phys. Chem. C* **2015**, *119*, 8290-8298.

135. Wang, S.; Song, Y.; Jin, S.; Liu, X.; Zhang, J.; Pei, Y.; Meng, X.; Chen, M.; Li, P.; Zhu, M. Metal Exchange Method Using Au_{25} Nanoclusters as Templates for Alloy Nanoclusters with Atomic Precision. *J. Am. Chem. Soc.*

2015, *137*, 4018-4021.

136. Yao, C.; Lin, Y.-j.; Yuan, J.; Liao, L.; Zhu, M.; Weng, L.-h.; Yang, J.; Wu, Z. Mono-cadmium vs Mono-mercury Doping of Au_{25} Nanoclusters. *J. Am. Chem. Soc.* **2015**, *137*, 15350-15353.

137. Yang, S.; Wang, S.; Jin, S.; Chen, S.; Sheng, H.; Zhu, M. A metal exchange method for thiolate-protected tri-metal $M_1Ag_xAu_{24-x}(SR)_{18}^0$ (M= Cd/Hg) nanoclusters. *Nanoscale*, **2015**, *7*, 10005-10007.

138. Yan, N.; Liao, L.; Yuan, J.; Lin, Y.-J.; Weng, L.-H.; Yang, J.; Wu, Z. Bimetal doping in nanoclusters: Synergistic or counteractive? *Chem. Mater.* **2016**, *28*, 8240-8247.

139. Bhat, S.; Baksi, A.; Mudedla, S. K.; Natarajan, G.; Subramanian, V.; Pradeep, T. $Au_{22}Ir_3(PET)_{18}$: An Unusual Alloy Cluster through Intercluster Reaction. *J. Phys. Chem. Lett.* **2017**, *8*, 2787-2793.

140. Jin, R.; Nobusada, K. Doping and alloying in atomically precise gold nanoparticles. *Nano Res.* **2014**, *7*, 285-300.

141. Melník, M.; Mikuš, P.; Holloway, C. E. Crystallographic and structural characterization of heterometallic platinum clusters. Part IX. Heterooligonuclear Pt clusters. *Open Chem.* **2015**, *13*, 709-724.

142. Krishnadas, K. R.; Ghosh, A.; Baksi, A.; Chakraborty, I.; Natarajan, G.; Pradeep, T. Intercluster Reactions between $Au_{25}(SR)_{18}$ and $Ag_{44}(SR)_{30}$. *J. Am. Chem. Soc.* **2016**, *138*, 140-148.

143. Jiang, D.-e.; Whetten, R. L. Magnetic doping of a thiolated-gold superatom: First-principles density functional theory calculations. *Phys. Rev. B: Condens. Matter Mater. Phys*. **2009**, *80*, 115402(5).

144. Kim, H. Y.; Kim, D. H.; Ryu, J. H.; Lee, H. M. Design of Robust and Reactive Nanoparticles with Atomic Precision: 13Ag-Ih and 12Ag−1X (X = Pd, Pt, Au, Ni, or Cu) Core−Shell Nanoparticles. *J. Phys. Chem. C* **2009**, *113*, 15559-15564.

145. Barcaro, G.; Sementa, L.; Fortunelli, A.; Stener, M. Optical properties of nanoalloys. *Phys. Chem. Chem. Phys.* **2015**, *17*, 27952-27967.

146. Sementa, L.; Barcaro, G.; Dass, A.; Stener, M.; Fortunelli, A. Designing

ligand-enhanced optical absorption of thiolated gold nanoclusters. *Chem. Commun.* **2015**, *51*, 7935-7938.

147. Smith, J. G.; Chakraborty, I.; Jain, P. K. In Situ Single-Nanoparticle Spectroscopy Study of Bimetallic Nanostructure Formation. *Angew. Chem., Int. Ed.* **2016**, *55*, 9979-9983.

148. Jin, R.; Zhao, S.; Xing, Y.; Jin, R. All-thiolate-protected silver and silver-rich alloy nanoclusters with atomic precision: stable sizes, structural characterization and optical properties. *CrystEngComm* **2016**, *18*, 3996-4005.

149. Wu, Z.; Suhan, J.; Jin, R. One-pot synthesis of atomically monodisperse, thiol-functionalized Au_{25} nanoclusters. *J. Mater. Chem.* **2009**, *19*, 622-626.

150. Yuan, X.; Zhang, B.; Luo, Z.; Yao, Q.; Leong, D. T.; Yan, N.; Xie, J. Balancing the Rate of Cluster Growth and Etching for Gram-Scale Synthesis of Thiolate-Protected Au_{25} Nanoclusters with Atomic Precision. *Angew. Chem., Int. Ed.* **2014**, *53*, 4623-4627.

151. Hassinen, J.; Pulkkinen, P.; Kalenius, E.; Pradeep, T.; Tenhu, H.; Häkkinen, H.; Ras, R. H. A. Mixed-Monolayer-Protected Au_{25} Clusters with Bulky Calix[4]arene Functionalities. *J. Phys. Chem. Lett.* **2014**, *5*, 585-589.

152. Templeton, A. C.; Wuelfing, W. P.; Murray, R. W. Monolayer-protected cluster molecules. *Acc. Chem. Res.* **2000**, *33*, 27-36.

153. Niihori, Y.; Matsuzaki, M.; Pradeep, T.; Negishi, Y. Separation of precise compositions of noble metal clusters protected with mixed ligands. *J. Am. Chem. Soc.* **2013**, *135*, 4946−4949.

154. Guo, R.; Song, Y.; Wang, G. L.; Murray, R. W. Does core size matter in the kinetics of ligand exchanges of monolayer-protected Au clusters? *J. Am. Chem. Soc.* **2005**, *127*, 2752-2757.

155. AbdulHalim, L. G.; Kothalawala, N.; Sinatra, L.; Dass, A.; Bakr, O. M. Neat and Complete: Thiolate-Ligand Exchange on a Silver Molecular Nanoparticle. *J. Am. Chem. Soc.* **2014**, *136*, 15865-15868.

156. Mathew, A.; Natarajan, G.; Lehtovaara, L.; Häkkinen, H.; Kumar, R. M.; Subramanian, V.; Jaleel, A.; Pradeep, T. Supramolecular Functionalization and Concomitant Enhancement in Properties of Au_{25} Clusters. *ACS Nano*

2014, *8*, 139-152.

157. Shibu, E. S.; Muhammed, M. A. H.; Tsukuda, T.; Pradeep, T. Ligand Exchange of $Au_{25}SG_{18}$ Leading to Functionalized Gold Clusters: Spectroscopy, Kinetics, and Luminescence. *J. Phys. Chem. C* **2008**, *112*, 12168-12176.
158. Si, S.; Gautier, C.; Boudon, J.; Taras, R.; Gladiali, S.; Bürgi, T. Ligand Exchange on Au_{25} Cluster with Chiral Thiols. *J. Phys. Chem. C* **2009**, *113*, 12966-12969.
159. Reyes, E. n.; Madueño, R.; Blázquez, M.; Pineda, T. Facile exchange of ligands on the 6-mercaptopurine-monolayer protected gold clusters surface. *J. Phys. Chem. C* **2010**, *114*, 15955-15962.
160. Knoppe, S.; Dharmaratne, A. C.; Schreiner, E.; Dass, A.; Bürgi, T. Ligand Exchange Reactions on Au_{38} and Au_{40} Clusters: A Combined Circular Dichroism and Mass Spectrometry Study. *J. Am. Chem. Soc.* **2010**, *132*, 16783-16789.
161. Y. Shichibu, Y. Negishi, T. Tsukuda and T. Teranishi, Large-Scale Synthesis of Thiolated Au_{25} Clusters via Ligand Exchange Reactions of Phosphine-Stabilized Au_{11} Clusters. *J. Am. Chem. Soc.*, **2005**, *127*, 13464-13465.
162. Habeeb Muhammed, M.; Ramesh, S.; Sinha, S.; Pal, S.; Pradeep, T. Two distinct fluorescent quantum clusters of gold starting from metallic nanoparticles by pH-dependent ligand etching. *Nano Res.* **2008**, *1*, 333-340.
163. Habeeb Muhammed, M. A.; Pradeep, T. Aqueous to Organic Phase Transfer of Au_{25} Clusters. *J. Cluster Sci.* **2009**, *20*, 365-373.
164. Heinecke, C. L.; Ni, T. W.; Malola, S.; Makinen, V.; Wong, O. A.; Häkkinen, H.; Ackerson, C. J. Structural and Theoretical Basis for Ligand Exchange on Thiolate Monolayer Protected Gold Nanoclusters. *J. Am. Chem. Soc.* **2012**, *134*, 13316-13322.
165. Xu, Q.; Wang, S.; Liu, Z.; Xu, G.; Meng, X.; Zhu, M. Synthesis of selenolate-protected $Au_{18}(SeC_6H_5)_{14}$ nanoclusters. *Nanoscale*, **2013**, *5*, 1176-1182.

166. Niihori, Y.; Kikuchi, Y.; Kato, A.; Matsuzaki, M.; Negishi, Y. Understanding Ligand-Exchange Reactions on Thiolate-Protected Gold Clusters by Probing Isomer Distributions Using Reversed-Phase High-Performance Liquid Chromatography. *ACS Nano*, **2015**, *9*, 9347-9356.

167. Niihori, Y.; Uchida, C.; Kurashige, W.; Negishi, Y. High-resolution separation of thiolate-protected gold clusters by reversed-phase high-performance liquid chromatography. *Phys. Chem. Chem. Phys.* **2016**, *18*, 4251-4265.

168. Niihori, Y.; Matsuzaki, M.; Uchida, C.; Negishi, Y. Advanced use of high-performance liquid chromatography for synthesis of controlled metal clusters. *Nanoscale*, **2014**, *6*, 7889-7896.

169. Ni, T. W.; Tofanelli, M. A.; Phillips, B. D.; Ackerson, C. J. Structural Basis for Ligand Exchange on $Au_{25}(SR)_{18}$. *Inorg. Chem.* **2014**, *53*, 6500-6502.

170. McKenzie, L. C.; Zaikova, T. O.; Hutchison, J. E. Structurally Similar Triphenylphosphine-Stabilized Undecagolds, $Au_{11}(PPh_3)_7Cl_3$ and $[Au_{11}(PPh_3)_8Cl_2]Cl$, Exhibit Distinct Ligand Exchange Pathways with Glutathione. *J. Am. Chem. Soc.*, **2014**, *136*, 13426-13435.

171. Fernando, A.; Aikens, C. M. Ligand Exchange Mechanism on Thiolate Monolayer Protected $Au_{25}(SR)_{18}$ Nanoclusters. *J. Phys. Chem. C* **2015**, *119*, 20179-20187.

172. Pengo, P.; Bazzo, C.; Boccalon, M.; Pasquato, L. Differential reactivity of the inner and outer positions of $Au_{25}(SCH_2CH_2Ph)_{18}$ dimeric staples under place exchange conditions. *Chem. Commun.* **2015**, *51*, 3204-3207.

173. Carducci, T. M.; Blackwell, R. E.; Murray, R. W. Charge-Transfer Effects in Ligand Exchange Reactions of Au_{25} Monolayer-Protected Clusters. *J. Phys. Chem. Lett.*, **2015**, *6*, 1299-1302.

174. Hossain, S.; Kurashige, W.; Wakayama, S.; Kumar, B.; Nair, L. V.; Niihori, Y.; Negishi, Y. Ligand Exchange Reactions in Thiolate-Protected Au_{25} Nanoclusters with Selenolates or Tellurolates: Preferential Exchange Sites and Effects on Electronic Structure. *J. Phys. Chem. C* **2016**, 120, 25861-25869.

175. Salassa, G.; Sels, A.; Mancin, F.; Bürgi, T. Dynamic Nature of Thiolate Monolayer in $Au_{25}(SR)_{18}$ Nanoclusters. *ACS Nano*, **2017**, *11*, 12609-12614.

176. Qian, H.; Zhu, Y.; Jin, R. Atomically precise gold nanocrystal molecules with surface plasmon resonance. *Proc. Natl. Acad. Sci. U. S. A.* **2012**, *109*, 696-700.

177. Negishi, Y.; Chaki, N. K.; Shichibu, Y.; Whetten, R. L.; Tsukuda, T. Origin of Magic Stability of Thiolated Gold Clusters: A Case Study on $Au_{25}(SC_6H_{13})_{18}$, *J. Am. Chem. Soc.* **2007**, *129*, 11322-11323.

178. Wang, Y.; Chen, J. T.; Yan, X. P. Fabrication of Transferrin Functionalized Gold Nanoclusters/Graphene Oxide Nanocomposite for Turn-On Near-Infrared Fluorescent Bioimaging of Cancer Cells and Small Animals. *Anal. Chem.* **2013**, *85*, 2529-2535.

179. Perala, S. R. K.; Kumar, S. On the mechanism of metal nanoparticle synthesis in the Brust-Schiffrin method. *Langmuir*, **2013**, *29*, 9863-9873.

180. Sreeprasad, T. S.; Maliyekkal, M. S.; Deepti, K.; Chaudhari, K.; Xavier, P. L.; Pradeep, T. Transparent, luminescent, antibacterial and patternable film forming composites of graphene oxide/reduced graphene oxide. *ACS Appl. Mater. Interfaces* **2011**, *3*, 2643-2654.

181. Knoppe, S.; Kothalawala, N.; Jupally, V. R.; Dass, A.; Burgi, T. Ligand dependence of the synthetic approach and chiroptical properties of a magic cluster protected with a bicyclic chiral thiolate. *Chem. Commun.* **2012**, *48*, 4630-4632.

182. Yao, H.; Fukui, T.; Kimura, K. Chiroptical Responses of d-/l-Penicillamine-Capped Gold Clusters under Perturbations of Temperature Change and Phase Transfer. *J. Phys. Chem. C* **2007**, *111*, 14968-14976.

183. Yao, H.; Saeki, M.; Kimura, K. Induced Optical Activity in Boronic-Acid-Protected Silver Nanoclusters by Complexation with Chiral Fructose. *J. Phys. Chem. C* **2010**, *114*, 15909-15915.

184. Yang, H.; Lei, J.; Wu, B.; Wang, Y.; Zhou, M.; Xia, A.; Zheng, L.; Zheng, N. Crystal structure of a luminescent thiolated Ag nanocluster with an octahedral Ag_6^{4+} core. *Chem. Commun.* **2013**, *49*, 300-302.

185. Shichibu, Y.; Negishi, Y.; Watanabe, T.; Chaki, N. K.; Kawaguchi, H.; Tsukuda, T. Biicosahedral Gold Clusters $[Au_{25}(PPh_3)_{10}(SC_nH_{2n+1})_5Cl_2]^{2+}$ (n = 2-18): A Stepping Stone to Cluster-Assembled Materials. *J. Phys. Chem. C* **2007**, *111*, 7845-7847.

186. Jin, R.; Liu, C.; Zhao, S.; Das, A.; Xing, H.; Gayathri, C.; Xing, Y.; Rosi, N.; Gil, R.; Jin, R. Tri-icosahedral Gold Nanocluster $[Au_{37}(PPh_3)_{10}(SC_2H_4Ph)_{10}X_2]^{+}$: Linear Assembly of Icosahedral Building Blocks. *ACS Nano*, **2015**, *8*, 8530-8536.

187. Higaki, T.; Zhou, M.; Lambright, K.; Kirschbaum, K.; Sfeir, M. Y.; Jin, R. Sharp Transition from Nonmetallic Au_{246} to Metallic Au_{279} with Nascent Surface Plasmon Resonance. *J. Am. Chem. Soc.* **2018**, *140,* 5691-5695.

188. Shichibu, Y.; Konishi, K. HCl-Induced Nuclearity Convergence in Diphosphine-Protected Ultrasmall Gold Clusters: A Novel Synthetic Route to “Magic-Number” Au_{13} Clusters. *Small*, **2010**, *6*, 1216-1220.

189. Qian, H.; Eckenhoff, W.; Bier, M.; Pintauer, T.; Jin, R. Crystal Structures of Au_2 Complex and Au_{25} Nanocluster and Mechanistic Insight into the Conversion of Polydisperse Nanoparticles into Monodisperse Au_{25} Nanoclusters. *Inorg. Chem.* **2011**, *50*, 10735-10739.

190. Kang, X.; Chong, H.; Zhu. M. $Au_{25}(SR)_{18}$: the captain of the great nanocluster ship, *Nanoscale*, **2018**, *10*, 10758-10834.

Chapter 2. Metal Doping of $Au_{25}(SR)_{18}^-$: Insights and Hindsights*

* Published: Fei, W.; Antonello, S.; Dainese, T.; Dolmella, A.; Lahtinen, M.; Rissanen, K.; Venzo, A.; Maran, F. Metal Doping of $Au_{25}(SR)_{18}^-$ Clusters: Insights and Hindsights. *J. Am. Chem. Soc.* **2019**, *141*, 16033-16045.

2.1 Introduction

Many thiolate-protected gold nanoclusters, especially those sufficiently small (typically, less than ca. 144 atoms) to display electrochemical,[1] optical,[2] and magnetic[3] molecular properties, can be prepared with atomic precision.[4,5] Recently, research has also been focusing on the selective doping of metal nanoclusters through introduction of foreign-metal atoms.[6-9] This is a very important area for both fundamental and applied (e.g., catalysis) purposes. Modification of the metal composition has been studied for several clusters, but most research has focused on $Au_{25}(SR)_{18}$, which is an atomically precise cluster that has been long considered a convenient benchmark system for understanding properties and devising applications of gold nanoclusters.[10,11]

Controlled doping of $Au_{25}(SR)_{18}^-$ has been carried out with the noble metals platinum[12-16] and palladium,[14,16-19] and less noble metals, such as cadmium[20-22] and mercury,[15,20-23] also because of the ease by which monodoping could be achieved with these metals as opposed to, say, copper and silver.[9] Mass spectrometry and single crystal X-ray crystallography were extensively employed to interpret the doping results and, particularly, assign the specific locations where these single foreign-metal atoms go. The platinum-doped clusters were prepared by direct synthesis, i.e., by reacting a mixture of tetrachloroauric and hexachloroplatinic acids with a given thiol, followed by sodium borohydride reduction.[12-15] The same procedure was applied to palladium[14,16-19] and mercury.[15] Cadmium[20-22] and mercury[20-23] were introduced into preformed $Au_{25}(SR)_{18}^-$, and studied from several viewpoints. Regarding cadmium, Wu and co-workers reported that when the metal source is a salt, $Cd(NO_3)_2$, doping occurs on the icosahedron.[21] The analysis of the data pertaining to

$Au_{24}Cd(SC2Ph)_{18}^0$ (SC2Ph = phenylethanethiolate; hereafter, we will indicate the number of carbon atoms of the alkyl chain simply as Cn) relied on X-ray crystallography and theoretical calculations of the experimental UV-vis-NIR spectrum, in comparison with the corresponding mercury monodoped cluster $Au_{24}Hg(SC2Ph)_{18}^0$ and the pertinent matrix-assisted laser desorption ionization time-of-flight (MALDI-TOF) mass spectrometry fragmentation patterns. The latter also was obtained using a salt as the metal source, $Hg(NO_3)_2$.[23] Interestingly, the two very similar syntheses led to doping at different positions: whereas Cd would go on the icosahedron,[21] for Hg the X-ray single-crystal diffraction results were interpreted to indicate that one of the staple Au atoms is replaced by Hg. Theoretical simulations of the experimental UV-vis-NIR spectrum, and the MALDI-TOF mass-spectrometry, thermogravimetric analysis, and electrochemical results provided further support to this conclusion.[23] Further work used this conclusion to understand what happens when Ag is used to dope a preformed $Au_{24}Hg(SC2Ph)_{18}^0$ cluster.[24] For both $Au_{24}Hg(SC2Ph)_{18}^0$ and the so-formed trimetallic cluster, the NMR results were taken as a further indication that Hg atom most probably occupies a staple position.

Cadmium and mercury were introduced by the Zhu group into preformed $Au_{25}(SC2Ph)_{18}^-$ by using a different approach in which the metal is added to the cluster solution as a thiolate, $Cd(SC2Ph)_2$ or $Hg(SC2Ph)_2$.[20] For Cd, single-crystal X-ray crystallographic data indicated that doping occurred at the central position. As to Hg, the cluster was concluded to have the same structure due to the same valence, NMR spectrum, and the loss of the same M_1Au_4 fragment in MALDI-TOF mass spectrometry. NMR was used only to rule out the possible presence of the tetraoctylammonium countercation, present in the native $Au_{25}(SC2Ph)_{18}^-$ solution. As for the metal-salt studies,[21,23,24] the NMR spectrum showed a complex pattern. The outcome of the stepwise formation of trimetallic clusters, $MAg_xAu_{24-x}(SC2Ph)_{18}$, was interpreted[25] on the basis of the aforementioned conclusions on the central position eventually occupied by Cd or Hg.[20] Some doped clusters were prepared with ligands other than phenylethanethiol. In particular, Thanthirige et al. prepared $Au_{24}M(SC6)_{18}^0$ (M = Pt, Hg) clusters by direct synthesis. Analysis of the MALDI-TOF mass spectrometry and X-ray photoelectron (XPS) spectra led to conclude that for both metals the doping occurred at the central position.[15] The preparation and other properties of $Au_{24}M(SC6)_{18}^0$ (M = Pt, Pd) were described by the Lee and Jiang groups in a previous publication.[14] Negishi et al. used dodecanethiol to prepare $Au_{24}Pd(SC12)_{18}^0$ and concluded, on the basis of experiments and density-functional theory (DFT) calculations that Pd occupies the center of the core.[17,18]

In a recent review article,[8] Zhu and co-workers concluded that "Doping specific number of heterometal atoms into specific positions of the nanocluster template is still one of the most challenging tasks in the nanofield." We could not agree more. Indeed, now the question is: How can we assign the specific position where these foreign-metal atoms actually go to? This is not just a problem per se, but also has far-reaching consequences because the results described above are consistently taken as the starting point for other investigations, whether related to different clusters or applications, as discussed in several review articles.[5,7-9,11,25-28] Here we address this problem by specifically focusing on the doping with Pt, Pd, Cd, and Hg atoms to form the corresponding $Au_{24}M(SR)_{18}^0$ clusters. As aforementioned, conclusions on the specific location of the foreign-metal atom have been drawn mostly on the basis of the interpretation of single-crystal X-ray crystallography and MALDI-TOF mass spectrometry data, sometimes with the support of DFT calculations, and results from XPS and UV-vis absorption spectroscopy. The structure of $Au_{25}(SR)_{18}$, whether in the anionic or neutral form,[29-31] is maintained in $Au_{24}M(SR)_{18}^0$,[16,19,20,21,23] and shows that there are three possible positions for the M atom: center (c), icosahedron (i), and staples (s) (Figure 2.1a); whereas there is only one central atom, the other positions are of 12-fold equivalency.

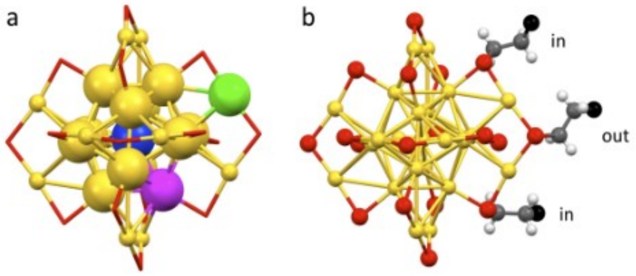

Figure 2.1. (a) Structure of $Au_{25}(SR)_{18}^{0/-}$ showing the three position types that can be occupied upon metal monodoping: central (blue), icosahedron (pink), and staple (green). The gold (yellow) and sulfur (red) atoms are shown, whereas the carbonaceous part of the ligands is omitted for clarity. (b) Structure of $Au_{25}(SR)_{18}^{0/-}$ showing the carbons (gray), hydrogens (white), and terminal groups (black) for both ligand types of one of the six staples.

Theoretical calculations have been performed to predict or explain the position of the heteroatom upon monometal doping, even ahead of substantial experimental work. Earlier DFT calculations by Jiang and Dai pointed to Cd and Hg as stable when in the center position.[32] On the other hand, other DFT calculations carried out by Walter and Moseler predicted that Pd should be more stable when at the center, whereas for Cd the lowest energy isomer is at the icosahedron, rather than elsewhere.[33] In a recent study, Taylor and Mpourmpakis used[34] their thermodynamic stability model (TSM), which attributes structure stability to a balance between the chemical potentials of the metal atoms in the core and the protecting shell,[35] to describe doping effects on nanoclusters. The TSM predictions were concluded to be in excellent agreement with experiments. The case of Hg is particularly interesting. As we saw, Hg has been described as being at the center[15,20] or in a staple position,[23] with the latter considered[34] as more likely and in agreement with the TSM. Although the icosahedral position, Hg(i), resulted close to the 95% prediction interval, a better proximity of the Hg(s) to the parity line (in a plot between shell-to-core bond energy and the metal-core cohesive energy) was seen as providing the first theoretical rationalization for the experimental observation of the Hg(s) position in $Au_{24}Hg(SR)_{18}^{0}$. Regarding Cd, which was also described that, depending of the synthetic method, could occupy two positions, center[20] or icosahedron,[21] the TSM results pointed to Cd(c) doping as being closer to the parity line than Cd(i) doping; thus, the authors also suggested that the latter could be potentially transformed into the former under proper experimental stimulus. Very recently, the Aikens group used DFT to study the doping process in a few clusters, including $Au_{24}M(SR)_{18}$.[36] Whereas group X dopants (Pd, Pt) resulted stable when at the central position, for dopants in groups XI− XIII (and thus also for Cd and Hg, group XII) the icosahedral position was found thermodynamically preferable mainly due to group theory and relativistic effects. As to the staple position compared to the central position, whereas for Cd the former has a slightly lower energy, for Hg the results point to Hg(c) as being quite more stable than Hg(s).

With the exception of Pt and Pd, for which there is no doubt that the direct synthesis yields a cluster monodoped at its central position, it is thus clear that for Cd and Hg available experimental data provide a number of opposite conclusions, possibly related to the specific synthetic method. DFT calculations have provided hints on this topic, though some analyses appear to be in contrast at least to some experimental conclusions. Here we use NMR spectroscopy, electrochemistry, MALDI-TOF, and single-crystal X-ray crystallography of each sample to demonstrate that in several cases the conclusions reached on the actual position of Cd and Hg atoms need to be drastically revised. Our study includes: (i) clusters protected by SC4 (Pt, Pd, Cd, Hg) and the SC2Ph (Cd, Hg) as the ligands; (ii) direct synthesis (Pt, Pd) and indirect synthetic methods, that is, metal exchange on both $Au_{25}(SR)_{18}^-$ (Cd, Hg) and $Au_{24}Cd(SR)_{18}^0$ (Hg); (iii) for Cd and Hg we used both the metal salt and the metal thiolate methods. This study is meant to provide new insights and perspectives into this general problem, and describe a possible experimental methodology to understand the actual doping location. The power of NMR spectroscopy and associated isotopic effects are especially highlighted. These results call for a warning about the reliability of conclusions based on mass-spectrometry fragmentation patterns and, especially, X-ray crystallography of doped clusters.

2.2 Results and Discussion

2.2.1 Synthesis

$Au_{24}Pt(SC4)_{18}^0$ was prepared by reacting a solution of $HAuCl_4$ and H_2PtCl_6 with the given thiol, followed by addition of $NaBH_4$.[12] $Au_{24}Pt(SC4)_{18}^0$ could be purified from the main co-product, $Au_{25}(SR)_{18}^-$, according to the procedure described by Qian et al.,[12] in which H_2O_2 is used to cause degradation of the undoped cluster through multiple oxidation processes. For reasons that will be discussed in the X-ray crystallography section, we used n-butanethiol. The synthesis of $Au_{24}Pt(SC4)_{18}^0$ was carried out according to a very similar protocol, but for the use of Na_2PdCl_6 in place of H_2PtCl_6. Two $Au_{25}(SR)_{18}^-$ clusters (R = C4, C2Ph), which were prepared as already described,[37-39] were allowed to react with $Cd(NO_3)_2$ or $Hg(NO_3)_2$, as described by the Wu group,[21,23] and $Cd(SR)_2$ or $Hg(SR)_2$, as described by the Zhu group.[20] These reactions are described in detail in the Experimental Section; we found that the same protocol works well for both C4 and C2Ph. In addition to using $Cd(NO_3)_2$ for making the thiolate, we used $CdCl_2$, and the reactions went equally well. This check was expedient to then carry out the exchange reactions on $Au_{25}(SR)_{18}^-$ clusters with $^{113}Cd(SR)_2$. Finally, on the two $Au_{24}Cd(SR)_{18}^0$ clusters we exchanged Cd with Hg, as described by the Wu group for R = C2Ph.[21] The clusters were carefully purified, recrystallized, and only afterward each sample batch was used for the NMR spectroscopy, UV-vis absorption spectroscopy (Figure 2.2 shows the SC4 series, whereas Figure 2.13 shows the SC2Ph series), MALDI-TOF mass spectroscopy, cyclic voltammetry (CV), and differential pulse voltammetry (DPV) measurements. The synthetic methods used only yielded monodoped clusters. Most of them were also studied by single crystal X-ray crystallography. To check the quality of the results further, some of the crystals studied at the University of Jyväskylä were also studied at the University of Padova.

2.2.2 $Au_{24}Pt(SC4)_{18}^0$ and $Au_{24}Pd(SC4)_{18}^0$

For both platinum and palladium, the direct synthesis of $Au_{24}M(SR)_{18}^0$ (R = C2Ph, C6, C12) has been consistently described to yield clusters doped at the center.[12-19] For R = C4, we followed the same synthetic and purification protocol described for platinum by Qian et al.[12] and adapted for palladium by Kwak et al..[14] MALDI-TOF mass spectrometry clearly indicated that the purified clusters only contain one foreign-metal atom, as shown in Figure 2.14 for $Au_{24}Pt(SC4)_{18}^0$, and no contamination from residual $Au_{25}(SC4)_{18}^-$ or $Au_{25}(SC4)_{18}^0$.

The NMR behaviors of $Au_{24}Pt(SC4)_{18}^0$ and $Au_{24}Pd(SC4)_{18}^0$ were studied in C_6D_6, at 1.5-2.1 mM concentration of the cluster, and the chemical shifts (δ) are referred to tetramethylsilane; these conditions were the same also for all other clusters studied. Beside the monodimensional ^1H NMR spectra, the clusters were studied by ^1H, ^1H-homonuclear correlation spectroscopy (COSY) and ^1H, ^{13}C-heteronuclear multiple quantum coherence (HMQC) spectroscopy. The 2D spectra, whose analysis allowed assigning all resonances, are provided in Figures 2.15-2.17, whereas Table 2.1 gathers all chemical shift values. $Au_{24}Pt(SC4)_{18}^0$ and $Au_{24}Pd(SC4)_{18}^0$ are diamagnetic, neutral species[16] and are thus directly comparable with the diamagnetic anion $[Au_{25}(SC4)_{18}^-](n\text{-}Oct_4N)^+$ (where n-Oct stands for norm-octyl), whose NMR data[37,38] are also provided in Table 2.1.

Au_{25} and monodoped clusters are known to share the same structural features: a central Au atom, 12 Au atoms forming an icosahedron, and an external shell composed of six–$(SR)_{in}$–Au–(SR) out –Au–(SR) in – double staples. Each staple consists of two inner thiolates (in) and one outer thiolate (out) (Figure 1b). The term inner indicates that the two SR groups also bind to the icosahedron Au atoms, whereas outer indicates that the SR group is at the outmost position of the double staple. In $[Au_{25}(SC4)_{18}^-]$ $(n\text{-}Oct_4N)^+$,[37,38] the two ligand types have different δ values, well-defined signals (corresponding to the methylene groups in positions α, β, and γ with respect to sulfur, and the methyl group in position δ), and for the same resonance the integrals are in the 2:1 ratio expected for the 12 inner and 6 outer ligands. The spectra of $Au_{24}Pt(SC4)_{18}^0$ and $Au_{24}Pd(SC4)_{18}^0$ exhibit exactly the same general features, but for slightly different chemical-shift values (Table 2.1). Figure 3 shows the comparison between the Pt-doped and the undoped clusters. This behavior clearly indicates that the symmetry of the ligands of the parent $Au_{25}(SC4)_{18}^{-}$ cluster is preserved upon monodoping, as also discussed for R = C2Ph by Qian et al.[12] and later by Tian et al.[16] For both Pt and Pd, the ^{1}H NMR spectra of $Au_{24}M(SC4)_{18}^{0}$ can thus be taken as representing the blueprint of the typical "uncomplicated" NMR behavior expected for a $Au_{24}M(SC4)_{18}^{0}$ cluster doped in its central position.

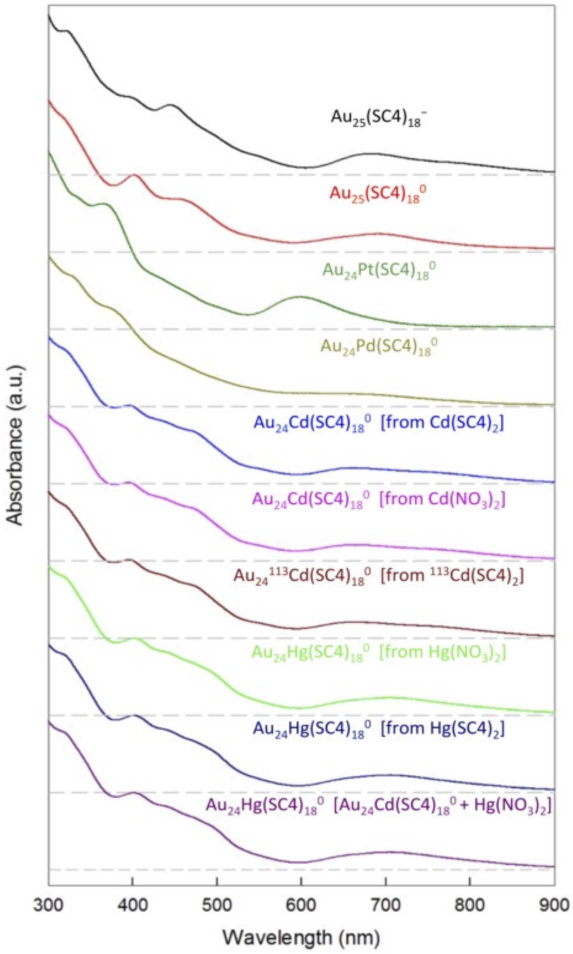

Figure 2.2. UV-vis absorption spectra of all SC4 samples (0.2 mM, 1 mm cuvette) in CH_2Cl_2. For the sake of better comparison, the curves have been shifted vertically. The dashed lines mark the corresponding zero absorbance.

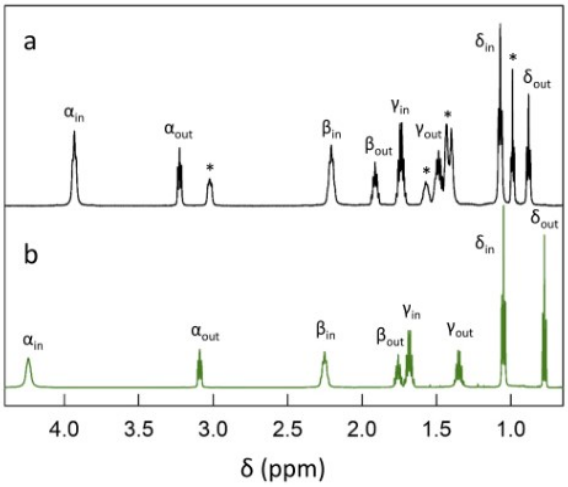

Figure 2.3. ^{1}H NMR spectra of (a) [n-Oct$_4$N$^+$][Au$_{25}$(SC4)$_{18}^-$] and (b) Au$_{24}$Pt(SC4)$_{18}^0$. The peaks marked with a star pertain to n-Oct$_4$N$^+$. Both samples were in C_6D_6 at 25 °C.

2.2.3 Au$_{24}$Hg(SC4)$_{18}^0$

The mercury-doped clusters were prepared according to three previously published methods (for C2Ph), i.e., by the (i) Au-exchange reaction of Au$_{25}$(SC4)$_{18}^-$ with Hg(SR)$_2$ (Wang et al.)[20] and (ii) Hg(NO$_3$)$_2$ (Liao et al.),[23] and by the (iii) Cd-exchange reaction of Au$_{24}$Cd(SC4)$_{18}^0$ with Hg(NO$_3$)$_2$ (Yao et al.).[21] After purification and recrystallization, all three methods led to obtain very pure Au$_{24}$Hg(SC4)$_{18}^0$ samples. The UV-vis absorption spectroscopy and MALDI-TOF spectra are shown in Figures 2.2 and 2.18, respectively.

We first consider the Au$_{24}$Hg(SC4)$_{18}^0$ sample prepared from Hg(SR)$_2$. Figure 2.4 shows its ^{1}H NMR spectrum and identification of the signals, as achieved by analysis of the COSY and total correlation spectroscopy (TOCSY) spectra (Figures 2.19 and 2.20); the integrals, carried out in the ranges indicated, are in a 2:1 ratio, as expected for the inner relative to the outer resonances. Figure 2.4 clearly shows that for this cluster the ligand symmetry is completely removed. Table 2.2 gathers all ^{1}H and ^{13}C chemical shifts. Perturbations from the simple pattern exhibited by the undoped cluster (Figure 2.3a) are seen for all resonances and are especially evident for the inner ligands and the protons nearer to the cluster core. It is noteworthy that signal complexity is observed even for the δ-$(CH_3)_{out}$ proton resonance, which, being the most distant from the core, in all gold nanocluster previously investigated[3] has always been the least sensitive to core size, charge, magnetic state, and environmental effects. The α-$(CH_2)_{in}$ and α-$(CH_2)_{out}$ resonances, which are at 4.07-3.78 and 3.15-3.05 ppm, respectively, exhibit particularly complex patterns. In particular, one of the α-$(CH_2)_{in}$ triplets (with an integral value corresponding to one ligand) is clearly separated from the others. It is also worth noticing that this lack of symmetry does not induce diastereotopic effects in the ligands, as opposed to what found for achiral ligands in the presence of interligand interactions and/or when the staple arrangement is chiral ($Au_{38}(SR)_{24}^0$ and $Au_{144}(SR)_{60}^0$).[40-42] Regarding the complexity of the proton signals for both the inner and outer ligands (see below), a quite similar behavior is also exhibited by the corresponding ^{13}C resonances and ^{13}C chemical shift values (HMQC experiments, Figure 2.21). In particular, for one of α-$(CH_2)_{in}$ carbons, which corresponds to the isolated ^1H triplet at 4.055 ppm, the ^{13}C chemical shift value is distinctly smaller (37.25 ppm) than the similar values shown by the other 11 ligands (39.01-38.79 ppm). A few differences are also detected for the β-$(CH_2)_{in}$, γ-$(CH_2)_{in}$, and δ-$(CH_3)_{in}$ ^{13}C resonances. Small differences are also present in the α-$(CH_2)_{out}$ and γ-$(CH_2)_{out}$ resonances, whereas β-$(CH_2)_{out}$ and δ-$(CH_3)_{out}$ appear isochronous.

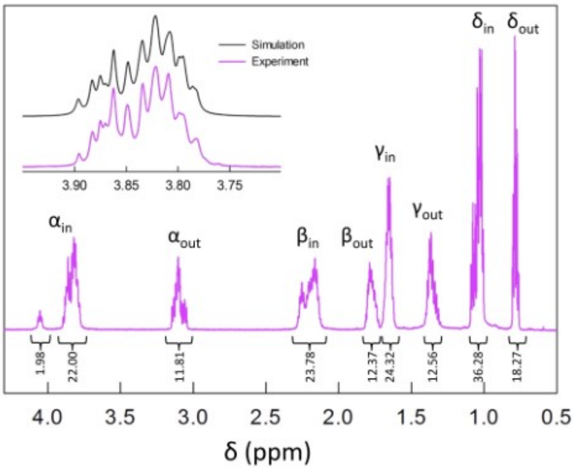

Figure 2.4. ^1H NMR spectra of 2.1 mM $Au_{24}Hg(SC4)_{18}^0$ in C_6D_6 at 25 °C. The Greek symbols have the usual meaning. The inset shows an enlarged part of the

spectral region (experiment and simulation) pertaining to 11 α-$(CH_2)_{in}$ resonances. Integrals refer to the number of protons.

Regarding the number of different inner ligands detectable in the ^{1}H NMR spectrum, we took advantage of the net separation of the α-$(CH_2)_{in}$ triplet at 4.055 ppm to simulate the cumulative signal pertaining to the remaining 11 inner resonances. By using the intensity of the isolated triplet as the starting point, we generated the convoluted signal by assigning and optimizing the chemical shifts of the 11 triplets. The indent in Figure 2.4 shows the satisfactory outcome of the simulation. The individual chemical shifts (the number of isochronous signals is given in parenthesis) are at 3.883 (1), 3.862 (2), 3.834 (1), 3.823 (4), 3.805 (1), 3.798 (1), and 3.794 (1) ppm.

A very similar set of results was obtained by analysis of the TOCSY spectrum (Figure 2.20): 3.883 (1), 3.854 (2), 3.818 (3), 3.808 (3), 3.786 (2) ppm. Despite small differences between the two methods, these results show that the perturbation caused by replacing one single Au atom with Hg generates at least 6 subgroups in the α-$(CH_2)_{in}$ resonances. Regarding the α-$(CH_2)_{out}$ triplets, analysis of the TOCSY spectrum shows that the complex signal at ca. 3.1 ppm is composed by 6 distinguishable triplets: 3.147 (1), 3.134 (1), 3.129 (1), 3.109 (1), 3.087 (1), and 3.053 (1) ppm. It is noteworthy that the effect of Hg is so strong that even all other inner and outer resonance types are affected. The ^{1}H and ^{13}C data are collected in Table 2.2.

Overall, these results clearly show that Hg cannot be located in the center of the cluster, as previously proposed for R = C2Ph.[20] On the other hand, the above NMR data cannot conclude whether Hg is in one of the icosahedral vertexes or one of the staples.

The second sample investigated was prepared from $Hg(NO_3)_2$, according to the method described by Liao et al..[23] It should be recalled that this method was described to yield an Hg(s) doped cluster, though starting from a different ligand (R = C2Ph). The ^{1}H NMR spectrum (Figure 2.22), associated 2D spectra, and integral values of recrystallized cluster are identical to those just described for the first sample.

In the third synthetic method, we prepared $Au_{24}Cd(SC4)_{18}^0$ (thiolate method, as described in the next section) and then reacted it with $Hg(NO_3)_2$ according to the protocol described for R = C2Ph by the Wu group.[21] The reaction proceeded rapidly (<10 min) and efficiently (90% yield). Once again, the ^1H NMR spectrum of the crystalline product turned out to be identical to those recorded for the other two samples (Figure 2.22). The spectrum of this specific sample was also tested for stability and found to be perfectly reproducible after 4 weeks at 10 °C.

It is finally noteworthy that all three samples gave the same fragmentation pattern in MALDI-TOF mass spectrometry (Figure 2.18) and identical UV-vis absorption spectra (Figure 2.2). Their electrochemical behavior will be discussed later.

As NMR is an extremely sensitive tool to detect even minor differences in molecular properties and chemical environment effects,[3] the results obtained for the three samples allow us to conclude that: (i) the specific synthetic approach, including the indirect method, does not yield clusters doped at different positions; (ii) mercury does not dope the cluster at the central position. At this stage, whether the three identical samples consist of Hg(s) or Hg(i) remains to be understood.

2.2.4 $Au_{24}Cd(SC4)_{18}^0$

The cadmium-doped clusters were prepared in three ways. The first two methods are based on the use of (i) $Cd(SR)_2$, obtained upon reaction of $Cd(NO_3)_2$ with the thiol (Wang et al.),[20] or (ii) $Cd(NO_3)_2$ (Yao et al.).[21]. The third approach consists in using $CdCl_2$ or $^{113}CdCl_2$ (instead of $Cd(NO_3)_2$) to make the thiolate. Figure 2.5a shows the typical ^1H NMR spectrum of the purified, recrystallized cluster obtained according to the $Cd(NO_3)_2$ method. Regardless of the synthetic procedure, however, the ^1H NMR spectra are identical (Figure 2.23). As for the Hg case, the ^1H NMR spectra show that the ligand symmetry is removed. The various signal types (position along the ligand chain and ligand type) were attributed through TOCSY analysis. The α-$(CH_2)_{in}$ and α-$(CH_2)_{out}$ resonances at 3.93-3.67 and 3.16-3.03 ppm, respectively, exhibit a complex pattern qualitatively similar to that of the Hg-doped clusters. Main differences are: (i) one of the α-$(CH_2)_{in}$ is separated from the others but is seen at higher fields (at 3.716 ppm); (ii) the separation of one of the α-$(CH_2)_{out}$ resonances (at 3.052 ppm) is more evident than for the Hg case. The integrals (Figure 5a) of the various inner and outer resonances are also in a 2:1 ratio.

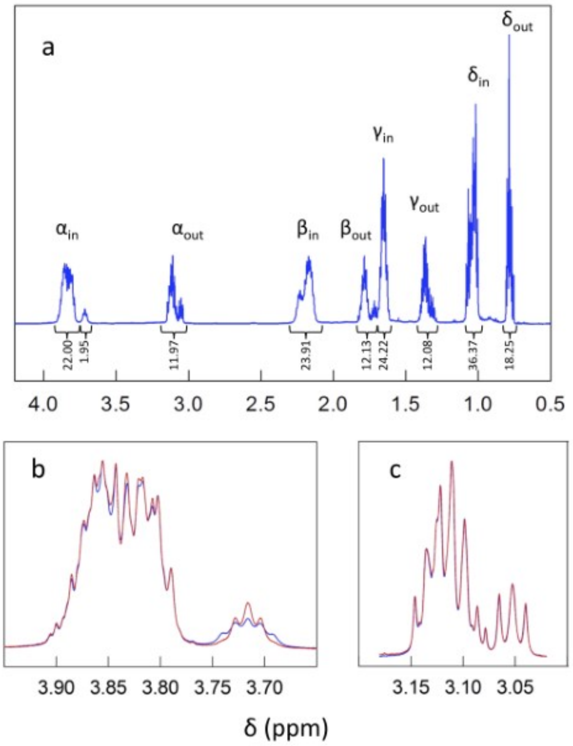

Figure 2.5. (a) ^{1}H-NMR spectrum of 2.1 mM $Au_{24}Cd(SC4)_{18}^0$ prepared from $Cd(NO_3)_2$ in C_6D_6 at 25 °C. Integrals refer to the number of protons. Graphs (b) and (c) refer to the α-$(CH_2)_{in}$ and α-$(CH_2)_{out}$ regions, respectively, for 2.1 mM $Au_{24}Cd(SC4)_{18}^0$ (red) and 2.1 mM $Au_{24}{}^{113}Cd(SC4)_{18}^0$ (blue); the latter was prepared using the thiolate obtained from $^{113}CdCl_2$.

The ^{1}H and ^{13}C data (Table 2.3) show very similar patterns as observed for the Hg-doped clusters. According to the TOCSY spectrum, the 12 α-$(CH_2)_{in}$ triplets are at 3.865 (2), 3.834 (6), 3.826 (2), 3.803 (1), and 3.716 (1) ppm, whereas the

6 α-$(CH_2)_{out}$ triplets are at 3.126 (1), 3.122 (1), 3.108 (3), and 3.052 (1) ppm. Differences are also seen along the ligand chain for both inner and outer ligands. Regarding ^{13}C, some differences are seen for α-$(CH_2)_{in}$ (whereas 11 ligands are at 38.2 ± 0.2 ppm, the isolated ligand in at 34.15 ppm), β-$(CH_2)_{in}$, δ-$(CH_3)_{in}$, α-$(CH_2)_{out}$, and β-$(CH_2)_{out}$; for γ$(CH_2)_{in}$, γ-(CH_2) out , and δ-$(CH_3)_{out}$, differences are undetectable or within experimental error.

We also note that the NMR pattern of the Cd-doped clusters does not show any diastereotopic effect, i.e., the protons of each CH_2 in each ligand type and ligand subgroup are equivalent (as already noted for the Hg-doped cluster). It is finally worth stressing that all three samples gave the same fragmentation pattern in MALDI-TOF mass spectrometry (Figure 2.24) and identical UV-vis absorption spectra (Figure 2.2). The electrochemical behavior will be discussed later.

To conclude, analysis of the three $Au_{24}Cd(SC4)_{18}^0$ samples shows that: (i) independently of the synthetic method doping always occurs at the same position and (ii) this position is not at the center of the cluster.

The question now is: is Cd on the icosahedron, as inferred by Wu and co-workers for SC2Ph,[21] or in one of the staples? To address this problem, we resorted to carry out the $Cd(SR)_2$ synthesis by starting from $^{113}CdCl_2$. Whereas the natural abundance of ^{113}Cd in Cd samples is 12.23%, enriched ^{113}Cd samples contain 95% of this spin 1/2 isotope. A point-by-point comparison between the ^1H NMR spectra of $Au_{24}{}^{113}Cd(SC4)_{18}^0$ and $Au_{24}Cd(SC4)_{18}^0$ (both obtained from the thiolate method) shows (Figure 2.25) that the effect of the isotopic enrichment is observed only for the signal at 3.716 ppm, while the rest of the spectrum is completely unchanged. Figure 2.5b shows a detail of the only change detected. In particular, the small bumps around the isolated α-$(CH_2)_{in}$ triplet of $Au_{24}Cd(SC4)_{18}^0$ are significantly enhanced in $Au_{24}{}^{113}Cd(SC4)_{18}^0$, in agreement with the ca. 8-fold isotopic enrichment. Conversely, the isolated and the other 5 convoluted α-$(CH_2)_{out}$ triplets are identical (Figure 2.5c).

^1H-^1H homodecoupling experiments were carried out by applying a standard pulse sequence. Decoupling was performed at the frequency of the β-$(CH_2)_{in}$ signal (2.173 ppm) that exhibits a scalar correlation with the isolated α-$(CH_2)_{in}$

signal at 3.716 ppm. Figure 2.6 shows the main details of the effects observed for the $Au_{24}{}^{113}Cd(SC4)_{18}{}^{0}$ and $Au_{24}Cd(SC4)_{18}{}^{0}$ samples. As expected on the basis of the ^{1}H-^{113}Cd coupling, whereas the enriched cluster shows a doublet (Figures 2.6a), the latter yields a singlet (Figure 2.6b), though accompanied by traces of a doublet (due to the presence of ^{113}Cd and ^{111}Cd, which is another spin 1/2 isotope with a natural abundance of 12.80%). The doublet in Figure 6a allows determining a $^{3}J(^{1}H\text{-}^{113}Cd)$ coupling constant of 14.3(0.1) Hz. For both $Au_{24}{}^{113}Cd(SC4)_{18}{}^{0}$ and $Au_{24}Cd(SC4)_{18}{}^{0}$, the same pulse sequence applied to the isolated β-$(CH_2)_{out}$ signal (1.719 ppm), which correlates with the corresponding isolated α-$(CH_2)_{out}$ signal at 3.052 ppm, transforms the latter into a sharp singlet, as could be anticipated on the basis of the uncomplicated shape of this triplet (Figures 2.6c,d). The slightly different position of the peaks in the decoupled spectra is due to the Bloch–Siegert shift, which causes resonances to move away from the decoupling frequency.

Figure 2.7a shows two models of the possible positions occupied by Cd. For Cd(s), the bond sequence from Cd to the α-$(CH_2)_{in}$ and α-$(CH_2)_{out}$ protons is the same, H-C-S-Cd, whereas for Cd(i) the distance from the α-$(CH_2)_{out}$ protons is larger by two bonds (H-C-S-Au-S-Cd bond sequence) than for the α-$(CH_2)_{in}$ protons. It is thus conceivable that for Cd(i) doping only the α-$(CH_2)_{in}$ protons are affected, as the experiments indeed indicate. On the other hand, if the exchange yields Cd(s), ^{113}Cd would have affected both the α-$(CH_2)_{in}$ and α-$(CH_2)_{out}$ protons with equal probability, which is in contrast to the experimental outcome.

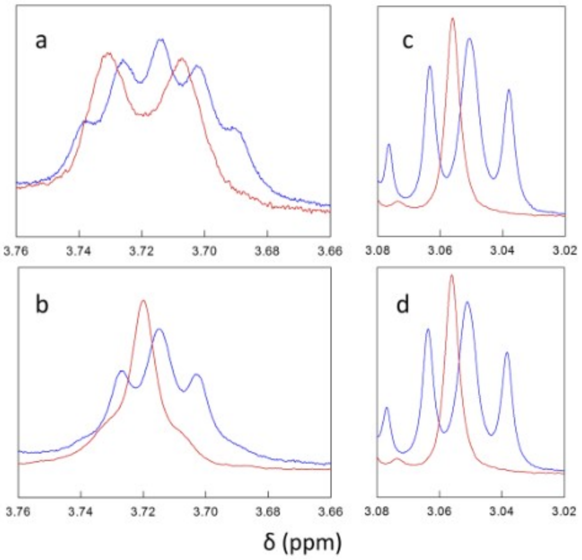

Figure 2.6. ^{1}H NMR spectra of 2.1 mM $Au_{24}{}^{113}Cd(SC4)_{18}{}^{0}$ (a,c) and 2.1 mM $Au_{24}Cd(SC4)_{18}{}^{0}$ (b,d) focusing on the α-$(CH_2)_{in}$ (a,b) and α-$(CH_2)_{out}$ (c,d) regions. The spectra are shown before (blue traces) and after ^{1}H-^{1}H homodecoupling (red traces). C_6D_6, 25 °C.

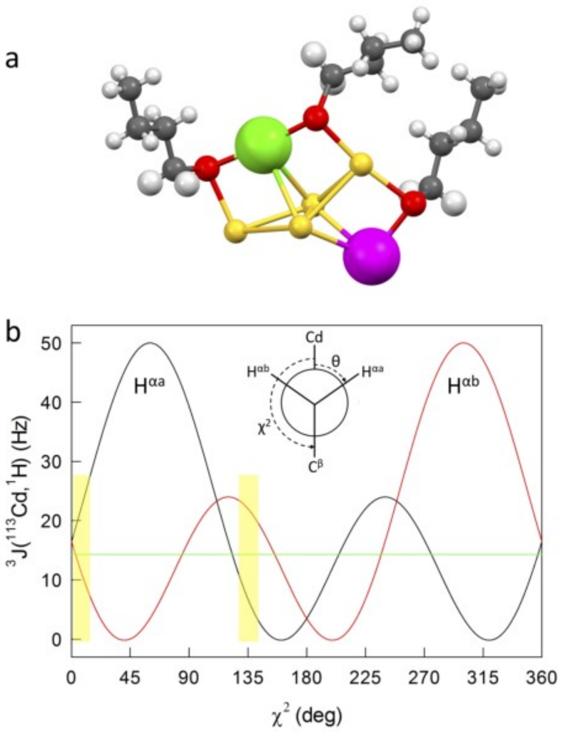

Figure 2.7. (a) Models of the possible positions occupied by Cd. (b) Karplus-like correlation of the $^3J(^1H-^{113}Cd)$ coupling constant as a function of the dihedral angle X^2. The Newman projection of the investigated bond sequence illustrates the relationship between the X^2 and θ dihedral angles. The areas highlighted in yellow show the regions where the average $^3J(^1H-^{113}Cd)$ coupling constant values are compatible with the experimentally determined J value.

To gain more quantitative insights into this aspect, we propose the use of a Karplus-type correlation, which was originally developed to describe the dihedral angle dependence of three bond $^1H-^1H$ coupling.[43] In 1994, Vašák and co-workers could demonstrate that a Karplus-type correlation describes nicely also the dihedral angle dependence of the three bond $^{113}Cd-^1H$ coupling, as obtained from HMQC data for Cd-substituted metalloproteins in comparison with the crystal structure data.[44,45] The correlation was observed for the cysteine H-C-S-Cd dihedral angle. The same group could previously demonstrate that the Cd-derivative is isostructural with the native protein.[46] Vašák and co-workers concluded that although heteronuclear couplings involving heavy nuclei generally depend on orbital angular momentum, electron-nucleus dipole-dipole interaction, and Fermi contact contributions, for Cd-substituted metalloproteins the dihedral angle is the principal determinant of the Fermi contact term and the dominant variable. Figure 2.7b, which is adapted from the original work,[44,45,47] illustrates the dependence of the $^3J(^1H-^{113}Cd)$ coupling constant on the dihedral angle θ, $^3J(^1H-^{113}Cd) = 36 (\cos^2\theta) -13 (\cos \theta) +1$, with $r^2 = 98.7\%$ and confidence limits of ca. 10 Hz; tetrahedral geometry around C^β is assumed. More precisely, Figure 2.7b shows the correlation as a function of X^2, which refers to the dihedral angle with respect to the β carbon atom. The inset to Figure 2.7b shows the Newman projection of the bond sequence and defines the relationship between the dihedral angles θ and X^2, where θ relates to H a (one of the two α-$(CH_2)_{in}$ protons). The correlation shows that a coupling constant should be detected no matter the magnitude of θ or X^2, as at least one of the two protons (H^a and H^b) always provides a finite coupling value. Regarding our Cd-doped clusters, the

Karplus-type correlation thus confirms that for the hypothetical Cd(s) some coupling with the α-$(CH_2)_{out}$ protons should be observed as well as with the α-$(CH_2)_{in}$ protons. This is not seen.

Let us now focus on the only resonance α-$(CH_2)_{in}$ affected by the presence of ^{113}Cd. Figure 2.7b shows that very few X^2 regions (in yellow; for symmetry, only the range from 0 to 180° needs to be considered), which determine the $^3J(^1H-^{113}Cd)$ coupling constant values, provide average $^3J(^1H-^{113}Cd)$ coupling constant values compatible with the experimentally determined J value of 14.3 Hz, at least within a prudential uncertainty of ca. ±3 Hz: 0-13 ° (J = 16.5 ÷ 17.2 Hz) and 128-143° (J = 17.2 ÷ 11.3 Hz). For steric reasons, however, the latter is the only plausible region. The reliability of this conclusion will be addressed for $Au_{24}Cd(SC2Ph)_{18}^0$.

2.2.5 $Au_{24}Cd(SC2Ph)_{18}^0$ and $Au_{24}Hg(SC2Ph)_{18}^0$

The results and conclusions so far reached regard the butanethiolate-protected clusters and thus the question arises as to whether they are extendable to other ligands, also considering that the seminal works carried out by the groups of Zhu and Wu on Cd- and Hg-doping focused on the phenylethanethiolate ligand. Indeed, since Donkers et al. described the first synthesis and isolation of Au_{25} protected by phenylethanethiolate ligands[48] (Note: this cluster was originally believed to be $Au_{38}(SC2Ph)_{24}$), followed some years later by the actual crystallographic structure determination of $[Au_{25}(SC2Ph)_{18}^-]$ $(n\text{-}Oct_4N)^+$,[29,30] phenylethanethiolate has been adopted by many research groups as sort of a reference ligand. We thus studied the Cd- and Hg-doping of $[Au_{25}(SC2Ph)_{18}^-]$ $(n\text{-}Oct_4N)^+$ according to the same sequence of reactions and tests already described for the SC4 ligand.

$Au_{24}Cd(SC2Ph)_{18}^0$ was prepared according to the $Cd(SC2Ph)_2$,[20] $Cd(NO_3)_2$,[21] and the $CdCl_2$ (or $^{113}CdCl_2$) - thiolate methods. As for the SC4 ligand, the corresponding MALDI-TOF (Figure 2.26) and UV-vis absorption spectroscopy spectra (Figure 2.13) show no differences. The ^1H NMR spectra of the $Au_{24}Cd(SC2Ph)_{18}^0$ sample obtained from $Cd(SC2Ph)_2$ (blue) and

$Au_{24}{}^{113}Cd(SC2Ph)_{18}{}^0$ (red) are shown in Figure 2.8. The perfect overlap of the spectra in Figure 2.8 (but for the feature magnified in the inset, as discussed below) and Figure 2.28, which pertain to the three samples, confirms that preparing this doped cluster with the thiolate,[20] the salt,[21] or the $CdCl_2$ - thiolate method produces the very same result. A previously reported spectrum (CD_2Cl_2, $Cd(SR)_2$ synthesis) shows similar features (Figure 2.19 in reference 20), whereas no NMR data were provided in the other report on Cd doping.[21]

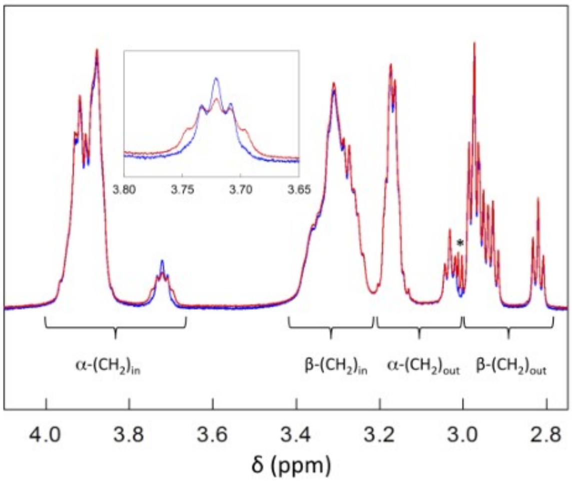

Figure 2.8. Full overlap of the ^1H NMR spectra of 2.2 mM $Au_{24}Cd(SC2Ph)_{18}{}^0$ (blue) and 2.2 mM $Au_{24}{}^{113}Cd(SC2Ph)_{18}{}^0$ (red) in C_6D_6 at 25 °C (region of the aliphatic C-H signals). The inset highlights the effect of isotopic enrichment on the isolated α-$(CH_2)_{in}$ resonance. The star marks a solvent impurity (methanol).

The spectrum shows that the ligand symmetry is disrupted, which, once again, is inconsistent with Cd(c) doping.[20] The COSY spectrum (Figure 2.27) allows attributing (Table 2.4) the complex signal at 4.0-3.8 ppm (integral corresponding to 11 ligands) to 22 α-$(CH_2)_{in}$ protons, the slightly distorted triplet at 3.722 ppm to the twelfth α-$(CH_2)_{in}$ ligand, and the multiplet at 3.43-3.21 ppm to the 24 β-$(CH_2)_{in}$ protons. The α-$(CH_2)_{in}$ signal at 3.722 ppm correlates with the β-$(CH_2)_{in}$ triplet at 3.287 ppm. The resonances corresponding to the 6 outer ligands appear as a complex multiplet of α-$(CH_2)_{out}$ resonances centered at 3.17 (10 protons) followed by one additional triplet at 3.031 ppm (2 protons), and a series of largely overlapped β-$(CH_2)_{out}$ triplets at 3.0-2.9 ppm (10 protons, five ligands) followed by one additional triplet (2 protons) at 2.820 ppm. The α-$(CH_2)_{out}$ and β-$(CH_2)_{out}$ triplets at 3.031 and 2.820 ppm correlate and thus belong to the same ligand. Careful analysis of the COSY spectrum, which was acquired during a particularly long time frame, allows distinguishing 12 nonisochronous inner ligands and 6 outer ligands (Table 2.4), which confirms on a quantitative basis the profound effect of Cd-doping on the ligand symmetry. Regarding the ^{13}C resonances, the values are pretty much isochronous (for the same position and ligand type), but for small differences for the isolated inner and outer signals.

The observation of an isolated triplet for both the inner and outer ligands is compatible with both Cd(i) and, intuitively, even more for Cd(s), as in this case both the α-$(CH_2)_{out}$ and β-$(CH_2)_{out}$ resonances are significantly affected. Can this be taken as the proof that the staple position is preferable? To clarify the position of the Cd atom, we followed the same procedure used for SC4. First, we checked that the reaction with $CdCl_2$ proceeds smoothly and then used $^{113}CdCl_2$ to prepare $Au_{24}{}^{113}Cd(SC2Ph)_{18}{}^0$. Figure 2.8 shows that only the isolated α-$(CH_2)_{in}$ is affected by ^{113}Cd, while the rest of the ^1H NMR spectrum is perfectly superimposable to that of $Au_{24}Cd(SC2Ph)_{18}{}^0$. The inset of Figure 2.8 shows the detail of this effect. Decoupling was carried out for both $Au_{24}{}^{113}Cd(SC2Ph)_{18}{}^0$ and $Au_{24}Cd(SC2Ph)_{18}{}^0$, and the effects on both α-$(CH_2)_{in}$ and α-$(CH_2)_{out}$ were tested. As expected on the basis of the ^1H NMR spectra, the only effect is on the isolated α-$(CH_2)_{in}$ resonance (Figure 2.29). Not only the effect is qualitatively the same as described for SC4, but also the $^3J(^1H\text{-}^{113}Cd)$ coupling constant is quite similar, 13.6(0.2) Hz. As observed for $Au_{24}Cd(SC2Ph)_{18}{}^0$ (Figure 2.6), a trace of the α-$(CH_2)_{in}$ doublet obtained upon decoupling could be detected also in the $Au_{24}Cd(SC2Ph)_{18}{}^0$ sample. These results confirm that the Cd dopant is on the icosahedron, as demonstrated above for the C4 cluster and originally suggested by Wu and co-workers for the C2Ph cluster.[21]

According to the correlation between the $^3J(^1H\text{-}^{113}Cd)$ coupling constant and the H-C-S-Cd dihedral angle,[43,44] the virtually identical coupling constants determined experimentally for the SC4 and SC2Ph ligands point to very similar

H-C-S-Cd dihedral angles. As described later, we could obtain the structures of both $Au_{24}Cd(SC4)_{18}^0$ and $Au_{24}Cd(SC2Ph)_{18}^0$ by single-crystal X-ray crystallography. Whereas the former is affected by intercluster interactions, the latter refers to unbounded clusters. $Au_{24}Cd(SC2Ph)_{18}^0$ thus provides an ideal case to test on quantitative grounds the validity of the $^3J(^1H-^{113}Cd)$ coupling constant correlation, which was originally described for metalloproteins, also for gold nanoclusters. According to the correlation, the experimentally determined J value corresponds (within ca. 3 Hz) to plausible angle X^2 values of 130 ÷ 145° (J = 16.6 ÷ 10.6 Hz). In the structure of $Au_{24}Cd(SC2Ph)_{18}^0$, we find that the average C^β-C^α-S-Cd dihedral angle X^2 is 149°; similar values can be obtained from the structures published by Wang et al., 150°,[20] and Yao et al., 133°.[21] These figures yield an average X^2 of 144°, which is indeed in excellent agreement with the estimated range, also considering the usual limits of comparing solid- to solution-phase results.

$Au_{24}Hg(SC2Ph)_{18}^0$ was also prepared in three ways: (i) metal exchange on $Au_{25}(SC2Ph)_{18}^-$ with $Hg(SC2Ph)_2$[20] and $Hg(NO_3)_2$,[23] and metal exchange on preformed $Au_{24}Cd(SC2Ph)_{18}^0$ with $Hg(NO_3)_2$.[21] After purification and recrystallization, the three $Au_{24}Hg(SC2Ph)_{18}^0$ samples were characterized by UV-vis absorption spectroscopy (Figure 2.13), electrochemistry (see next section), and MALDI-TOF mass spectrometry, which gave the same fragmentation pattern (Figure 2.30).

The three $Au_{24}Hg(SC2Ph)_{18}^0$ samples exhibit identical ^1H NMR spectra, even from the viewpoint of minor features (Figure 2.31 allows appreciating the perfect correspondence of the three spectra). The typical ^1H NMR pattern of $Au_{24}Hg(SC2Ph)_{18}^0$ is exemplified in Figure 2.9a, which pertains to the sample obtained upon metal exchange on a preformed $Au_{24}Cd(SC2Ph)_{18}^0$ cluster. Please note that whereas the $Hg(NO_3)_2$ synthesis is supposed to yield Hg(s),[23] for the double exchange we purposely used $Au_{24}Cd(SC2Ph)_{18}^0$ obtained using $Cd(SR)_2$, as this sample is that supposed to produce Cd(c).[20]

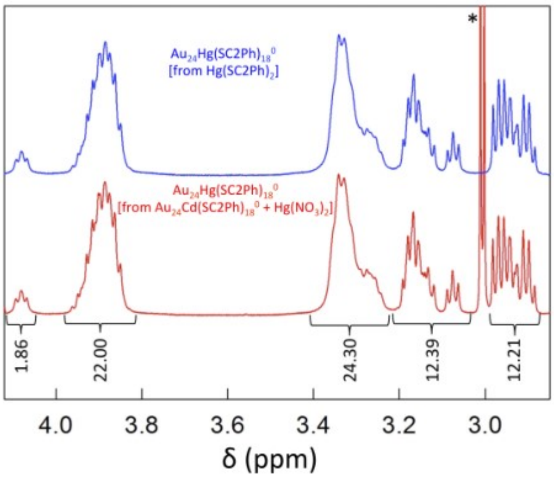

Figure 2.9. ^{1}H NMR spectrum of 2.2 mM $Au_{24}Hg(SC2Ph)_{18}^{0}$ (aliphatic C-H signals) obtained from $Hg(SC2Ph)_2$ (blue trace) or after exchange on a preformed $Au_{24}Cd(SC2Ph)_{18}^{0}$ cluster (red trace). The integrals and ligand types are indicated. The asterisk marks a solvent impurity (methanol).

The ^{1}H NMR spectrum exhibits four groups of peaks. Assignments were carried out through COSY measurements (Figure 2.32), and the corresponding ^{1}H and ^{13}C chemical shifts are provided in Table 2.5. As for $Au_{24}Cd(SC2Ph)_{18}^{0}$, the inner resonances α-$(CH_2)_{in}$ and β-$(CH_2)_{in}$ are clearly separated from the two outer resonances α-$(CH_2)_{out}$ and β-$(CH_2)_{out}$. For both α-$(CH_2)_{in}$ and α-$(CH_2)_{out}$, one of the triplets is well separated from the others. As for SC4, the isolated α-$(CH_2)_{in}$ signal is downfield with respect to the group of the remaining 11 ligands, whereas it is upfield for the outer ligands. The COSY analysis of the α-$(CH_2)_{in}$ and α-$(CH_2)_{out}$ resonances allowed estimating the presence of each of the 12 and 6 ligands, respectively. Nonisochronous signals are also detected for the corresponding β-$(CH_2)_{in}$ and β-$(CH_2)_{out}$ resonances. As to ^{13}C, the signals are isochronous, with a few exceptions. Once again, the number of clearly distinguishable resonances and isochronous signals witnesses the significant loss of symmetry undergone upon Hg-doping. It is worth noticing that the ^{1}H NMR spectra obtained for $Au_{24}Hg(SC2Ph)_{18}^{0}$ (Figure 2.28 in reference 24 and Figure 2.19 in reference 20) show very similar features (our data were obtained in C_6D_6, whereas those published data pertain to CD_2Cl_2), though they were not specifically discussed. Overall, the NMR analysis shows that the Hg atom cannot be at the central position of the cluster, as previously hypothesized.[20]

As to its actual position, we argued that the fast Hg exchange on a preformed $Au_{24}Cd(SC2Ph)_{18}^0$ cluster occurs on the icosahedron as well, i.e., directly on the site occupied by Cd(i), rather than involving a complicate molecular rearrangements where first Hg exchanges Cd(i) and then switches position with the nearby Au(s) atom. To gain insights into this problem, we applied the same decoupling sequence used for the Cd-doped clusters. The goal was to detect a possible $^3J(^1H-^{199}Hg)$ coupling by relying on the fact that ^{199}Hg has a natural abundance of 16.94% and is a spin 1/2 isotope. Assuming that a Karplus-type correlation is valid also for the three-bond system H-C-S-Hg, one would expect to see some $^3J(^1H-^{199}Hg)$ coupling only for α-$(CH_2)_{in}$ or both α-$(CH_2)_{in}$ and α-$(CH_2)_{out}$ for Hg(i) and Hg(s), respectively. Radiating the corresponding β-$(CH_2)_{in}$ signal (assessed via TOCSY) transforms the α-$(CH_2)_{in}$ signal into a singlet accompanied by a doublet (Figure 2.33a) that allows calculating a $^3J(^1H-^{199}Hg)$ coupling constant of 36 Hz. Conversely, radiating the β-$(CH_2)_{out}$ signal transforms the corresponding isolated α-$(CH_2)_{out}$ signal into an uncomplicated singlet (Figure 2.33b). We also applied the same decoupling analysis to the isolated α-$(CH_2)_{in}$ signal of $Au_{24}Hg(SC4)_{18}^0$, obtained the same outcome, and calculated the very similar value of 37 Hz (Figure 2.10), whereas no effect was detected for the isolated α-$(CH_2)_{out}$ resonance. Although to the best of our knowledge a Karplus-like dependence has never been observed for ^{199}Hg, it is conceivable that a periodic dependence such as that found for $^3J(^1H-^{113}Cd)$[44,45] should be qualitatively valid also for of the $^3J(^1H-^{199}Hg)$ coupling. The virtually identical values determined for C2Ph and C4 would thus point to very similar average dihedral angles, as determined for the Cd-doped clusters. Most important, these results provide compelling evidence that Hg-doping, whether performed directly on $Au_{25}(SR)_{18}^-$ or indirectly on $Au_{24}Cd(SR)_{18}^0$, consistently yields Hg(i), rather than Hg(s).[23]

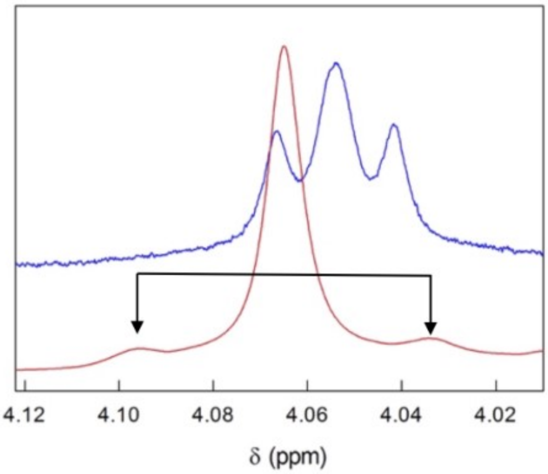

Figure 2.10. ^{1}H NMR spectra of 2.1 mM $Au_{24}Hg(SC4)_{18}^0$, focusing on the isolated α-$(CH_2)_{in}$ region before (blue) and after (red) ^{1}H-^{1}H homodecoupling at the frequency of the corresponding β-$(CH_2)_{in}$ signal. The two spectra are vertically shifted for clarity and the arrows mark the doublet. C_6D_6, 25 °C.

To conclude, NMR demonstrates that both Cd and Hg are exchanged on the icosahedron, no matter the synthetic method employed or the nature of the ligand. It should be also noted that the MALDI-TOF mass spectra of the samples obtained for each doped clusters are identical (Figures 2.18, 2.24, 2.26 and 2.30). As either foreign-metal atom is on the icosahedron, differences in the fragmentation patterns observed between the Hg and Cd doped clusters should not to be taken as indicating a different doping position.[23] Rather, they just reflect the effect of the specific doping element, as also supported by the similar fragmentation patterns exhibited for the same doping metal by the SC4 and SC2Ph protected clusters.

2.2.6 Electrochemistry of $Au_{24}M(SR)_{18}$

The electrochemical measurements were carried out in dichloromethane (DCM) containing 0.1 M tetrabutylammonium hexafluorophosphate (TBAH), using a glassy carbon (GC) microdisk electrode. Figure 2.11a compares the DPV behavior of $Au_{24}M(SR)_{18}$ for M = Au, Pt, Cd, and Hg. Figure 11b shows the DPV behavior of the $Au_{24}M(S2CPh)_{18}$ samples (M = Au, Cd, Hg). As expected, for both the Hg- and Cd-doped clusters the various samples exhibit exactly the same DPV pattern and formal potential (E°) values. This is exemplified for both ligands in Figure 2.34, which shows the DPVs of the Hg samples obtained with the $Hg(NO_3)_2$, thiolate, and Cd exchange methods.

The DPVs of $Au_{24}Hg(SC4)_{18}^0$ and $Au_{24}Cd(SC4)_{18}^0$ are qualitatively similar to that of $Au_{25}(SC4)_{18}^-$. The doped clusters undergo two successive one-electron oxidations ($E°_1$ and $E°_2$) at 0.364 and 0.684 V, $Au_{24}Hg(SC4)_{18}^0$, and 0.332 and 0.636 V, $Au_{24}Cd(SC4)_{18}^0$. In the timescale of voltammetry experiments, both processes are reversible. Further oxidation processes are detectable at more positive potentials, though with formation of chemically labile species. The *E*° for the first peak of these doped clusters is more positive than that of $Au_{25}(SC4)_{18}^-$ ($E°_1 = -0.188$, $E°_2 = 0.139$ V, respectively)[49] by 0.552 and 0.520 V, respectively. For $Au_{24}Hg(SC2Ph)_{18}^0$ ($E°_1 = 0.451$, $E°_2 = 0.703$ V) and $Au_{24}Cd(SC2Ph)_{18}^0$ ($E°_1 = 0.430$, $E°_2 = 0.668$ V) similar considerations apply. With respect to $Au_{25}(SC2Ph)_{18}^-$ ($E°_1 = -0.077$, $E°_2 = 0.226$ V),[50] the positive shifts of $E°_1$ are 0.528 and 0.507 V, respectively. For both Hg and Cd, this remarkable positive shift was already observed.[23,51]

Regarding the first reduction peak, which for $Au_{24}Hg(SC4)_{18}^0$ and $Au_{24}Cd(SC4)_{18}^0$ occurs at −1.23 and −1.39 V, respectively, the formation of the anion is chemically irreversible. For the latter, increasing the CV potential scan rate (v) allows to detect reversibility, and therefore, determine an *E*° value of -1.38 V. We described this procedure in detail for a series of $Au_{25}(SR)_{18}$ clusters.[50,52,53] The electrochemical gap of $Au_{24}Cd(SC4)_{18}^0$ can thus be calculated from the *E*° difference between the +1/0 and 0/-1 redox couples. The corresponding HOMO-LUMO gap can then be estimated by subtracting the charging-energy contribution, obtained from the *E*° difference between the +2/+1 and +1/0 states.[54] The value so-obtained, 1.41 eV, is in very good agreement with the HOMO-LUMO gap of 1.37 eV estimated from the onset of optical absorption (Figure 2.2). For $Au_{24}Cd(SC2Ph)_{18}^0$ we observed the same behavior, and this allows calculating an *E*° value of −1.26 V for the 0/−1 redox couple. The HOMO-LUMO gap is thus estimated to be 1.46 eV, to be compared with that obtained from the optical spectrum (Figure 2.13), 1.41 eV and the value of 1.4 (0.1) eV obtained by time-resolved spectroscopic analysis.[22]

For both SC4 and SC2Ph ligands, the analysis of the reduction of the Hg-doped clusters is more complicated because the voltammetric peak exhibits features that suggest interaction with the electrode surface. Furthermore, for both Hg-doped clusters the peak is irreversible also at high *v* values (up to 50 V s^{-1}). However, at low temperature (−45 °C) and high *v* some reversibility is detectable, which allows estimating *E*°. By comparing this result with the corresponding *E*° determined at the same temperature for $Au_{25}(SC2Ph)_{18}^{-}$, the E° values of the two $Au_{24}Hg(SR)_{18}^{0}$ clusters at 25 °C could be estimated. Calculation of the HOMO-LUMO gap yields 1.28 (SC4) and 1.29 (SC2Ph), respectively; these gaps are thus slightly smaller than those electrochemically determined for $Au_{25}(SC4)_{18}^{-}$ and $Au_{25}(SC2Ph)_{18}^{-}$, 1.30 and 1.34 eV, respectively.[49,55] A very recent time-resolved spectroscopy analysis led for $Au_{24}Hg(SC2Ph)_{18}^{0}$ and $Au_{25}(SC2Ph)_{18}^{-}$ to the similar values of 1.2 (0.1) and 1.3 (0.1) eV, respectively.[22] Very recent calculations provided a similar decrease in the HOMO-LUMO gap energy on going from Cd to Hg, as well as valuable insights into the electronic effects introduced by dopants.[36]

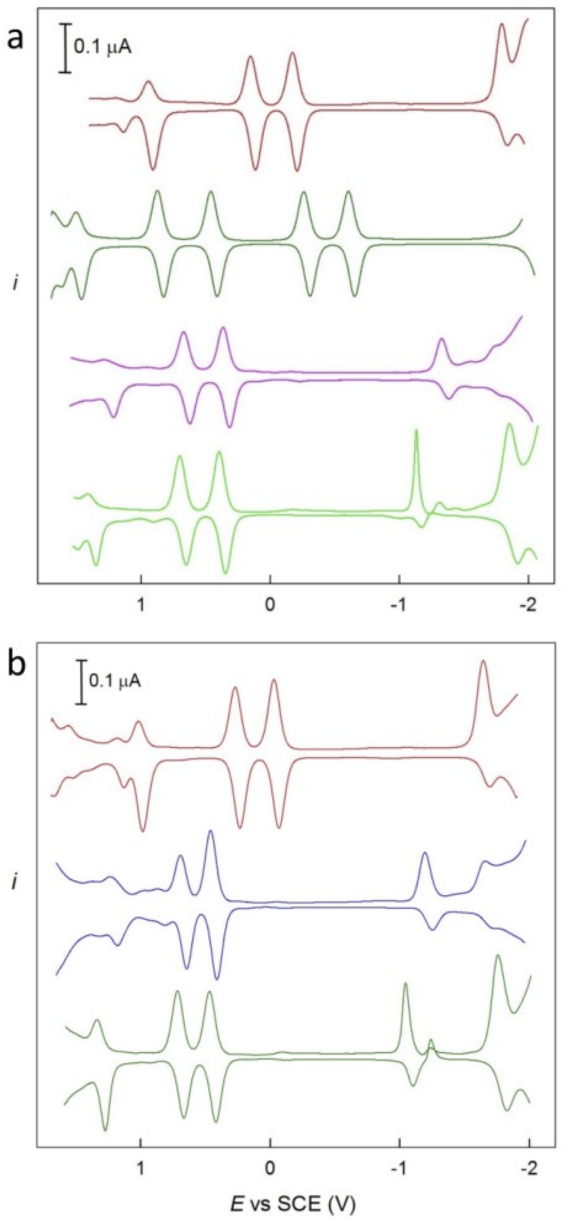

Figure 2.11. Comparison between the DPV curves for (top to bottom): (a) $Au_{25}(SC4)_{18}^{-}$, $Au_{24}Pt(SC4)_{18}^{0}$, $Au_{24}Cd(SC4)_{18}^{0}$, and $Au_{24}Hg(SC4)_{18}^{0}$; (b) $Au_{25}(SC2Ph)_{18}^{-}$, $Au_{24}Cd(SC2Ph)_{18}^{0}$, and $Au_{24}Hg(SC2Ph)_{18}^{0}$. Glassy-carbon electrode, DCM/0.1 M TBAH, 25 °C.

The DPV of $Au_{24}Pt(SC4)_{18}^{0}$ clearly points to a different orbital-energy distribution. It shows two pairs of peaks corresponding to the formation of the mono- and dication on the positive-going scan (*E*° of 0.475 and 0. 853 V), and the mono- and dianion on the negative-going scan (*E*° of -0.287 and -0.622 V). Each of these charge states is chemically stable. For this cluster, a HOMO-LUMO gap of 0.384 eV can be estimated from the electrochemical data (for the charging energy correction, we used the potential difference calculated for the two oxidation peaks, 0.378 V) is much lower than for the other clusters investigated. A previous electrochemical analysis carried out on $Au_{24}Pt(SC6)_{18}^0$ yielded the similar value of 0.34 eV.[14] With SC4, however, we fail to detect the large potential difference reported for the $E°_1$ of $Au_{25}(SC6)_{18}^-$ and the first reduction peak of $Au_{24}Pt(SC6)_{18}^0$.[14]

Overall, some of our electrochemical data essentially confirm previous electrochemical conclusions on the position occupied by Pt upon Au_{25} -doping[14] and the effect of Hg-doping.[23] Most important, however, they provide further compelling evidence that Hg- and Cd-doping always occur on the same metal site, no matter the ligand and how metal exchange is carried out.

2.2.7 Single Crystal X-Ray Crystallography

We could solve the structure of most of the clusters, sometimes also as the result of different syntheses and in two laboratories, as specified: $Au_{24}Pt(SC4)_{18}^0$ (Padova), $Au_{24}Hg(SC4)_{18}^0$ (from $Hg(SC4)_2$, Jyväskylä), $Au_{24}Cd(SC4)_{18}^0$ (from $Cd(NO_3)_2$, Jyväskylä), $Au_{24}Cd(SC4)_{18}^0$ (from $Cd(SC4)_2$, Jyväskylä), $Au_{24}Hg(SC2Ph)_{18}^0$ (from $Hg(NO_3)_2$, Padova and Jyväskylä), $Au_{24}Hg(SC2Ph)_{18}^0$ (from $Hg(NO_3)_2$ + $Au_{24}Cd(SC2Ph)_{18}^0$, Padova and Jyväskylä), and $Au_{24}Cd(SC2Ph)_{18}^0$ (from $Cd(SC4)_2$, Jyväskylä). Here we will focus on the most salient aspects, whereas full discussion on these results is provided in the Supporting Information.

For both $Au_{24}Hg(SC4)_{18}^0$ and $Au_{24}Cd(SC4)_{18}^0$, the structure shows the very same features discovered for $Au_{25}(SC4)_{18}^0$ (this cluster is a neutral radical)[37] and $Au_{25}(SC5)_{18}^0$:[39] (i) the clusters form linear polymers of interconnected clusters; (ii) the connecting staples form S-Au-Au-S dihedral angles of nearly 90° (for both Hg- and Cd-doping, 81-85°); (iii) the neighboring clusters are connected via aurophilic Au-Au bonds. Formation of the polymers is thus granted by a twistand-lock mechanism[37] in which the orientation of the alkyl chains and their van der Waals interaction opens up two opposite sides of the Au-S-Au staples and favor a closer approach between neighboring clusters, thereby causing formation of an intercluster Au-Au aurophilic bond. In the doped clusters, this bond has a similar length, 3.09 Å (Hg- doping) and 3.10 Å (Cd-doping), as found in $Au_{25}(SC4)_{18}^0$ (3.15 Å) 37 and $Au_{25}(SC5)_{18}^0$ (2.98 ÷ 3.03 Å).[39] These results thus point to the importance of the alkanethiolate ligand, and show that formation of the intercluster aurophilic bond is possible regardless of the magnetic state of the cluster: in fact, as opposed to $Au_{25}(SC4)_{18}^0$, both the Hg- and Cd-doped clusters are diamagnetic, as evinced from the NMR results and previously shown for $Au_{24}Hg(SC2Ph)_{18}^0$ by electron paramagnetic resonance.[23]

With that being said, we note that $Au_{24}Pt(SC4)_{18}^0$, which was purposely prepared with the SC4 ligand, does not form polymers. Its structure does not show any rotation of the staples, which remains virtually parallel, and shows a relatively large minimum intercluster Au-Au distance of 3.88 Å. This is as previously observed for, say, $Au_{25}(SC2)_{18}^0$, which shows a minimum intercluster Au-Au distance of 4.12 Å,[54] and $Au_{25}(SC3)_{18}^0$.[38] Overall, this may suggest that electronic factors may also play a role in determining the different behavior observed for $Au_{24}Pt(SC4)_{18}^0$.

Crystallographic analysis alone is not distinctive enough for determining the positions of these doping metals with reliable accuracy. This is due to the very small electron-density differences between Au and the Pt, Hg, and Cd metals, especially for Pt and Hg that differ from Au by only one electron. Thus, an Au site substituted by Hg or Pt should show an electron density higher or lower than that of Au by only 1.2%, respectively. This figure will be significantly lowered if the doping metal is disordered over two or more locations (~0.1% difference when all 12 icosahedral sites are partially but evenly occupied; even less if distribution also involves the staples) and/or if the quality of the crystal is less than ideal. This implies that for these clusters small differences in electron densities cannot be determined reliably even with the highest quality data obtained by the modern in-house diffractometers. However, thorough analysis of the structure of the Cd doped clusters (the electron-density difference between Cd and Au is ~60%) using several data sets with the highest possible data quality (data redundancy of 5) allowed us to refine the structure of the Cd-doped cluster quite satisfactorily. Consistently with the NMR analysis, refinement indicated that Cd is most likely disorderly located on the icosahedral sites instead of the center or staples. For the Hg and Pt doped $Au_{24}M(SC4)_{18}^{0}$ clusters, on the other hand, the electron-density difference is just too small to draw similar conclusions.

Regarding the SC2Ph-protected clusters, $Au_{24}Hg(SC2Ph)_{18}^{0}$ and $Au_{24}Cd(SC2Ph)_{18}^{0}$ show exactly the same structure, where the orientation of the ligands with respect to plane of the staple is always of the up-down-up type (Figure 2.12). This is, therefore, identical to the ligand orientation seen in $Au_{25}(SC2Ph)_{18}^{0}$,[39] though different from that observed in $Au_{25}(SC2Ph)_{18}^{-}$, which is always of the up-down-down type.[31,32] Finally, we checked the two structures of $Au_{24}Hg(SC2Ph)_{18}^{0}$ obtained upon metal exchange in either $Au_{25}(SC2Ph)_{18}^{-}$ or $Au_{24}Cd(SC2Ph)_{18}^{0}$, and found they are identical. Further discussion on the SC4- and SC2Ph-protected clusters is provided in the Supporting Information.

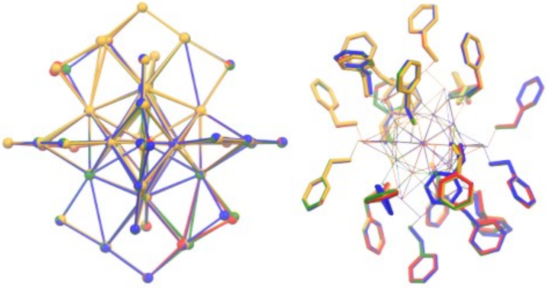

Figure 2.12. Overlap of the structures of the Hg- and Cd-doped clusters with that of $Au_{25}(SC2Ph)_{18}^{0}$.[39] The Au/M-S core units are shown on the left-hand side (ligands removed), whereas the full clusters are shown on the right-hand side (metal core units are faded, for clarity) to evidence full overlapping of the ligands (mixed colors). The color codes are: red = Hg-doped cluster (from $Hg(NO_3)_2$), blue = Hg-doped cluster (from $Hg(SC2Ph)_2$), green = Cd-doped cluster, and yellow = $Au_{25}(SC2Ph)_{18}^{0}$.

2.3 Conclusions

This study was meant to obtain insights into the monodoping of $Au_{25}(SR)_{18}^{-}$ clusters with foreign metal atoms. Accurate selection of chemicals, NMR analysis, electrochemical data, and critical analysis of crystallographic data allowed us to highlight hindsights into the challenge of understanding where the foreign-metal atoms are eventually located in the cluster structure, and how to characterize these quite elusive nanosystems. Using the NMR results obtained for $Au_{24}Pt(SC4)_{18}^{0}$ and $Au_{24}Pd(SC4)_{18}^{0}$ as a reference for the behavior expected when the cluster is doped in its central position, we show that Cd- and Hg-doping does not occur at the central position.[20] We also show that the Cd-doping mode is not different from that of Hg-doping, as opposed to what previously concluded.[21,23] Rather, we find that both Cd- and Hg-doping occurs in one of the icosahedral positions, independently of the specific ligand. Equally important, we demonstrate that the metal-exchange doping methods so-far developed always yield the very same species. Besides being important from a fundamental viewpoint, these results are also liable to impact applications of doped clusters, e.g., in catalysis, which is a promising growing area of research for atomically precise metal clusters.[56] This is because proper understanding of the doping site affects the analysis of the catalytic mechanism.[51] Finally, we provide a warning about reaching conclusions on the doping site on the basis of different fragmentation patterns in mass spectra, and especially, single-crystal X-ray crystallography results. We also hope that these new insights will be useful for theoreticians as a sound experimental basis to refine their calculation models.

2.1 Experimental Section

The $Au_{25}(SC4)_{18}^{-}$ and $Au_{25}(SC2Ph)_{18}^{-}$ clusters were prepared and purified as already described.[37,42] Full details on chemicals and the preparation of $Au_{24}Pt(SC4)_{18}^{0}$, $Au_{24}Pd(SC4)_{18}^{0}$, $Au_{24}Hg(SC4)_{18}^{0}$, $Au_{24}Cd(SC4)_{18}^{0}$, $Au_{24}Hg(SC2Ph)_{18}^{0}$, and $Au_{24}Cd(SC2Ph)_{18}^{0}$ are described in the Supporting Information.

The UV-vis absorption spectra of the clusters were obtained in DCM with a Thermo Scientific Evolution 60S spectrophotometer. The spectra were recorded with a spectral resolution of 0.5 nm. The samples were at 0.2 mM concentration in 1 mm cuvettes. MALDI-TOF mass spectrometry experiments were carried out with an Applied Biosystems 4800 MALDI-TOF/TOF spectrometer equipped with a Nd:YAG laser operating at 355 nm. The laser-firing rate was 200 Hz and the accelerating voltage was 25 kV. trans-2-[3-(4-tert-butylphenyl)-2-methyl-2-propenylidene] malononitrile (DCTB) was used as the matrix. Depending on the experiment, the instrument was calibrated with $Au_{25}(SC4)_{18}^0$ or $Au_{25}(SC2Ph)_{18}^0$. The clusters were dissolved in DCM containing DCTB to obtain 0.1 mM solutions with a 1:400 nanocluster/matrix ratio. A 5 μl solution was drop cast onto the sample plate and air-dried. All spectra were recorded using the reflector positive-ion mode.

The electrochemical experiments were carried out under an Ar atmosphere, in a glass cell at room temperature, unless otherwise stated. The solvent-electrolyte system was DCM containing 0.1 M TBAH. The working electrode was a glassy carbon microdisk (9.1×10^{-4} cm^2), prepared and activated as already described.[57] As a quasi-reference electrode, we used a silver wire, which was kept in a tube filled with the same electrolyte solution and separated from the main compartment by a Vycor frit. Its calibration was performed by addition of ferrocene at the end of the experiments; in DCM/0.1 M TBAH, the ferricenium/ferrocene redox couple has $E°$ = 0.460 V against the KCl saturated calomel electrode (SCE). All potential values are reported against SCE. The counter-electrode was a Pt wire. We used a CHI 660c electrochemical workstation. In CV, we used the positive feedback correction to minimize the ohmic drop between the working and the reference electrodes. For DPV, we used peak amplitude of 50 mV, pulse width of 0.05 s, 2 mV increments per cycle, and pulse period of 0.1 s.

^1H and ^{13}C NMR spectra were obtained on a Bruker Avance DMX-600 MHz spectrometer operating at 599.90 and 150.61 MHz, respectively, and equipped with a 5 mm TX-1 inverse probe powered by field gradients along the x, y, z-axes.

The probe temperature was controlled (±0.1 °C) with a Bruker BVT3000 temperature controller. The chemical shift (δ) values are given as ppm downfield from internal tetramethylsilane, for both ^1H and ^{13}C nuclei. To ensure a complete relaxation for all the resonances, the integrals of the proton spectra were obtained using a pre-scan delay of 10 s. All measurements were carried out in benzene-d_6. The proton assignments were performed by COSY or TOCSY, whereas the ^{13}C chemical shift values were obtained from HMQC experiments. (^1H-^1H) homodecoupling experiments were performed with the standard zghd pulse sequence provided in the Bruker library.

Single-crystal X-ray data for the metal doped $Au_{24}M(SR)_{18}{}^0$ clusters were collected either with a Rigaku Oxford Diffraction SuperNova dual-source X-ray diffractometer using hi-flux Mo and Cu micro-focus sources (Mo K_α; $\lambda = 0.71073$ Å and Cu K_α; $\lambda = 1.54184$ Å) and an Atlas CCD detector (University of Jyväskylä), and/or with an Oxford Diffraction Xcalibur Gemini diffractometer with Mo-radiation and Eos CCD detector (University of Padova). Data collection, reduction processes, and analytical numeric absorption corrections by multifaceted crystal models and/or empirical absorption correction using spherical harmonics, were all carried out using the program CrysAlisPro (v. 39.46).[58] Structures were solved by direct methods with program SHELXT 59 and refined by full-matrix least-squares on F^2 by SHELXL 60 in the OLEX 2 (v. 1.2.10) program.[61]

2.4 Supporting Information

2.4.1 Chemicals and Methods

$HAuCl_4 \cdot 3H_2O$ (Aldrich, 99.9%), Na_2PdCl_6 (Sigma-Aldrich, ≥99.99%), $Hg(NO_3)_2$ (Sigma-Aldrich, ≥99.99%), $Cd(NO_3)_2$ (Carlo Erba Reagents, 99%), $CdCl_2$ (Sigma-Aldrich, 99.99%), $^{113}CdCl_2$ (Trace Sciences International Inc., enriched 95%+), tetra-n-octylammonium bromide (Aldrich, 98%), n-butanethiol (Aldrich, 99.8%), phenylethanethiol (Aldrich, 99.8%), $NaBH_4$ (Aldrich, 99%), tetrahydrofuran (THF, Sigma-Aldrich, 99.9%), toluene (Sigma-Aldrich, 99.7%), diethyl ether (Sigma-Aldrich, 99.8%), methanol (Aldrich, 99.8%), $H_2PtCl_6 \cdot xH_2O$ (Alfa Aesar, 99.9%), trimethylamine (Sigma-Aldrich, ≥99.5%), trans-2-[3-(4-tert-butylphenyl)-2-methyl-

2-propenylidene] malononitrile (DCTB, Sigma-Aldrich, ≥98%), and benzene-d_6 (Aldrich or Eurisotop, 99.96%, d_6) were used as received. For electrochemistry, dichloromethane (DCM anhydrous, Sigma-Aldrich, ≥99.8%) was stored under an argon atmosphere. n-$BuNPF_6$ (Fluka, 99%) was recrystallized from ethanol. Low conductivity water was milliQ Water pro analysis (Merck). Column chromatography was carried out using silica gel from Macherey-Nagel (MN-Kieselgel 60 M, 230-400 mesh).

2.4.2 Synthesis of $Au_{24}M(SC4)_{18}^0$ (M = Pt, Pd)

Both $Au_{24}Pt(SC4)_{18}^0$ and $Au_{24}Pd(SC4)_{18}^0$ were synthesized and purified according to the procedures reported by Qian et al.[12] and Kwak et al.,[14] with some modifications. $H_2PtCl_6{\cdot}xH_2O$ (41 mg, 0.1 mmol), $HAuCl_4{\cdot}3H_2O$ (157 mg, 0.4 mmol), and TOABr (317 mg, 0.58 mmol) were dissolved in 15 mL of THF in a 250 mL flask. After vigorous stirring for 1 h, the color of the solution changed from yellow to dark red. n-Butanethiol (0.27 mL, 2.5 mmol) was added without changing the stirring speed, and after 15 min the color of the solution changed from dark red to faint yellow. $NaBH_4$ (190 mg, 5 mmol) dissolved in 6 mL of cold water was then added at once. After stirring for 5 h, THF was rotary evaporated to leave a black oily solid covered by the aqueous phase, which was decanted. The oily solid was dissolved in 20 mL toluene and washed with water (5 × 20 mL) in a separatory funnel to remove water-soluble impurities. Toluene was rotary evaporated, the resulting product was thoroughly washed with a 4:1 methanol-water mixture (5 × 20 mL), and then collected by centrifugation. A mixture of $Au_{25}(SC4)_{18}^-$ and $Au_{24}Pt(SC4)_{18}^0$ was obtained through repeated extractions with acetone (5 × 10 mL). Subsequently, the cluster mixture was dissolved in 10 mL DCM, and 5 mL H_2O_2 solution (30%) was added under vigorous stirring to oxidatively destroy $Au_{25}(SC4)_{18}^-$. After 1.5 hour, DCM was evaporated, and the aqueous phase was decanted. The so-obtained crude product was washed with acetonitrile (5 × 10 mL) and methanol (5 × 10 mL). $Au_{24}Pt(SC4)_{18}^0$ was extracted three times with a 2:1 DCM-acetonitrile solution, then the product was further purified by silica-gel column chromatography using a 1:5 DCM-hexane solution.

Crystals could be obtained from a 1:5 pentane-ethanol solution after 2-3 days at 10 °C. $Au_{24}Pd(SC4)_{18}^0$ was synthesized and purified in a very similar way, but for the use of Na_2PdCl_6 (29 mg, 0.1 mmol).

2.4.3 Synthesis of $Au_{24}Hg(SC4)_{18}^0$

Thiolate Method.

$Hg(NO_3)_2$ (324.6 mg, 1 mmol) was dissolved in 5 mL methanol. A solution of butanethiol (0.54 mL, 5 mmol) and triethylamine (2 mL, 15 mmol) in 5 mL methanol was then added under vigorous stirring. After 1 h, the solvent was evaporated. The so-obtained white precipitate was washed with H_2O (5 × 10 mL) and methanol (5 × 10 mL), to obtain $Hg(SC4)_2$ as a white powder. $Au_{24}Hg(SC4)_{18}^0$ was synthesized according to the procedure described by the Zhu group,[20] with some modifications. 10 mg $Au_{25}(SC4)_{18}^-$ was dissolved in 5 mL toluene at r.t., and then 2 mg $Hg(SC4)_2$ was added to the solution under vigorous stirring. The reaction was allowed to proceed for 20 min. The organic layer was separated from excess $Hg(SC4)_2$ and the solution evaporated to dryness. $Au_{24}Hg(SC4)_{18}^0$ was extracted with pentane. Crystals of the $Au_{24}Hg(SC4)_{18}^0$ could be obtained from a pentane, toluene, and ethanol solution after 3-5 days at r.t..

Salt Method.

The clusters were synthesized according to the procedure reported by Wu and his coworkers with some modifications.[23] $Au_{25}(SC4)_{18}^-$ (10 mg, 0.0014 mmol) was dissolved in 100 mL acetonitrile at r.t.. 1 Equiv $Hg(NO_3)_2$ (0.05 M, aqueous solution) was added under vigorous stirring at r.t.. After 50 min, stirring was interrupted and the mixture was left as such overnight. A black precipitate formed. The crude product was washed with acetonitrile (3 × 5 mL) and methanol (3 × 5 mL) to remove impurities and excess $Au_{25}(SC4)_{18}^-$. Crystals of the $Au_{24}Hg(SC4)_{18}^0$ could be obtained from a toluene, pentane, and ethanol mixture after 3-5 days at r.t.. Crystallization was repeated 5 times.

Exchange Method.

The cluster was synthesized according to the procedure described by Wu and his coworkers, with some modifications.[21] $Au_{24}Cd(SC4)_{18}^{0}$ (10 mg, 0.0016 mmol) was dissolved in 1 mL THF, and 1 equivalent of $Hg(NO_3)_2$ (0.05 M, aqueous solution) was added without stirring. The reaction was left to proceed for 10-15 min, during which the color of the mixture changed from dark green to brownish red. UV-vis spectroscopy was used to monitor the progress of the reaction. Most THF was then removed. After addition of 10 mL methanol, a precipitate formed. The crude product was washed with water (3 × 5 mL) and methanol (3 × 5 mL), to remove impurities. Crystals of $Au_{24}Hg(SC4)_{18}^{0}$ could be obtained from a toluene, pentane, and ethanol mixture after 3-5 days at r.t..

2.4.4 Synthesis of $Au_{24}Cd(SC4)_{18}^{0}$

Thiolate Method.

$Cd(NO_3)_2$ (308.47 mg, 1 mmol) was dissolved in 5 mL methanol. The rest of the procedure is as already described for $Hg(SC4)_2$. $Cd(SC4)_2$ was also obtained by starting from $CdCl_2$ or $^{113}CdCl_2$ (183.32 mg, 1 mmol) in 5 mL of methanol. Regardless of the method, $Cd(SC4)_2$ was obtained as a white powder. $Au_{24}Cd(SC4)_{18}^{0}$ was prepared according to the method reported by Zhu and co-workers,[20] with some modifications. 10 mg $Au_{25}(SC4)_{18}^{-}$ was dissolved in 5 mL toluene at 55 °C. 0.2 mg aliquots of $Cd(SC4)_2$ were added (as a powder) to the solution every hour, for a total of 10 times. The reaction was carried out for no less than 50 h. The solution was then centrifuged to separate the excess $Cd(SC4)_2$, and evaporated to dryness. The product was extracted with pentane. Crystals of $Au_{24}Cd(SC4)_{18}^{0}$ could be obtained from a toluene, pentane, and ethanol solution after 3-5 days at r.t..

Salt Method.

The cluster was synthesized according to the procedure reported by Wu and his coworkers,[21] with some modifications. $Au_{25}(SC4)_{18}^{-}$ (10 mg, 0.0014 mmol) was dissolved in 100 mL acetonitrile at 50 °C. 10 mL acetonitrile containing $Cd(NO_3)_2$ (8.8 mg, 0.0286 mmol) was then added with vigorous stirring at 50 °C. After 50 min, the solution was left to rest in the fridge overnight. Some black solid precipitated. The crude product was washed with acetonitrile (3 × 5 mL) and methanol (3 × 5 mL) to remove impurities and excess $Au_{25}(SC4)_{18}^{-}$. Crystals of $Au_{24}Cd(SC4)_{18}^{0}$ could be obtained from a toluene, pentane, and ethanol solution after 3-5 days at r.t.. This procedure was repeated 5-8 times.

2.4.5 Synthesis of $Au_{24}Hg(SC2Ph)_{18}^{0}$

Thiolate, Salt, and Exchange Methods.

Each method was based on the same procedure already described for SC4, but for the use of $Au_{25}(SC2Ph)_{18}^{-}$ and phenylethanethiol instead of $Au_{25}(SC4)_{18}^{-}$ and n-butanethiol. Crystals of $Au_{24}Hg(SC2Ph)_{18}^{0}$ could be obtained from a toluene-acetonitrile solution after 1-2 days at r.t..

2.1.1 Synthesis of $Au_{24}Cd(SC2Ph)_{18}^{0}$

Thiolate Method.

$Cd(NO_3)_2$ (308.47 mg, 1 mmol) was dissolved in 5 mL methanol. To this vigorously stirred solution, phenylethanethiol (0.67 mL, 5 mmol) and triethylamine (2 mL, 15 mmol) in 5 mL methanol was added. After 1 h, white solids precipitated. The mixture was centrifuged, and the solvent removed. The white precipitate was washed with H_2O (5 × 10 mL) and methanol (5 × 10 mL) to obtain $Cd(SC2Ph)_2$ as a white powder. A similar procedure was employed for $CdCl_2$ and $^{113}CdCl_2$. $Au_{24}Cd(SC2Ph)_{18}^{0}$ was synthesized according to the procedure described by the Zhu group,[20] with some modifications. 10 mg A $Au_{25}(SC2Ph)_{18}^{-}$ was dissolved in 5 mL of toluene at 55 °C. $Cd(SC2Ph)_2$ was added as described for $Cd(SC4)_2$, and the reaction was carried out as already described for $Au_{24}Cd(SC4)_{18}^{0}$. The final product was extracted with 1:1 DCM-acetonitrile. Crystals of $Au_{24}Cd(SC2Ph)_{18}^{0}$ were obtained from a solution of toluene, acetonitrile, and methanol after 7-10 days at r.t..

Salt Method.

This reaction was carried out as already described for $Au_{24}Cd(SC4)_{18}^{0}$, but for the use of $Au_{25}(SC2Ph)_{18}^{-}$ and phenylethanethiol instead of $Au_{25}(SC4)_{18}^{-}$ and n-butanethiol. Crystals of $Au_{24}Cd(SC2Ph)_{18}^{0}$ were obtained from a solution of toluene, acetonitrile, and methanol after 7-10 days at r.t..

2.4.6 Figures 2.13-2.33

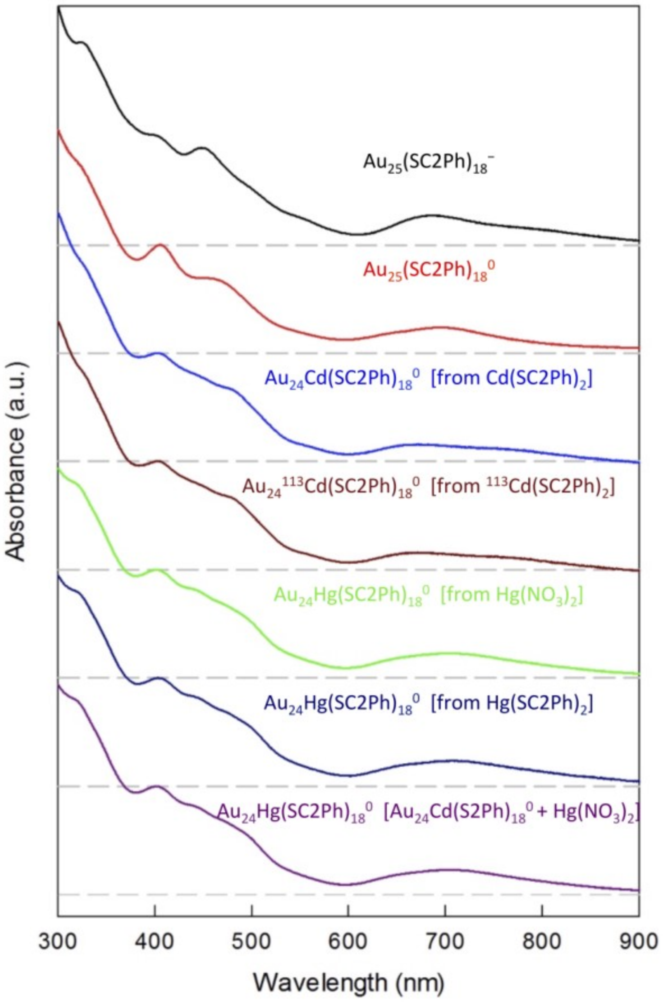

Figure 2.13. UV-vis absorption spectra of all SC2Ph samples (0.2 mM) in CH_2Cl_2. For the sake of better comparison, the curves have been shifted vertically. The dashed lines mark the corresponding zero absorbance.

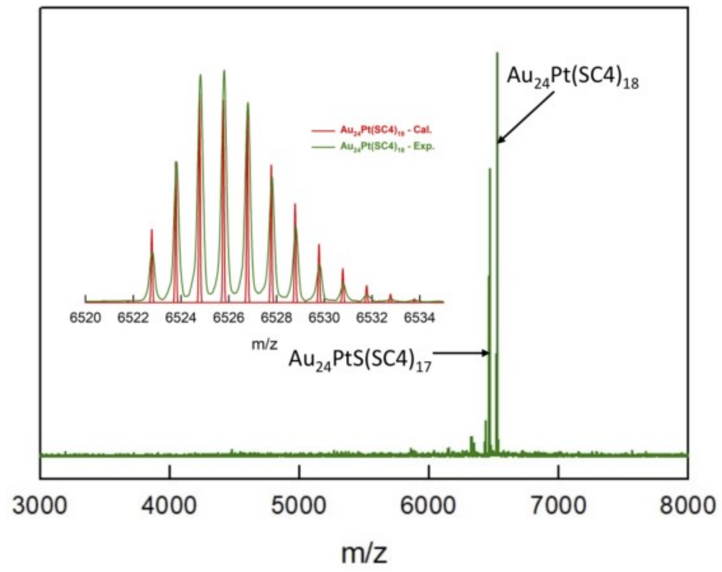

Figure 2.14. MALDI-TOF mass spectrum of Au$_{24}$Pt(SC4)$_{18}^{0}$. The inset shows the calculated (red) and experimental (green) isotopic pattern.

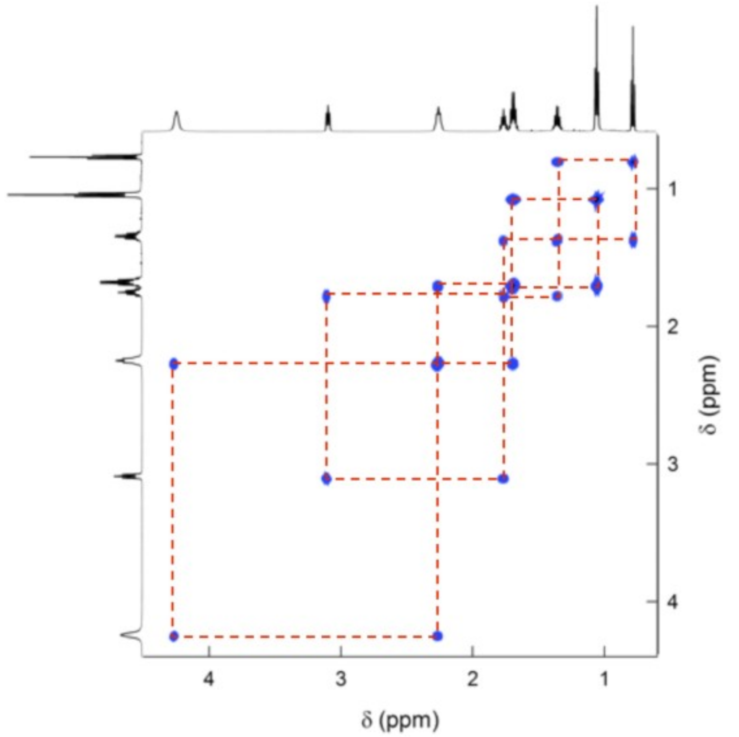

Figures 2.15. COSY spectrum of 2.1 mM Au$_{24}$Pt(SC4)$_{18}^{0}$ in C_6D_6 at 25 °C.

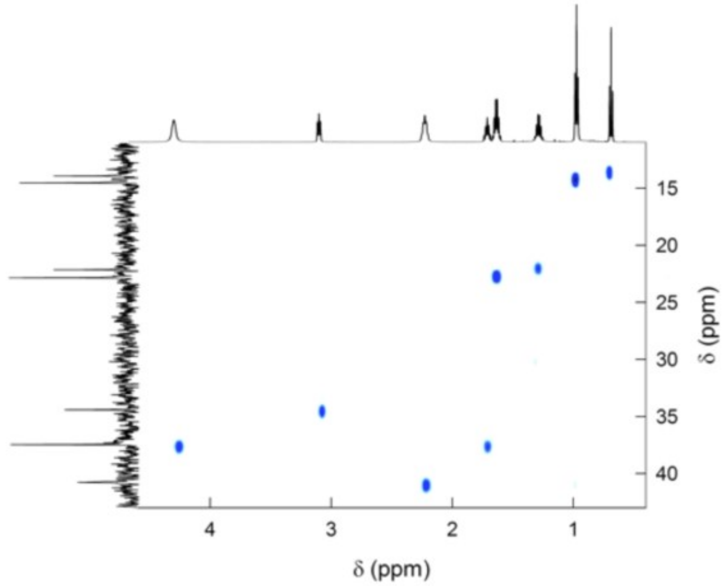

Figure 2.16. HMQC spectrum of 2.1 mM $Au_{24}Pt(SC4)_{18}^{0}$ in C_6D_6 at 25 °C.

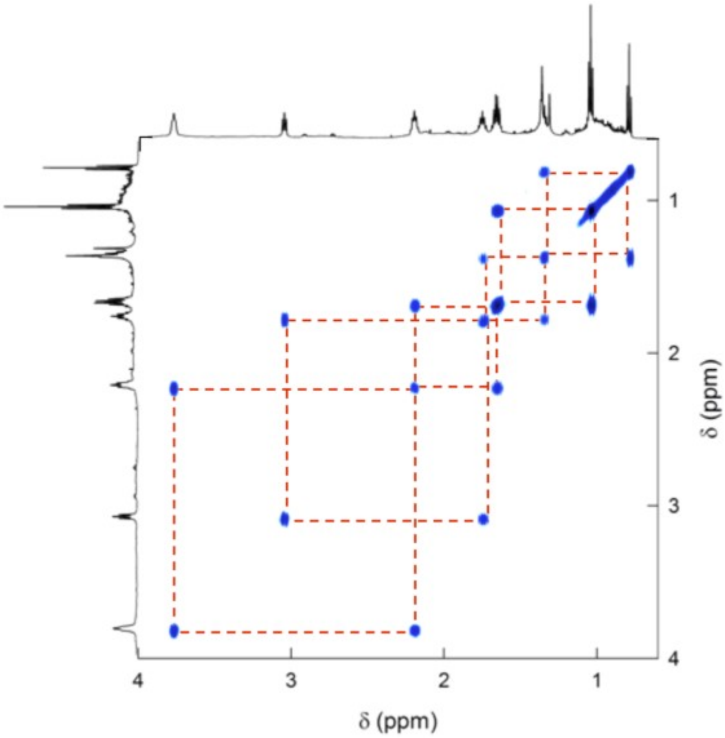

Figures 2.17. COSY spectrum of 1.5 mM $Au_{24}Pd(SC4)_{18}^{0}$ in C_6D_6 at 25 °C.

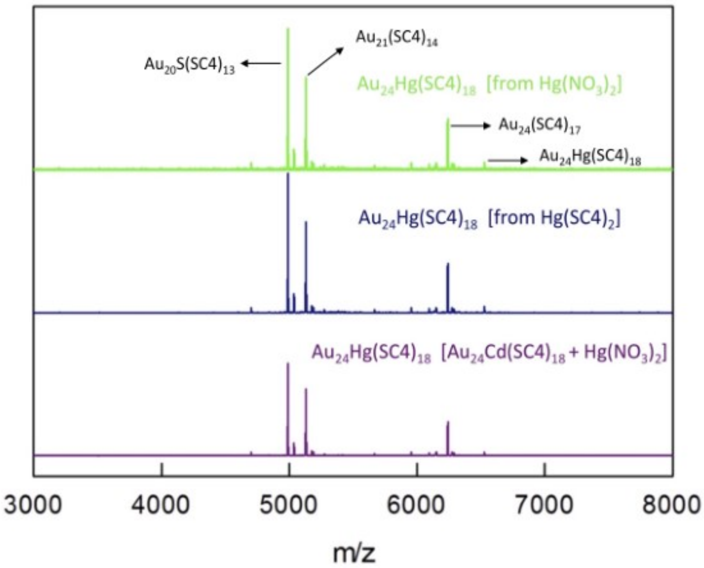

Figure 2.18. MALDI-TOF spectra of $Au_{24}Hg(SC4)_{18}^0$ prepared according to three different methods.

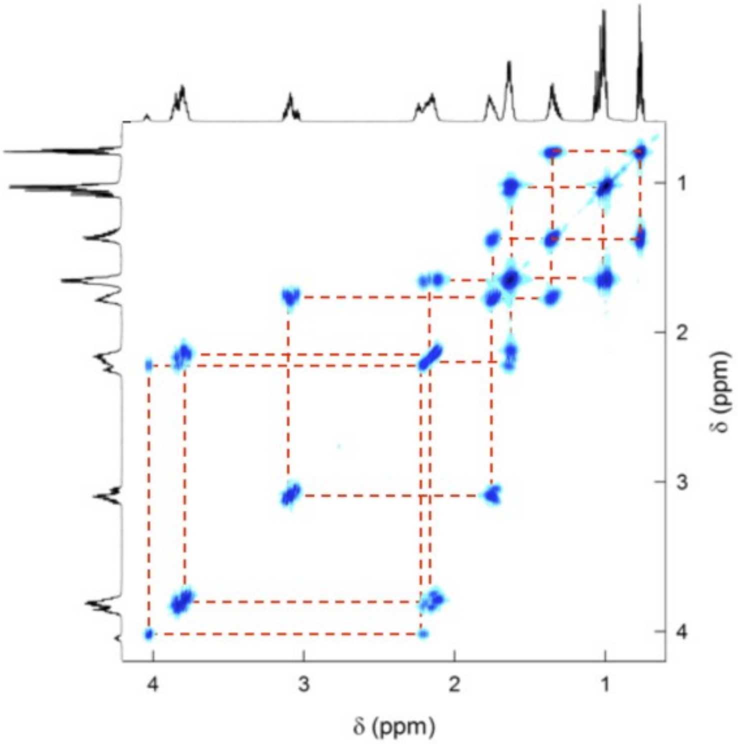

Figures 2.19. COSY spectrum of 2.1 mM $Au_{24}Hg(SC4)_{18}^0$ in C_6D_6 at 25 °C.

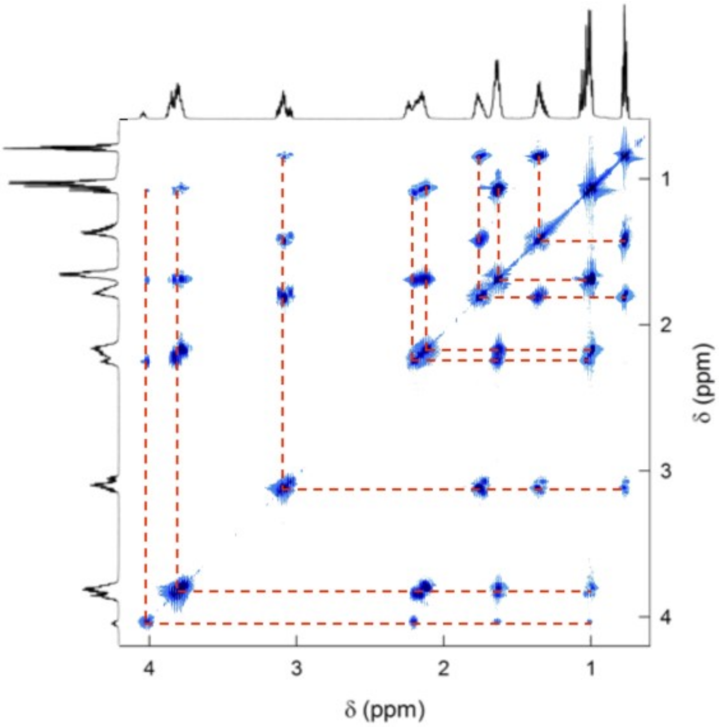

Figure 2.20. TOCSY spectrum of 2.1 mM $Au_{24}Hg(SC4)_{18}^0$ in C_6D_6 at 25 °C.

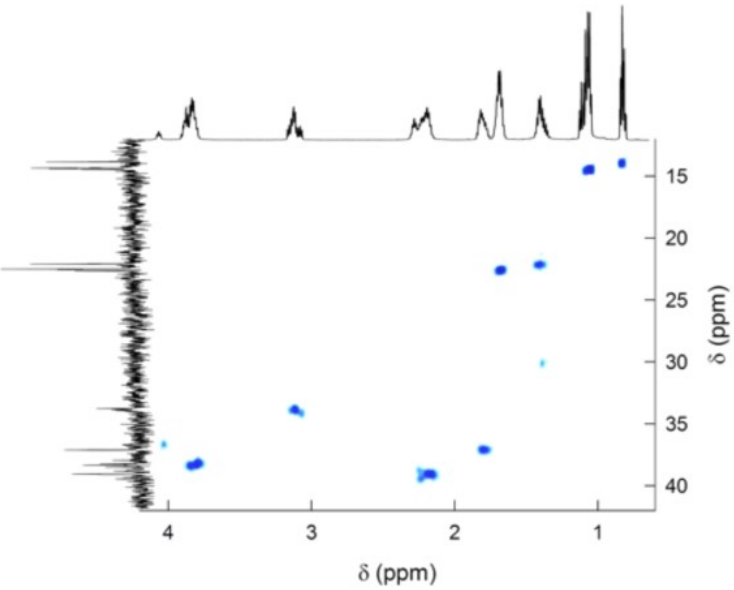

Figure 2.21. HMQC spectrum of 2.1 mM $Au_{24}Hg(SC4)_{18}^0$ in C_6D_6 at 25 °C.

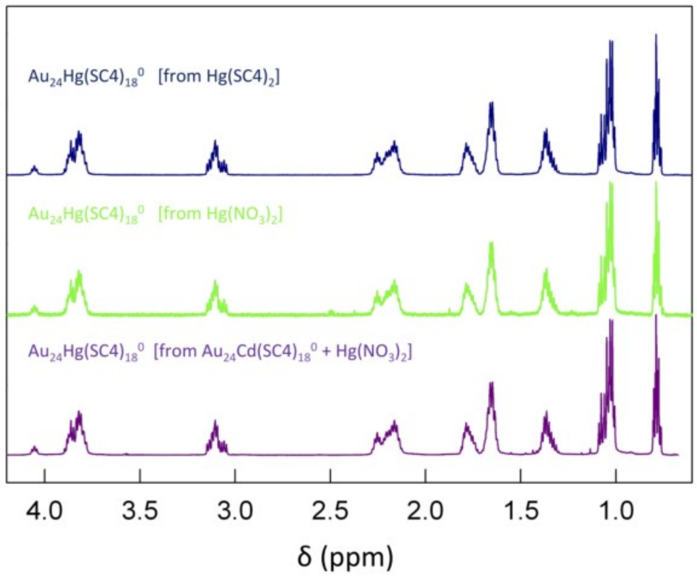

Figure 2.22. ^{1}H NMR of the three $Au_{24}Hg(SC4)_{18}^0$ samples in C_6D_6 at 25 °C.

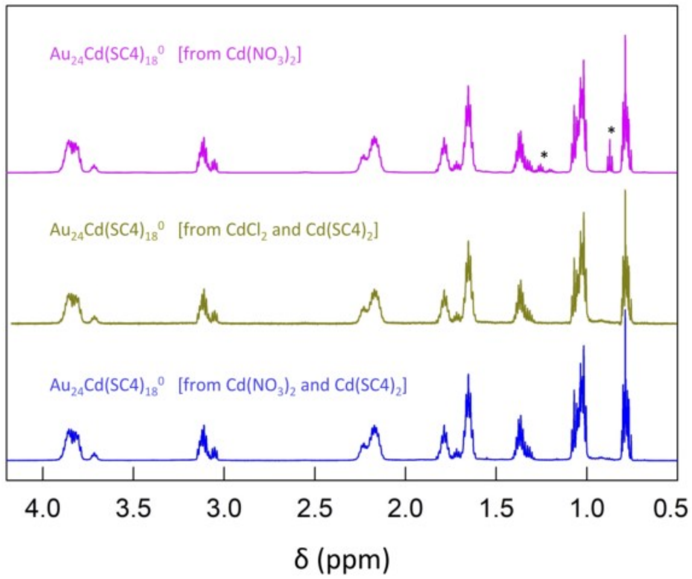

Figure 2.23. ^{1}H NMR of the three $Au_{24}Cd(SC4)_{18}^0$ samples in C_6D_6 at 25 °C. The asterisks mark a solvent impurity (pentane).

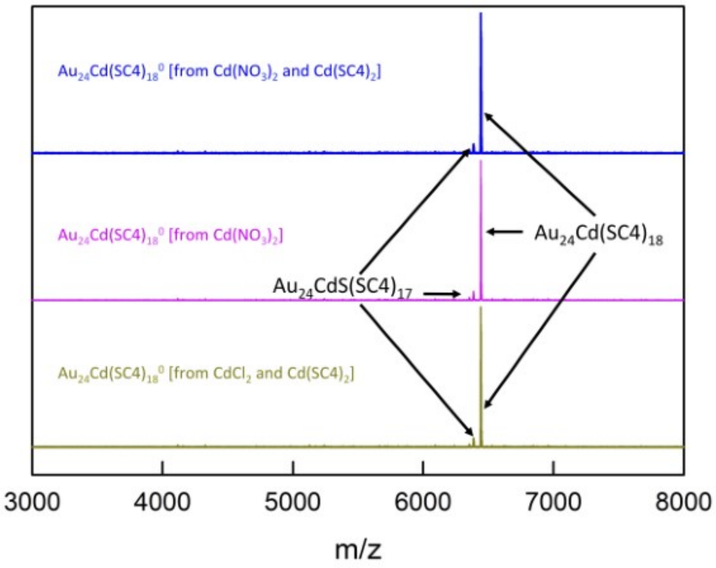

Figure 2.24. MALDI-TOF spectra of $Au_{24}Cd(SC4)_{18}^0$ prepared according to three different methods.

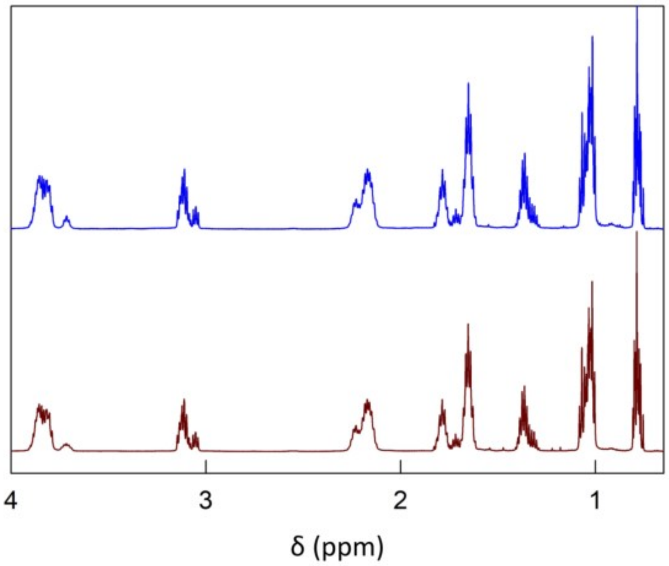

Figure 2.25. ^1H NMR spectra of 2.1 mM $Au_{24}Cd(SC4)_{18}^0$ (top) and 2.1 mM $Au_{24}{}^{113}Cd(SC4)_{18}^0$ (bottom) in C_6D_6 at 25 °C. The samples were prepared from $Cd(NO_3)_2$ and $^{113}Cd(SC4)_2$, respectively.

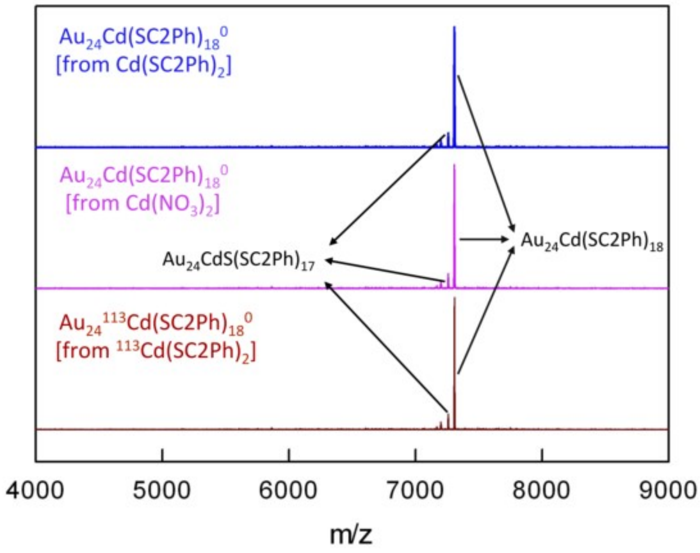

Figure 2.26. MALDI-TOF spectra of $Au_{24}Cd(SC2Ph)_{18}^0$ prepared according to three different methods.

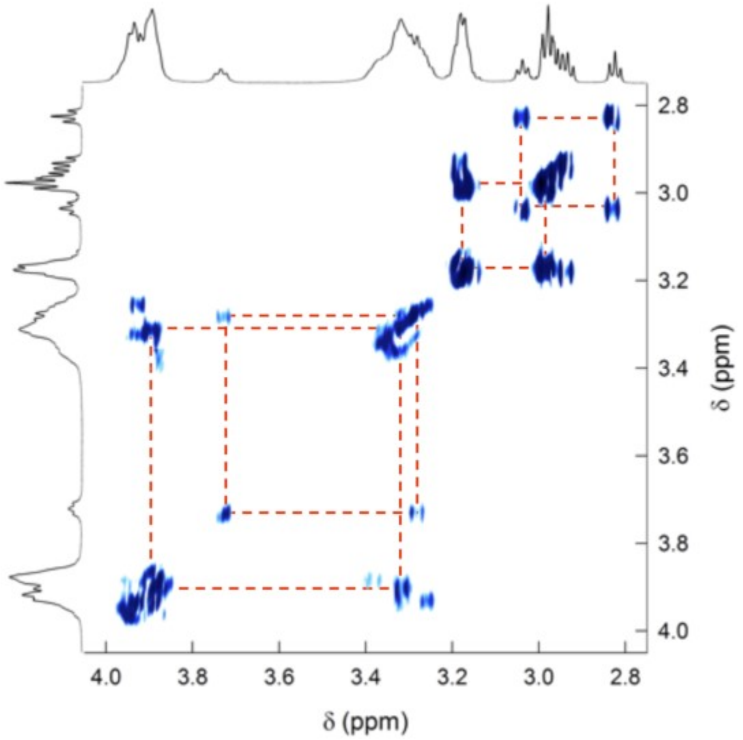

Figure 2.27. COSY spectrum of 2.2 mM $Au_{24}Cd(SC2Ph)_{18}^0$ in C_6D_6 at 25 °C.

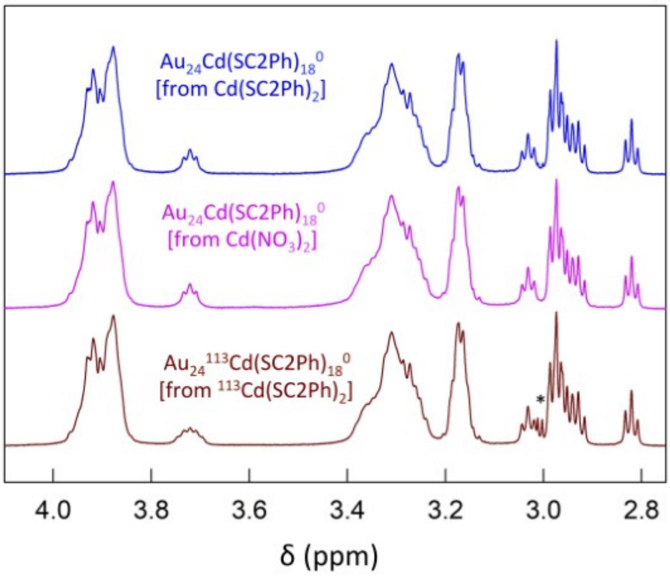

Figure 2.28. ^1H NMR of the various $Au_{24}Cd(SC2Ph)_{18}^0$ samples. The asterisk marks a solvent impurity (methanol).

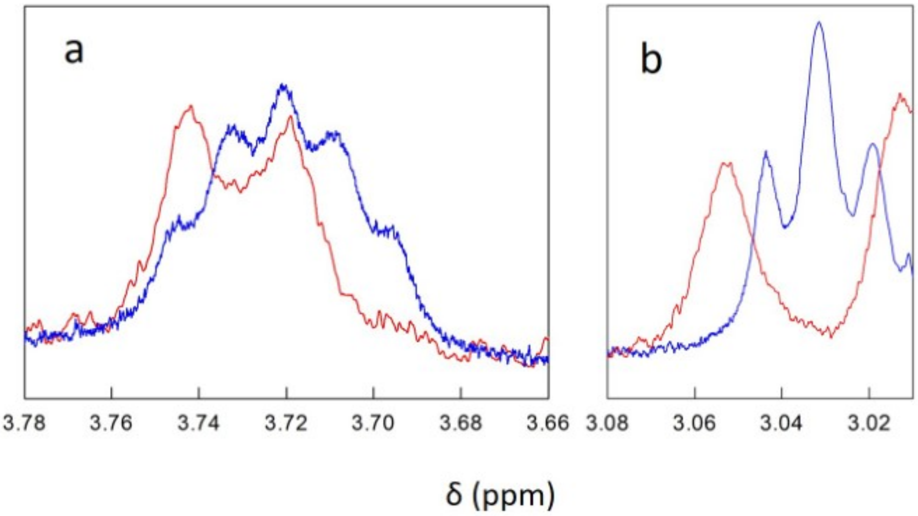

Figure 2.29. ^1H NMR spectra of 2.2 mM $Au_{24}{}^{113}Cd(SC2Ph)_{18}^0$ focusing on the α-$(CH_2)_{in}$ (a) and α-$(CH_2)_{out}$ (b) regions. The spectra are shown before (blue traces) and after ^1H-^1H homodecoupling (red traces). C_6D_6, 25 °C.

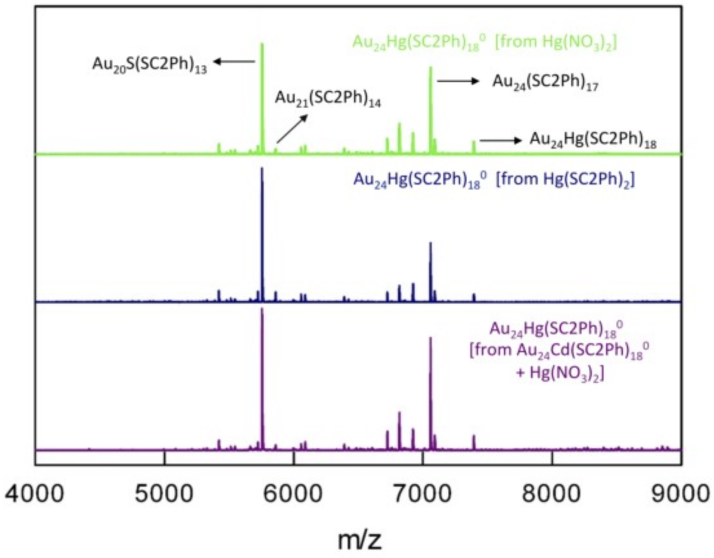

Figure 2.30. MALDI-TOF spectra of $Au_{24}Hg(SC2Ph)_{18}^0$ prepared according to three different methods.

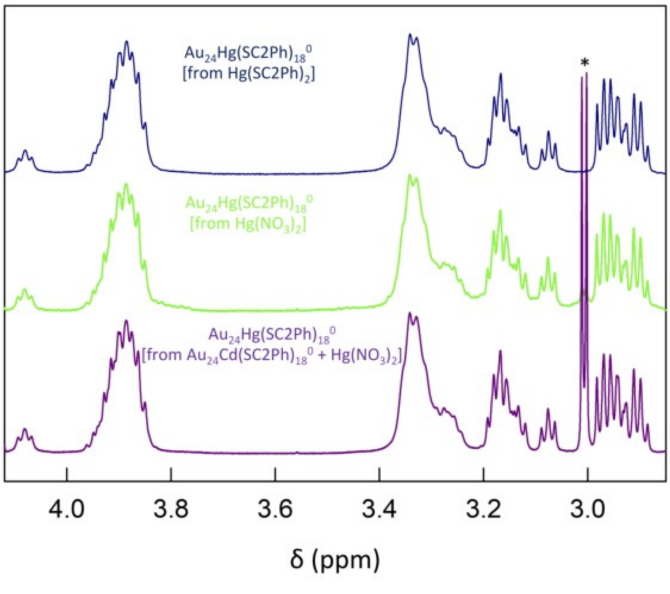

Figure 2.31. ^{1}H NMR of the three $Au_{24}Hg(SC2Ph)_{18}^0$ samples in C_6D_6 at 25 °C. The asterisk marks a solvent impurity (methanol).

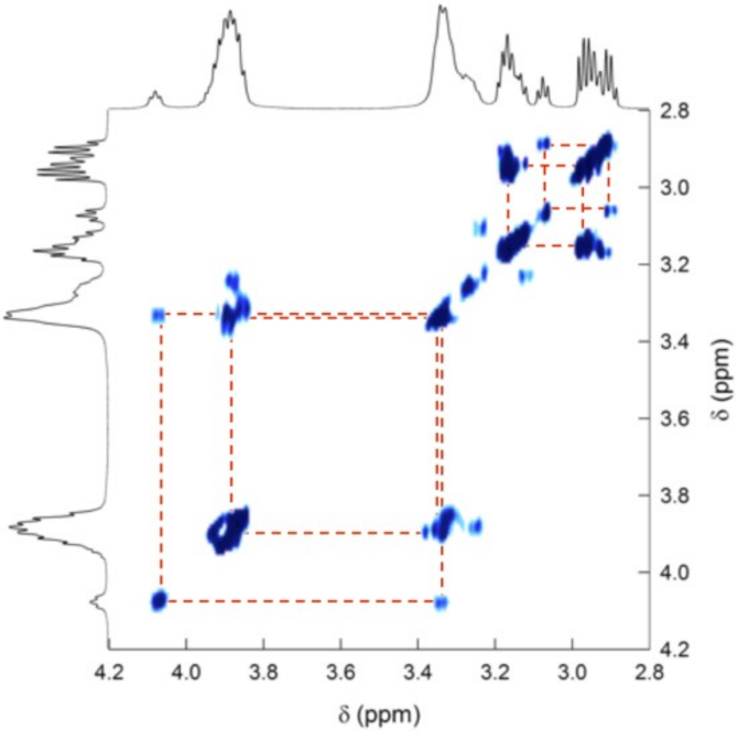

Figure 2.32. COSY spectrum of 2.2 mM $Au_{24}Hg(SC2Ph)_{18}^0$ in C_6D_6 at 25 °C.

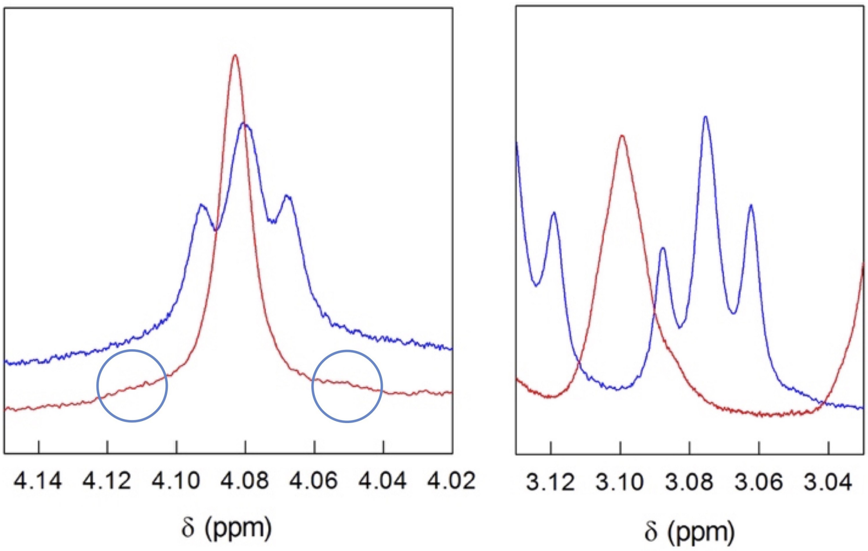

Figure 2.33. ^1H NMR spectra of 2.2 mM $Au_{24}Hg(SC2Ph)_{18}^0$ focusing on the isolated α-$(CH_2)_{in}$ (left) and α-$(CH_2)_{out}$ regions (right) before (blue) and after (red) ^1H-^1H homodecoupling at the frequency of the corresponding β-(CH_2) signals.

C_6D_6, 25 °C. In graph on the right-hand side, the two spectra have been vertically shifted, for clarity, and the circles mark the doublet.

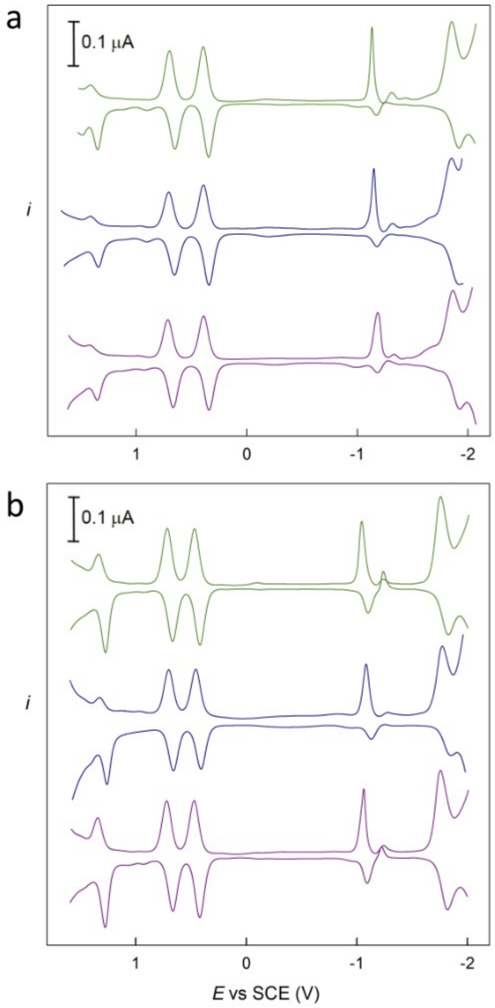

Figure 2.34. Comparison between the DPV curves of: (a) $Au_{24}Hg(SC4)_{18}^{0}$ obtained according to (top to bottom) the $Hg(NO_3)_2$, $Hg(SC4)_2$, and the exchange on $Au_{24}Cd(SC4)_{18}^{0}$ methods. (b) $Au_{24}Hg(SC2Ph)_{18}^{0}$: same sequence as in (a). Glassy-carbon electrode, DCM/0.1 M TBAH, 25 °C.

2.4.7 Tables 2.1-2.5

Table 2.1. ^{1}H and ^{13}C NMR chemical shifts for $Au_{25}(SC4)_{18}^{-}$, $Au_{24}Pt(SC4)_{18}^{0}$, and $Au_{24}Pd(SC4)_{18}^{0}$ in C_6D_6.

Cluster	Ligand Type	Nucleus	α-CH	β-CH	γ-CH	δ-CH
$Au_{25}(SC4)_{18}^{-}$	In	^{1}H	3.933	2.207	1.732	1.072
		^{13}C	38.10	40.98	22.71	13.78
	Out	^{1}H	3.226	1.912	1.485	0.881
		^{13}C	38.92	31.57	21.85	14.37
$Au_{24}Pt(SC4)_{18}^{0}$	In	^{1}H	4.241	2.252	1.683	1.049
		^{13}C	37.47	40.79	28.82	14.47
	Out	^{1}H	3.090	1.757	1.348	0.775
		^{13}C	34.42	37.47	22.11	13.87
$Au_{24}Pd(SC4)_{18}^{0}$	In	^{1}H	3.830	2.118	1.667	1.035
		^{13}C	37.86	39.85	22.72	14.45
	Out	^{1}H	3.089	1.716	1.351	0.777
		^{13}C	34.43	37.55	22.14	13.93

[a] From reference 38.

Table 2.2. ^{1}H and ^{13}C NMR chemical shifts for $Au_{24}Hg(SC4)_{18}^{0}$ in C_6D_6.

Ligand Type	Nucleus	Isochronous Signals	α-CH	β-CH	γ-CH	δ-CH
In	^{1}H	1	4.055	2.239	1.672	1.067
		1	3.883	2.217	1.681	1.058
		2	3.854	2.204	1.671	1.041
		3	3.818	2.204	1.669	1.034
		3	3.808	2.155	1.681	1.018
		2	3.786	2.146	1.646	1.025
	^{13}C	1	37.25	40.06	23.04	14.85
		1	39.01	39.76	23.04	14.85
		2	38.98	39.67	23.04	14.85
		3	38.91	39.67	23.04	14.78
		3	38.88	39.67	23.04	14.84

		2	38.79	39.67	22.96	14.82
Out	^{1}H	1	3.147	1.765	1.382	0.802
		1	3.134	1.786	1.382	0.800
		1	3.129	1.785	1.360	0.790
		1	3.109	1.774	1.350	0.782
		1	3.087	1.771	1.350	0.774
		1	3.053	1.761	1.342	0.774
	^{13}C	1	34.71	37.71	22.71	14.28
		1	34.49	37.71	22.71	14.28
		1	34.49	37.71	22.56	14.28
		1	34.43	37.71	22.54	14.28
		1	34.41	37.71	22.51	14.28
		1	34.41	37.71	22.51	14.28

Table 2.3. ^{1}H and ^{13}C NMR chemical shifts for $Au_{24}Cd(SC4)_{18}^{0}$ in C_6D_6.

Ligand Type	Nucleus	Isochronous Signals	*α*-CH	*β*-CH	*γ*-CH	*δ*-CH
In	^{1}H	2	3.865	2.234	1.660	1.070
		6	3.834	2.166	1.658	1.016
		2	3.826	2.171	1.658	1.035
		1	3.803	2.183	1.628	1.024
		1	3.716	2.173	1.634	1.013
	^{13}C	2	38.43	39.58	22.36	14.33
		6	38.33	38.96	22.36	14.18
		2	38.07	39.02	22.36	14.20
		1	38.06	38.93	22.36	14.13
		1	34.15	39.01	22.36	14.10
Out	^{1}H	1	3.126	1.778	1.350	0.785
		1	3.122	1.786	1.354	0.795

		3	3.108	1.788	1.357	0.788
		1	3.052	1.719	1.321	0.768
	^{13}C	1	33.71	36.95	21.93	13.69
		3	33.63	36.95	21.93	13.68
		1	33.72	36.95	21.93	13.62
		1	34.30	36.85	21.86	13.51

Table 2.4. ^{1}H and ^{13}C NMR chemical shifts (aliphatic groups) for $Au_{24}Cd(SC2Ph)_{18}^{0}$ in C_6D_6.

Ligand Type	Nucleus	Isochronous Signals	*α*-CH	*β*-CH
In	^{1}H	1	3.929	3.259
		1	3.927	3.261
		1	3.923	3.248
		1	3.922	3.239
		1	3.919	3.252
		1	3.903	3.320
		1	3.897	3.322
		1	3.895	3.301
		1	3.895	3.298
		1	3.876	3.361
		1	3.872	3.384
		1	3.722	3.273
	^{13}C	1	39.5	43.0
		1	39.5	43.0
		1	39.5	43.0
		1	39.5	43.0
		1	39.5	43.0
		1	39.5	42.9

		1	39.4	42.9
		1	39.4	42.9
		1	39.4	42.9
		1	39.4	42.9
		1	39.4	42.9
		1	35.60	40.42
Out	^{1}H	1	3.179	2.941
		1	3.175	2.917
		1	3.172	2.986
		1	3.168	2.968
		1	3.165	2.960
		1	3.032	2.820
	^{13}C	1	35.3	41.2
		1	35.3	41.2
		1	35.3	41.2
		1	35.3	41.2
		1	35.3	41.2
		1	35.62	40.55

Table 2.5. ^{1}H and ^{13}C NMR chemical shifts for $Au_{24}Hg(SC2Ph)_{18}^0$ in C_6D_6.

Ligand Type	Nucleus	Isochronous Signals	*α*-CH	*β*-CH
In	^{1}H	1	4.081	3.342
		1	3.949	3.286
		1	3.940	3.312
		1	3.936	3.383
		1	3.928	3.337
		1	3.915	3.359
		1	3.901	3.264

		1	3.897	3.247
		1	3.886	3.291
		1	3.875	3.324
		1	3.863	3.397
		1	3.849	3.265
	^{13}C	1	37.6	42.9
		1	39.4	42.9
		1	39.4	42.9
		1	39.4	42.9
		1	39.4	42.9
		1	39.4	42.9
		1	39.4	42.9
		1	39.4	42.9
		1	39.4	42.9
		1	39.4	42.9
		1	39.4	42.9
		1	39.4	35.4
Out	^{1}H	1	3.181	2.904
		1	3.175	2.928
		1	3.168	2.981
		1	3.166	2.960
		1	3.122	2.951
		1	3.075	2.902
	^{13}C	1	35.2	41.1
		1	35.2	41.1
		1	35.2	41.1
		1	35.2	41.1
		1	43.2	41.1
		1	35.3	41.1

2.4.8 X-Ray Crystallography, Figures 2.35-2.40, and Tables 2.6-2.7

Single-crystal X-ray data for all metal doped $Au_{24}M(SR)_{18}^0$ clusters, except for $Au_{24}Pt(SC4)_{18}^0$, were collected at the University of Jyväskylä with a Rigaku Oxford Diffraction SuperNova dual-source X-ray diffractometer at -153 °C using either hi-flux Mo or Cu micro-focus sources (Mo K_α, λ = 0.71073 Å and Cu K_α, λ = 1.54184 Å) and an Atlas CCD detector. X-ray data for $Au_{24}Pt(SC4)_{18}^0$, and further data for $Au_{24}Hg(SC2Ph)_{18}^0$ were collected at the University of Padova with Oxford Diffraction Xcalibur Gemini diffractometer at 21 °C using graphite–monochromated Mo-radiation (Mo K_α, λ = 0.71073 Å) and an Eos CCD detector. Data collection, reduction processes, and analytical numeric absorption corrections by multifaceted crystal models (empirical absorption correction using spherical harmonics was applied for the Pt-doped cluster), were all carried out using the program CrysAlisPro (v. 171.39.46).[58] Structures were solved by direct methods with program SHELXT S8 and refined using SHELXL S9 least-squares full-matrix minimization on $|F|^2$ within the OLEX 2 (v. 1.2.10) program.[61] Thermal displacement factors of all non-hydrogen atoms were refined anisotropically, whereas the hydrogen atoms were calculated isotropically and refined as riding atoms with U iso parameters 1.2−1.5 times of their host atoms. Occupancies of disordered ligands were determined using free variables in the refinement.

As suggested by the other characterization methods used in this study, atomic positions of the foreign-metal metal atoms (Cd or Hg) were set identical (EXYZ command) with a fixed 1/12 (0.0833) occupancy to each of the 12 icosahedron Au sites. Their thermal parameters were set to refine as the (EADP command) to that of the paired (PART 1 and 2) Au atom, in order to afford fully converged refinement. In addition to the atom substitution disorder, structural disorder was occasionally observed for sulfur and staple Au atoms. Those were conventionally handled with free variables. The slightly high residual electron densities on some of the structures were partly caused by the somewhat nonideal correction for absorption, despite the best possible correction method (analytical multi-facet) was applied. Heavily absorbing crystals (μ/mm^{-1} varied from 44 to 60) were measured with Cu-radiation. The noteworthy advantage of using Cu- over Mo-radiation is its significantly enhanced detection sensitivity for the lighter elements, particularly on complexes including heavy elements. Secondly, by Cu-radiation data collection time can substantially be shortened for large crystal structures. For all $Au_{24}M(SR)_{18}^{0}$ clusters, but for $Au_{24}Pt(SC4)_{18}^{0}$, two or three parallel full data sets and consequent structure analyses were carried out using different crystals. To further improve representativeness of the crystallographic analysis, some of the crystals of the same crystallization batch were analyzed in parallel at the University of Padova.

Crystallographic data for the metal doped $Au_{24}M(SR)_{18}^{0}$ (M = Pt, Hg, Cd) clusters are shown in Tables 2.6 and 2.7, at the end of this section, and the structures are illustrated in Figures 2.35 – 2.40. $Au_{24}Pt(SC4)_{18}^{0}$ crystallizes in triclinic crystal system P-1 having half a cluster in an asymmetric unit with a volume of 3010 Å^3. The Hg and Cd monodoped $Au_{24}M(SR)_{18}^{0}$ clusters, regardless of the synthetic method (for Cd, we analyzed the crystals obtained from both the $Cd(NO_3)_2$ and $Cd(SC4)_2$ methods), also crystallize in the same P-1 space group but with larger unit-cell settings (V = 5860 Å^3). Noteworthy, both $Au_{24}Hg(SC4)_{18}^{0}$ and $Au_{24}Cd(SC4)_{18}^{0}$ are ordered as 1-dimensional polymers running along the (011) lattice direction. The asymmetric unit of the polymeric cluster consists of two halves of the Au clusters that are connected via a single Au-Au aurophilic bond (between Au13-Au14 atoms, ~3.1 Å). Geometry, bond distances and angles of the cluster cores are closely similar in all these structures (Figure 2.35), which show an icosahedral framework of 12 metal atoms that surround a central metal atom, 12 Au atoms at staple sites, and 18 thiolate ligands.

As indicated by the NMR studies, monodoping with Pt, Hg, and Cd (two exchange methods) yields substitution at the center for Pt and on one of the icosahedral sites in the case of Hg and Cd. Thorough structural analysis of $Au_{24}Cd(SC4)_{18}^{0}$ (electron density difference of Cd to Au is ~60 %) using several data sets with the highest possible data quality (data redundancy of 5) allowed us to refine the structure in an especially satisfactory manner. The Cd atom was found to be most likely disorderly located on the icosahedral sites instead of the center or staple positions. On the other hand, Hg and Pt differ from Au by only one electron. As explained in the main text, for these clusters the electron-density difference is thus just too small to draw conclusions as safely as for Cd. Therefore, for these doped systems the position of the foreign metal was set in the structures according to the observations made by NMR analysis, that is, Pt in the center of the core and Hg disordered by 1/12 occupancy over 12 possible icosahedral sites (similarly to the case of the Cd-doped cluster).

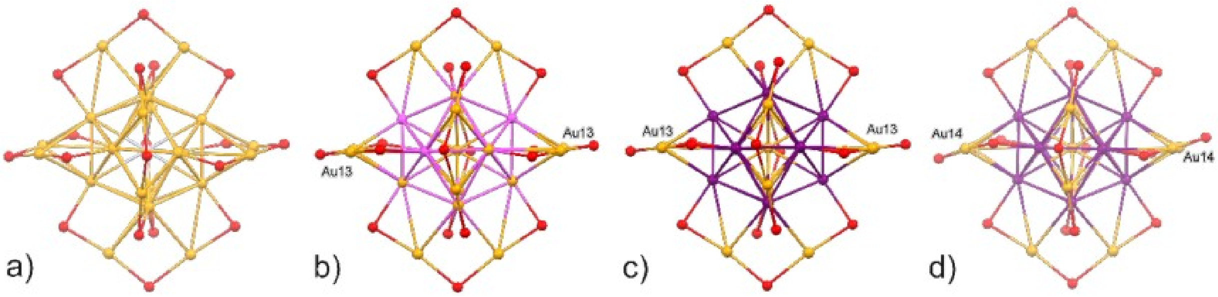

Figure 2.35. Au/M-S cores of foreign-metal monodoped $Au_{24}M(SC4)_{18}^0$ (M = Pt, Hg, Cd): (a) Pt (silver) in the center position and (b) Hg (cyan), (c) Cd (purple; obtained via the $Cd(NO_3)_2$ method), and (d) Cd (purple; obtained via the $Cd(SC4)_2$ method) all having the doping metal disordered over 12 icosahedral Au sites.

In $Au_{24}Pt(SC4)_{18}^0$ (Figure 2.36a), the orientation of butanethiolate ligands, in relation to the plane via atoms S9, S8, S4, Pt, S4, S8 and S9 (Figure 2.36d), is four consecutive ligands below (Figure 2.36d, blue-colored ligands in the order S1, S4, S9 and S8) and the next four above (green-colored ligands in the order S1, S4, S9 and S8) the plane in a clockwise order. A similar plane can be defined across the two other staple directions: for the second plane, the ligand arrangement is equivalent to the first one, whereas in the direction of the third plane, the ligands alternate above and below the plane in a sequence of four ligands and then next four ligands below and above, in an opposite order.

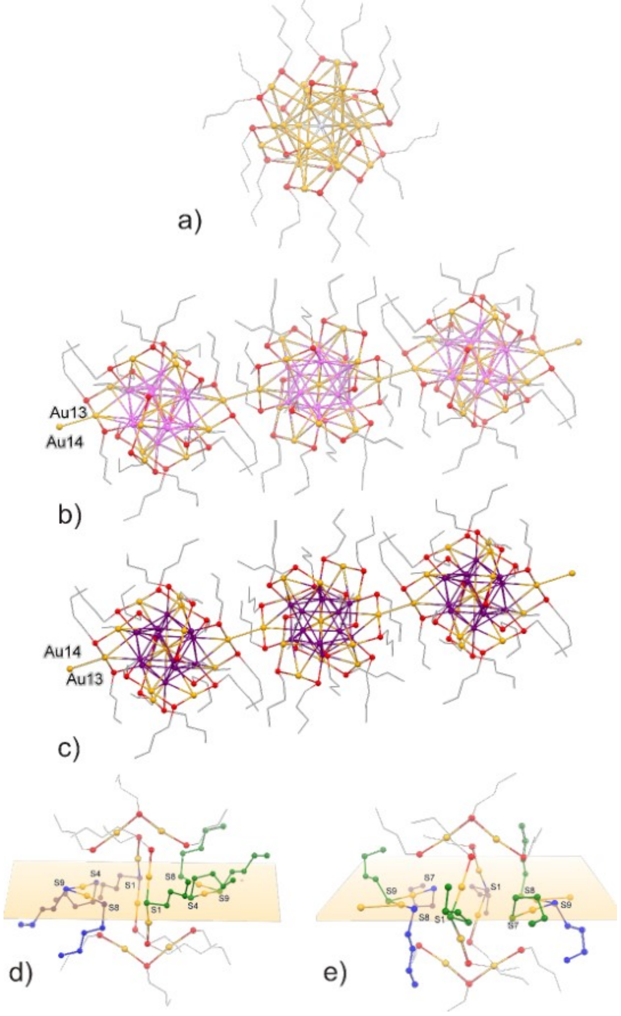

Figure 2.36. Partial views of the metal doped $Au_{24}M(SC4)_{18}^0$ structures. (a) Isolated cluster unit of $Au_{24}Pt(SC4)_{18}^0$, (b) polymeric $Au_{24}Hg(SC4)_{18}^0$, (c) polymeric $Au_{24}Cd(SC4)_{18}^0$ (the structure is representative for both Cd-doping methods), (d) orientation of the ligands (green above and blue below) in $Au_{24}Pt(SC4)_{18}^0$ and (e) the polymeric clusters. Disordered Au/M positions of Au/Hg and Au/Cd are evidenced by cyan and purple colors, respectively. Ligand disorder, hydrogen atoms, and for (d) and (e) all Au atoms except for those in the staples are omitted for the clarity.

On the polymeric Hg and Cd doped clusters (Figures 2.36b, c, and e), the ligands are oriented in relation to the plane (via atoms S9, S7, S8, Au(center), S7, S8, S9) by consecutively alternating above (S1 and S9, green) and below (S8 and S7, blue) the plane in a clockwise order, and then alternating in opposite below and above order (S1 and S9 below, S8 and S7 above). A similar ligand arrangement is found also for the other two plane directions. The packing of the clusters in the crystal lattices is exemplified in Figure 2.37. In the molecular packing of the Pt doped cluster, the metallic core units are distinctively isolated by the ligands forming the organic medium between the metallic cores in all three cell dimensions. In the Hg and Cd doped 1-D polymers the chains of clusters run along the (011) lattice direction and are isolated by the ligands on two remaining cell axis directions.

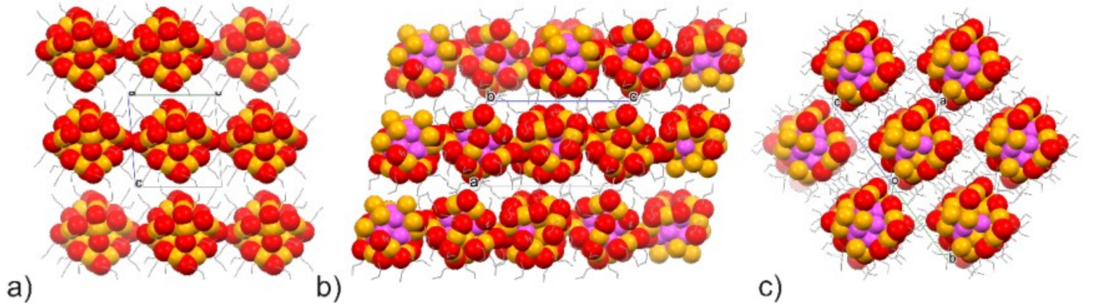

Figure 2.37. Molecular packing of (a) Pt doped along the a-axis, and the Hg (or Cd) doped $Au_{24}M(SC4)_{18}^{0}$ clusters along the (b) b- and (c) (011) lattice direction. Hydrogen atoms are removed for clarity.

All Hg and Cd doped $Au_{24}M(SC2Ph)_{18}^{0}$ clusters (phenylethylthiolate ligands) crystallize in the same orthorhombic crystal system with Pccn symmetry and have a half molecule in an asymmetric unit (Table 2.7). The core units of the three doped clusters are identical showing icosahedral shape along with 12 Au atoms on the staples and one in the center (Figure 2.38), i.e., in keeping with the aforementioned structures and to various $Au_{24}M(SC2Ph)_{18}^{0}$ clusters (M = Au, Pt, Hg, Cd) reported in the literature.[16, 19, 20, 21, 23, 39, 62] As discussed above and according to the NMR analysis, for the final structure models the positions of Hg and Cd atoms were placed evenly disordered over 12 icosahedral Au sites (Figure 2.38). The ligand orientations in these three clusters follow that found for $Au_{25}(SC2Ph)_{18}^{0}$,[39, 62] that is, ligands pointing alternately above and below the planes (Figures S27 and S28a: e.g. S9, S8 S7, Au(center), S7, S9 and S8). Molecular packing of the clusters is exemplified in Figure 2.40b. Clusters pack in orthogonal way showing apparent rows of molecules along the c-axis that are somewhat more apart along the a- and b-axes.

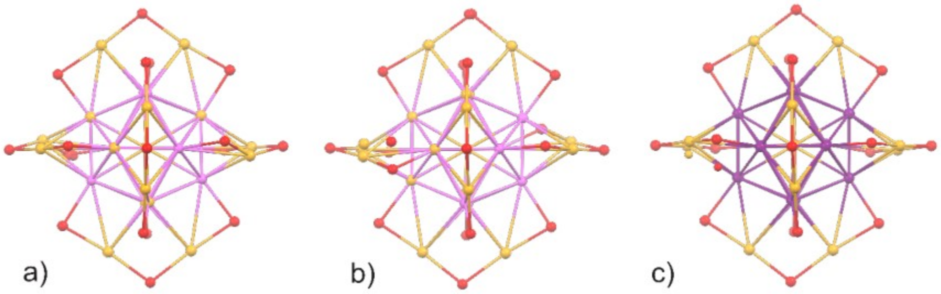

Figure 2.38. Au/M-S cores of metal doped $Au_{24}M(SC2Ph)_{18}^0$ (M = Hg or Cd) clusters: (a) $Au_{24}Hg(SC2Ph)_{18}^0$ ($Hg(NO_3)_2$ method), (b) $Au_{24}Hg(SC2Ph)_{18}^0$ ($Hg(NO_3)_2$ exchange on $Au_{24}Cd(SC2Ph)_{18}^0$), and (c) $Au_{24}Cd(SC2Ph)_{18}^0$ ($Cd(SC2Ph)_2$ method). Hg and Cd atoms are disordered over 12 icosahedral Au sites and are shown by cyan and purple color, respectively.

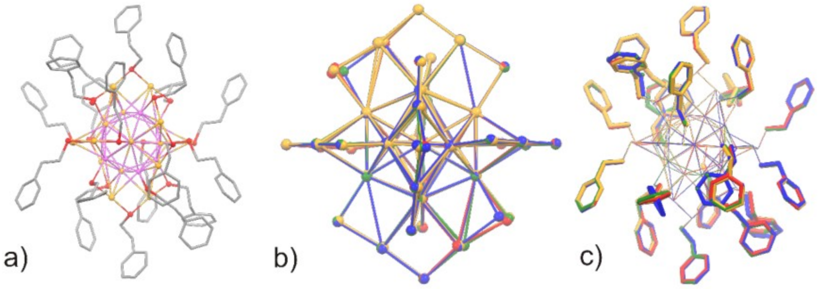

Figure 2.39. Partial views of $Au_{24}M(SC2Ph)_{18}^0$ Au clusters. All three SC2Ph clusters are isostructural, as can be exemplified by (a) the Hg-doped cluster ($Hg(NO_3)_2$ method). Further structural similarity is revealed by overlapping the structures of the Hg and Cd doped clusters with that of $Au_{25}(SC2Ph)_{18}^0$.[39] Structure (b) shows the Au/M-S core units and structure (c) the full clusters (core units are faded for clarity). The color codes are: red = Hg-doped cluster (from $Hg(NO_3)_2$), blue = Hg-doped cluster (from $Hg(NO_3)_2$ + $Au_{24}Cd(SC2Ph)_{18}^0$), green = Cd-doped cluster, and yellow = $Au_{25}(SC2Ph)_{18}^0$.

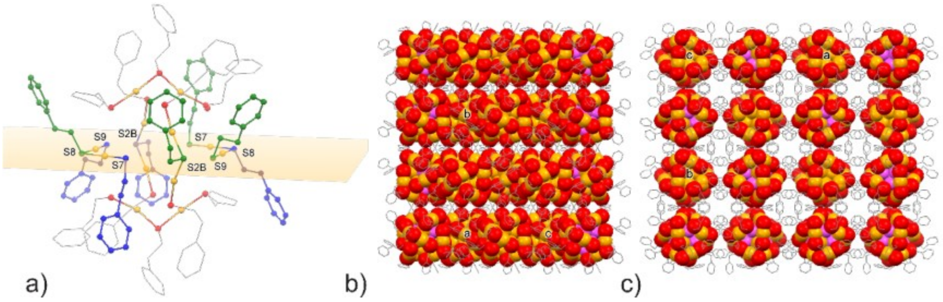

Figure 2.40. a) Ligand orientation (green above and blue below), and molecular packing b) along the a-axis and c) c-axis can be exemplified for all Au$_{24}$M(SC2Ph)$_{18}^{0}$ clusters by the Hg-doped cluster (Hg(NO$_3$)$_2$ method). Hydrogen atoms and for a) all Au atoms, except for those on the staple sites, are removed for clarity.

Table 2.6. Crystallographic data for Au$_{24}$Pt(SC4)$_{18}^{0}$, Au$_{24}$Hg(SC4)$_{18}^{0}$ [from Hg(SC4)$_2$], Au$_{24}$Cd(SC4)$_{18}^{0}$ [from Cd(NO$_3$)$_2$] and Au$_{24}$Cd(SC4)$_{18}^{0}$ [from Cd(SC4)$_2$].

	Au$_{24}$Pt(SC4)$_{18}^{0}$	Au$_{24}$Hg(SC4)$_{18}^{0}$	Au$_{24}$Cd(SC4)$_{18}^{0}$	Au$_{24}$Cd(SC4)$_{18}^{0}$
CCDC no.	1938192	1938193	1938194	1938195
Empirical formula	$C_{72}H_{162}Au_{24}PtS_{18}$	$C_{72}H_{162}Au_{24}HgS_{18}$	$C_{72}H_{162}Au_{24}CdS_{18}$	$C_{72}H_{162}Au_{24}CdS_{18}$
Formula weight	6527.37	6532.87	6444.68	6444.68
Temperature/K	293.8(4)	120.01(10)	120.01(10)	120.00 (10)
Crystal system	triclinic	triclinic	triclinic	triclinic
Space group	*P* -1	*P* -1	*P* -1	*P* -1
a/Å	13.2398(4)	16.2584(2)	16.2635(2)	16.2535(2)
b/Å	15.4546(5)	17.3297(3)	17.3283(2)	17.3097(2)
c/Å	16.4064(5)	25.0056(4)	25.0097(3)	25.0233(3)
α/°	80.144(3)	107.6140(10)	107.5800(10)	107.5790(10)
β/°	71.118(3)	91.3950(10)	91.3370(10)	91.4000(10)
γ/°	71.938(3)	117.1740(10)	117.2220(10)	117.2510(10)
Volume/Å^3	3010.46(18)	5863.11(17)	5865.40(13)	5855.45(13)
Z	1	2	2	2
ρ_{calc}g/cm^3	3.600	3.700	3.649	3.655

μ/mm^{-1}	30.604	60.324	59.438	59.539
F(000)	2856.0	5716.0	5652.0	5652.0
Crystal size/mm^3	0.8 × 0.12 × 0.08	0.442 × 0.051 × 0.04	0.223 × 0.06 × 0.03	0.195 × 0.102 × 0.061
Radiation	MoKα (λ = 0.71073)	CuKα (λ = 1.54184)	CuKα (λ = 1.54184)	CuKα (λ = 1.54184)
2Θ range for data collection/°	5.22 to 56.784	6.126 to 143.994	5.96 to 144	5.966 to 143.98
Index ranges	$-17 \le h \le 17$, $-19 \le k \le 20$, $-21 \le l \le 21$	$-20 \le h \le 20$, $-21 \le k \le 21$, $-30 \le l \le 30$	$-20 \le h \le 20$, $-21 \le k \le 21$, $-30 \le l \le 30$	$-20 \le h \le 19$, $-21 \le k \le 21$, $-30 \le l \le 30$
Reflections collected	57646	134803	141581	98087
Independent reflections	13325 [R_{int} = 0.1228, R_{sigma} = 0.1101]	23033 [R_{int} = 0.0726, R_{sigma} = 0.0392]	23069 [R_{int} = 0.0773, R_{sigma} = 0.0385]	23013 [R_{int} = 0.0570, R_{sigma} = 0.0430]
Data/restraints/parameters	13325/401/551	23033/12/1040	23069/52/1058	23013/137/1043
Goodness-of-fit on F^2	1.058	1.040	1.026	1.039
Final R indexes [I>=2σ (I)]	R_1 = 0.0672, wR_2 = 0.1425	R_1 = 0.0396, wR_2 = 0.1040	R_1 = 0.0399, wR_2 = 0.1043	R_1 = 0.0481, wR_2 = 0.1275
Final R indexes [all data]	R_1 = 0.1242, wR_2 = 0.1752	R_1 = 0.0437, wR_2 = 0.1075	R_1 = 0.0432, wR_2 = 0.1075	R_1 = 0.0520, wR_2 = 0.1322
Largest diff. peak/hole/ e Å^{-3}	4.76/-4.89	2.04/-3.39	2.93/-2.84	4.59/-3.21

Table 2.7. Crystallographic data for $Au_{24}Hg(SC2Ph)_{18}^{0}$ [from $Hg(NO_3)_2$], $Au_{24}Hg(SC2Ph)_{18}^{0}$ [from $Hg(NO_3)_2$ exchange on $Au_{24}Cd(SC2Ph)_{18}^{0}$], and $Au_{24}Cd(SC2Ph)_{18}^{0}$ [from $Cd(SC2Ph)_2$].

	$Au_{24}Hg(SC2Ph)_{18}^{0}$	$Au_{24}Hg(SC2Ph)_{18}^{0}$	$Au_{24}Cd(SC2Ph)_{18}^{0}$
CCDC no.	1938196	1938197	1938198

Empirical formula	$C_{144}H_{162}Au_{24}HgS_{18}$	$C_{144}H_{162}Au_{24}HgS_{18}$	$C_{144}H_{162}Au_{24}CdS_{18}$
Formula weight	7397.59	7397.59	7309.40
Temperature/K	120.01(10)	120.01(10)	120.00 (10)
Crystal system	orthorhombic	orthorhombic	orthorhombic
Space group	Pccn	Pccn	Pccn
a/Å	31.2563(11)	31.2914(4)	31.3135(5)
b/Å	26.9439(5)	27.0095(3)	27.0073(3)
c/Å	18.4570(5)	18.5163(2)	18.5226(2)
α/°	90	90	90
β/°	90	90	90
γ/°	90	90	90
Volume/Å^3	15543.9(7)	15649.3(3)	15664.4(3)
Z	4	4	4
ρ_{calc}g/cm^3	3.161	3.140	3.099
μ/mm^{-1}	23.817	23.657	44.677
F(000)	13160.0	13160.0	13032.0
Crystal size/mm^3	0.199 × 0.115 × 0.02	0.3 × 0.17 × 0.03	0.16 × 0.088 × 0.013
Radiation	MoKα (λ = 0.71073)	MoKα (λ = 0.71073)	CuKα (λ = 1.54184)
2Θ range for data collection/°	3.734 to 58.608	3.726 to 57	4.32 to 146.97
Index ranges	-34 ≤ h ≤ 40, -36 ≤ k ≤ 23, -24 ≤ l ≤ 20	-40 ≤ h ≤ 31, -35 ≤ k ≤ 36, -24 ≤ l ≤ 21	-38 ≤ h ≤ 37, -32 ≤ k ≤ 33, -22 ≤ l ≤ 21
Reflections collected	46697	71320	61448
Independent reflections	18174 [R_{int} = 0.0940, R_{sigma} = 0.1498]	19473 [R_{int} = 0.0579, R_{sigma} = 0.0459]	15745 [R_{int} = 0.0738, R_{sigma} = 0.0587]
Data/restraints/parameters	18174/33/483	19473/7/822	15745/29/763
Goodness-of-fit on F^2	1.136	1.235	1.055

Final R indexes [I>=2σ (I)]	R_1 = 0.0824, wR_2 = 0.1301	R_1 = 0.0407, wR_2 = 0.0797	R_1 = 0.0559, wR_2 = 0.1446
Final R indexes [all data]	R_1 = 0.1395, wR_2 = 0.1504	R_1 = 0.0497, wR_2 = 0.0826	R_1 = 0.0651, wR_2 = 0.1512
Largest diff. peak/hole/ e Å^{-3}	2.99/-3.05	1.75/-1.81	2.31/-2.27

2.5 References

1. Antonello, S.; Maran, F. Molecular Electrochemistry of Monolayer-Protected Clusters. *Curr. Opin. Electrochem.* **2017**, *2*, 18-25.
2. Jin, R. Atomically Precise Metal Nanoclusters: Stable Sizes and Optical Properties. *Nanoscale* **2015**, *7*, 1549-1565.
3. Agrachev, M.; Ruzzi, M.; Venzo, A.; Maran, F. Nuclear and Electron Magnetic Resonance Spectroscopies of Atomically Precise Gold Nanoclusters. *Acc. Chem. Res*. **2019**, *52*, 44-52.
4. Tsukuda, T.; Häkkinen, H. Eds. Protected Metal Clusters: From Fundamentals to Applications. *Frontiers of Nanoscience*; Elsevier: Amsterdam, 2015; Vol. 9.
5. Jin, R.; Zeng, C.; Zhou, M.; Chen, Y. Atomically Precise Colloidal Metal Nanoclusters and Nanoparticles: Fundamentals and Opportunities. *Chem. Rev.* **2016**, *116*, 10346-10413.
6. Jin, R.; Nobusada, K. Doping and alloying in atomically precise gold nanoparticles. *Nano Res.* **2014**, *7*, 285-300.
7. Gan, Z.; Xia, N.; Wu, Z. Discovery, Mechanism, and Application of Antigalvanic Reaction. *Acc. Chem. Res.* **2018**, *51*, 2774-2783.
8. Wang, S.; Li, Q.; Kang, X.; Zhu, M. Customizing the Structure, Composition, and Properties of Alloy Nanoclusters by Metal Exchange. *Acc. Chem. Res.* **2018**, *51*, 2784-2792.
9. Hossain, S.; Niihori, Y.; Nair, L. V.; Kumar, B.; Kurashige, W.; Negishi, Y. Alloy Clusters- Precise Synthesis and Mixing Effects. *Acc. Chem. Res.* **2018**, *51*, 3114-3124.

10. Parker, J. F.; Fields-Zinna, C. A.; Murray, R. W. The Story of a Monodisperse Gold Nanoparticle: $Au_{25}L_{18}$. *Acc. Chem. Res.* **2010**, *43*, 1289-1296.
11. Kang, X.; Chong, H.; Zhu, M. $Au_{25}(SR)_{18}$: The Captain of the Great Nanocluster Ship. *Nanoscale* **2018**, *10*, 10758-10834.
12. Qian, H.; Jiang, D.-e.; Li, G.; Gayathri, C.; Das, A.; Gil, R. R.; Jin, R. Monoplatinum Doping of Gold Nanoclusters and Catalytic Application. *J. Am. Chem. Soc.* **2012**, *134*, 16159-16162.
13. Christensen, S. L.; MacDonald, M. A.; Chatt, A.; Zhang, P.; Qian, H. F.; Jin, R. Dopant Location, Local Structure, and Electronic Properties of $Au_{24}Pt(SR)_{18}$ Nanoclusters. *J. Phys. Chem. C* **2012**, *116*, 26932-26937.
14. Kwak, K.; Tang, Q.; Kim, M.; Jiang, D.-e.; Lee, D. Interconversion between Superatomic 6-Electron and 8-Electron Configurations of $M@Au_{24}(SR)_{18}$ Clusters (M = Pd, Pt). *J. Am. Chem. Soc.* **2015**, *137,* 10833-10840.
15. Thanthirige, V. F.; Kim, M.; Choi, W.; Kwak, K.; Lee, D.; Ramakrishna, G. Temperature-Dependent Absorption and Ultrafast Exciton Relaxation Dynamics in $MAu_{24}(SR)_{18}$ Clusters (M = Pt, Hg): Role of the Central Metal Atom. *J. Phys. Chem. C* **2016**, *120*, 23180-23188.
16. Tian, S. B.; Liao, L. W.; Yuan, J. Y.; Yao, C. H.; Chen, J. S.; Yang, J. L.; Wu, Z. K. Structures and Magnetism of Mono-Palladium and Mono-Platinum Doped $Au_{25}(PET)_{18}$ Nanoclusters. *Chem. Commun.* **2016**, *52*, 9873-9876.
17. Negishi, Y.; Kurashige, W.; Niihori, Y.; Iwasa, T.; Nobusada, K. Isolation, Structure, and Stability of a Dodecanethiolate-Protected Pd_1Au_{24} Cluster. *Phys. Chem. Chem. Phys.* **2010**, *12*, 6219-6225.
18. Negishi, Y.; Kurashige, W.; Kobayashi, Y.; Yamazoe, S.; Kojima, N.; Seto, M.; Tsukuda, T. Formation of a $Pd@Au_{12}$ Superatomic Core in $Au_{24}Pd_1(SC_{12}H_{25})_{18}$ Probed by Au_{197} Mossbauer and Pd K-Edge EXAFS Spectroscopy. *J. Phys. Chem. Lett.* **2013**, *4*, 3579-3583.
19. Tofanelli, M. A.; Ni, T. W.; Phillips, B. D.; Ackerson, C. J. Crystal Structure of the $PdAu_{24}(SR)_{18}^0$ Superatom. *Inorg. Chem.* **2016**, *55*, 999-1001.
20. Wang, S.; Song, Y.; Jin, S.; Liu, X.; Zhang, J.; Pei, Y.; Meng, X.; Chen, M.; Li, P.; Zhu, M. Metal Exchange Method Using Au_{25} Nanoclusters as Templates

for Alloy Nanoclusters with Atomic Precision. *J. Am. Chem. Soc.* **2015**, *137*, 4018-4021.

21. Yao, C.; Lin, Y.-j.; Yuan, J.; Liao, L.; Zhu, M.; Weng, L.-h.; Yang, J.; Wu, Z. Mono-Cadmium vs Mono-Mercury Doping of Au_{25} Nanoclusters. *J. Am. Chem. Soc.* **2015**, *137*, 15350-15353.
22. Zhou, M.; Yao, C.; Sfeir, M. Y.; Higaki, T.; Wu, Z.; Jin, R. Excited-State Behaviors of $M_1Au_{24}(SR)_{18}$ Nanoclusters: The Number of Valence Electrons Matters. *J. Phys. Chem. Lett.* **2018**, *122*, 13435-13442.
23. Liao, L.; Zhou, S.; Dai, Y.; Liu, L.; Yao, C.; Fu, C.; Yang, J.; Wu, Z. Mono-Mercury Doping of Au_{25} and the HOMO/LUMO Energies Evaluation Employing Differential Pulse Voltammetry. *J. Am. Chem. Soc.* **2015**, *137*, 9511-9514.
24. Yan, N.; Liao, L.; Yuan, J.; Lin, Y.-j; ; Weng, L.-h.; Yang, J.; Wu, Z. Bimetal Doping in Nanoclusters: Synergistic or Counteractive? *Chem. Mater.* **2016**, *28*, 8240-8247.
25. Yang, S.; Wang, S.; Jin, S.; Chen, S.; Sheng, H.; Zhu, M. A metal exchange method for thiolate-protected tri-metal $M_1Ag_xAu_{24-x}(SR)_{18}^0$ (M = Cd/Hg) nanoclusters. *Nanoscale* **2015**, *7*, 10005-10007.
26. Niihori, Y.; Hossain, S.; Sharma, S.; Kumar, B.; Kurashige, W. Negishi, Y. Understanding and Practical Use of Ligand and Metal Exchange Reactions in Thiolate-Protected Metal Clusters to Synthesize Controlled Metal Clusters Exchange reactions in thiolate-protected metal clusters. *Chem. Rec.* **2017**, *17*, 473-484.
27. Zheng, Y.; Jiang, H.; Wang, X. Multiple Strategies for Controlled Synthesis of Atomically Precise Alloy Nanoclusters. *Acta Phys. Chim. Sin.* **2018**, *34*, 740-754.
28. Yao, Q.; Yuan, X.; Chen, T.; Leong, D. T.; Xie, J. Engineering Functional Metal Materials at the Atomic Level. *Adv. Mater.* **2018**, 1802751.
29. Heaven, M.W.; Dass, A.; White, P.S.; Holt, K.M.; Murray R. W. Crystal Structure of the Gold Nanoparticle $[N(C_8H_{17})_4]$-$[Au_{25}(SCH_2CH_2Ph)_{18}]$. *J. Am. Chem. Soc.* **2008**, *130*, 3754-3755.

30. Zhu, M.; Aikens, C. M.; Hollander, F. J.; Schatz, G. C.; Jin, R. Correlating the Crystal Structure of a Thiol-Protected Au_{25} Cluster and Optical Properties. *J. Am. Chem. Soc.* **2008**, *130*, 5883-5885.
31. Zhu, M.; Aikens, C. M.; Hendrich, M. P.; Gupta, R.; Qian, H.; Schatz, G. C.; Jin, R. Reversible Switching of Magnetism in Thiolate-Protected Au_{25} Superatoms. *J. Am. Chem. Soc.* **2009**, *131*, 2490-2492.
32. Jiang, D.-e.; Dai, S. From Superatomic $Au_{25}(SR)_{18}^{-}$ to Superatomic $M@Au_{24}(SR)_{18}^{q}$ Core-Shell Clusters. *Inorg. Chem.* **2009**, *48*, 2720-2722.
33. Walter, M.; Moseler, M. Ligand-Protected Gold Alloy Clusters-Doping the Superatom. *J. Phys. Chem. C* **2009**, *113*, 15834-15837.
34. Taylor, M. G.; Mpourmpakis, G. Rethinking Heterometal Doping in Ligand-Protected Metal Nanoclusters. *J. Phys. Chem. Lett.* **2018**, *9*, 6773-6778.
35. Taylor, M. G.; Mpourmpakis, G. Thermodynamic Stability of Ligand-Protected Metal Nanoclusters. *Nat. Commun.* **2017**, *8*, 15988.
36. Alkan, F.; Pandeya, P.; Aikens, C. M. Understanding the Effect of Doping on Energetics and Electronic Structure for Au_{25}, Ag_{25} and Au_{38} Clusters. *J. Phys. Chem. C* **2019**, *14*, 9516-9527.
37. De Nardi, M.; Antonello, S.; Jiang, D.; Pan, F.; Rissanen, K.; Ruzzi, M.; Venzo, A.; Zoleo, A.; Maran, F. Gold Nanowired: A Linear $(Au_{25})_n$ Polymer from Au_{25} Molecular Clusters. *ACS Nano* **2014**, *8*, 8505-8512.
38. Agrachev, M., Antonello, S., Dainese, T., Gascón, J. A., Pan, F., Rissanen, K., Ruzzi, M., Venzo, A., Zoleo, A.; Maran F. A Magnetic Look into the Protecting Layer of Au_{25} Clusters. *Chem. Sci.* **2016**, *7*, 6910-6918.
39. Antonello, S.; Dainese, T.; Pan, F.; Rissanen, K.; Maran, F. Electrocrystallization of Monolayer Protected Gold Clusters: Opening the Door to Quality, Quantity and New Structures. *J. Am. Chem. Soc.* **2017**, *139*, 4168-4174.
40. Qian, H.; Zhu, M.; Gayathri, C.; Gil, R. R.; Jin, R. Chirality in Gold Nanoclusters Probed by NMR Spectroscopy. *ACS Nano* **2011**, *11*, 8935-8942.
41. Dainese, T.; Antonello, S.; Bogialli, S.; Fei, W.; Venzo, A.; Maran, F. Gold Fusion: From $Au_{25}(SR)_{18}$ to $Au_{38}(SR)_{24}$, the Most Unexpected Transformation

of a Very Stable Nanocluster. *ACS Nano* **2018**, *12*, 7057-7066.

42. Dainese, T.; Agrachev, M.; Antonello, S.; Badocco, D.; Black, D. M.; Fortunelli, A.; Gascón, J. A.; Stener, M.; Venzo, A.; Whetten, R. L.; Maran, F. Atomically Precise $Au_{144}(SR)_{60}$ Nanoclusters (R=Et, Pr) are Capped by 12 Distinct Ligand Types of 5-fold Equivalence and Display Gigantic Diastereotopic Effects. *Chem. Sci.* **2018**, *9*, 8796-8805.
43. Karplus, M. Contact Electron-Spin Coupling of Nuclear Magnetic Moments. *J. Chem. Phys.* **1959**, *30*, 11-15.
44. Zerbe, O.; Pountney, D. L.; von Philipsborn, W.; Vašák, M. ^{113}Cd, ^{1}H-Cysteine Coupling in Cd-Substituted Metalloproteins Follows a Karplus-Type Dependence. *J. Am. Chem. Soc.* **1994**, *116*, 377-378.
45. Zerbe, O.; Pountney, D. L.; von Philipsborn, W.; Vašák, M. ^{113}Cd, ^{1}H-Cysteine Coupling in Cd-Substituted Metalloproteins Follows a Karplus-Type Dependence. [Erratum to document cited in CA120:49322]. *J. Am. Chem. Soc.* **1994**, *116*, 7957-7957.
46. Henehan, C. J.; Pountney, D. L.; Zerbe, O.; Vašák, M. Identification of Cysteine Ligands in Metalloproteins using Optical and NMR Spectroscopy: Cadmium-substituted Rubredoxinasa Model $[Cd(CysS)_4]^{2-}$ Center. *Protein Sci.* **1993**, *2*, 1756-1764.
47. Pountney, D. L.; Zerbe, O.; von Philipsborn, W.; Egan, J. B.; Vašák, M. $^{3}J(^{113}Cd, {}^{1}H)$ Couplings in Cd(S-Cys) and Cd-μ_2-(S-Cys)-Cd Moieties Follow a Karplus-like Dependence with the H^{β}-C^{β}-S^{γ}-Cd Torsion Angle: Application to Protein. *Bull. Magn. Reson.* **1995**, *17*, 145-147.
48. Donkers, R. L.; Lee. D.; Murray, R. W. Synthesis and Isolation of the Molecule-like Cluster $Au_{38}(PhCH_2CH_2S)_{24}$. *Langmuir*, **2004**, *20*, 1945-1952.
49. Antonello, S.; Dainese, T.; De Nardi, M.; Perotti, L.; Maran, F. Insights into the Interface between the Electrolytic Solution and the Gold Core in Molecular Au_{25} Clusters. *ChemElectroChem.* **2016**, *3*, 1237-1244.
50. Antonello, S.; Holm, A. H.; Instuli, E.; Maran, F. Molecular Electron-Transfer Properties of Au_{38} Clusters. *J. Am. Chem. Soc.* **2007**, *129*, 9836-9837.
51. Deng, H.; Wang, S.; Jin, S.; Yang, S.; Xu, Y.; Liu, L.; Xiang, J.; Hu, D.; Zhu. M.

Active metal (cadmium) doping enhanced the stability of inert metal (gold) nanocluster under O_2 atmosphere and the catalysis activity of benzyl alcohol oxidation. *Gold Bull.* **2015**, *48*, 161-167.

52. Antonello, S.; Dainese, T.; Maran, F. Exploring Collective Substituent Effects: Dependence of the Lifetime of Charged States of $Au_{25}(SC_nH_{2n+1})_{18}$ Nanoclusters on the Length of the Thiolate Ligands. *Electroanalysis* **2016**, *28*, 2771-2776.
53. Antonello, S.; Perera, N. V.; Ruzzi, M.; Gascón, J. A.; Maran, F. Interplay of Charge State, Lability, and Magnetism in the Molecule-like $Au_{25}(SR)_{18}$ Cluster. *J. Am. Chem. Soc.* **2013**, *135*, 15585–15594
54. Lee, D.; Donkers, R. L.; Wang, G.; Harper, A. S.; Murray, R. W. Electrochemistry and Optical Absorbance and Luminescence of Molecule-like Au_{38} Nanoparticles. *J. Am. Chem. Soc.* **2004**, *126*, 6193-6199.
55. Dainese, T.; Antonello, S.; Gascón, J. A.; Pan, F.; Perera, N. V.; Ruzzi, M.; Venzo, A.; Zoleo, A.; Rissanen, K.; Maran, F. Au25(SEt)18, a Nearly Naked Thiolate-Protected Au_{25} Cluster: Structural Analysis by Single Crystal X-ray Crystallography and Electron Nuclear Double Resonance. *ACS Nano* **2014**, *8*, 3904-3912.
56. Du. Y.; Sheng. H.; Astruc. D.; Zhu. M. Atomically Precise Noble Metal Nanoclusters as Efficient Catalysts: A Bridge between Structure and Properties. *Chem. Rev.* **2019**. DOI: 10.1021/acs.chemrev.8b00726.
57. Meneses, A. B.; Antonello, S.; Arévalo, M.-C; Maran, F. Double-Layer Correction for Electron-Transfer Kinetics at Glassy Carbon and Mercury Electrodes in N,N-Dimethylformamide. *Electroanal.* **2006**, *18*, 363-370.
58. Rigaku Oxford Diffraction, Version 1.171.39.46, **2018**.
59. Sheldrick, G. M. SHELXT – Integrated space-group and crystal-structure determination. *Acta Cryst.* **2015**, *A71*, 3-8.
60. Sheldrick, G. M. Crystal structure refinement with SHELXL. *Acta Cryst*. **2015**, *C71*, 3-8.
61. Dolomanov, O. V.; Bourhis, L. J.; Gildea, R. J.; Howard, J. A. K.; Puschmann, H. OLEX2: a complete structure solution, refinement and analysis program. *J.*

Appl. Cryst. **2009**, *42*, 339-341.

62. Zhu, M.; Eckenhoff, W. T.; Pintauer, T.; Jin, R. Conversion of Anionic $[Au_{25}(SCH_2CH_2Ph)_{18}]^-$ Cluster to Charge Neutral Cluster via Air Oxidation. *J. Phys. Chem. C* **2008**, *112*, 14221-14224.

2.6 Acknowledgements

I am particularly thankful to Dr. Alfonso Venzo for his contribution to the NMR measurements, and Prof. Kari Rissanen, Dr. Manu Lahtinen (University of Jyväskylä) and Prof. Alessandro Dolmella (University of Padova) for the X-ray crystallographic studies.

Chapter 3. Understanding and Controlling the Efficiency of $Au_{24}\mathit{M}(S\mathit{R})_{18}$ Nanoclusters as Singlet-Oxygen Photosensitizers

3.1 Introduction

Singlet oxygen, $^1O_2$, is the first excited state ($^1\Delta_g$) of molecular oxygen. Depending on the experimental conditions, its lifetime can span orders of magnitude.[1-3] $^1O_2$ eventually converts to ground-state triplet oxygen ($^3\Sigma_g^-$), $^3O_2$. Because singlet oxygen is significantly more reactive than triplet oxygen, it finds uses in several applications, especially organic synthesis, photocatalysis, and nanomedicine (photodynamic therapy).[4-9] Singlet oxygen[10-12] can be produced by direct excitation, although the $^3O_2 \rightarrow {}^1O_2$ is a spin-forbidden transition with a very low absorption coefficient. A more efficient way to generate singlet oxygen is by using photosensitizers.[10,13] The sensitizer is photoexcited to its singlet state, undergoes intersystem crossing (ISC) to form the excited triplet state, and then transfers energy to triplet oxygen to yield $^1O_2$; the last step is efficient because the overall angular moment is now conserved. Suitable photosensitizers are molecules that exhibit a sufficiently high value of the excited triplet-state energy (the $^3\Sigma_g^-$ to $^1\Delta_g$ excitation energy, E_{exc}, is 94 kJ mol^{-1}), a high quantum yield for ISC, and a long triplet lifetime. On the other hand, it has been long acknowledged that the sensitizer and/or products of its photoreactions can also quench singlet oxygen by converting it back to $^3O_2$.[14,15] These quenching reactions may significantly diminish the $^1O_2$ lifetime and, consequently, affect the overall efficiency of the photosensitization process. An ideal photosensitizer should, therefore, maximize generation efficiency and minimize deactivation. This is not, however, an easy task to achieve.[10]

The detection of singlet oxygen in fluid solution is routinely carried out with optical specific probe of singlet oxygen is the 1275 nm $^1O_2 \rightarrow {}^3O_2$ phosphorescence, particularly when it is monitored in a time-resolved experiment. To overcome the low-sensitivity limitations, several approaches have been proposed, mostly relying on the introduction of a fluorescent probe activated by energy transfer from $^1O_2$. For example, phthalocyanines, naphthalocyanines, and porphyrazines exhibit strong delayed luminescence upon energy transfer from two $^1O_2$.[16] This luminescence is emitted in the visible-light region and its quantum yield exceeds that of $^1O_2$ phosphorescence by 2-4 orders of magnitude. These molecules, however, are also good sensitizers for the formation of $^1O_2$, thereby complicating detection. Chemical traps have also been extensively employed.[17] Singlet oxygen rapidly and irreversibly reacts with aromatic compounds to yield endoperoxides that do not fluoresce and whose absorption spectrum differs significantly from that of the original molecule. However, chemical traps may also be reactive toward other reactive oxygen species. Because of the difficulties associated with direct detection and indirect methods, alternative approaches for the detection of $^1O_2$ generated by photosensitizers are thus sought.

Possible photosensitizer candidates that meet several of the aforementioned requirements are atomically precise gold nanoclusters, $Au_n(SR)_m$ (where SR = thiolate). Nowadays, many of these clusters can be prepared in a very pure, controlled state.[18] This implies full molecular control on structure and properties, which cannot be achieved with the larger gold nanoparticles. Because the electronic structure and thus the optical properties of these clusters depend on the values of n and m, ultrasmall gold nanoclusters might be, in principle, optimized for efficient production of $^1O_2$. So far, the research in this field has been quite limited,[19-31] with very few examples describing the behavior of truly atomically precise gold nanoclusters. This is the case of $Au_{25}(SR)_{18}$, which is a stable cluster that shows distinct electrochemical,[34] optical,[18] and magnetic features,[35,36] and is consistently considered the benchmark system for understanding and controlling many properties of gold nanoclusters.[37,38] Kawasaki *et al.* were the first to describe the formation of singlet oxygen using $Au_{25}(SR)_{18}$ (HSR = phenylethanethiol or captopril) as photosensitizer.[19] The photosensitization was detected optically and with chemical quenchers. $Au_{38}(SC_2H_4Ph)_{24}^0$, another well-established molecular cluster, was found to be significantly less efficient. More recently, Ho-Wu et al. compared the photosensitization efficiency of Au_{25}, Ag_{32}, Au_{144}, larger gold nanoparticles, and a conventional dye photosensitizer.[29] This study, which was carried out with indirect optical methods (1,3-diphenylisobenzofuran quencher), concluded that Au_{144} provides the most efficient system. A size dependence order of $Au_{144} > Au_{38} > Au_{25}$ was observed for the aerobic oxidation of D-Glucose on carbon-supported clusters.[31] The efficiency of $^1O_2$ generation using $Au_{38}S_2(SAdm)_{20}$ (SAdm = adamantanethiolate) nanoclusters was found to be higher than that of $Au_{25}(SC_2H_4Ph)_{18}^-$.[32] The ultrasonic activation of Au_{25}(Captopril)$_{18}$ to generate $^1O_2$ was also demonstrated.[33]

Here we describe the photosensitizing behavior of a series of $Au_{25}(SR)_{18}^-$, where R = n-C_3H_7 (C3), n-C_4H_9 (C4), spectroscopies. The most and C_2H_4Ph (C2Ph) (hereafter, we will indicate the number of carbon atoms of the alkyl chain simply as Cn), and monodoped $Au_{25}M(SR)_{18}$ (M = Cd, Hg) clusters (Figure 3.1). Besides studying the effect of the protecting ligand, the analysis was extended to monodoped clusters because their optical and especially electrochemical behaviors show significant differences from those of the undoped clusters.[39] Regarding detection, we relied on continuous-wave and, especially, time-resolved electron paramagnetic resonance techniques (CWEPR and TREPR, respectively). TREPR spectroscopy provides an efficient and sensitive method to detect even very low concentrations of $^1O_2$ generated by photosensitization in solution.[40,41] Moreover, TREPR is selective toward singlet oxygen, which is unequivocally detected and identified, while other reactive oxygen species are not revealed. As we will show, TREPR allowed us to characterize in detail the photosensitization behavior of the investigated clusters, and could confirm that the cluster's excited state responsible for the activation of triplet oxygen is indeed a triplet. Most notably, we found that proper design of the redox properties of the cluster yields results comparable to those of tetraphenylporphirin (TPP), which is a well-known reference photosensitizer.[10] Finally, we obtained important insights into the $^1O_2$ quenching mechanism by gold nanoclusters, how to control it, and why properly doped gold nanoclusters may perform so well in $^1O_2$ photosensitization.

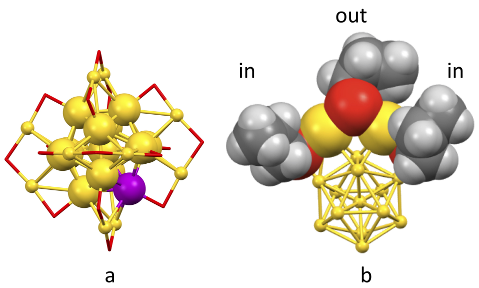

Figure 3.1. (a) Typical structure of the $Au_{24}M(SR)_{18}$ nanocluster. One of the icosahedron positions (pink) corresponds to M (M = Au, Hg, Cd). The gold (yellow) and sulfur (red) atoms are shown, whereas the carbonaceous part of the ligands is omitted for clarity. (a) Structure of $Au_{25}(SC3)_{18}^{0}$ showing the C (gray) and H atoms (white) for both inner (in) and outer (out) ligand types of one of the six staples.

3.2 Results and Discussion

3.2.1 $^1O_2$ photosensitization with TREPR detection

TREPR spectroscopy is especially suitable to study the kinetics of photogenerated paramagnetic species exhibiting lifetimes ranging from few to several hundred μs.[42] In particular, TREPR detection of $^1O_2$ is based on the radical triplet pair (RTP) mechanism.[43] Triplet quenching by a stable free radical, such as a nitroxide (which is a doublet, ^2R, and exhibits three, very similar CWEPR signals due to the hyperfine interaction of the unpaired electron with the N nucleus), induces populations of the radical spin sublevels of the latter that differ significantly from those at thermal equilibrium. This phenomenon, which is commonly referred to as chemically induced dynamic electron polarization,[44] can be sensitively detected by TREPR in the form of transient intensities of the EPR signals associated with the radical probe. Importantly, polarization may be also caused by a singlet state, as in the case of $^1O_2$.[45,46]

Briefly, photoexcitation of the sensitizer fundamental singlet state (^1PS) yields a singlet excited state ($^1PS^*$) that is quickly converted into a triplet state ($^3PS^*$) via ISC. In the absence of oxygen, the excited triplet state undergoes quenching by interaction with a nitroxide radical, and *polarized emissive* TREPR signals are observed. The emissive polarization is interpreted according to the quartet-precursor RTP (Q-RTP) theory,[47] as described by eq 1:

(1) $^{3}PS^{*} + {}^{2}R \longrightarrow {}^{1}PS + {}^{2}R^{*}\downarrow$

where $^{2}R^{*}\downarrow$ indicates the emissive spin polarization generated in ^{2}R by the quenching of the $^{3}PS^{*}$ state. Radicals, on the other hand, are also able to quench singlet states, though now the spin polarization is opposite to that just described: in an air-saturated solution of a nitroxide and a triplet sensitizer, a *reinforced absorptive polarization* for the signals of the nitroxide is indeed expected. This absorptive character of the polarization is a consequence of the initial energy exchange of the triplet state of the sensitizer by triplet oxygen to form $^{1}O_2$ (eq 2), which then polarizes the radical ^{2}R (eq 3):

(2) $^{3}PS^{*} + {}^{3}O_2 \longrightarrow {}^{1}PS + {}^{1}O_2$

(3) $^{1}O_2 + {}^{2}R \longrightarrow {}^{3}O_2 + {}^{2}R^{*}\uparrow$

where $^{2}R^{*}\uparrow$ now refers to the radical in which reinforced absorptive spin polarization is generated. This mechanism is the equivalent of the doublet-precursor RTP (D-RTP) theory,[45] the only difference being that now the nitroxide interacts with a singlet, rather than a triplet state. Very important, the magnitude of this net absorptive spin polarization is *extraordinarily large* even for traces of singlet oxygen.[46]

All clusters were prepared and characterized by mass spectrometry, NMR spectroscopy, and UV-vis spectroscopy as described previously.[39,48-50] Special care was paid on controlling properly the charge state.[51,52] TREPR experiments were carried out in toluene at 240 K, and refer to 1 mM cluster and 0.5 mM 2,2,6,6-tetramethyl-4-oxo-1-piperidinyloxy (TEMPONE), unless otherwise stated. In TREPR, a laser pulse (we used 4 ns at 532 nm) triggers the aforementioned photochemical reaction/s and eventually generates the polarized paramagnetic species ($^{2}R^{*}\uparrow$ or $^{2}R^{*}\downarrow$). The ensuing EPR transient is recorded at the given value of the magnetic field (B). This procedure is applied by scanning B until the entire field range is covered. The sequence is then repeated many times, and the corresponding series of transients is averaged. The resulting TREPR spectrum is usually displayed in a 3D form (Figure 3.2), where the TREPR intensity is plotted as a function of *B* and time (*t*). No field modulation is applied and thus the observed signals do not exhibit the derivative shape typical of the corresponding CWEPR spectra (Figure 3.3c, d).

Figure 3.2a shows the spectrum obtained using $Au_{25}(SC3)_{18}^{-}$ as the photosensitizer under aerobic conditions. The TREPR spectrum of TEMPONE consists in three signals of equal intensity that decay in a few μs. The polarized TREPR signals show the net absorptive character expected when the overall photosensitization process (excitation, ISC, and energy transfer) is efficient and followed by step 3. In the control experiment carried out in the absence of oxygen, only emissive polarization is observed (Figure 3.2b). According to the Q-RTP mechanism, the emissive polarized transient spectra are consistent with the direct interaction of the nitroxide with the triplet state of $Au_{25}(SR)_{18}^{-}$. The extent of emissive polarization strongly depends on the quantum yield of the latter and the actual lifetime of the cluster triplet state. In this connection, the different time scales of the transients in the two plots of Figure 3.2 are worth noticing. These results already allow us to draw a very important conclusion. So far, photoexcitation of clusters has been generically described as generating excited states, as no conclusive evidence about the formation of an excited triplet state could be gathered. In the first report on singlet oxygen generation by photoexcited Au clusters, the term triplet state was used for the very same reason that the photoexcited cluster was generating $^1O_2$.[19] On the other hand, singlet oxygen may form in several different ways.[53] In the present context, the TREPR results observed under anaerobic conditions definitely prove that, indeed, photoexcitation of $Au_{25}(SR)_{18}^{-}$ eventually leads to an excited triplet state, as the polarized emissive signals can only be generated when the nitroxide exchange energy with a triplet state.[46]

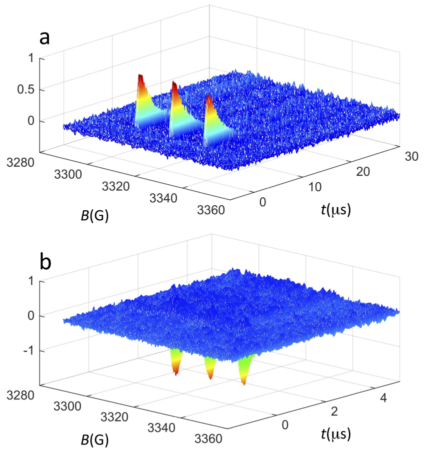

Figure 3.2. TREPR surfaces recorded for 0.5 mM TEMPONE and 1 mM $Au_{25}(SC3)_{18}^{-}$ in (a) air-saturated and (b) deaerated toluene solution at 240 K.

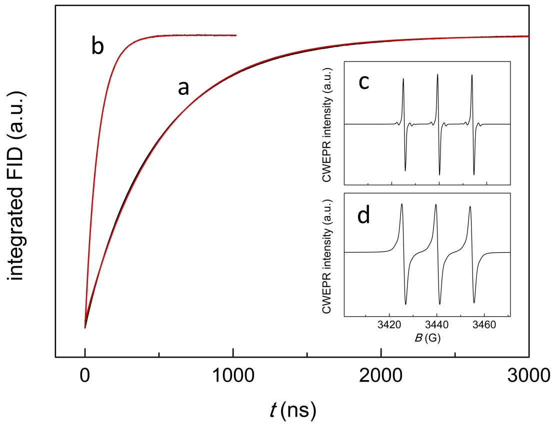

Figure 3.3. Inversion recovery curves for a toluene solution of 0.5 mM TEMPONE and 1 mM $Au_{25}(SC3)_{18}^{-}$ (black) under anaerobic (trace a) and aerobic conditions (trace b), with the corresponding exponential fits to the data (red: for both curves, r^2 = 1.000). The CWEPR spectra refer to the corresponding anaerobic (c) and aerobic conditions (d).

3.2.2 Analysis of the $^1O_2$ Lifetime and Validation of the TREPR Method.

The decay kinetics depends on several parameters. In a deaerated solution, the decay of the emission-polarized signals (Figure 3.2b) is determined by the lifetime of the cluster triplet state and the characteristic magnetic-relaxation times of the nitroxide, T1 and T2.[54] T1, which is the spin-lattice longitudinal relaxation time, can be determined independently, by pulsed EPR inversion recovery experiments (Figure 3.3, trace a), to be 499.1(0.6) ns. In the absence of the cluster, we obtained the virtually identical value of 501.8(0.7) ns (r^2 = 1.000). T2 is the transverse spin-spin relaxation time, and could be estimated to be 0.43(0.01) μs from the reciprocal of the full-width-at-half-height of the integral of the CWEPR spectrum shown in Figure 3.3c, as illustrated in Figure 3.12. In deaerated solution, the reciprocal of the TREPR decay rate-constant value obtained from the emission data (Figure 3.13) is 0.45(0.01) μs (r^2 = 0.983), and therefore, is comparable to the relaxation parameters of TEMPONE. These results point to the TEMPONE spin relaxation as a particularly relevant factor determining the TREPR decay kinetics, and thus imply that the lifetime of the cluster triplet state should be shorter than ~ 0.3 μs.

In the presence of air, the CWEPR spectrum of TEMPONE shows broader peaks (Figure 3.3d). The T1 measured by pulsed EPR inversion recovery experiments in the presence of $Au_{25}(SC3)_{18}^-$ (Figure 3.3b) is now only 64(0.2) ns (r^2 = 1.000), that is, about one order of magnitude shorter than the T1 determined under anaerobic conditions. Similarly, T2 decreases from 0.43 to 0.04 μs. These effects are caused by the known interaction of TEMPONE with triplet oxygen.[55] Under aerobic conditions, the decay of the TREPR signals also depends on the singlet-oxygen lifetime. A scheme of the general process is provided in the inset of Figure 3.4. The average of the TREPR transients (Figure 3.4) can be fit to single exponential (r^2 = 0.969) yielding an observed decay rate constant (k_Δ) of 3.02 x 10^5 s^{-1}, which corresponds to a lifetime (τ_Δ) of 3.31(0.05) μs. τ_Δ is thus nearly two orders of magnitude longer than the corresponding T1 value, and this indicates that now the observed decay of spin polarization is only controlled by the $^1O_2$ lifetime. In other words, while the polarized signals decay on the T1 time scale, there is still some singlet oxygen in solution that continuously contributes to generate further polarization in the TEMPONE molecules. Under these conditions, the decay of the TREPR signal lifetime can thus be used to calculate the singlet-oxygen lifetime.

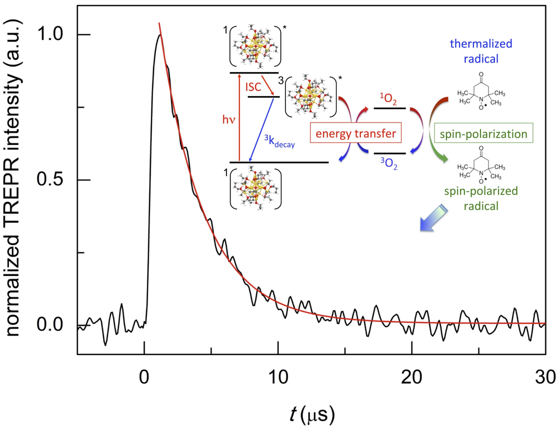

Figure 3.4. TREPR (normalized) transient observed for 0.5 mM TEMPONE and 1 mM $Au_{25}(SC3)_{18}^{-}$ in toluene under aerobic conditions (black) at 240 K. The red curve is the exponential fit to the data. The inset provides a schematic representation of the TREPR detection of $^1O_2$ generation through photoexcitation of the cluster.

In any given experimental condition, the observed $^1O_2$ lifetime is determined by the species present in solution.[10] In the absence of solutes other than oxygen, on the other hand, the intrinsic $^1O_2$ decay pseudo-first order rate constant (k_Δ^S) only depends on the solvent (S) through two terms (eq 4):

(4) $k_\Delta^S = k_{nr}[S] + k_r[S]$

where k_{nr} and k_r refer to the nonradiative and radiative components, respectively.[10,56] From available data obtained in toluene as a function of temperature, we calculate for the intrinsic lifetime of $^1O_2$ (τ_Δ^S) at 240 K the values of 31.7[57] and 34.6 μs.[56] These figures are significantly longer than the value of 3.31 μs obtained with the TEMPONE/$Au_{25}(SC3)_{18}^{-}$ system, and therefore, show that in our experimental conditions significant quenching of singlet oxygen must take place. Comparison of τ_Δ with τ_Δ^S (hereafter, we will refer to the most recent determination, 34.6 μs)[56] yields a relative τ_Δ decrease of $100(\tau_\Delta^S - \tau_\Delta)/\tau_\Delta^S = 90.4\%$.

Besides the solvent, there are two possible candidates as quenchers: TEMPONE and the cluster itself. To address this issue, we carried out further experiments. The majority of photosensitizers currently employed in photodynamic therapy are cyclic tetrapyrrolic structures, such as porphyrin derivatives.[58] It is thus instructive to compare the polarized signals observed for $Au_{25}(SC3)_{18}^{-}$ with those obtained for tetraphenylporphyrin (TPP), which is a well-known reference photosensitizer, yet showing some quenching of $^1O_2$.[59] TPP was used at the same concentration of the cluster (1 mM) and qualitatively gave the same TREPR spectrum, but for the two differences that the signal intensity at its maximum is ~3 times larger than for $Au_{25}(SC3)_{18}^{-}$ and, particularly important, the decay is much slower (Figure 3.5). It should be noted that for $t < 0.5$ μs the presence of a negative spike indicates that a (small) fraction of the amount of the TPP molecules in their triplet excited state (for TPP, the fraction of singlet excited state species that undergo radiationless decay to form the triplet excited state is $\Phi_T = 0.71$;[60] in the presence of oxygen, this value is expected to increase slightly)[61] reacts with TEMPONE according to the Q-RTP theory (eq 1). The fact that the TREPR intensity maximum is attained in 1.5-2 μs, indicates that the majority of the TPP triplet reacts with $^3O_2$ within less than 1 μs. This is in keeping with a lifetime of 196 ns measured for the TPP triplet state in toluene at room temperature.[62]

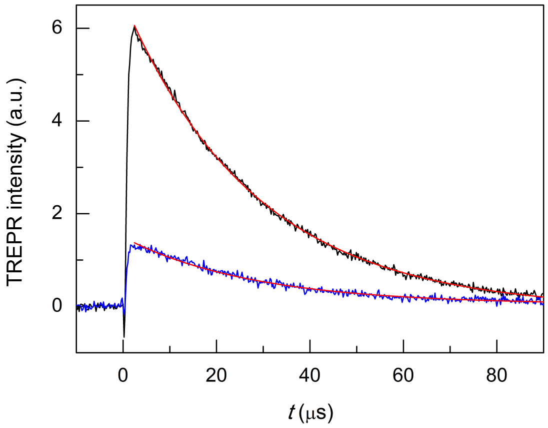

Figure 3.5. TREPR transients observed under aerobic conditions for samples of 1 mM TPP and 0.5 (black) or 0.1 mM (blue) TEMPONE in toluene at 240 K. The corresponding exponential fits to the data are in red.

Best fit of the decay data obtained for $t > 3$ μs gives $k_\Delta = 3.54 \times 10^4$ s^{-1} ($r^2 = 0.999$), corresponding to a lifetime τ_Δ of 28.2(0.1) μs. This shows that TPP is, as expected, a very good photosensitizer. Comparison of this τ_Δ value with τ_Δ^S, however, evidences a relative τ decrease of 18.5%. To obtain information on a possible effect of TEMPONE as a quencher, we carried out further TPP photosensitization experiments in which the TEMPONE concentration was varied, as exemplified by the two traces in Figure 3.5. We obtained: [TEMPONE] = 0.2 mM, $k_\Delta = 3.36 \times 10^4$ s^{-1}, $\tau_\Delta = 29.8(0.4)$; ([TEMPONE] = 0.1 mM, $k_\Delta = 3.66 \times 10^4$ s^{-1}, $\tau_\Delta = 27.4$ (0.6). The very similar τ_Δ values, therefore, show that under our experimental conditions the TEMPONE concentration does not affect the observed $^1O_2$ lifetime. Besides confirming that indeed TPP acts as a quencher, these results also indicate that despite the intense TREPR signals, TEMPONE polarization must involve a very small amount of the $^1O_2$ present in solution. These tests validated the TREPR methodology and indicated that 0.5 mM TEMPONE could be consistently used with no detectable effect on the $^1O_2$ lifetime. The experiments described below were carried out under these conditions.

3.2.3 Tuning the Photosensitizing Properties of Au_{25} Nanoclusters.

The TREPR data confirm that $Au_{25}(SR)_{18}^-$ can be used as a photosensitizer.[19] They also show that the $^1O_2$ lifetime measured in the presence of $Au_{25}(SC3)_{18}^-$ is much shorter than the τ_Δ^S value. The cluster is, therefore, a good sensitizer but also a good quencher, as observed for many sensitizers.[10] We will now specifically focus on this aspect. The decay of singlet-oxygen can proceed by physical quenching, leading to deactivation of $^1O_2$, and chemical reactions, in which $^1O_2$ irreversibly reacts with some other species in solution.[10] In the presence of a generic molecule (M) capable of quenching or chemically reacting with $^1O_2$, eq 4 must include further terms (eq 5):[10,56]

(5) $k_\Delta = k_{nr}[S] + k_r[S] + k_q[M] + k_{cr}[M]$

where k_q and k_{cr} are the second-order rate constants referring to the quenching and chemical reaction components, respectively. The gold nanoclusters do not react chemically with $^1O_2$. Although $Au_{25}(SR)_{18}^-$ may react with $^1O_2$ by electron transfer (ET), the effect of this reaction is detected only on a much longer time scale. For example, we found that flashing a $Au_{25}(SC4)_{18}^{-}$ sample (by using the same pulse sequence as in the TREPR experiments) in the presence of oxygen for 2 h transforms 8.8% of the anion into the corresponding neutral cluster (Figure S3). We can now thus focus only on the physical quenching paths, which consist in the first three terms in eq 5. Physical quenching is the consequence of interactions with the solvent (terms k_{nr} and k_r) and solute/s (term k_q). For many solvents, including toluene, k_{nr} is dominant over k_r.[10] As to k_{nr}, solvent molecules deactivate singlet oxygen by electronic-vibrational energy transfer and by perturbing singlet oxygen with the result of facilitating its transition to $^3O_2$.[12,56] An effective physical quenching route is also attributed to the formation of a charge-transfer (CT) complex between singlet oxygen and the photosensitizer.[10,63,64] The resulting exciplex is a bimolecular excited state that can be described as a resonance of the excited and full ET states. The exciplex implies a partial (δ) CT and its formation is especially favored when the photosensitizer is a good electron-donating compound[10] This is a condition that applies particularly well to $Au_{25}(SR)_{18}^{-}$ clusters, whose formal potential ($E°$) values ($Au_{25}(SR)_{18}^{0}/Au_{25}(SR)_{18}^{-}$ redox couple) are, compared with usual photosensitizers,[10] exceptionally low. In dichloromethane (DCM) containing 0.1 M tetrabutylammonium hexafluorophosphate (TBAH), which is the solvent/electrolyte system generally used to study and compare the electrochemical behavior of metal nanoclusters,[34] the $E°$ of, *e.g.*, the $Au_{25}(SC3)_{18}^{0}/Au_{25}(SC3)_{18}^{-}$ redox couple is -0.171 V (298 K, potentials versus the saturated calomel electrode, SCE),[49] whereas that of the $O_2/O_2^{\ -}$ is -0.85 V (this work). Exciplex formation favors ISC[64-67] by providing a spin-orbit coupling contribution that helps overcoming the spin constrain associated with the $^1O_2 \rightarrow {}^3O_2$ transition.[68]

The easiest way to tune the properties of Au_{25} is to change the capping ligands. Whereas this change does not affect the structure and the absorption spectrum,[18,69] other properties, especially the electrochemical potentials,[34,70] may change appreciably. Finally, the ligands provide a nanoenvironment surrounding the cluster core that determines the effective dielectric constant[70] and porosity of the capping monolayer,[69] and these factors may exert an influence on the quenching mechanisms of the excited states and ultimately the effective singlet-oxygen lifetime. To gain insights into this aspect, we compared the outcome of TREPR measurements carried out on Au_{25} clusters capped by SC3, SC4, and SC2Ph thiolates. The ligand choice was primarily dictated by their ability to change the $E°$ of the $Au_{25}(SR)_{18}^{0}/Au_{25}(SR)_{18}^{-}$ redox couples quite significantly.[70,71]

$Au_{25}(SC4)_{18}^{-}$ and $Au_{25}(SC2Ph)_{18}^{-}$ display TREPR surfaces similar to $Au_{25}(SC3)_{18}^{-}$. Figure 3.6 compares the reinforced absorptive-polarized transient signals observed upon $^1O_2$ photosensitization by $Au_{25}(SC4)_{18}^{-}$, $Au_{25}(SC3)_{18}^{-}$, and $Au_{25}(SC2Ph)_{18}^{-}$ (red, black, and blue traces, respectively). The growth of the polarized signals occurs within 1 μs (that is, a bit faster than for TPP) and the maximum signal intensities are very similar, pointing to similar photosensitization efficiency (in Figure 3.6 the intensities are normalized for the sake of better comparison of the transients). Monoexponential fit to the decay data reveals small, yet clearly detectable differences in the value of k_{Δ}, which increases in the order $Au_{25}(SC2Ph)_{18}^{-}$ (2.17×10^5 s^{-1}, $r^2 = 0.990$) < $Au_{25}(SC3)_{18}^{-}$ (3.02×10^5 s^{-1}, $r^2 = 0.974$) < $Au_{25}(SC4)_{18}^{-}$ (3.69×10^5 s^{-1}, $r^2 = 0.986$); the corresponding lifetimes τ_{Δ} are 4.61(0.05), 3.31(0.05), and 2.71(0.04) μs, respectively. This order indeed matches that of the decreasing $E°$s of the anionic clusters (DCM/0.1 M TBAH, 298 K, E vs SCE), which are -0.077, -0.171, and -0.188 V, respectively.[70,71] These data point to the ease of oxidation (smaller $E°$ value) as an important factor enhancing the cluster quenching ability, and are thus in keeping with the effect noted for other sensitizer families.[10]

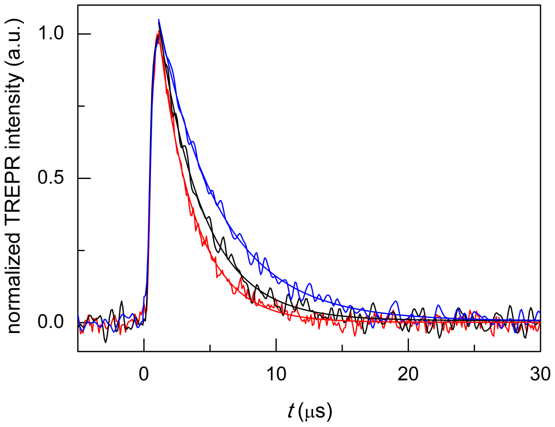

Figure 3.6. TREPR (normalized) transients and corresponding exponential fits to the data for air-saturated toluene solutions of 0.5 mM TEMPONE and 1 mM $Au_{25}(SC4)_{18}^{-}$ (red), $Au_{25}(SC3)_{18}^{-}$ (black), and $Au_{25}(SC2Ph)_{18}^{-}$ (blue). Temperature = 240 K.

3.2.4 Tuning the Photosensitizing Properties of Au_{25} Nanoclusters through Metal Doping.

Overall, these results evidence a detectable effect of the cluster oxidation potential on the singlet-oxygen decay kinetics, and thus confirm an active role of the cluster also as a quencher. With alkanethiolate ligands, however, the potentials cannot be changed substantially.[34,70] A more substantial way to modify the physicochemical properties of gold nanoclusters is by doping their core with other metals. We thus focused on modifying $Au_{25}(SC4)_{18}^{-}$ to prepare the corresponding $Au_{24}M(SC4)_{18}^{0}$ clusters, with M = Hg, Cd. For these metals, monodoping is conveniently accomplished by carrying out the metal exchange on a preformed $Au_{25}(SR)_{18}^{-}$ cluster by using a salt or thiolate of the exogenous metal.[39,71-74] We focused on these two metals because they both dope the cluster on one of the icosahedron positions, as we could demonstrate very recently.[39] While in their neutral state, the resulting $Au_{24}M(SC4)_{18}^{0}$ clusters are diamagnetic and thus match the same magnetic state of anion $Au_{25}(SC4)_{18}^{-}$.

Monodoping affects the HOMO-LUMO gap. The values that can be estimated from the electrochemical peaks are:[39,70] Au, 1.30 eV; Hg, 1.28 eV; Cd, 1.41 eV. Similar differences are found for the optical bandgaps.[39,75] These differences are indeed noteworthy because, for example, a progressive change in the number of carbon atoms from 2 to 12 in $Au_{25}(SCn)_{18}$ does not affect the HOMO-LUMO gap, which remains constant at 1.30 eV.[70] Besides these differences, Hg and Cd doping affects the electrochemical potentials very significantly. In particular, the first oxidation of the $Au_{24}M(SC4)_{18}$ clusters occurs ($E°$ values) at -0.188 (Au), +0.364 (Hg), and +0.332 V (Cd).[39] In electrochemical terms, a positive shift of the first oxidation step by more than 0.5 V is indeed massive.

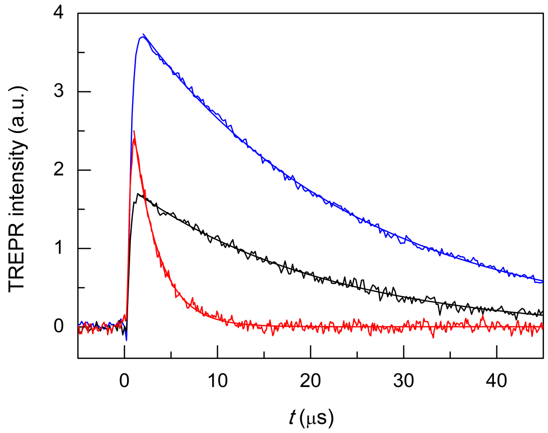

Figure 3.7. Comparison of the TREPR transients and corresponding exponential fit to the data for air-saturated toluene solutions of 0.5 mM TEMPONE and 1 mM $Au_{24}Hg(SC4)_{18}^{0}$ (black), $Au_{24}Cd(SC4)_{18}^{0}$ (blue), and $Au_{25}(SC4)_{18}^{-}$ (red). Temperature = 240 K.

Hg doping induces remarkable changes in the TREPR transients (Figure 7, black trace). First, in $Au_{24}Hg(SC4)_{18}^{0}$ the photosensitization efficiency is about two thirds that of $Au_{25}(SC4)_{18}^{-}$ (red trace). This decrease may be caused by a shorter triplet lifetime, a less efficient cluster-to-oxygen energy transfer to form singlet oxygen, or a lower quantum yield for the formation of the triplet. In this context, an important piece of information is provided in a recent study by Zhu et al. about the excited-state lifetime of similar (R = C2Ph) clusters, as the values determined for $Au_{24}Hg(SC2Ph)_{18}^{0}$ and $Au_{25}(SC2Ph)_{18}^{-}$ are 50 and 100 ns, respectively.[75] The observed TREPR intensities are indeed in rather good agreement with this ratio, and therefore, we may arguably conclude that the efficiency of singlet-oxygen generation is mainly determined by the cluster triplet lifetime. Regarding the hypothesis of a less efficient cluster-to-oxygen energy transfer, we note that the HOMO-LUMO gap of $Au_{24}Hg(SC4)_{18}^{0}$ (1.28 eV) is slightly smaller than for $Au_{25}(SC2Ph)_{18}^{-}$ (1.30 eV): the same should be true also for the corresponding triplet states and this may affect the cluster-oxygen energy transfer, although to a very small extent. Finally, ISC in the cluster should occur on the low ns timescale and very efficiently (Φ_T = 0.87), as evaluated by Wen *et al.* for films of BSA-protected Au_{25} clusters.[76]

The most important effect brought about by the introduction of a single Hg atom, however, is to increase the singlet-oxygen lifetime by more than one order of magnitude: 19.5(0.2) (k_Δ = 5.13 × 10^4 s^{-1}, r^2 = 0.990) vs 2.71 μs (k_Δ = 3.69 × 10^5 s^{-1}), which indicates that the mechanism of $^1O_2$ quenching is much less efficient than for the corresponding Au_{25} cluster. Still, compared with the reference τ_Δ^S of 34.6 μs, the relative τ_Δ decrease is quite significant: 43.6%.

To make the cluster even more performing, the foreign-metal atom should minimize quenching effects without losing the photosensitization efficiency or possibly even increasing it with respect to Au_{25}. The doped cluster should, therefore, exhibit electrochemical properties similar to those of $Au_{24}Hg(SC4)_{18}^0$, a more significant population of the photogenerated triplet state, and ultimately, allow for a longer $^1O_2$ lifetime. A cluster that satisfies these requirements is $Au_{24}Cd(SC4)_{18}^0$, as it is almost as resistant toward oxidation than $Au_{24}Hg(SC4)_{18}^0$ (0.332 V vs + 0.364 V), its HOMO-LUMO gap is the largest of the three SC4 clusters, and according to Zhou et al.[71] its excited-state lifetime (in supposedly aerated solution) is 200 ns (R = C2Ph), *i.e.*, two and four times longer than those of $Au_{25}(SC2Ph)_{18}^-$ and $Au_{24}Hg(SC2Ph)_{18}^0$, respectively. In this regard, it is worth mentioning that TREPR (emission decay lifetime of 0.44(0.01) μs, r^2 = 0.988) points to a higher limit of ~0.3 μs for the lifetime of the triplet of $Au_{24}Cd(SC4)_{18}^0$ under anaerobic conditions (Figure 3.15), as already noted and discussed for $Au_{25}(SC3)_{18}^-$. These general expectations of better performance are fully met: use of the Cd-doped cluster yields a longer singlet-oxygen lifetime (k_Δ = 4.31 × 10^4 s^{-1}, r^2 = 0.999, τ_Δ = 23.2(0.09) μs) than $Au_{24}Hg(SC4)_{18}^0$, a smaller relative τ_Δ decrease (32.9%), and a more significant photosensitization efficiency (Figure 3.7, blue trace). In particular, the maximum intensity of the TREPR signals is ~1.5 times larger than that observed for $Au_{25}(SC4)_{18}^-$ and more than two times larger than that of $Au_{24}Hg(SC4)_{18}^0$. The photosensitization efficiency of $Au_{24}Cd(SC4)_{18}^0$ is significant also in comparison with the TPP photosensitizer, as the TREPR signal intensity of the former is ~1/2 that of TPP. That the amount of triplet excited state obtained from $Au_{24}Cd(SC4)_{18}^0$ is quite significant is also supported by the presence of the negative spike for *t* < 0.5 μs, which, as already commented upon for TPP, is attributed to the Q-RTP component (eq 1).

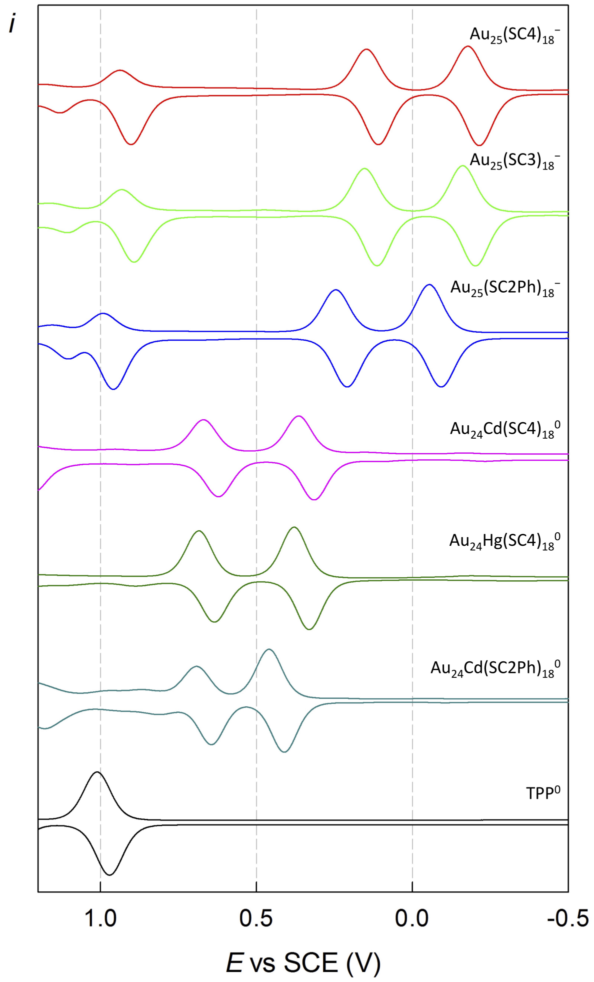

Figure 3.8. Comparison between the DPV curves (oxidation region) of $Au_{25}(SC4)_{18}^{-}$, $Au_{25}(SC3)_{18}^{-}$, $Au_{25}(SC2Ph)_{18}^{-}$, $Au_{24}Cd(SC4)_{18}^{0}$, $Au_{24}Hg(SC4)_{18}^{0}$, $Au_{24}Cd(SC2Ph)_{18}^{0}$, and TPP. Glassy carbon electrode, DCM/0.1 M TBAH, 25 °C.

Finally, we tested the Cd-doped cluster that has an even more positive oxidation potential, $Au_{24}Cd(SC2Ph)_{18}^{0}$, whose *E*° is 0.430 V (vs 0.332 V for $Au_{24}Cd(SC4)_{18}^{0}$).[39] The DPV curves (oxidation region) of all clusters investigated and TPP are gathered in Figure 3.8. Also for this cluster we estimate (Figure 3.16: TREPR emission decay lifetime of 0.44(0.01) μs, r^2 = 0.989) a higher limit of ~0.3 μs for its triplet lifetime under anaerobic conditions. Indeed, the photosensitization outcome further improves (Figure 3.9, blue trace), as the observed singlet-oxygen lifetime is even longer ($k_\Delta = 3.58 \times 10^4$ s^{-1}, $r^2 = 0.997$, τ_Δ = 27.9(0.25) μs). In particular, this τ_Δ value and the relative τ_Δ decrease, 19.3%, are virtually identical to those of TPP (Figure 3.9, black trace), 28.2(0.1) μs and 18.5%, though the latter is more difficult to oxidize by as much as 0.563 V(Figure 3.8). Besides the redox potentials, a comparison between the aforementioned estimated lifetime values (aerobic vs anaerobic conditions) obtained for the Cd-doped clusters and TPP (whose triplet-state lifetime in the absence of oxygen increases by orders of magnitude)[13,62] shows that despite the much shorter intrinsic lifetime of their triplet state, the Cd-doped clusters are perfectly fine to accomplish the $^1O_2$ photosensitization job very efficiently.

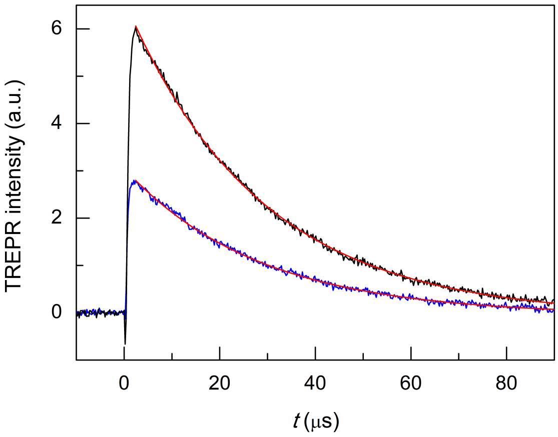

Figure 3.9. TREPR transients and corresponding exponential fit to the data for air-saturated toluene solutions of 0.5 mM TEMPONE and 1 mM $Au_{24}Cd(SC2Ph)_{18}^0$ (blue) and TPP (black). Temperature = 240 K

3.2.5 Chemical Quenching.

To compare further the performance of doped and undoped clusters, we performed photosensitization experiments in the presence of 9,10-diphenylanthracene (DPA), which reacts with singlet oxygen to yield the endoperoxide 9,10-diphenyl-9,10-epidioxyanthracene (DPA-O_2) with rate constants on the order of 10^6 M^{-1} s^{-1}.[77] Its formation can be conveniently monitored through the decrease in the excitation and fluorescence spectra of DPA. Figure 3.10 compares the fluorescence spectra of DPA in air-saturated toluene (at room temperature) containing the photosensitizer $Au_{24}Cd(SC4)_{18}^{0}$ (panel a) or $Au_{25}(SC4)_{18}^{-}$ (panel b) before and after 10 min pulsed irradiation (carried out as in the TREPR experiments) with a 532 nm laser at 240 K (for details, see Experimental section).

For $Au_{24}Cd(SC4)_{18}^{0}$, the strong emission band of DPA at ~430 nm (excitation at 360 nm) is markedly quenched (by 56.9%), which confirms its particular efficiency as a photosensitizer. Instead, when $Au_{25}(SC4)_{18}^{-}$ is used as photosensitizer, only 13.6% quenching of the DPA emission is observed at ~430 nm. The different behavior of the two clusters is also quantitatively detected in the excitation spectra obtained at 450 nm: $Au_{24}Cd(SC4)_{18}^{0}$ causes a strong decrease of the absorption band of DPA (56.9%), whereas the variation is much less significant for $Au_{25}(SC4)_{18}^{-}$ (11.0%) (Figures 3.17 and 3.18). The absorption spectra of the solutions of the two clusters, which only show the optical features of the nanoclusters because its concentration is 100 times larger than that of DPA (the molar extinction coefficients of DPA,[78] $Au_{24}Cd(SC4)_{18}^{0}$, and $Au_{25}(SC4)_{18}^{-}$ are 1.4×10^{4} M^{-1} cm^{-1} (372.5 nm), 4.68×10^{4} M^{-1} cm^{-1} (398 nm) and 4.58×10^{4} M^{-1} cm^{-1} (401 nm), respectively), exhibit no differences before and after laser irradiation (Figures 3.19 and 3.20), thereby pointing to their photostability (no change of the spectrum associated with cluster oxidation) in the given experimental conditions. These results thus show that $Au_{24}Cd(SC4)_{18}^{0}$ is a significantly better photosensitizer than $Au_{25}(SC4)_{18}^{-}$, in full agreement with the TREPR results.

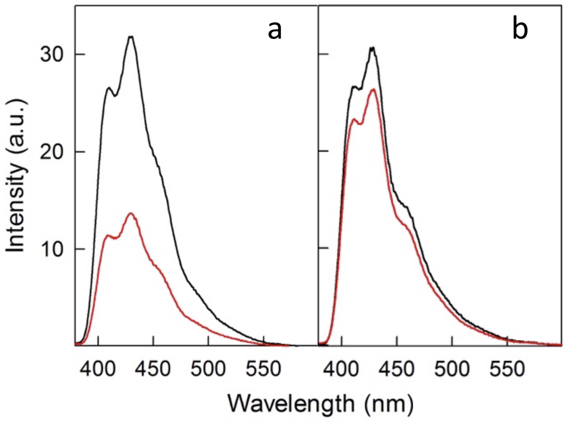

Figure 10. Emission spectra (λ_{exc} = 360 nm) of 1.3 x 10^{-3} mM DPA in aerated toluene containing 0.13 mM (a) $Au_{24}Cd(SC4)_{18}^0$ or (b) $Au_{25}(SC4)_{18}^-$. The spectra correspond to before (black) and after 10 min irradiation (red) at 532 nm at 240 K. The spectra were obtained at room temperature.

3.2.6 Mechanism of Physical Quenching by Au Nanoclusters.

The sequence of the observed τ_Δ values is in very good agreement with the cluster oxidation potentials (Figure 3.11).

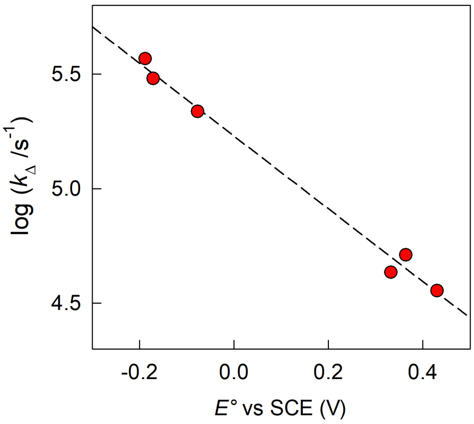

Figure 3.11. Dependence of the $^1O_2$ quenching rate constant k_Δ on the formal potentials for the oxidation of the clusters. The dashed line shows the linear fit to the data.

Due to the aforementioned reasons, eq 5 can be effectively simplified to eq 6:

(6) $k_{\Delta} = k_{nr}[S] + k_{q}[M]$

k_q can thus be obtained from the k_{Δ} value determined experimentally and the $k_{nr}[S]$ term, which can be calculated from literature data[56] to be 2.89 x 10^4 s^{-1} at 240 K. According to the CT-ISC mechanism, the quenching process involving $^1O_2$ and the molecular Au nanocluster (M) can be summarized by eqs 7-9:

$$^1O_2 + M \underset{k_{-d}}{\overset{k_d}{\rightleftharpoons}} \left(^1O_2\,,\,M\right) \tag{7}$$

$$\left(^1O_2\,,\,M\right) \underset{k_{-CT}}{\overset{k_{CT}}{\rightleftharpoons}} {}^1\!\left(O_2^{\delta-}\,,\,M^{\delta+}\right) \tag{8}$$

$${}^1\!\left(O_2^{\delta-}\,,\,M^{\delta+}\right) \xrightarrow{k_{ISC}} {}^3\!\left(O_2^{\delta-}\,,\,M^{\delta+}\right) \xrightarrow{k_{-d}} {}^3O_2 + M \tag{9}$$

$$\left(^1O_2\,,\,M\right) \underset{k_{-PET}}{\overset{k_{PET}}{\rightleftharpoons}} \left(O_2^{-\bullet}\,,\,M^{+\bullet}\right) \xrightarrow{k_{-d}} O_2^{-\bullet} + M^{+\bullet} \tag{10}$$

$$\left(O_2^{-\bullet}\,,\,M^{+\bullet}\right) \xrightarrow{k_{-ET}} \left(^3O_2\,,\,M\right) \xrightarrow{k_{-d}} {}^3O_2 + M \tag{11}$$

There, k_d and k_{-d} are the diffusion rate constants for the formation and dissociation of the caged species, k_{CT} and k_{-CT} are the forward and backward rate constants of the transfer of a partial charge δ between the caged $^1O_2$,M species, and k_{ISC} is the rate constant for ISC in the exciplex.

Reactions 10 and 11 can be seen as competitive to the sequence 8-9 in quenching $^1O_2$: whereas k_{PET} and k_{-PET} are the forward and backward rate constants for the oxidation of the cluster by $^1O_2$ (that is, the possibility of recrossing to the excited donor surface included), k_{-ET} is the backward rate constants for the ET between M and $^3O_2$ (that is, charge recombination). It should be noted that eqs 7-11 are generically written for two neutral species. Whereas this is valid for the doped clusters, for $Au_{25}(SR)_{18}^-$ the negative charge of the cluster must be taken into account in eqs 7-11. The fact that the cluster may carry a charge does not prevent the formation of the exciplex, as shown very recently for a cationic excited state acceptor.[79] Charge-transfer activation of oxygen by both anionic and neutral gold nanoclusters has been described.[80,81] Very recent mass spectrometry results would indeed point to an effective interaction of oxygen and $Au_{25}(SC2Ph)_{18}^{-}$, at least in DCM.[82]

We first focus on the quenching caused by the irreversible ISC inside the solvent cage (the competition by the ET path, eqs 10 and 11, will be discussed later). Applying the steady-state approximation to the encounter complex and the singlet exciplex leads to the following expression (eq 12) for the k_q term in eq. 5:

$$(12)\quad k_q = \frac{k_d}{1 + \frac{k_{-d}}{k_{CT}} + \frac{k_{-d}}{k_{ISC}} \exp\left(\frac{\Delta G°_{CT}}{RT}\right)}$$

We start by considering $Au_{25}(SC4)_{18}^{-}$, which exhibits the less positive oxidation potential and the fastest quenching rate, and then we will discuss the differences caused by making the cluster oxidation more difficult. For this cluster, k_{Δ} = 3.69 x 10^5 s^{-1}. The term k_q[M] can be obtained from eq 6 by subtracting the rate constant for the intrinsic $^1O_2$ lifetime (τ_{Δ}^{S} = 34.6 μs, $k_{\Delta}^{S} = k_{nr}[S]$ = 2.89 x 10^4 s^{-1}). Hence, a value of k_q = 3.40 x 10^8 $M^{-1}s^{-1}$ is calculated by taking into account that [M] = 1 mM.

The diffusion rate constant k_d is calculated with the Smoluchowski equation, $k_d = 4pN_A(D_O + D_M)(r_O + r_M)$, where N_A is the Avogadro number, and r_O and r_M are the radii of O_2 (1.73 Å)[10] and $Au_{25}(SC4)_{18}^{-}$ (9.4 Å).[70] As to the diffusion coefficients, D_O can be estimated from a correlation with the solvent viscosity η, $D = (2.6 \times 10^{-7})\,\eta^{-2/3}$;[83] use of 1.39 centipoise for the toluene's viscosity at 240 K[84] yields D_O = 2.1 x 10^{-5} cm^2 s^{-1}. For the much larger cluster, the use of the Stokes-Einstein equation ($D = k_BT/6\pi\eta r_M$, where k_B is the Boltzmann constant) is licit and yields D_M = 1.35 x 10^{-6} cm^2 s^{-1}. Hence, k_d = 1.9 x 10^{10} M^{-1} s^{-1}. The equilibrium constant for cage formation (K_d) can be calculated according to the Debye equation,[85,86] which for the specific case is $K_d = 4\pi N_A(r_O + r_M)^2\delta r/1000$. By using for δr the typical value of ~1 Å,[87] K_d and k_{-d} are calculated to be 0.94 M^{-1} and 2 x 10^{10} s^{-1}, respectively.

The equilibrium constant K_{CT}, and thus $\Delta G°_{CT}$, is unknown. However, $\Delta G°_{CT}$, which refers to the transfer of the charge fraction δ, is conceivably related to $\Delta G°_{ET}$,[10] which refers to the full ET between the cluster and singlet oxygen (eq

10). k_{CT} may be similarly estimated (eq 13) using a Marcus expression for the activation free energy $\Delta G^{\neq}_{\mathrm{CT}}$ (eq 14). The process is considered as adiabatic and thus occurring at contact distance between singlet oxygen and the cluster, as supported by recent results.[80-82]

(13) $k_{\mathrm{CT}} = Z \exp[-\Delta G^{\neq}_{\mathrm{CT}}/RT]$

(14) $\Delta G^{\neq}_{\mathrm{CT}} = \Delta G_0^{\neq}{}_{\mathrm{CT}}\,[1+ (\Delta G^{\circ}_{\mathrm{CT}}/4\Delta G_0^{\neq}{}_{\mathrm{CT}})]^2$

Z is estimated (eq 15) by taking into account the role of solvent friction in determining the rate of crossing the barrier.[88]

(15) $Z = \dfrac{1}{\tau_L}\left(\dfrac{\Delta G^{\neq}_{0CT}}{4\pi RT}\right)^{\frac{1}{2}}$ with $\tau_L = \dfrac{\varepsilon_\infty}{\varepsilon_s}\tau_D$ and $\tau_D = \dfrac{4\pi\eta r^3}{k_B T}$

There, τ_{L} is the longitudinal relaxation time, τ_{D} is the Debye relaxation, and ε_{S} and ε_∞ are the static and high-frequency permittivities. For toluene at 240 K, τ_{L} was estimated from the linear temperature dependence of the two permittivities[89] and using for the average molecular radius of toluene, r, the value obtained from its density.

$\Delta G_0^{\neq}{}_{\mathrm{CT}}$ is the intrinsic barrier, that is, the value of $\Delta G^{\neq}_{\mathrm{CT}}$ at zero driving force. In analogy to the ET intrinsic barrier ($\Delta G_0^{\neq}{}_{\mathrm{ET}}$), $\Delta G_0^{\neq}{}_{\mathrm{CT}}$ can be seen as composed of a solvent reorganization term, $\Delta G_{0,\mathrm{s}}^{\neq}{}_{\mathrm{CT}}$, and an inner component, $\Delta G_{0,\mathrm{i}}^{\neq}{}_{\mathrm{CT}}$, which describes the molecular deformation of bond lengths and bond angles of the reacting system. For a full ET,[86,87] $\Delta G_0^{\neq}{}_{\mathrm{ET}}$ can be calculated from the homogeneous self-exchange $(\Delta G_0^{\neq}{}_{\mathrm{ET}})_{\mathrm{hom,ex}}$ values of the two redox couples (here, $\mathrm{M}^{\bullet+}/\mathrm{M}$ and $^1\mathrm{O}_2/\mathrm{O}_2^{\bullet-}$), that is (eq 16):

(16) $\Delta G_0^{\neq}{}_{\mathrm{ET}} = [(\Delta G_0^{\neq}{}_{\mathrm{ET}})_{\mathrm{hom,ex,M}\bullet+/\mathrm{M}} + (\Delta G_0^{\neq}{}_{\mathrm{ET}})_{\mathrm{hom,ex,O2/O2}\bullet-}]/2$

The two $(\Delta G_0^{\neq}{}_{\mathrm{ET}})_{\mathrm{hom,ex}}$ values can be estimated from the corresponding standard heterogeneous rate constants through equation 17:[90]

(17) $(\Delta G_0^{\neq}{}_{\mathrm{ET}})_{\mathrm{het}} = 2.391 + 0.528\ (\Delta G_0^{\neq}{}_{\mathrm{ET}})_{\mathrm{hom,ex}}$

For the cluster, we use the electrochemical $(\Delta G_0^{\neq}{}_{\mathrm{ET}})_{\mathrm{het}} = 0.222$ eV, which was obtained in DCM/0.1 M TBAH, at 298 K from the standard heterogeneous rate constant,[69] using $k^{\circ}_{\mathrm{het}} = Z_{\mathrm{el}} \exp[-(\Delta G_0^{\neq}{}_{\mathrm{ET}})_{\mathrm{het}}/RT]$ with $Z_{\mathrm{el}} = (RT/2\pi M)^{1/2}$ (M = molar mass). For $^1\mathrm{O}_2/\mathrm{O}_2^{\bullet-}$ and under the assumption that the intrinsic barriers of $^1\mathrm{O}_2/\mathrm{O}_2^{\bullet-}$ and $^3\mathrm{O}_2/\mathrm{O}_2^{\bullet-}$ are the same, we obtained $(\Delta G_0^{\neq}{}_{\mathrm{ET}})_{\mathrm{het}} = 0.408$ eV by cyclic-voltammetry analysis of the oxygen reduction peak, as described in the Experimental. The solvent intrinsic barrier $\Delta G_{0,s}{}^{\neq}{}_{ET}$ depends on both solvent and temperature through the Pekar factor, $\varepsilon_{op}{}^{-1}$ - $\varepsilon_{S}{}^{-1}$, where ε_{op} is the optical (usually taken as n^2, where n = refractive index) dielectric constant, whereas the inner component $\Delta G_{0,i}{}^{\neq}{}_{ET}$ can be considered as essentially independent. The corresponding solvent intrinsic barrier values, were obtained from the empirical equation $(\Delta G_{0,s}{}^{\neq}{}_{ET})_{het} = 0.604/r$ (were r = molecular radius).[90] $(\Delta G_{0,i}{}^{\neq}{}_{ET})_{het}$ is thus obtained by subtracting $(\Delta G_{0,s}{}^{\neq}{}_{ET})_{het}$ from the intrinsic barrier. For both species, we use a heuristic approach in which $(\Delta G_{0}{}^{\neq}{}_{ET})_{het}$ is transformed into a toluene/240 K intrinsic barrier by using the same $(\Delta G_{0,i}{}^{\neq}{}_{ET})_{het}$ value and the $(\Delta G_{0,s}{}^{\neq}{}_{ET})_{het}$ corrected for the ratio between the appropriate Pekar factors (using the temperature dependence of ε_{op} and ε in toluene). Use of eqs 17 and then 16 yields for the $^1O_2/Au_{25}(SC4)_{18}{}^-$ system a value of $\Delta G_{0}{}^{\neq}{}_{ET}$ = 0.18 eV. It is worth mentioning that for DCM at 298 K, $\Delta G_{0}{}^{\neq}{}_{ET}$ is much larger (0.40 eV): this reflects the fact that the very low polarity of toluene makes the solvent reorganization term very small, with the result that the already significant inner reorganization of Au_{25} clusters[69-71,91] and possibly oxygen[92] becomes largely dominant (~94%).

Both k_{CT} and K_{CT} require calculating $\Delta G°_{ET}$ and how to relate it to $\Delta G°_{CT}$. Additionally, k_{CT} requires converting $\Delta G_{0}{}^{\neq}{}_{ET}$ into $\Delta G_{0}{}^{\neq}{}_{CT}$. For $^1O_2$ quenching $\Delta G°_{CT}$ is usually taken as a fraction f of $\Delta G°_{ET}$,[10] to account for the partial character δ of ET in the formation of the exciplex. $\Delta G°_{ET}$ can be estimated according to Rehm and Weller,[93,94] using eq 18. Because the process here considered involves a neutral and a charged species, $^1O_2/Au_{25}(SC4)_{18}{}^-$, the Coulombic term associated with formation of charges is zero (the full ET process is a charge shift). In eq 18, the actual charge of the cluster is explicit.

(18) $\Delta G°_{ET} = nFE°(M^{\bullet}/M^-) - nFE°(O_2/O_2{}^{-\bullet}) - E_{exc}$

There, n is the number of exchanged electrons (for a full ET, n = 1), F is the Faraday constant, $E°(M^{\bullet}/M^-)$ and $E°(O_2/O_2{}^{-\bullet})$ are the formal potentials of the $M^{\bullet}/M^-$ and oxygen/superoxide redox couples, respectively. E_{exc} = 94 kJ mol^{-1} is the $^3\Sigma_g$ to $^1\Delta_g$ excitation energy (the entropy difference between the ground and excited states is neglected). Eq 18 (also including the Coulombic term) provides a reasonable estimate of $\Delta G^{\circ}_{\mathrm{ET}}$: using the powerful phase-modulated voltammetry technique,[95] Jones and Fox[96] found that the actual excited-state redox potentials are roughly consistent with the estimates from the Rehm-Weller approach. In the present case, the excited species, $^1O_2$, is the same for all clusters and thus any error would be systematic. $E^{\circ}(^1O_2/O_2^{-\bullet})$ will be taken as $E^{\circ}(O_2/O_2^{-\bullet}) - E_{\mathrm{exc}}/F = -0.850 + 0.975 = 0.125$ V (DCM/0.1 M TBAH). The E° values of the clusters refer to DCM, whose dielectric constant ($\varepsilon = 9.1$, or 12.5 if the presence of the supporting electrolyte is included)[70] is not much larger than that of toluene ($\varepsilon = 2.4$). This is a mild approximation, especially if one considers that these calculations are generally performed using E° values obtained in polar solvents,[10] such as acetonitrile ($\varepsilon = 37.5$), which introduces a quite severe approximation when used for processes carried out in low-polarity solvents. It should be also noted that due to the presence of the permeable monolayer protecting the cluster,[69] the effective dielectric constant ($\varepsilon_{\mathrm{eff}}$) experienced by the gold core and the nearby oxygen molecule is (i) smaller than that of DCM (for SC3, we estimated $\varepsilon_{\mathrm{eff}} = 7.7$)[70] and, for the same reason, (ii) slightly larger than that of toluene, 2.4, as the ligands provide a intrinsic contribution to $\varepsilon_{\mathrm{eff}}$ of 3-3.6.[70] This kind of nanoenvironment is obviously not encountered for common sensitizers.

As to the fraction f of $\Delta G^{\circ}_{\mathrm{ET}}$, it has been proposed that $\delta \sim f^{1/2}$, as inferred from experimental trends involving neutral donors.[10] Because of the charge here involved, however, we will use a linear dependence in which δ simply replaces $n = 1$ in eq 18. Hence:

(19) $\Delta G^{\circ}_{\mathrm{CT}} = \delta F[E^{\circ}(M^{\bullet}/M^{-}) - E^{\circ}(^1O_2/O_2^{-\bullet})]$

Regarding the conversion of $\Delta G_0{}^{\neq}{}_{\mathrm{ET}}$ into $\Delta G_0{}^{\neq}{}_{\mathrm{CT}}$, we consider that $\Delta G_0{}^{\neq}{}_{\mathrm{ET}}$ is the sum of $\Delta G_{0,s}{}^{\neq}{}_{\mathrm{ET}}$ and $\Delta G_{0,i}{}^{\neq}{}_{\mathrm{ET}}$. The former depends on the square of the exchanged charge (the electron). The latter arguably follows a similar dependence: the ET takes to a new equilibrium position of the relevant nuclei, and the inner reorganization is described as a parabolic function of the nuclear displacement. $\Delta G_0{}^{\neq}{}_{\mathrm{CT}}$ can thus be estimated as $\Delta G_0{}^{\neq}{}_{\mathrm{CT}} \sim \delta^2 \Delta G_0{}^{\neq}{}_{\mathrm{ET}}$.

At this point, k_{CT} can be obtained from the appropriate preexponential factor (eqs 13 and 15, with Z = 9.47 x 10^9 s^{-1}), provided a reasonable δ value is used for eq 19. δ is, in fact, unknown. We will follow an approach similar to that used for other series of photosensitizers.[10,66,67] In ETs, the transfer coefficient α is introduced to describe how the activation free energy responds to changes in the reaction driving force, that is, $\alpha = d\Delta G^{\neq}_{ET}/d\Delta G°_{ET} = -RT d\ln k_{ET}/d\Delta G°_{ET}$. Because of the quadratic expression relating $\Delta G^{\neq}_{ET}$ to $\Delta G°_{ET}$, α is expected to be 0.5 at zero driving force.[87] We will focus on the three Au_{25} clusters, which are self-consistent in terms of cluster charge. The corresponding driving forces for ET (eq 18) range from -0.312 (SC4) and -0.201 (SC2Ph) eV, that is, these processes are exergonic yet not too far from $\Delta G°_{ET}$ = 0. The corresponding $\log k_q$ vs $\Delta G°_{ET}$ provides a slope corresponding to the very small α value of 0.10. Adjusting δ in eq 19, shows that α ~ 0.5 is obtained when δ = 0.2. This corresponds to $\Delta G°_{CT}$ values ranging from -0.06 to -0.04 eV. This value of δ is indeed quite similar to values previously proposed for $^1O_2$ quenching by other photosensitizers,[10,66,67] although we should note that δ should decrease as the reaction free energy becomes more positive,[79] which is the actual situation valid for all other photosensitizers (due to the much more positive oxidation potentials) so far used.[10]

The use of δ = 0.2, allows defining all remaining quantities in eq 12. Hence, an experimental rate constant (SC4) of k_q = 3.40 x 10^8 $M^{-1}s^{-1}$, corresponds to $\Delta G°_{CT}$ = -0.06 eV, k_{CT} = 5.9 x 10^9 s^{-1}, and k_{ISC} = 3.9 x 10^8 s^{-1}. For common photosensitizers, ISC is also a fast process, with rate constant values estimated to be ~5 x 10^9 s^{-1} and mildly increasing as the CT process becomes more favored.[66] Despite the several inputs and assumptions, this kinetic analysis would point to the same CT-ISC mechanism proposed for $^1O_2$ quenching by other photosensitizers.

On the other hand, Au_{25} clusters provide unprecedented negative free energies for ET. This situation may indeed make the reactions 10,11 competitive to reactions 8,9. Indeed, we already noted that for long times some oxidation of the $Au_{25}(SC4)_{18}^-$ cluster takes place, which point to the occurrence of reaction 10.

The quantities already estimated, allow us to estimate this possible competition. The resulting relevant rate constants are k_{PET} = 5.9 x 10^8 s^{-1}, k_{-ET} = 9.0 x 10^9 s^{-1}. Both ETs can be considered as irreversible because the corresponding k_{-PET} and k_{ET} are 1.6 x 10^2 and 1.1 x 10^{-4} s^{-1}, respectively, and thus escape from the cage is much faster. The process described in eq 11, which is essentially rate limited by k_{PET}, corresponds to an ET-induced ISC, that is, is the equivalent of eq 9. Because of the many assumptions involved, all these rate-constant values should be considered only as estimates. A comparison with the actual k_q (assuming that only eqs 7 and 10 are kinetically relevant) indeed shows that k_{PET} is overestimated. For example, a slight increase of the intrinsic barrier for the ET in eq 10 by, say, 0.04 eV, would decrease k_{PET} by a factor of ~5. However, it is quite interesting that the ET path of eqs 7,10, and 11 provides a rate comparable to the observed quenching rate. Most probably, the mechanism involves a competition of the two paths.

A final comment regards the spin constrains. For the complete ET pathway, the triplet-singlet spin transition rate is particularly important for the overall quenching rate constant. Indeed, spin-forbidden transitions can be 4-6 orders of magnitude slower than the corresponding allowed transition,[97] and this may affect the back ET in eq 11. Both species are radical and, thus, while in the cage exchange interaction between them takes place, giving rise to non-degenerate singlet and triplet states (spin-correlated radical pair). In our case, the singlet state has a higher energy and, as the precursor is a singlet ($^1O_2$), it is initially more populated. Although a more extensive analysis could be carried out[97] and the back ET rate constant should be considered as an upper limit, the rate is still large enough to make $^3O_2$ formation very probable, with some competition from cage dissociation in eq 10. Overall, we thus conclude that for Au_{25} clusters both quenching mechanisms are competitive.

For the doped clusters, there is no competition by eqs 10,11, as the ET is unfavored, with k_{PET} dropping by orders of magnitude. Determining the value of k_{ISC}, however, is very complicated because $\Delta G°_{CT}$ in eq 19 requires adding the Coulombic term, as two opposite charges form. In principle, this correction could be performed according to Rhem-Weller,[93,94] which consider this term as negative (stabilization of the opposite charges). However, this view has been recently shown to be incorrect for photoinduced ETs. Due to desolvation, the free energies of contact radical ion pairs are 0.06 eV higher (instead of lower by -0.06 eV) in acetonitrile than those of the solvated radical ions.[98] This difference should increase further in low-polarity solvents. Using eq 12 to estimate k_{ISC}, therefore, would introduce further, significant approximations. Indeed, whereas the effect on k_{ISC} may be small,[66] the effect on k_{CT} should be more relevant. To conclude, we believe that the issue of the Coulombic term would require more extensive investigation and analysis based on a larger series of neutral clusters, including further estimates of δ as a function of the resulting CT free energy.

Regardless, the sequence of the observed τ_Δ values illustrated in Figure 3.11 demonstrates that the Au_{25} clusters can be good photosensitizers and their efficiently as singlet oxygen quencher can be nicely modulated through proper changes of ligands and doping metals. We expect that an even more positive $E°$ would allow us to obtain even better results, and possibly reach the physiological limit of τ_Δ^{S} = 34.6 μs, i.e., no physical quenching by the cluster. According to Figure 3.11, whose linear fit has the good r^2 value of 0.990, the "ideal" cluster should have an oxidation potential at least more positive than ~0.49 V. This target is indeed reachable through proper selection of the ligands to cap a cluster of the $Au_{24}Cd(SR)_{18}^{0}$ family, which appears to have the longest triplet lifetime, as we already discussed.

3.3 Experimental Section

The syntheses of the undoped and doped clusters were carried out as described previously.[39,48-50]

For the CWEPR measurements, we used a continuous wave Bruker ER200D X-band spectrometer. The spectra were recorded with 100 KHz field modulation, 20 dB of 200 mW microwave power, 0.10 mT modulation amplitude, 10.24 ms time constant, and 81.92 ms conversion time. The sample solutions were placed in a 4 mm outer-diameter (o.d.) quartz tubes. To remove oxygen from the samples, the solutions were carefully degassed by several freeze-pump-thaw cycles, and sealed under vacuum conditions (10^{-3} Torr).

For the TREPR measurements, a pulsed laser beam from a Nd:YAG laser (Quantel Brilliant, pulse length 5 ns, pulse energy 5 mJ, pulse repetition rate 20 Hz) was used for the optical excitation of the samples at 532 nm. At this wavelength, the absorption of all $Au_{24}M(SR)_{18}$ clusters is significantly larger than for nitroxides. The measurements were carried out by using a Bruker ER200D (X-band) spectrometer with an extended detection bandwidth (6 MHz), disabling the magnetic field modulation, and working in a direct detection mode. The temperature of the sample inside the EPR cylindrical cavity (8 mm optical access) was controlled to 240 K by a variable-temperature nitrogen flow system. The time-dependent EPR signals were digitized using a digital oscilloscope (LeCroy Model LT344) with a maximum acquisition rate of 500 megasample/s synchronized with the laser pulse. The time resolution of the instrument was ~150 ns. Data collection was performed with a personal computer and software that allowed controlling the magnetic field and setting the digital oscilloscope. Typically, 300 transient signals were averaged at on-resonance conditions and subtracted from those accumulated off-resonance to eliminate the background signal induced by the laser pulse. A complete two-dimensional data set that shows the EPR signal as a function of both time and magnetic field consists typically of a set of transient signals, containing 500 points each, recorded at 128 different magnetic field positions. The 500 × 128 matrix gave a two-dimensional time/field data set from which the transient spectra were extracted.

The inversion recovery EPR experiments were performed using a pulsed Bruker ER580 X-band spectrometer. The solutions of the samples were placed in 3 mm o.d. quartz tubes. A two-pulse inversion recovery pulse sequence was used. In this experiment the direction of the net magnetization of TEMPONE is initially switched by a π pulse from $+z$ to $-z$. After a variable delay time t, a $\pi/2$ pulse brings the magnetization to the xy plane and a free induction decay (FID) signal is detected. By plotting the FID amplitude *vs* t, one obtains the inversion recovery curve, which represents the recovery of the inverted z component of the magnetization to the thermal equilibrium. The initial time interval *t* between the first π pulse and second π/2 pulse was 200 ns. The π/2 pulse length of 32 ns was chosen to avoid spin diffusion phenomena, after checking that the recovery curves did not change by further increasing the pulse length. The field value was set at the maximum of the central hyperfine line of the integrated CW-EPR spectrum of TEMPONE (corresponding to the 0 value in the first derivative spectrum). The inversion recovery curve was obtained plotting the area of the FID *vs* the time interval. We recorded 1024 points corresponding to different *t* values, with a time step Δ*t* of 4 ns. 300 FIDs were recorded and averaged for each *t* value. A time delay of 1500 μs was set between each pulse sequence to allow the full recovery of magnetization. To obtain the T1 value, a single exponential function was fit to the FID amplitude vs. *t* curves.

The UV-vis absorption spectra of the clusters were obtained in toluene with a Thermo Scientific Evolution 60S spectrophotometer. The spectra were recorded with a spectral resolution of 0.5 nm. The samples were either diluted to 0.2 mM (photostability experiments related to the TREPR experimental conditions) or used as such (0.13 mM, excitation/emission experiments) in 1 mm cuvettes. The extent of oxidation was determined through analysis of the derivative UV-vis spectrum at 390 nm.[51]

Emission spectra were recorded at room temperature in aerated toluene solutions in 1-mm quartz cuvettes with a FluoroMax-3 spectrofluorometer (HORIBA). A front-face configuration (tilted angle of 60°) was used to acquire the emission spectra and an average of average of three independent measurements was performed for each sample. The concentration of $Au_{25}(SC4)_{18}^{-}$ and $Au_{24}Cd(SC4)_{18}^{0}$ was adjusted by using the absorbance spectrum and the pertinent molar extinction coefficient, that is, 4.58×10^4 $M^{-1}cm^{-1}$ (398 nm) and 4.68×10^4 M^{-1} cm^{-1} (401 nm) respectively. Each experiment was carried out by using a freshly prepared 300 μl toluene solution of 1 mM nanocluster and 0.01 mM DPA in a 3 mm o.d., 2 mm inner diameter EPR glass tube. The sample was cooled to 240 K and irradiated with the Nd:YAG laser used for the TREPR experiments at a wavelength of 532 nm for 10 min. The solution was let to reach room temperature and was then diluted (30 µl in 200 µl toluene) in a 1 mm optical-path length quartz cuvette before recording the absorption, emission and excitation spectra. Dilution was meant to minimize the inner filter effects due to the strong absorbance of the nanoclusters in the same optical region of the DPA emission, i.e., 400-500 nm. The optical measurements were recorded 30 min after the laser irradiation.

The DPV and CV measurements were carried out in DCM/0.1 M TBAH, under an Ar atmosphere, in a glass cell, at 25 °C. For DPV we used a CHI 660c electrochemical workstation, whereas for the electrode kinetics CV experiments we used an EG&G-PARC 173/179 potentiostat-digital coulometer, an EG&G-PARC 175 universal programmer, and a Nicolet 3091 12-bit resolution digital oscilloscope. The working electrode was a glassy carbon microdisk (9.1×10^{-4} cm^2), prepared and activated as already described.[99] The counter-electrode was a Pt wire. A silver wire, which was kept in a tube filled with the same electrolyte solution and separated from the main compartment by a Vycor frit, served as a quasi-reference electrode. At the end of the experiments, its potential was calibrated after addition of ferrocene, as the ferricenium/ferrocene redox couple has $E°$ = 0.460 V (SCE) in DCM/0.1 M TBAH. All potential values are reported against SCE. Standard DPV parameters were employed: peak amplitude = 50 mV, pulse width = 0.05 s, increments per cycle = 2 mV, pulse period = 0.1 s. For CV, we applied the positive feedback correction to minimize the ohmic drop between the working and the reference electrodes. The standard heterogeneous rate constant, $k°_{\text{het}}$, for oxygen reduction on a glassy carbon electrode was determined by analysis of the CVs obtained at various scan rates (v). In DCM/TBAH 0.1 M the separation between the cathodic and anodic peak potentials is large also at low v values (*e.g.*, 0.228 V at 0.2 V s^{-1}) pointing to a small $k°_{\text{het}}$ value. The latter was determined by digital simulation of the experimental CVs. For digital simulation, we used the DigiSim 3.03 software, using a step size of 1 mV and an exponential expansion factor of 0.5.

3.4 Supporting Information

Chemicals. $HAuCl_4\cdot 3H_2O$ (Aldrich, 99.9%), $Hg(NO_3)_2$ (Sigma-Aldrich, ^{3}99.99%), $Cd(NO_3)_2$ (Carlo Erba Reagents, 99%), tetra-*n*-octylammonium bromide (Aldrich, 98%), *n*-propanethiol (Aldrich, 99%), *n*-butanethiol (Aldrich, 99%), phenylethanethiol (Aldrich, ^{3}99%), $NaBH_4$ (Aldrich, 99%), tetrahydrofuran (THF, Sigma-Aldrich, 99.9%), toluene (Sigma-Aldrich, 99.7%), diethyl ether (Sigma-Aldrich, 99.8%), methanol (Aldrich, 99.8%), triethylamine (Sigma-Aldrich, ^{3}99%), 2,2,6,6-tetramethyl-4-oxo-1-piperidinyloxy (TEMPONE, Aldrich), 9,10-diphenylanthracene (DPA, Alfa Aesar, 99%), *meso*-tetraphenylporphyrin (TPP, Sigma-Aldrich ≥99%, were used as received. For electrochemistry, dichloromethane (DCM anhydrous, Sigma-Aldrich, ^{3}99.8%) was stored under an argon atmosphere. Tetra-*n*-butylammonium hexafluorophosphate (Fluka, 99%) was recrystallized from ethanol. Low conductivity water was milliQ Water pro analysis (Merck). Column chromatography was carried out using silica gel from Macherey-Nagel (MN-Kieselgel 60 M, 230-400 mesh).

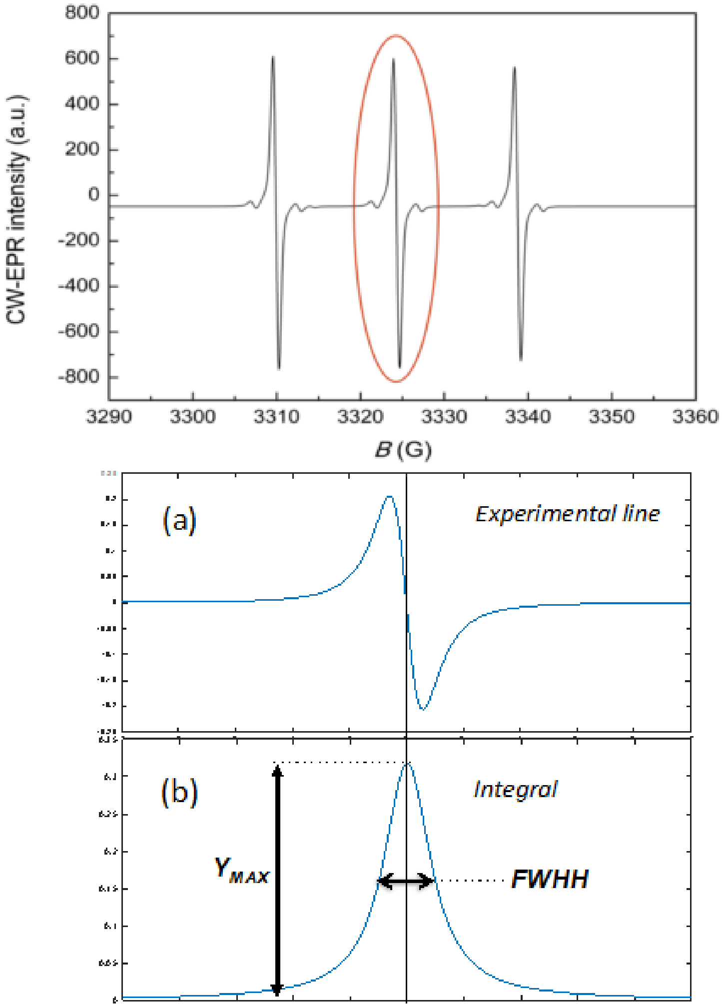

Figure 3.12. Determination of T2 from the reciprocal of the full-width-at-half-height (FWHH) of the integral of the CWEPR spectrum. The central line of the CWEPR spectrum of TEMPONE (top) is analyzed by transforming the experimental line (a) into its integral (b). The full-width-at-half-height is obtained by simulating the peak as a Lorentzian curve.

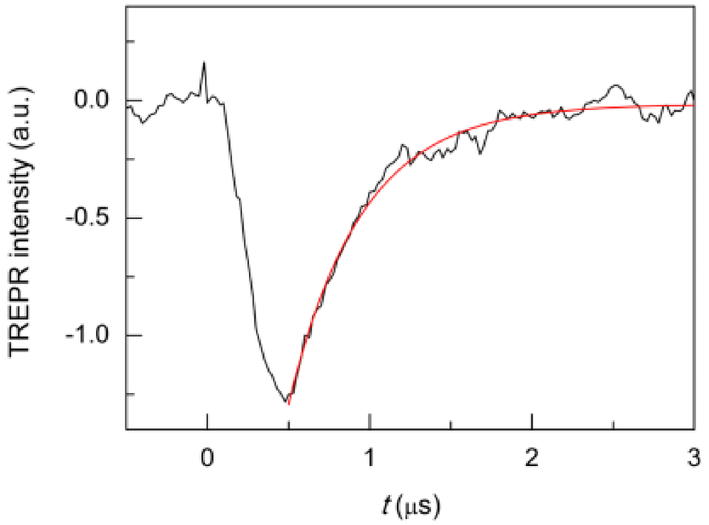

Figure 3.13. TREPR transient of the emission-polarized signal (average of the three signals) observed for 1 mM $Au_{25}(SC3)_{18}^{-}$ and 0.5 mM TEMPONE in toluene under anaerobic conditions (black), with monoexponential fit to the data (red).

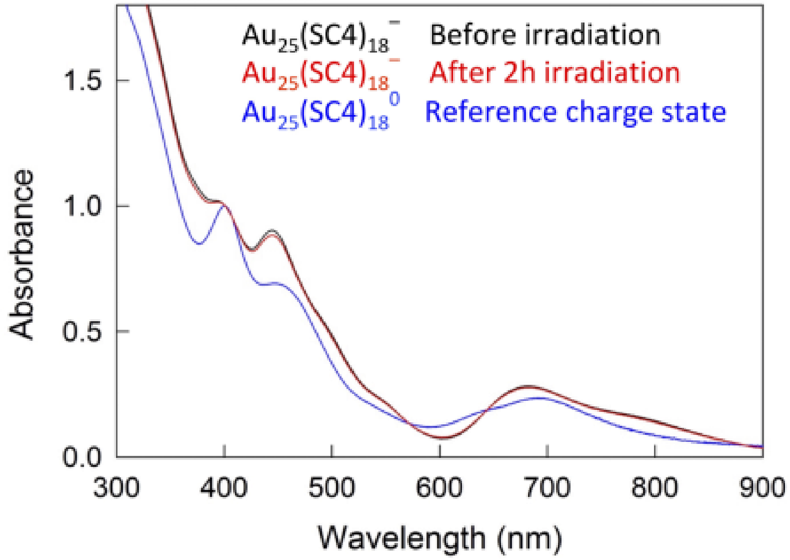

Figure 3.14. UV–Vis absorption spectra of $Au_{25}(SC4)_{18}^{-}$ in toluene in the presence of TEMPONE (1:0.5) before irradiation (black) and after 2 h irradiation (red). The blue trace shows the spectrum of pure $Au_{25}(SC4)_{18}^{0}$. The irradiation was carried out on a 1 mM $Au_{25}(SC4)_{18}^{-}$ solution, whereas for obtaining the optical spectra the samples were diluted to 0.2 mM. 1 mm quartz cuvette, room

temperature. The spectra were normalized to obtain A = 1 at 400 nm. The extent of oxidation, 8.8%, was calculated by using the absorbance derivative at 390 nm, according to a method previously developed.

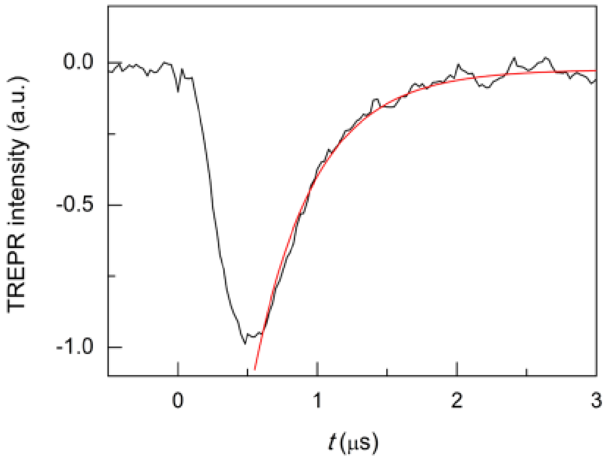

Figure 3.15. TREPR transient of the emission-polarized signal (average of the three signals) observed for 1 mM $Au_{24}Cd(SC4)_{18}^0$ and 0.5 mM TEMPONE in toluene under anaerobic conditions (black), with monoexponential fit to the data (red).

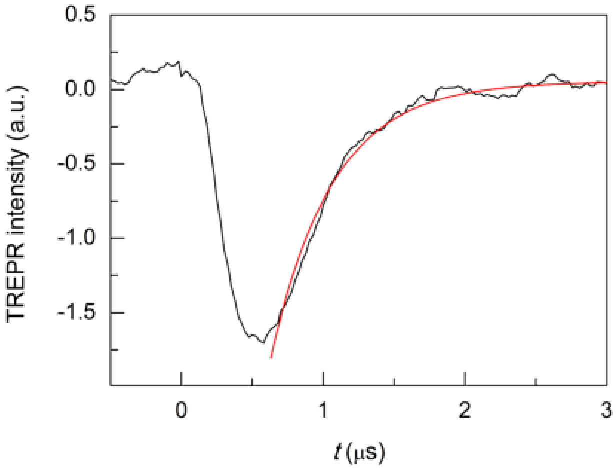

Figure 3.16. TREPR transient of the emission-polarized signal (average of the three signals) observed for 1 mM $Au_{24}Cd(SC2Ph)_{18}^0$ and 0.5 mM TEMPONE in

toluene under anaerobic conditions (black), with monoexponential fit to the data (red).

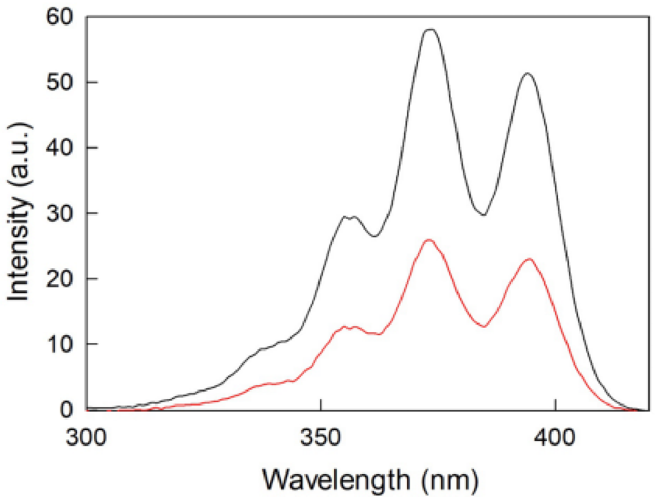

Figure 3.17. Excitation Spectra (λ_{exc} = 450 nm) of a toluene solution of 1.3 x 10^{-3} mM DPA and 0.13 mM $Au_{24}Cd(SC4)_{18}^{0}$ before (black trace) and after (red trace) 10 min irradiation at 532 nm at 240 K. The spectra were obtained at room temperature with a 1 mm path length cuvette in a front-face configuration.

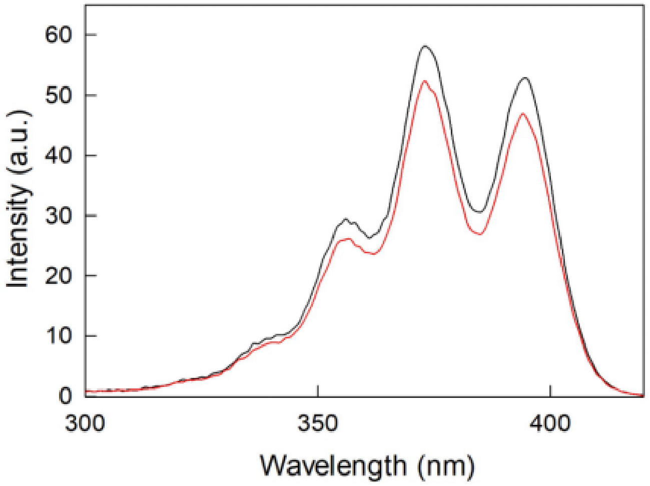

Figure 3.18. Excitation Spectra (λ_{exc} = 450 nm) of a toluene solution of 1.3 x 10^{-3} mM DPA and 0.13 mM $Au_{25}(SC4)_{18}^{-}$ before (black trace) and after (red trace) 10

min irradiation at 532 nm at 240 K. The spectra were obtained at room temperature with a 1 mm path length cuvette in a front-face configuration.

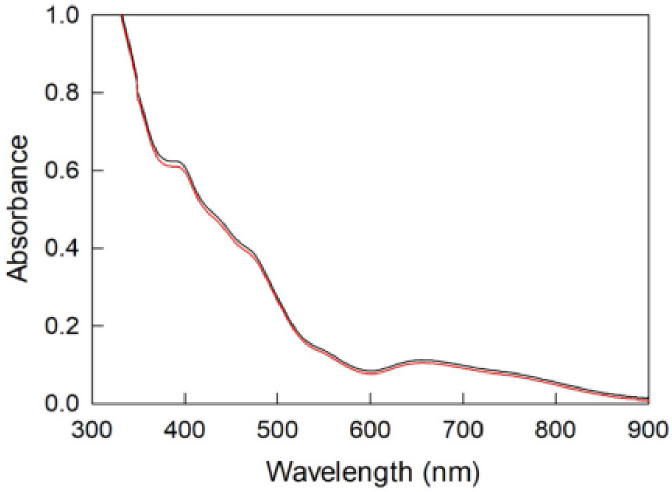

Figure 3.19. Absorption spectra of a toluene solution of 1.3 x 10^{-3} mM DPA and 0.13 mM $Au_{24}Cd(SC4)_{18}^0$ before (black trace) and after (red trace) 10 min irradiation at 532 nm at 240 K. The spectra were obtained at room temperature with a 1 mm cuvette.

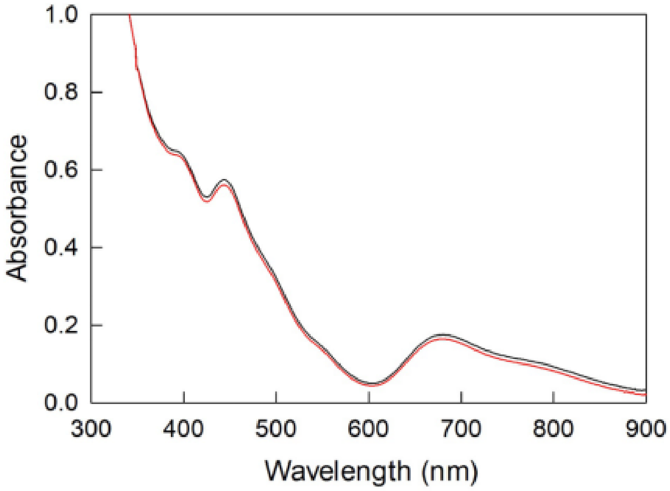

Figure 3.20. Absorption spectra of a toluene solution of 1.3 x 10^{-3} mM DPA and 0.13 mM $Au_{25}(SC4)_{18}^-$ before (black trace) and after (red trace) 10 min irradiation

at 532 nm at 240 K. The spectra were obtained at room temperature a 1 mm cuvette.

3.5 References

1. Becker, K. H.; Groth, W.; Schurath, U. The quenching of metastable $O_2(^1\Delta_g)$ and $O_2(^1\Sigma_g^+)$ molecules. *Chem. Phys. Lett*. **1971**, *8*, 259-262.

2. (a) Wilkinson, F.; Helman, W. P.; Ross, A. B. Rate Constants for the Decay and Reactions of the Lowest Electronically Excited Singlet State of Molecular Oxygen in Solution. An Expanded and Revised Compilation. *J. Phys. Chem. Ref. Data* **1995**, *24*, 663−1021. (b) Wilkinson, F.; Brummer, J. G. Rate constants for the decay and reactions of the lowest electronically excited singlet state of molecular oxygen in solution. *J. Phys. Chem. Ref. Data* **1981**, *10*, 809-999.

3. Ruzzi, M.; Sartori, E.; Moscatelli, A.; Khudyakov, I. V.; Turro, N. J. Time-resolved EPR study of singlet oxygen in the gas phase. *J. Phys. Chem. A* **2013**, *117*, 5232-5240.

4. Amato, I. Cancer therapy. Hope for a magic bullet that moves at the speed of light. *Science* **1993**, *262*, 32-33.

5. Greer, A. Christopher Foote's Discovery of the Role of Singlet Oxygen $[^1O_2(^1\Delta_g)]$ in Photosensitized Oxidation Reactions. *Acc. Chem. Res*. **2006**, *39*, 797−804.

6. Turro, N. J.; Ramamurthy, V.; Scaiano, J. C. Molecular Oxygen and Organic Photochemistry. In *Modern Molecular Photochemistry of Organic Molecules*; University Science Books: Sausalito, CA, 2010; Chapter 14.

7. Ghogare, A. A.; Greer, A. Using Singlet Oxygen to Synthesize Natural Products and Drugs. *Chem. Rev.* **2016**, *116*, 9994−10034.

8. Nosaka, Y.; Nosaka, A. Y. Generation and Detection of Reactive Oxygen Species in Photocatalysis. *Chem. Rev.* **2017**, *117*, 11302−11336.

9. Dolmans, D. E.; Fukumura, D.; Jain, R. K. Photodynamic therapy for cancer. *Nat. Rev. Cancer* **2003**, 3, 380–387.

10. Schweitzer, C.; Schmidt, R. Physical Mechanisms of Generation and Deactivation of Singlet Oxygen. *Chem. Rev.* **2003**, *103*, 1685–1757.

11. Ogilby, P. R. Singlet Oxygen: There is Indeed Something New Under the Sun. *Chem. Soc. Rev.* **2010**, *39*, 3181-3209.

12. Bregnhoj, M.; Westberg, M.; Minaev, B. F.; Ogilby, P. R. Singlet Oxygen Photophysics in Liquid Solvents: Converging on a Unified Picture. *Acc. Chem. Res.* **2017**, *50*, 1920-1927.

13. DeRosa M. C.; Crutchley, R. J. Photosensitized singlet oxygen and its applications. *Coord. Chem. Rev*. **2002**, *233–234*, 351-371.

14. Hurst, J. R.; McDonald, J. D.; G. B. Schuster, G. B. Lifetime of singlet oxygen in solution directly determined by laser spectroscopy *J. Am. Chem. Soc.* **1982**, *104*, 2065–2067.

15. Ogilby, P. R.; Foote, C. S. Chemistry of singlet oxygen. 42. Effect of solvent, solvent isotopic substitution, and temperature on the lifetime of singlet molecular oxygen ($^1\Delta_g$). *J. Am. Chem. Soc.* **1983**, *105*, 3423–3430.

16. Krasnovsky, A. A., Jr.; Bashtanov, M. E.; Drozdova, N. N.; Yuzhakova, O. A.; Luk'yanets, E. A. Laser induced singlet-oxygen-sensitised delayed fluorescence of dyes in aqueous solutions. *Quantum. Electron* **2002**, *32*, 83-86.

17. You, Y. Chemical tools for the generation and detection of singlet oxygen. *Org. Biomol. Chem.* **2018**, *16*, 4044-4060.

18. Jin, R.; Zeng, C.; Zhou, M.; Chen, Y. Atomically Precise Colloidal Metal Nanoclusters and Nanoparticles: Fundamentals and Opportunities. *Chem. Rev.* **2016**, *116*, 10346-10413.

19. Kawasaki, H.; Kumar, S.; Li, G.; Zeng, C.; Kauffman, D. R.; Yoshimoto, J.; Iwasaki, Y.; Jin, R. Generation of Singlet Oxygen by Photoexcited $Au_{25}(SR)_{18}$ Clusters. *Chem. Mater.* **2014**, *26*, 2777-2788.

20. Sakamoto, M.; Tachikawa, T.; Fujitsuka, M.; Majima, T. Photochemical Reactivity of Gold Clusters: Dependence on Size and Spin Multiplicity. *Langmuir* **2009**, *25*, 13888- 13893.

21. Das, T.; Ghosh, P.; Shanavas, M. S.; Maity, A.; Mondala, S.; Purkayastha, P. Protein-templated gold nanoclusters: size dependent inversion of fluorescence emission in the presence of molecular oxygen. *Nanoscale* **2012**, *4*, 6018-6024.

22. Zhao, J. Y.; Cui, R; Zhang, Z. L.; Zhang, M.; Xie, Z. X.; Pang, D. W. Cytotoxicity of nucleus-targeting fluorescent gold Nanoclusters. *Nanoscale* **2014**, *6*, 13126-13134.

23. Vankayala, R.; Kuo, C. L.; Nuthalapati, K.; Chiang, C. S.; Hwang, K. C. Nucleus‐Targeting Gold Nanoclusters for Simultaneous In Vivo Fluorescence Imaging, Gene Delivery, and NIR‐Light Activated Photodynamic Therapy. *Adv. Funct. Mater.* **2015**, *25*, 5934-5945.

24. Yang, D.; Yang, G.; Gai, S.; He F.; An, G.; Dai, Y.; Lv, R.; Yang, P. Au_{25} clusters functionalized metal-organic nanostructures for magnet targeted photodynamic/photothermal therapy triggered by a single 808 nm near-infrared light. *Nanoscale* **2015**, *7*, 19568-19578.

25. Yamamoto, M.; Osaka, I.; Yamashita, K.; Hasegawa, H.; Arakawa, R.; Kawasaki, H. Effects of ligand species and cluster size of biomolecule-protected Au nanoclusters on efficiency of singlet-oxygen generation. *J. Lumin.* **2016**, *180*, 315-320.

26. Yamamoto, M.; Shitomi, K.; Miyata, S.; Miyaji, H.; Aota, H.; Kawasaki, H. Bovine serum albumin-capped gold nanoclusters conjugating with methylene blue for efficient $^1O_2$ generation via energy transfer. *J. Colloid. Interface Sci.* **2018**, *510*, 221-227.

27. Miyata, S.; Miyaji, H.; Kawasaki, H.; Yamamoto, M.; Nishida, E.; Takita, H.; Akasaka, T.; Ushijima, N.; Iwanaga, T. Sugaya, T. Antimicrobial Photodynamic Activity and Cytocompatibility of $Au_{25}(Capt)_{18}$ Clusters Photoexcited by Blue LED Light irradiation. *Int. J. Nanomed*. **2017**, *12*, 2703-2716.

28. Hikosou, D.; Saita, S.; Miyata, S.; Miyaji, H.; Furuike, T.; Tamura, H.; Kawasaki, H. Aggregation/Self-Assembly-Induced Approach for Efficient AuAg Bimetallic Nanocluster-Based Photosensitizers. *J. Phys. Chem. C* **2018**, *122*, 12494-12501.

29. Ho-Wu, R.; Hei Yau, S.; Goodson III, T. Efficient Singlet Oxygen Generation in Metal Nanoclusters for Two-Photon Photodynamic Therapy Applications. *J. Phys. Chem. B* **2017**, *121*, 10073-10080.

30. Zhang, G.; Wang, R.; Li, G. Non-metallic gold nanoclusters for oxygen activation and aerobic oxidation. *Chin. Chem. Lett.* **2018**, *29*, 687-693.

31. Zhang, J.; Li, Z.; Huang, J.; Liu, C.; Hong, F.; Zheng, K. Li, G. Size dependence of gold clusters with precise numbers of atoms in aerobic oxidation of D-glucose. *Nanoscale* **2017**, *9*, 16879-16886.

32. Li, Z.; Liu, C.; Abroshan, H.; Kauffman, D. R.; Li, G. $Au_{38}S_2(SAdm)_{20}$ Photocatalyst for One-Step Selective Aerobic Oxidations. *ACS Catal.* **2017**, *7*, 3368-3374.

33. Kawamura, K.; Hikosou, D.; Inui, A.; Yamamoto, K.; Yagi, J. Saita, S.; Kawasaki, H. Ultrasonic Activation of Water-Soluble $Au_{25}(SR)_{18}$ Nanoclusters for Singlet Oxygen Production. *J. Phys. Chem. C* **2019**, *123*, 26644-26652.

34. Antonello, S.; Maran, F. Molecular Electrochemistry of Monolayer-Protected Clusters. *Curr. Opin. Electrochem*. **2017**, *2*, 18-25.

35. Agrachev, M.; Antonello, S.; Dainese, T.; Ruzzi, M.; Zoleo, A.; Aprà, E.; Govind, N.; Fortunelli, A.; Sementa, L.; Maran, F. Magnetic Ordering in Gold Nanoclusters. *ACS Omega* **2017**, *2*, 2607-2617. Correction to Magnetic Ordering in Gold Nanoclusters. *ACS Omega* **2017**, *2*, 3595.

36. Agrachev, M.; Ruzzi, M.; Venzo, A.; Maran, F. Nuclear and Electron Magnetic Resonance Spectroscopies of Atomically Precise Gold Nanoclusters. *Acc. Chem. Res*. **2019**, *52*, 44-52.

37. Parker, J. F.; Fields-Zinna, C. A.; Murray, R. W. The Story of a Monodisperse Gold Nanoparticle: $Au_{25}L_{18}$. *Acc. Chem. Res.* **2010**, *43*, 1289-1296.

38. Kang, X.; Chong, H.; Zhu, M. $Au_{25}(SR)_{18}$: the captain of the great nanocluster ship. *Nanoscale* **2018**, *10*, 10758-10834.

39. Fei, W.; Antonello, S.; Dainese, T.; Dolmella, A.; Lahtinen, M.; Rissanen, K.; Venzo, A.; Maran, F. Metal Doping of $Au_{25}(SR)_{18}^-$ Clusters: Insights and Hindsights. *J. Am. Chem. Soc.* **2019**, *141*, 16033-16045.

40. Mitsui, M.; Takeda, K.; Kobori, Y.; Kawai, A.; Obi, K. Unusually Large Dynamic Electron Polarization in an $O_2(^1\Delta_g)$-2,2,6,6-Tetramethylpiperidine-1-oxyl Radical System. *J. Phys. Chem. A* **2004**, *108*, 1120-1126.

41. Martinez, C. G.; Jockusch, S.; Ruzzi, M.; Sartori, E.; Moscatelli, A.; Turro, N. J.; Buchachenko, A. L. Chemically Induced Dynamic Electron Polarization Generated through the Interaction between Singlet Molecular Oxygen and Nitroxide Radicals. *J. Phys. Chem. A* **2005**, *109*, 10216-10221.

42. Corvaja, C. Electron Paramagnetic Resonance of Modified Fullerenes. In *Fullerenes: From Synthesis to Optoelectronic Properties*. Guldi, D. M. and Martin N. *Eds., Kluwer Academic Publishers*, **2002**, 213-236.

43. Blättler, C.; Jent, F.; Paul, H. A novel radical-triplet pair mechanism for chemically induced electron polarization (CIDEP) of free radicals in solution. *Chem. Phys. Lett.* **1990**, *166*, 375-380.

44. Salikhov, K. M; Molin, Yu. N.; Sagdeev, R. Z.; Buchachenko, A. L. In: *Spin Polarization and Magnetic Effects in Radical Reactions*; Molin, Y., Ed.; Elsevier: Amsterdam, 1984.

45. Mitsui, M.; Takeda, K.; Kobori, Y.; Kawai, A.; Obi, K. The first observation of CIDEP generated through the interaction between an excited singlet oxygen molecule and a free radical. *Chem Phys. Lett.* **1996**, *262*, 125-130.

46. Mitsui, M; Takeda, K.; Kobori, Y.; Kawai, A.; Obi, K. Unusually Large Dynamic Electron Polarization in an $O_2(^1\Delta_g)$-2,2,6,6-Tetramethylpiperidine-1-oxyl Radical System. *J. Phys. Chem. A* **2004**, *108,* 1120-1126.

47. Kawai, A.; Okutsu, T.; Obi, K. Spin polarization generated in the triplet-doublet interaction: hyperfine-dependent chemically induced dynamic electron polarization *J. Phys. Chem.* **1991**, *95*, 9130-9134.

48. De Nardi, M.; Antonello, S.; Jiang, D.; Pan, F.; Rissanen, K.; Ruzzi, M.; Venzo, A.; Zoleo, A.; Maran, F. Gold Nanowired: A Linear $(Au_{25})_n$ Polymer from Au_{25} Molecular Clusters. *ACS Nano* **2014**, *8*, 8505-8512;

49. Agrachev, M., Antonello, S., Dainese, T., Gascón, J. A., Pan, F., Rissanen, K., Ruzzi, M., Venzo, A., Zoleo, A.; Maran F. A Magnetic Look into the Protecting Layer of Au_{25} Clusters. *Chem. Sci.* **2016**, *7*, 6910-6918.

50. Antonello, S.; Dainese, T.; Pan, F.; Rissanen, K.; Maran, F. Electrocrystallization of Monolayer Protected Gold Clusters: Opening the Door to Quality, Quantity and New Structures. *J. Am. Chem. Soc.* **2017**, *139*, 4168-4174.

51. Venzo, A.; Antonello, S.; Gascón, J. A.; Guryanov, I.; Leapman, R. D.; Perera, N. V.; Sousa, A.; Zamuner, M.; Zanella, A.; Maran, F. Effect of the Charge State (z = -1, 0, +1) on the Nuclear Magnetic Resonance of Monodisperse $Au_{25}[S(CH_2)_2Ph]_{18}^z$ Clusters. *Anal. Chem.* **2011**, *83*, 6355-6362.

52. Antonello, S.; Hesari, M.; Polo, F.; Maran, F. Electron Transfer Catalysis with Monolayer Protected Au_{25} Clusters. *Nanoscale* **2012**, *4*, 5333-5342.

53. Rosenthal, I. Chemical and Physical Sources of Singlet Oxygen. In *Singlet* O_2; Frimer, A. A. *Ed.; CRC Press: Boca Raton, FL*, **1985**, *1*, 13-38.

54. Kawai, A.; Shibuya, K. Electron spin dynamics in a pair interaction between radical and electronically-excited molecule as studied by a time-resolved ESR method. *J. Photochem. Photobiol. C: Photochem. Rev.* **2006**, *7*, 89-103.

55. Povich, M. J. Electron Spin Resonance Oxygen Broadening *J. Phys. Chem.* **1975**, *79*, 1106-1109.

56. Bregnhøj, M.; Westberg, M.; Jensen, F.; Ogilby, P. R. Solvent-dependent singlet oxygen lifetimes-temperature effects implicate tunneling and charge-transfer interactions. *Phys. Chem. Chem. Phys.* **2016**, *18*, 22946-22961.

57. Gorman, A. A.; Hamblett, I.; Lambert, C.; Spencer, B.; Standen, M. C. Identification of Both Preequilibrium and Diffusion Limits for Reaction of Singlet Oxygen, $O_2(^1\Delta_g)$, with Both Physical and Chemical Quenchers: Variable-Temperature, Time-Resolved Infrared Luminescence Studies. *J. Am. Chem. Soc.* **1988**, *110*, 8053-8059.

58. Zhang, J.; Jiang, C.; Figueiró Longo, J. P.; Azevedo, R. B.; Zhang, H.; Muehlmann, L. A. An updated overview on the development of new photosensitizers for anticancer photodynamic therapy. *Acta Pharm. Sinica B* **2018**, *8*,137-146.

59. Tanielian, C.; Wolff, C. Mechanism of physical quenching of singlet molecular oxygen by chlorophylls and related compounds of biological interest. *Photochem. Photobiol*. **1988**, *48*, 277-280.

60. Bachilo, S. M.; Weisman, R. B. Determination of Triplet Quantum Yields from Triplet-Triplet Annihilation Fluorescence. *J. Phys. Chem. A* **2000**, *104*, 7711-7714.

61. Tanielian, C.; Wolff, C. Porphyrin-Sensitized Generation of Singlet Molecular Oxygen: Comparison of Steady-State and Time-Resolved Methods. *J. Phys. Chem.* **1995**, *99*, 9825-9830.

62. Pineiro, M.; Carvalho, A. L.; Pereira, M. M.; Rocha Gonsalves, A. M. d'A.; Arnaut, L. G.; Formosinho, S. J. Photoacoustic Measurements of Porphyrin Triplet-State Quantum Yields and Singlet-Oxygen Efficiencies. *Chem. Eur. J.* **1998**, *4*, 2299-2307.

63. Ouannès, C.; Wilson, T. Quenching of singlet oxygen by tertiary aliphatic amines. Effect of DABCO (1,4-diazabicyclo[2.2.2]octane) *J. Am. Chem. Soc.* **1968**, *90*, 6527-6528.

64. Schweitzer, C.; Mehrdad, Z.; Shafii, F.; Schmidt, R. Charge transfer induced quenching of triplet sensitizers by ground state oxygen and of singlet oxygen by ground state sensitizers: A common deactivation channel. *Phys. Chem. Chem. Phys*. **2001**, *3*, 3095-3101.

65. Ogryzlo, E. A.; Tang, C. W. Quenching of Oxygen ($^1\Delta_g$) by Amines. *J. Am. Chem. Soc.* **1970**, *92*, 5034-5036.

66. Darmanyan, A. P.; Jenks, W. S.; Jardon, P. Charge-Transfer Quenching of Singlet Oxygen $O_2(^1\Delta_g)$ by Amines and Aromatic Hydrocarbons. *J. Phys. Chem. A* **1998**, *102*, 7420-7426.

67. Schweitzer, C.; Mehrdad, Z.; Shafii, F.; Schmidt, R. Common Marcus Type Dependence of the Charge Transfer Induced Processes in the Sensitization and Quenching of Singlet Oxygen by Naphthalene Derivatives. *J. Phys. Chem. A*, **2001**, *105*, 5310-5316.

68. Minaev, B. F. Spin-Orbit Coupling of Charge-Transfer States and the Mechanism for Quenching Singlet Oxygen by Amines. *Theor. Exp. Chem*. **1984**, *20*, 199-201.

69. Antonello, S.; Arrigoni, G.; Dainese, T.; De Nardi, M.; Parisio, G.; Perotti, L.; René, A.; Venzo, A.; Maran, F. Electron Transfer through 3D Monolayers on Au_{25} Clusters. *ACS Nano* **2014**, *8*, 2788-2795.

70. Antonello, S.; Dainese, T.; De Nardi, M.; Perotti, L.; Maran, F. Insights into the Interface between the Electrolytic Solution and the Gold Core in Molecular Au_{25} Clusters. *ChemElectroChem.* **2016**, *3*, 1237-1244.

71. Antonello, S.; Holm, A. H.; Instuli, E.; Maran, F. Molecular Electron-Transfer Properties of Au_{38} Clusters. *J. Am. Chem. Soc.* **2007**, *129*, 9836-9837.

72. Wang, S.; Song, Y.; Jin, S.; Liu, X.; Zhang, J.; Pei, Y.; Meng, X.; Chen, M.; Li, P.; Zhu, M. Metal Exchange Method Using Au_{25} Nanoclusters as Templates for Alloy Nanoclusters with Atomic Precision. *J. Am. Chem. Soc.* **2015**, *137*, 4018-4021.

73. Yao, C.; Lin, Y.-j.; Yuan, J.; Liao, L.; Zhu, M.; Weng, L.-h.; Yang, J.; Wu, Z. Mono-Cadmium vs Mono-Mercury Doping of Au_{25} Nanoclusters. *J. Am. Chem. Soc*. **2015**, *137*, 15350-15353.

74. Liao, L.; Zhou, S.; Dai, Y.; Liu, L.; Yao, C.; Fu, C.; Yang, J.; Wu, Z. Mono-Mercury Doping of Au_{25} and the HOMO/LUMO Energies Evaluation Employing Differential Pulse Voltammetry. *J. Am. Chem. Soc*. **2015**, *137*, 9511-9514.

75. Zhou, M.; Yao, C.; Sfeir, M. Y.; Higaki, T.; Wu, Z.; Jin, R. Excited-State Behaviors of $M_1Au_{24}(SR)_{18}$ Nanoclusters: The Number of Valence Electrons Matters. *J. Phys. Chem. C* **2018**, *122*, 13435-13442.

76. Wen, X.; Yu, P.; Toh, Y. R.; Hsu, A. C.; Lee, Y. C.; Tang, J. Fluorescence Dynamics in BSA-Protected Au_{25} Nanoclusters. *J. Phys. Chem. C* **2012**, *116*, 19032-19038.

77. Castro-Olivares, R.; Günter, G.; Zanocco, A. L.; Lemp, E. Linear free energy relationship analysis of solvent effect on singlet oxygen reactions with mono and disubstituted anthracene derivatives. *J. Photochem. Photobiol. A - Chemistry* **2009**, *207*, 160-166.

78. Berlman, I. B. Handbook of Fluorescence Spectra of Aromatic Molecules: Academic Press, New York, 1971.

79. Dinnocenzo, J. P.; Merkel, P. B.; Farid, S. Cationic (Charge Shift) Exciplexes. *J. Phys. Chem. A* **2017**, *121*, 7903-7909.

80. Woodham, A. P.; Meijer, G.; Fielicke, A. Activation of Molecular Oxygen by Anionic Gold Clusters. *Angew. Chem., Int. Ed*. **2012**, *51*, 4444-4447.

81. Woodham, A. P.; Meijer, G.; Fielicke, A. Charge Separation Promoted Activation of Molecular Oxygen by Neutral Gold Clusters. *J. Am. Chem. Soc.* **2013**, *135*, 1727-1730.

82. Bhat, S.; Narayanan, R. P.; Baksi, A.; Chakraborty, P.; Paramasivam, G.; Methikkalam, R. R. J.; Nag, A.; Natarajan, G.; Pradeep, T. Detection of $[Au_{25}(PET)_{18}(O_2)_n]^-$ (n = 1, 2, 3) Species by Mass Spectrometry. *J. Phys. Chem. C* **2018**, *122*, 19455-19462.

83. Schumpe, A.; Lührlng, P. Oxygen Diffusivities in Organic Liquids at 293.2 K. *J. Chem. Eng. Data* **1990**, *35*, 24-25.

84. Santos, F. J. V.; Nieto de Castro, C. A.; Dymond, J. H.; Dalaouti, N. K.; Assael, M.J.; Nagashima A. Standard Reference Data for the Viscosity of Toluene. *J. Phys. Chem. Ref. Data* **2006**, *35*, 1-8.

85. Debye, P. Reaction Rates in Ionic Solutions. *J. Electrochem. Soc.* **1942**, *82*, 265-272.

86. Sutin, N. Theory of Electron Transfer Reactions: Insights and Hindsights. *Progr. Inorg. Chem* **1983**, *30*, 441-498.

87. Marcus, R. A.; Sutin, N. Electron Transfers in Chemistry and Biology. *Biochim. Biophys. Acta* **1985**, *811*, 265-322.

88. Zusman, L. D. Outer-sphere electron transfer in polar solvents. *Chem. Phys*. **1980**, *49*, 295-304.

89. Hassel, W. F.; Walker, S. Dielectric Studies. Part 4.-Relaxation Processes of Four Monoalkylbenzenes. *Tras. Farad. Soc.* **1966**, *62*, 861-873.

90. Meneses, A. B.; Antonello, S.; Arévalo, M. C.; González, C. C.; Sharma, J.; Wallette, A. N.; Workentin, M. S.; Maran, F. Electron Transfer to Sulfides and Disulfides: Intrinsic Barriers and Relationship between Heterogeneous and Homogeneous Electron-Transfer Kinetics. *Chem. Eur. J*. **2007**, *13*, 7983-7995.

91. Antonello, S.; Perera, N. V.; Ruzzi, M.; Gascón, J. A.; Maran, F. Interplay of Charge State, Lability, and Magnetism in the Molecule-like $Au_{25}(SR)_{18}$ Cluster. *J. Am. Chem. Soc.* **2013**, *135*, 15585–1559.

92. Ignaczak, A.; Schmickler, W.; Bartenschlager, S. Electrochemical reduction of the O_2 molecule to the O_2^- radical ion – A theoretical approach. *J. Electroanal. Chem.* **2006**, *586*. 297-307.

93. Rehm, D.; Weller, A. Kinetics of Fluorescence Quenching by Electron and H‐Atom Transfer. *Isr. J. Chem*. **1970**, *8*, 259-271.

94. IUPAC. Compendium of Chemical Terminology, 2nd ed. (the "Gold Book"). Compiled by A. D. McNaught and A. Wilkinson. Blackwell Scientific Publications, Oxford (1997). Online version (2019-) created by S. J. Chalk. ISBN 0-9678550-9-8. https://doi.org/10.1351/goldbook.

95. Wayner, D. D. M.; McPhee, D. J.; Griller, D. Oxidation and Reduction Potentials of Transient Free Radicals. *J. Am. Chem. Soc.* **1988**, *110*, 132-137.

96. Jones, W. E. Jr.; Fox, M. A. Determination of Excited-State Redox Potentials by Phase-Modulated Voltammetry. *J. Phys. Chem.* **1994**, *98*, 5095-5099.

97. Minaev, B. F. Electronic mechanism of molecular oxygen activation *Russ. Chem. Rev.* **2007**, *76*, 988-1010.

98. Farid, S.; Dinnocenzo, J. P.; Merkel, P. B.; Young, R. H.; Shukla, D. Bimolecular Electron Transfers That Follow a Sandros-Boltzmann Dependence on Free Energy. *J. Am. Chem. Soc*. **2011**, *133*, 4791-4801.

99. Meneses, A. B.; Antonello, S.; Arévalo, M.-C; Maran, F. Double‐Layer Correction for Electron‐Transfer Kinetics at Glassy Carbon and Mercury Electrodes in *N,N*‐Dimethylformamide. *Electroanal.* **2006**, *18*, 363-370.

Chapter 4. Gold Fusion: From $Au_{25}(SR)_{18}$ to $Au_{38}(SR)_{24}$, the Most Unexpected Transformation of a Very Stable Nanocluster*

* Published: Dainese, T.; Antonello, S.; Bogialli, S.; Fei, W.; Venzo, A.; Maran, F. Gold Fusion: From $Au_{25}(SR)_{18}$ to $Au_{38}(SR)_{24}$, the Most Unexpected Transformation of a Very Stable Nanocluster. *ACS Nano* **2018**, *12*, 7057-7066.

4.1 Introduction

Ligand-protected metal clusters are of continuously growing fundamental and applied interest.[1-3] Several of these systems can be synthesized with atomic precision, and this has allowed understanding that differences of only one gold atoms, variations in the number or type of ligands, or even structural isomerism may affect their stability and properties very significantly.[1-7] The preparation of specific thiolated gold nanoclusters can be controlled through proper balance of thiol selection, relative concentrations of the reactants, experimental conditions, and modus operandi.[8-10] Importantly, the library of atomically precise gold nanoclusters can be expanded significantly by exploiting reactions to transform a structure into another.[11,12] A way to do it, resulting in smaller clusters, is by thermal etching.[13] The methodology normally employed, however, is the ligand place exchange induced size transformation, which involves thermal activation of the clusters in the presence of a large excess of an exogenous thiol.[11,14,15] For this reaction to be successful, the incoming thiol should be quite different than the endogenous thiolate (SR).

There are several reports of transformations of gold nanoclusters into smaller structures. For example, $Au_{144}(SR)_{60}$ can be converted into $Au_{99}(SR')_{42}$ or $Au_{133}(SR')_{52}$ through thermochemical etching with exogenous thiols (HSR′).[16,17] Similarly, $Au_{38}(SR)_{24}$ and $Au_{25}(SR)_{18}$ can be converted into $Au_{36}(SR')_{24}$[18] and $Au_{20}(SR')_{16}$,[19] respectively. Instead, the conversion from a smaller to a larger nanocluster is rarely seen. By focusing on clusters of known structure, this is the case of $Au_{23}(SR)_{16}$ to $Au_{24}(SR')_{20}$,[20] $Au_{25}(SR)_{18}$ to $Au_{28}(SR')_{20}$,[21] $Au_{30}(SR)_{18}$ to

$Au_{36}(SR')_{24}$,[22] $Au_{99}(SR)_{42}$ to $Au_{103}S_2(SR')_{41}$,[23] and $Au_{38}(SR)_{24}$ to $Au_{60}S_6(SR')_{36}$.[24] These transformations require thermal activation and the presence of an exogenous thiol in large excess and thus imply ligand place exchange reactions.

The smaller-to-larger nanocluster conversion is indeed especially important because, in principle, larger nanostructures could be prepared by assembling specific units with atomic precision. On theoretical grounds, the icosahedral Au_{13} core provides a particularly promising building block.[5, 25–31] Experimental examples of clusters containing the Au_{13} core are $Au_{13}(PMe_2Ph)_{10}Cl_2^{3+}$,[32] $Au_{13}(dppe)_5Cl_2^{3+}$ (dppe = $Ph_2P-(CH_2)_2PPh_2$),[33] $Au_{16}(AsPh_3)_8Cl_6$,[34] $[Au_{19}(C{\equiv}CR)_9(Hdppa)_3]^{2+}$ (Hdppa = $HN(PPh_2)_2$),[35] $Au_{20}(PR)_4Cl_4$ (R = $P[(CH_2)_2PPh_2]_3$),[36] and $Au_{25}(SR)_{18}$.[37, 38] Gold clusters whose cores can be portrayed as the assembly of 2, 3, or 5 vertex-fused Au_{13} units (i.e., where the icosahedra share one vertex Au atom) are $Au_{25}(PR_3)_{10}(SR)_5Cl_2^{2+}$,[39] $Au_{37}(PR_3)_{10}(SR)_{10}Cl_2^{+}$,[40] and $[Au_{60}Se_2(PPh_3)_{10}(SePh)_{15}]^{-}(SbF_6)$,[41] respectively. Other gold nanoclusters in which the core can be described as face-fused Au_{13} units are $Au_{38}(SR)_{24}$,[42] which is composed of 2 face-fused Au_{13} icosahedra, and $Au_{44}(SR)_{24}$,[43] which also consists of 2 face-fused Au_{13} icosahedra with the addition of an Au_6-bottom-cap motif. A dimeric structure missing the shared vertex was also solved.[44] Very importantly, however, is that in none of aforementioned examples were the vertex or face-sharing polyicosahedral clusters indeed obtained by an effective experimental assembly of “monomeric” Au_{13} units. The polymeric $Au_{25}(SR)_{18}$ clusters that we obtained in the form of bundles of parallel $[Au_{25}(SR)_{18}]_n$ nanowires are the only examples of structures in which each individual Au_{13} core is preserved upon formation of a larger structure.[45,46] In these linear polymers, which are stable in the solid state, the $Au_{25}(SR)_{18}$ clusters are connected by Au−Au bonds between staple Au atoms.

$Au_{25}(SR)_{18}$ is, by far, the most studied thiolate-protected nanocluster that can be prepared with atomic precision.[47] As such, it has been the object of numerous studies focusing on its charge- and ligand-dependent structure[37,38,45-51] and optical and NMR properties,[48-50,52–54] magnetism,[50,55] electrochemistry,[56] photophysics,[57] theory,[58-61] and several applications.[1-3] $Au_{25}(SR)_{18}$ has thus provided an effective benchmark for testing or developing investigation methodologies suitable to study fine details of these nanosystems, and the resulting information was borrowed to obtain insights into the properties and behavior of other molecular clusters. The success of the studies focusing on $Au_{25}(SR)_{18}$ has been facilitated by a series of experimental factors, particularly that this cluster is quite easy to make in a very pure form and its charge state can be controlled precisely. $Au_{38}(SR)_{24}$ is another of those clusters of known structure,[7,42] exhibiting well-defined molecular properties,[42,62-64] and whose study extended our understanding of molecular ligand-protected clusters, such as regarding the intrinsic chirality of some of them.[6,42,64,65]

$Au_{38}(SR)_{24}$ is usually synthesized by the etching of a mixture of poly-disperse larger nanoparticles, capped by glutathione, with an excess of an exogenous thiol.[42] Only very recently, it has been shown that $Au_{25}(SR)_{18}^-$ can be transformed into $Au_{38}(SR)_{24}$ or $Au_{44}(SR)_{26}^{2-}$ by seed-mediated reactions involving Au(I)-SR complexes and the mild reductant CO[66] or $Au_{38}(SR)_{26}$ by acetic-acid etching at 80 °C.[67] So far, however, the general understanding is that in the absence of co-reactants or promoters, both $Au_{25}(SR)_{18}$ and $Au_{38}(SR)_{24}$ are very stable clusters.

Here we demonstrate that it is possible to transform $Au_{25}(SR)_{18}$ directly into $Au_{38}(SR)_{24}$ by just dissolving the former in an inert solvent. This unexpected molecular transformation of the most-studied gold nanocluster does not require any co-reagent. This process not only provides a much simpler way of making $Au_{38}(SR)_{24}$ but is also conceptually different from any other known conversion of a gold nanocluster from a definite structure into another. This fusion thus provides the demonstration of the long-sought solution-phase nanocluster assembly starting from the fundamental building block Au_{13}.

4.2 Results and Discussion

4.2.1 Fusion Reaction

$Au_{25}(SC_3H_7)_{18}^0$ and $Au_{25}(SC_4H_9)_{18}^0$, here after indicated as $Au_{25}(SC3)_{18}^0$ and $Au_{25}(SC4)_{18}^0$, were prepared as already described.[45, 50] The clusters were dissolved in 0.1−0.4 mL toluene to form 30 mM solutions, and the reaction vessel was taken at the given temperature. In the following, we will focus on reactions carried out at 65 °C, although the same results were obtained at lower temperatures. At given reaction times, small aliquots (2 μL) were withdrawn from the reaction vessel, diluted to obtain a 0.6 mL toluene solution at room temperature, and their UV−vis spectra taken. Figure 4.1 shows (top graph) a collection of such spectra for $Au_{25}(SC4)_{18}^{0}$, as a function of time. The spectra were normalized at 400 nm. The graph at the bottom shows the corresponding derivative spectra, which help highlight the observed changes. The original spectrum of $Au_{25}(SC4)_{18}^{0}$ (black curve) undergoes progressive changes that are particularly evident in the range from 500 to 800 nm. After 10−14 days, the reaction solution was cooled to room temperature and $Au_{38}(SR)_{24}$ was isolated by silica gel (Macherey-Nagel MN-Kieselgel 60 M, 230−400 mesh) column chromatography, under a nitrogen flux, and using hexane-toluene 5:1 as the eluent. UV−vis absorption spectra of the clusters or cluster trans-formations were obtained in toluene with 2 mm cuvettes. The spectra were recorded with a CARY 5000 spectrophotometer. The spectra resolution was 0.5 nm. The purified product has the spectrum shown in blue in Figure 4.1 The latter is virtually identical to the originally published $Au_{38}(SC_2H_4Ph)_{24}$ spectrum.[42] The same behavior is observed for $Au_{25}(SC3)_{18}^{0}$ (Figure 4.2).

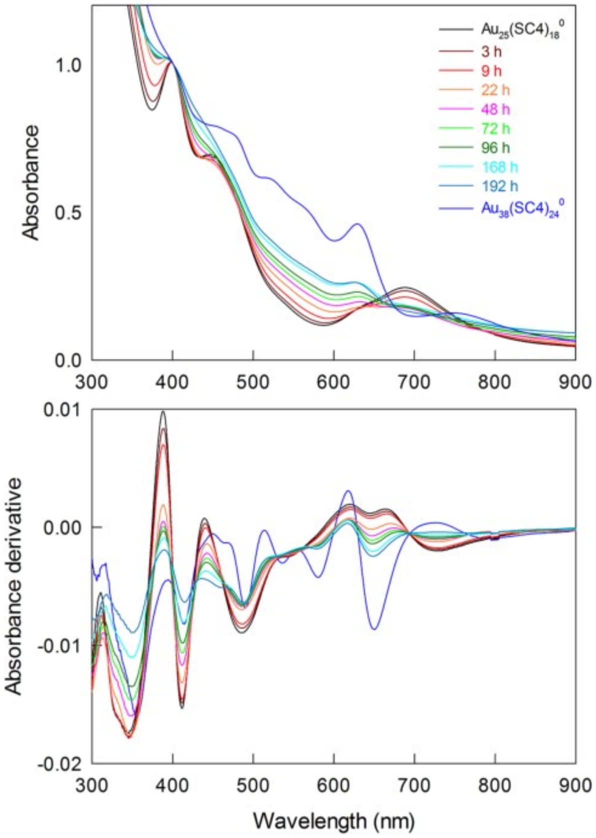

Figure 4.1. UV−vis absorption spectra of samples taken (see text) at different times (see legends) during the reaction of 30 mM $Au_{25}(SC4)_{18}^0$ at 65 °C in toluene (top graph). The lower graph shows the corresponding absorption-derivative plots. The black and the blue curves show the spectra of $Au_{25}(SC4)_{18}^0$ and the purified product, respectively.

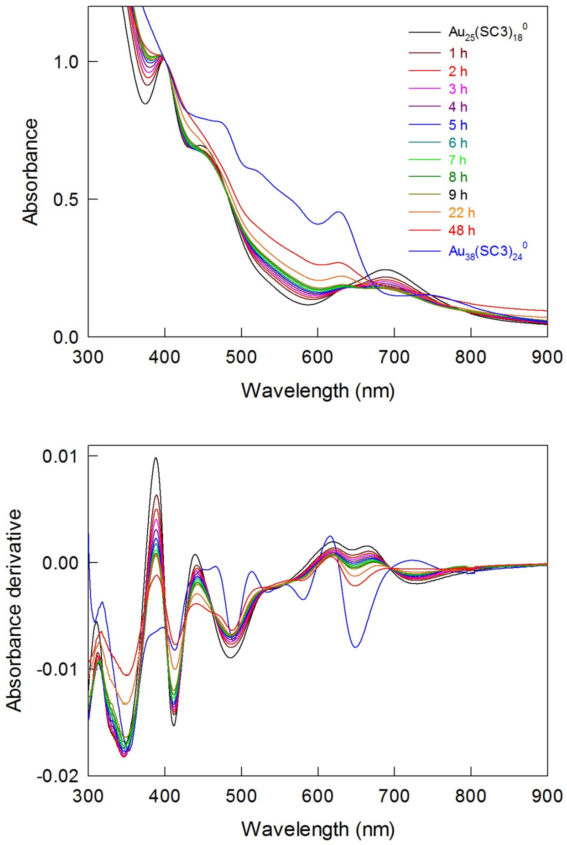

Figure 4.2. UV-vis absorption spectra of samples taken at different times (see legends) during the reaction of 30 mM $Au_{25}(SC3)_{18}{}^0$ at 65 °C in toluene. The lower graph shows the corresponding derivative plots. The black and the top blue curves show the spectra of $Au_{25}(SC3)_{18}{}^0$ and the purified product, respectively.

4.2.2 ESI Mass Spectrometry

The two purified clusters were analyzed by electrospray ionization (ESI) high-resolution mass spectrometry. The analyses were carried out by using a 0.01 mg/mL solution in dichloromethane. Figure 4.3 shows the mass spectrum of $Au_{38}(SC4)_{24}$. Although the molecular ions $[M]^+$ of $Au_{38}(SC3)_{24}$ (base peak 9287.37 m/z) and $Au_{38}(SC4)_{24}$ (base peak 9623.75 m/z) exceeded the instrumental mass range, for both clusters, the spectra show an intense base peak (4643.78 and 4811.94 m/z, respectively) that corresponds very nicely to the expected double-charged molecular ion $[M]^{2+}$. Both accuracies and isotopic patterns (e.g., inset in Figure 4.2) satisfactory matched the theoretical values. The data thus confirm that both clusters have the formula $Au_{38}(SR)_{24}$, in full agreement with the UV−vis absorption spectroscopy results.

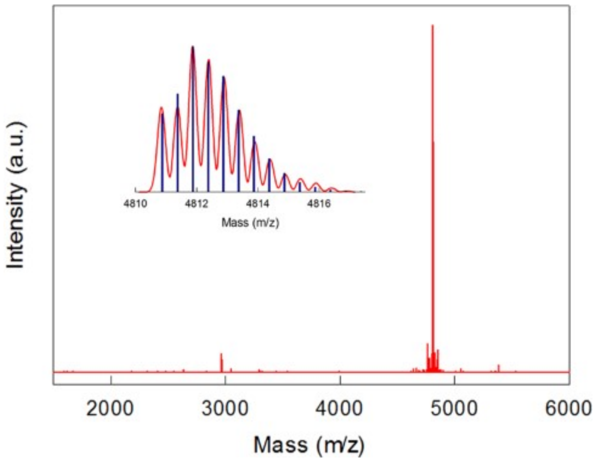

Figure 4.3. ESI mass spectrum of $Au_{38}(SC4)_{24}$. The inset shows the theoretical (blue) and experimental (red) isotopic pattern of $[M]^{2+}$.

4.2.3 NMR Spectroscopy

After carrying out a preliminary survey of the temperature effect on the ^1H NMR spectroscopy pattern in C_6D_6 (Figures 4.4 and 4.5), the spectra of both $Au_{38}(SR)_{24}$ samples were consistently studied at 45 °C, which provides a good compromise between signal resolution (which increases upon raising the temperature), peak separation, and the time required to carry out some of the measurements (1 and 4 days for total correlation spectroscopy, TOCSY, and heteronuclear multiple quantum coherence, HMQC, respectively).

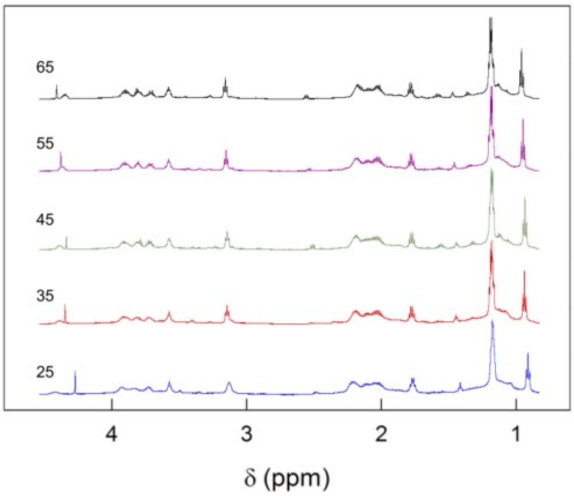

Figure 4.4 Temperature effect on the ^{1}H NMR spectrum of 3 mM $Au_{38}(SC3)_{24}$ in C_6D_6. Temperatures (°C) are indicated.

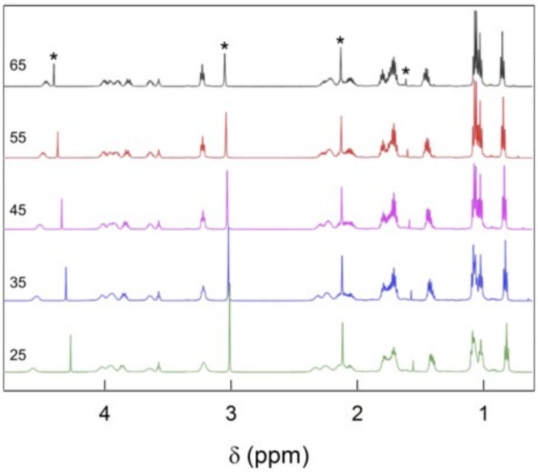

Figure 4.5. Temperature effect on the ^{1}H NMR spectrum of 3 mM $Au_{38}(SC4)_{24}$ in C_6D_6. Temperatures (°C) are indicated. The asterisks mark residual signals from solvents (right to left: acetone, toluene, methanol, and DCM).

We start by analyzing the spectral features of $Au_{38}(SC3)_{24}$. The observed resonances can be subdivided into three regions. The region at 0.89−1.24 ppm (Figure 4.6a), which is the region typical of the methyl groups (γ-position with respect to the sulfur atom), shows one triplet and a group of overlapping signals. Then, a series of sextets, most of which largely overlapped, at 1.72−2.28 ppm

(Figure 4.6b) are assigned to the methylene protons at the β-position (β-CH_2). The third region is seen at 3.05−4.45 ppm (Figure 4.6c) and consists of one triplet and a series of multiplets, assigned to the α-CH_2 resonances. Assignments were made by correlation analysis in TOCSY (Figure 4.9) and HMQC experiments (Figure 4.10). Furthermore, these spectra show that the cluster has four different types of $S\text{-}CH_2\text{-}CH_2\text{-}CH_3$ ligands, whose ^1H and ^{13}C chemical shift values (δ) are gathered in Table 4.1.

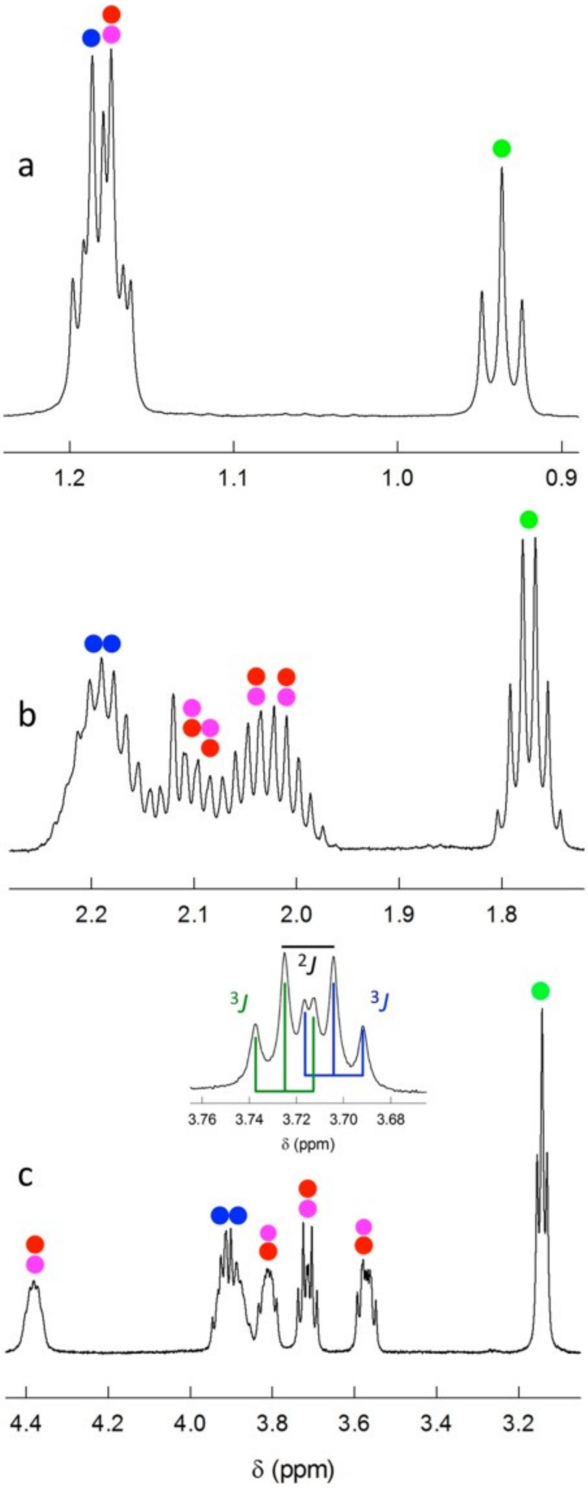

Figure 4.6. ^{1}H NMR spectrum of 3 mM $Au_{38}(SC3)_{24}$ in C_6D_6 at 45°C. For convenience, the spectrum has been divided into three parts (see text). The

colors refer to correlated resonances (cf. Table 4.1 and Figure 4.7). The inset to the lower spectrum (c) shows a detail of the signal at 3.715 ppm.

Table 4.1. NMR Chemical Shifts (*δ*) of $Au_{38}(SR)_{24}$^{a}

Au_{38}	**ligand type**		***α*-CH**	***β*-CH**	***γ*-CH**	***δ*-CH**
C3	*Out*	^{1}H	3.143	1.773	0.937	-
		^{13}C	35.94	28.27	13.29	-
	in-1	^{1}H	3.878	2.183	1.187	-
		^{1}H	3.922	2.201		
		$\Delta\delta$	**0.044**	**0.016**		
		^{13}C	49.74	30.32	13.77	-
	in-2 or S	^{1}H	3.574	2.087	1.172	-
		^{1}H	3.813	2.103		
		$\Delta\delta$	**0.239**	**0.016**		
		^{13}C	40.05	29.66	13.77	-
	S or in-2	^{1}H	3.715	2.017	1.175	-
		^{1}H	4.384	2.040		
		$\Delta\delta$	**0.668**	**0.023**		
		^{13}C	40.20	31.32	13.77	-
	Out	^{1}H	3.222	1.791	1.421	0.829
		^{13}C	33.63	27.28	22.22	13.93
	in-1	^{1}H	3.967	2,248	1.700	1.070
		^{1}H	4.028	2.304	1.729	
		$\Delta\delta$	**0.061**	**0.056**	**0.029**	
		^{13}C	38.42	39.96	22.75	14.43
C4	*in-2 or S*	^{1}H	3.657	2.138	1.713	1.055
		^{1}H	3.932	2.223	1.726	
		$\Delta\delta$	**0.275**	**0.085**	**0.013**	

	^{13}C	38.95	38.67	22.67	14.37
S or in-2	^{1}H	3.842	2.054	1.756	1.020
	^{1}H	4.527	2.098	1.766	
	$\Delta\delta$	**0.685**	**0.044**	**0.010**	
	^{13}C	38.77	39.05	22.47	14.43

$^{a}C_6D_6$, T = 45 °C. ^{13}C-NMR values are in italics, whereas the chemical-shift differences between coupled proton signals ($\Delta\delta$) are in bold type.

The integral count shows that these four types of ligands are present in exactly the same amount. Because of the stoichiometry (24 ligands), this means that each group refers to six NMR-equivalent thiolates. This result is thus in line with the structure solved for $Au_{38}(SC_2H_4Ph)_{24}$.[65] This cluster can be seen as the result of a fusion of two Au_{13} icosahedra sharing a common Au_3 face. Figure 4.7, which is based on the structure of $Au_{38}(SC_2H_4Ph)_{24}$, illustrates the fusion plane and the four groups of ligands here denoted as Out for the outer position in the double staples -SR-Au-SR-Au-SR-; In-1 and In-2 for the two nonequivalent inner positions in the same double staples, to stress the bond with the core (In-1 and In-2 are bonded to positions farther and closer to the fusion plane, respectively); and S for the ligands in the single staples -SR-Au-SR- surrounding the fusion plane of the $Au_{38}(SR)_{24}$ structure.

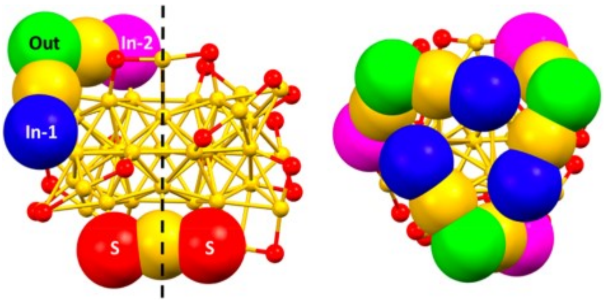

Figure 4.7. In the structure of $Au_{38}(SR)_{24}$,[65] where only gold (yellow) and sulfur (red) atoms are shown, four ligand types can be identified (evidenced as van der Waals rendering): outer (sulfur in green), inner (sulfur in magenta or blue, depending on whether the Au−S bond is near, In-2, or distant from the fusion

plane, In-1), and single-staple ligands (sulfur in red). The fusion plane is marked as a dashed line. On the right-hand side, the structure shows the clockwise orientation (as one of the two possible orientations) of the three double staples capping one end of the elongated Au_{23} core.

Figure 4.8 focuses on the bottom-left part of the TOCSY spectrum (cf. Figure 9), which corresponds to the α-CH_2 protons. The spectrum shows that in three of the four groups of resonances (cf. Table 4.1), the protons of the same α-CH_2 are nonequivalent, with chemical-shift differences ($\Delta\delta$) ranging from 0.044 to 0.668 ppm. It is worth noticing that the proton signal at 3.715 ppm (inset in Figure 4.6c) features the case of a perfectly resolved doublet of triplets due to a ^3J = 7.5 Hz with the two vicinal β-protons and a ^2J = 12.5 Hz of the geminal protons, which demonstrates further the nonequivalence of the protons of this methylene group. The same general splitting behavior is observed for the β-CH_2 protons, although the $\Delta\delta$ values are now significantly smaller (0.016−0.023 ppm). For each couple, the correlation of both protons with the same ^{13}C nucleus, as observed in the heterocorrelated ^1H−^{13}C HMQC spectrum (Figure 4.10), confirms these findings. Finally, for both the α-CH_2 and β-CH_2 proton resonances, the sum of the integrals of each couple is 2/3 the value of the integral of the isolated methyl group at 0.937 ppm. These observations are attributed to diastereotopicity, as noted for phenylethanethiolate ligands by Qian et al.[68] The chirality observed in $Au_{38}(SC_2H_4Ph)_{24}$ is the consequence of the two possible orientations of the dimeric staples, as illustrated in Figure 4.7 for the clockwise rotation.[65] The fact that the same effect is observed for linear ligands clearly points to the staple arrangement of these new clusters as having the same structural features.

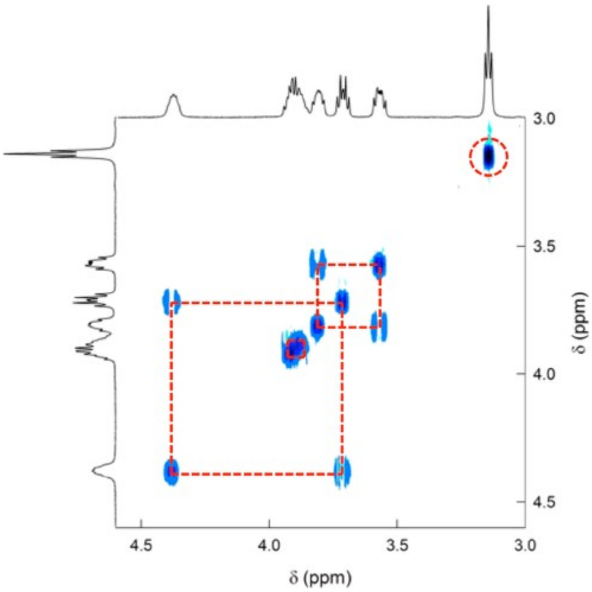

Figure 4.8. TOCSY spectrum of 3 mM $Au_{38}(SC3)_{24}$ in C_6D_6 at 45°C. The spectrum shows the α-CH_2 proton region. The squares highlight the three correlations, whereas the circle highlights the only α-CH_2 group of equivalent protons.

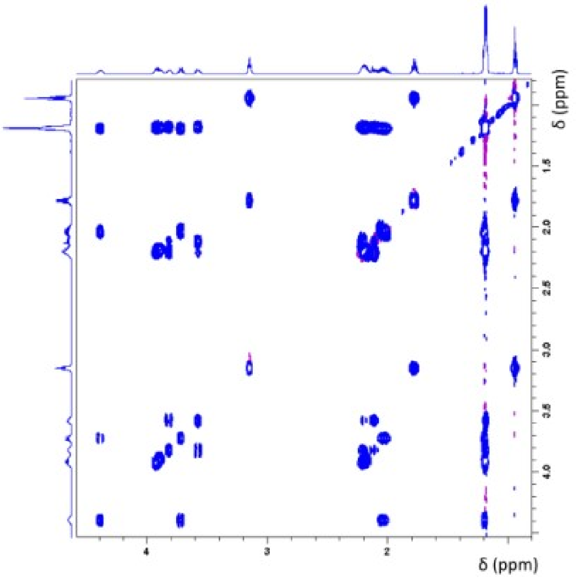

Figure 4.9 TOCSY spectrum of 3 mM $Au_{38}(SC3)_{24}$ in C_6D_6 at 45 °C.

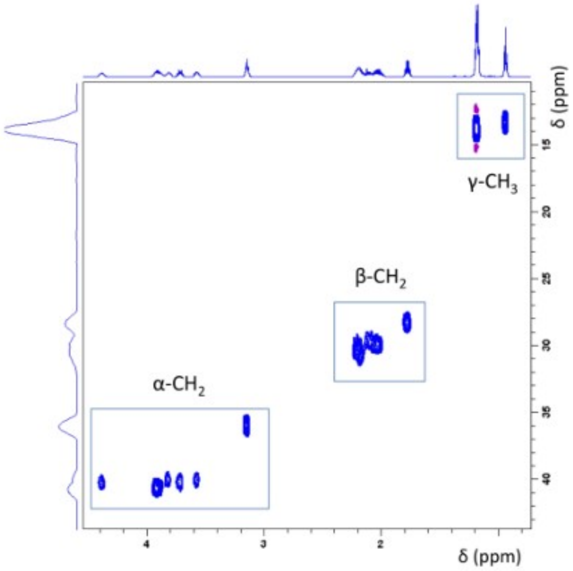

Figure 4.10. HMQC spectrum of 3 mM $Au_{38}(SC3)_{24}$ in C_6D_6 at 45 °C.

In Table 4.1, we assigned some of the observed resonances to specific ligand types. One group of proton resonances is nondiastereotopic, and both the ^{1}H and ^{13}C signals are upfield with respect to those of the corresponding diastereotopic nuclei. These resonances can be safely assigned to the outer ligands because these CH_2 groups are the farthest from where chirality originates. This assignment is also in line with the fact that in clusters showing the same double-staple motif, as in $Au_{25}(SR)_{18}$,[53,55,56] the resonances of the outer ligands are those less affected by the cluster core. We looked for a possible interligand nuclear Overhauser effect (NOE) between the *α*-CH_2 protons. The NOESY map (Figure 4.11) was analyzed by eliminating the cross peaks due to scalar correlations (from TOCSY). As to the Out ligands, the NOESY spectrum shows only a weak interaction of the *α*-CH_2 at 3.143 ppm with those at 3.878 and 3.922 ppm, which pertain to the In-1 ligands. Inspection of the $Au_{38}(SC_2H_4Ph)_{24}$ structure shows that indeed these protons can be as close as 2.5 Å, whereas the other two *α*-CH_2 types appear to be more distant. The so-identified In-1 ligands show very small diastereotopic effects, which is in keeping with their distance from the main body of the cluster. The only other detectable NOE correlations are between the proton at 4.384 ppm and those at 3.813 and 3.574 ppm, which correspond to the *α*-CH_2 protons of the S and In-2 ligands. In this case too, the available structural data show distances as close as 2.5 Å. On the basis of the data, it is unclear which of the two groups of resonance the In-2 and S ligands correspond to. We stress, however, that this analysis is based on a comparison between solid-state structural data and NMR results in solution. In the latter, the dynamics of the monolayer is much more pronounced, and therefore, our conclusions should only be considered as plausible.

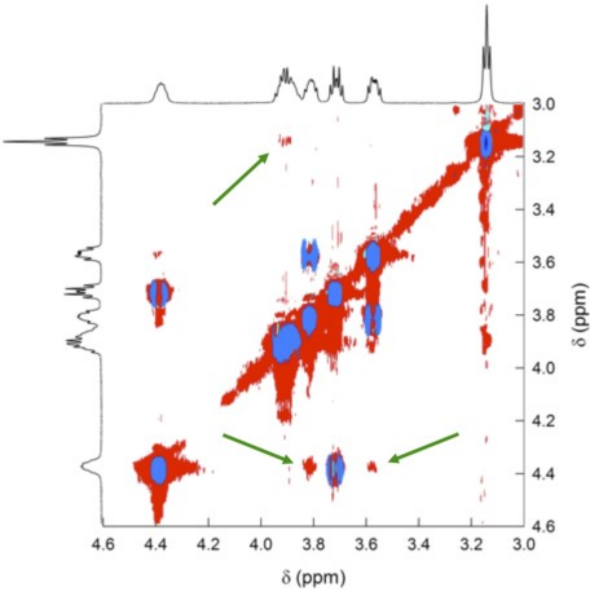

Figure 4.11. NOESY spectrum of 3 mM $Au_{38}(SC3)_{24}$ (in red) in C_6D_6 at 45 °C. The cross peaks due to scalar correlations, from TOCSY, are in blue. The green arrows mark the weak interactions discussed in the text.

The NMR results obtained for $Au_{38}(SC3)_{24}$ are in line with those of $Au_{38}(SC3)_{24}$ (Table 4.1). Its ^{1}H NMR spectrum (Figure 4.6) shows a smaller chemical-shift range for the methyl resonances (*δ*-CH_3, from 0.8 to 1.1 ppm), a complicated signal shape at 1.4−1.85 ppm caused by the signals of the *β*-CH_2 and *γ*-CH_2 protons, and a series of multiplets at 3.15−4.55 ppm. The TOCSY (Figure 4.12) and HMQC (Figure 4.13) analyses demonstrate the presence of four nonequivalent types of butanethiolate ligands. This information, together with the integrals, shows that each type represents 6 equiv thiolates, in equal amount.

The first ligand type shows a perfectly resolved CH_2-CH_2-CH_2-CH_3 spin system in which the protons in each CH_2 are magnetically equivalent. As for $Au_{38}(SC3)_{24}$, we assign these resonances to the outer ligands. In the other ligand types, the CH_2 methylene protons display a well-defined diastereotopicity with $\Delta\delta$ values of 0.061−0.685 ppm (α-CH_2), 0.044−0.085 ppm (β-CH_2), and 0.010−0.029 ppm (γ-CH_2). As to the other resonance types, the NOESY (Figure 4.14) shows the same correlations discussed for $Au_{38}(SC4)_{24}$. The case of $Au_{38}(SC4)_{24}$ thus shows very similar features to $Au_{38}(SC3)_{24}$, but also provides the further piece of information that the diastereotopicity effect propagates as far as at least 3 carbon atoms from the cluster surface, though the $\Delta\delta$ now is very small. For both clusters, the NMR pattern is thus extremely detailed and informative. This is in net contrast to a recent report of a very similar cluster, $Au_{38}(SC3)_{24}$ (where C6 stands for hexanethiolate), whose NMR spectrum is shown as displaying only the peaks of the free ligand.[68]

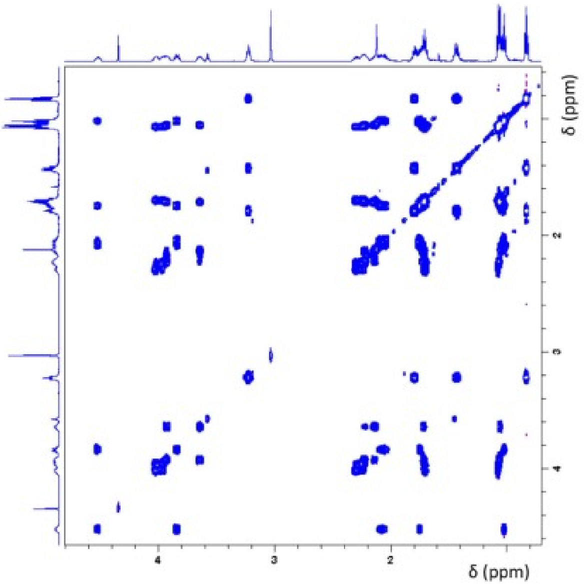

Figure 4.12 TOCSY spectrum of 3 mM $Au_{38}(SC4)_{24}$ in C_6D_6 at 45 °C.

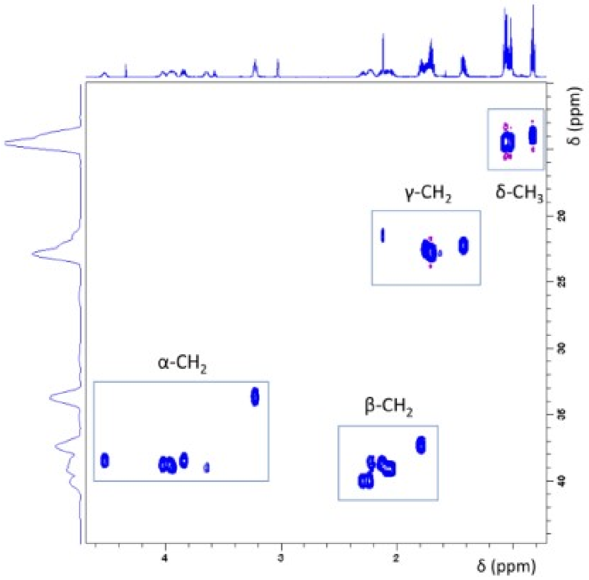

Figure 4.13 HMQC spectrum of 3 mM $Au_{38}(SC4)_{24}$ in C_6D_6 at 45 °C.

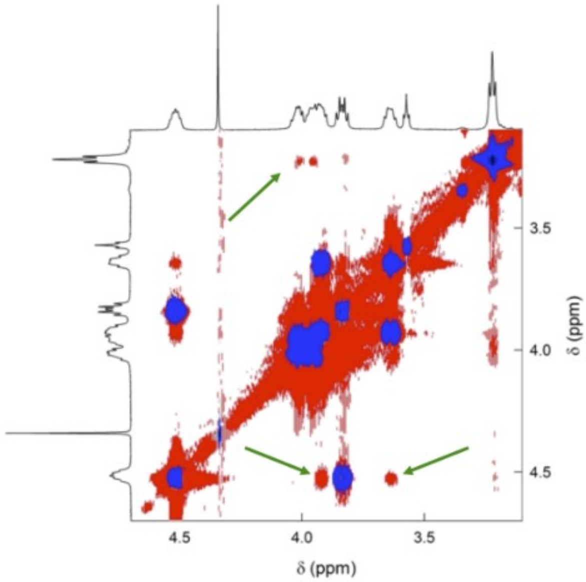

Figure 4.14 NOESY spectrum of 3 mM $Au_{38}(SC4)_{24}$ (in res) in C_6D_6 at 45 °C. The cross peaks due to scalar correlations, from TOCSY, are in blue. The green arrows mark the weak interactions discussed in the text.

4.2.4 Electrochemistry and Kinetics

Table 4.2 summarizes the main redox potentials for both clusters and thiolate ligands.

Table 4.2 Electrochemical Formal Potential and Diffusion Coefficient Data[a]

Redox couple or D	$Au_{25}C3$	$Au_{38}C3$	$Au_{25}C4$	$Au_{38}C4$
+4/+3		1.177[b]		1.220[b]
+3/+2	1.119	1.030[b]	1.169	1.058
+2/+1	0.924	0.510	0.932	0.520
+1/0	0.145	0.231	0.139	0.203
0/−1	−0.171	−0.966	−0.188	−0.992
−1/−2	−1.795	−1.197	−1.814	−1.247
−2/−3		−1.561[b]		−1.614[b]
D	6.2×10^{-6}	4.8×10^{-6}	5.6×10^{-6}	4.1×10^{-6}

[a] Formal potentials (E° vs SCE, V) in DCM/0/1 M TBAH at 25°C. Diffusion coefficients ($cm^2 s^{-1}$), obtained by cyclic voltammetry measurements at low scan rates. [b] Redox potentials: The formation of these charge states is affected by subsequent chemical reactions.

Whereas we already described the DPV pattern of the two $Au_{25}(SR)_{18}$ clusters,[69,70] a comparison between the two $Au_{38}(SC4)_{24}$ clusters shows that the only difference is a larger potential separation between the peaks of $Au_{38}(SC4)_{24}$ with respect to $Au_{38}(SC3)_{24}$.

The electrochemical gap can be calculated as the formal potential (E°) difference between the +1/0 and 0/−1 redox couples, whereas the HOMO−LUMO gap can be estimated by subtracting from such a potential difference the charging energy.[69] The latter can be obtained either by the E° difference between the +2/+1 and +1/0 states or the 0/−1 and −1/−2 states. For $Au_{38}(SC3)_{24}$ and $Au_{38}(SC4)_{24}$, we can thus calculate an average HOMO−LUMO gap of 0.88 and 0.85 eV, respectively, and for $Au_{25}(SC3)_{18}$ and $Au_{25}(SC4)_{18}$, the corresponding gaps are 1.31 and 1.30 eV, respectively.[69]

The progressive transformation of $Au_{25}(SR)_{18}$ into $Au_{38}(SR)_{24}$ can be studied very effectively by electrochemistry. In a typical experiment, a 0.4 mL solution of 30 mM $Au_{25}(SR)_{18}^0$ was taken to 65 °C, and then small aliquots (20 μL) were collected at various reaction times. These samples were quenched by dilution (100×) and storage in the fridge. For the electrochemical measurements, each sample was dried and added to a cell containing 1 mL of DCM/0.1 M tetrabutylammonium hexafluorophosphate (TBAH). After deoxygenation with argon, the sample was studied by differential pulse voltammetry (DPV) at 25 °C. Figure 4.15 shows the DPV behaviors of $Au_{25}(SC4)_{18}$, purified $Au_{38}(SC4)_{24}$, and a series of DPVs recorded at different reaction times. The DPV sequence evidences the progressive decrease of the current of the peaks of $Au_{25}(SC4)_{18}$ and the corresponding birth and growth of those of $Au_{38}(SC4)_{24}$. Traces of the $Au_{38}(SC4)_{24}$ peaks are already observable after 4 h. A very similar trend was observed for the transformation of $Au_{25}(SC3)_{18}^0$.

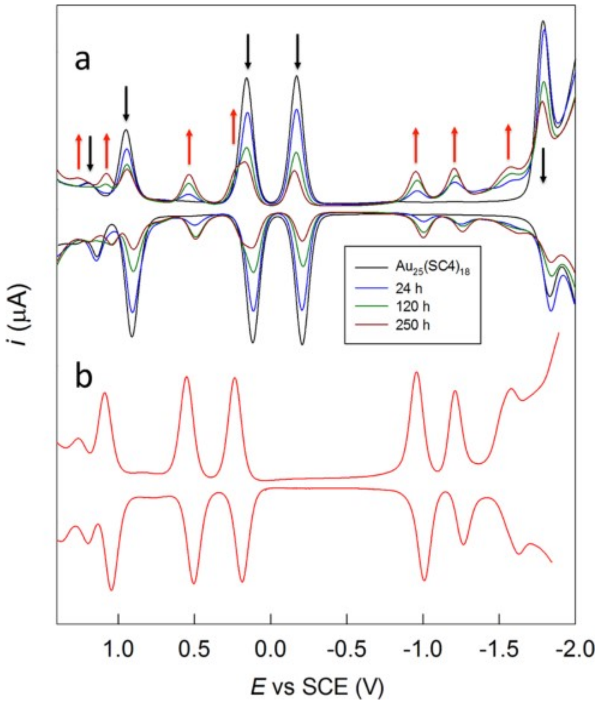

Figure 4.15 (a) DPV curves of samples taken (see text) at different times (see legends) during the fusion of 30 mM $Au_{25}(SC4)_{18}^0$ at 65°C in toluene. The black and red arrows mark the decrease of the peaks of $Au_{25}(SC4)_{18}^0$ and the increase

of those of $Au_{38}(SC4)_{24}$, respectively. (b) DPV of purified $Au_{38}(SC4)_{24}$. The DPV experiments were carried out in DCM/0.1 M TBAH, at 25 °C, and using a glassy carbon electrode.

The kinetic analysis for the disappearance of $Au_{25}(SC4)_{18}^{0}$ was studied by monitoring the time evolution of the 0/−1 redox couple. Figure 4.7 shows the concentration vs time profile, the second-order fit to the data, and the corresponding second-order plot for the irreversible disappearance of Au_{25}. The latter is linear ($r^2 = 0.996$) and allows calculating a rate constant k of 1.28×10^{-4} $M^{-1}\ s^{-1}$, and thus an initial half-life time of 72.3 h. A similar analysis was carried out for the increase of the DPV peak current of the +2/+1 redox couple of $Au_{38}(SC4)_{24}$, normalized for the square root of D. The increase in Au_{38} is quite complementary, in a 1:2 ratio, to the decrease of Au_{25}. For times longer than ca. 10 h, however, the increase in concentration of Au_{38} is less than the quantitative increase (eventually, by ca. 30%) expected on the basis of the disappearance rate of Au_{25}. We checked whether this was due to a similar self-fusion reaction affecting the concentration of $Au_{38}(SC4)_{24}$, but found that a 30 mM toluene solution of pure $Au_{38}(SC4)_{24}$ does not change even after 1 week at 65 °C (Figure 16). This indicates that a small fraction of $Au_{38}(SC4)_{24}$ reacts with the fragments released during the fusion reaction (eq 1):

$$2\ Au_{25}(SC4)_{18}^{0} \rightarrow Au_{38}(SC4)_{24} + 12\ Au(SC4) \qquad (1)$$

For the disappearance of $Au_{25}(SC3)_{18}^{0}$, we obtained similar plots and could determine a fusion rate constant of 3.7×10^{-4} $M^{-1}s^{-1}$.

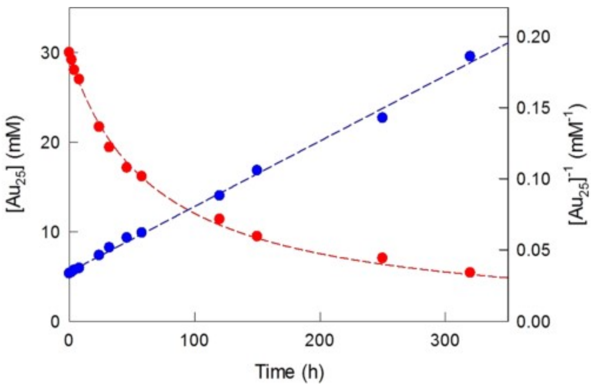

Figure 4.16 Concentration vs time profile (red symbols, scale on left) for the fusion of 30 mM $Au_{25}(SC4)_{18}^{0}$ at 65 °C in toluene, as measured by monitoring the decrease of the DPV peak pertaining to the 0/−1 redox couple. The red curve is the second-order best fit to the data, which are also shown in blue (with the corresponding linear fit) as the variation of the reciprocal of the $Au_{25}(SC4)_{18}^{0}$ concentration (scale on right).

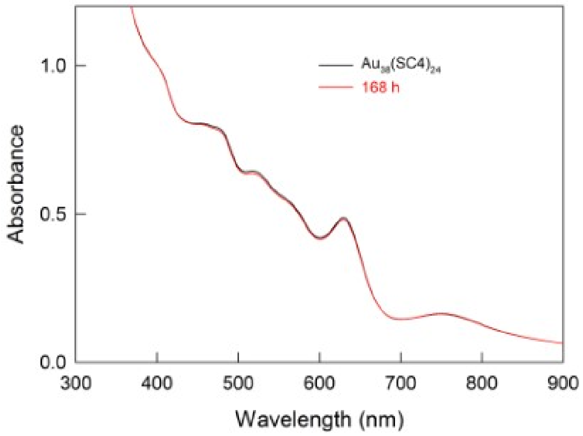

Figure 4.17 UV-vis absorption spectra of samples (t = 0 and t = 168 h) withdrawn from 30 mM $Au_{38}(SC4)_{24}$ in toluene at 65 °C.

UV−vis spectroscopy is also suitable to provide the fusion rate constants, although here the analysis is less straightforward than in the electrochemical approach due to the overlap between the spectra of the two clusters. The rate constant was obtained by second-order kinetic analysis of the variation in absorbance observed at 588 nm, taking into account the molar extinction coefficients of the two clusters (for $Au_{25}(SC4)_{18}^{0}$ and $Au_{38}(SC4)_{24}$ the values at 588 nm are 6.28×10^{3} and 2.97×10^{4} $M^{-1}cm^{-1}$, respectively) and limiting the analysis to the initial hours of the transformation. For $Au_{25}(SC3)_{18}^{0}$ and $Au_{25}(SC4)_{18}^{0}$, we estimated 6×10^{-4} and 1.7×10^{-4} $M^{-1}s^{-1}$, respectively, in fair agreement with the more accurate electrochemical results.

4.2.5 Mechanistic Insights

This fusion reaction is indeed very unexpected because of the well-known stability of $Au_{25}(SR)_{18}$. To gain some insights into its mechanism and the reasons why such a transformation was never observed before, we carried out a series of specific experiments. Each one was carried out by keeping the concentration and temperature constant at 30 mM and 65 °C, respectively. It is worth noting that, so far, most research groups have focused on studying the as-prepared anionic form of $Au_{25}(SR)_{18}$, whereas in our experiments we consistently used its one-electron oxidation product, namely the neutral, paramagnetic species. We thus run an experiment using $[Oct_4N^+]$ $[Au_{25}(SC3)_{18}^-]$, in which Oct_4N^+ is the tetraoctylammonium countercation, and found that no reaction occurs even after 1 week (Figure 4.18). This is in keeping with the reaction being hampered by repulsion between the negative charges carried by the clusters. It is worth mentioning that a somehow similar attempt was carried out using $[Oct_4N^+]$ $[Au_{25}(SC_2H_4Ph)_{18}^-]$ in the presence of PhC_2H_4SH (toluene, 80 °C), although this resulted in decomposition of the cluster.[71]

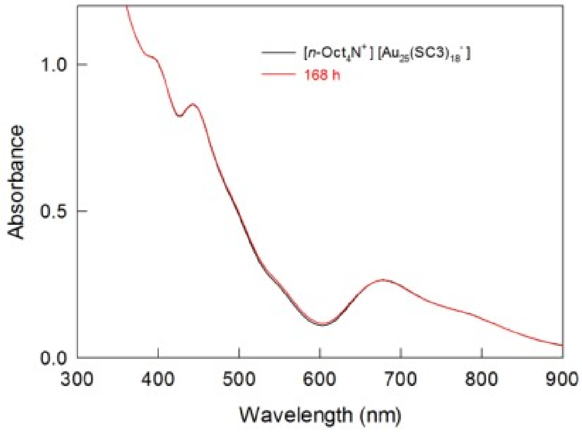

Figure 4.18 UV-vis absorption spectra of samples (t = 0 and t = 168 h) withdrawn from 30 mM $[Oct_4N^+]$ $[Au_{25}(SC3)_{18}^-]$ in toluene at 65 °C.

We then prepared $Au_{24}Hg(SC3)_{18}^0$. This cluster was synthesized according to a published method[72] and was characterized by UV−vis absorption spectroscopy and ESI mass spectrometry (Figures 4.19 and 4.20). The DPV or the cyclic voltammetry (Figure 4.21) of $Au_{24}Hg(SC3)_{18}^0$ shows that exchange of Au with Hg shifts the peaks very significantly toward more positive potential values; in particular, the E° of the 0/−1 redox couple shifts by 0.55 V, which is consistent with a previous findings for $Au_{24}Hg(SC2H4Ph)_{18}^0$.[72] This minor structural modification (1 out of 6 staples) should not affect the fusion rate significantly. The rationale of comparing the behaviors of $Au_{24}Hg(SC3)_{18}^0$ and $Au_{25}(SC3)_{18}^0$ is that the former is both neutral and diamagnetic.[72] In our test experiment, we observed that no reaction occurs after 60 h. In particular, Figure 22 shows that the spectrum of $Au_{24}Hg(SC3)_{18}^0$ only undergoes a small decrease in absorbance but no variation in its pattern and features (when normalized for the absorbance, the two spectra are overlapping very well). Conversely, the time evolution (48 h) of the spectrum of $Au_{25}(SC3)_{18}^0$ exhibits the already discussed changes caused by the progressive Au_{25} to Au_{38} fusion. This result suggests that besides charge, the unpaired electron of $Au_{25}(SR)_{18}^0$ should also play a role in making the fusion reaction possible.

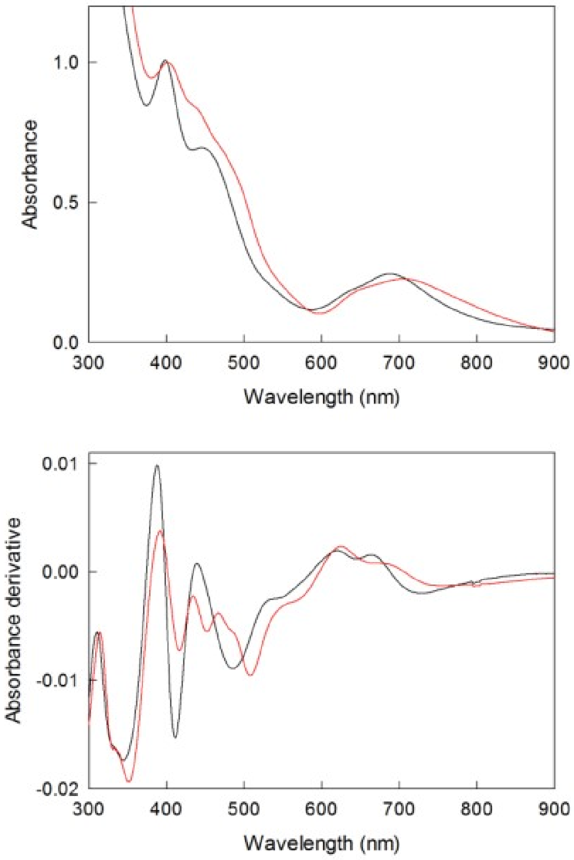

Figure 4.19 UV-vis absorption spectrum of $Au_{24}Hg(SC3)_{18}^0$ (red curve) in comparison with $Au_{25}(SC3)_{18}^0$ (black curve). The lower graph shows the corresponding derivative plots.

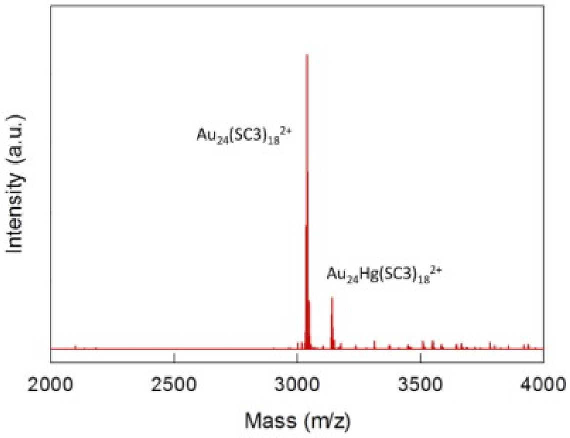

Figure 4.20 ESI mass spectrum of $Au_{24}Hg(SC3)_{18}$. The molecular weight of this cluster is 6280.47. The ESI mass spectrum of $Au_{24}Hg(SC3)_{18}$ shows two main signals. The signal at m/z 3139.89 corresponds to the base peak of $[M]^{2+}$ for $Au_{24}Hg(SC3)_{18}$, whereas the signal at 3039.90 m/z is assigned to loss of Hg from the previous cluster, to yield $Au_{24}(SC3)_{18}$. The spectrum was acquired at quite low voltage (3 kV) to inhibit in-source fragmentation.

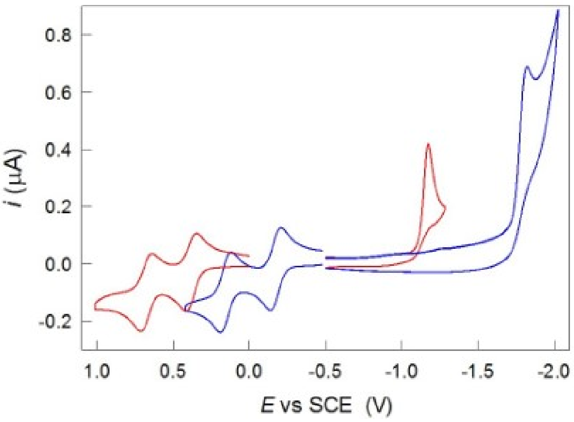

Figure 4.21 Cyclic-voltammetry curves for the two-step two-electron oxidation and the single-step multielectron reduction of 0.60 mM $Au_{24}Hg(SC3)_{18}^{0}$ (red traces) and 0.60 mM $Au_{25}(SC3)_{18}^{-}$ (blue traces). Glassy-carbon electrode, 0.2 V s^{-1}, DCM/0.1 M TBAH, 25 °C.

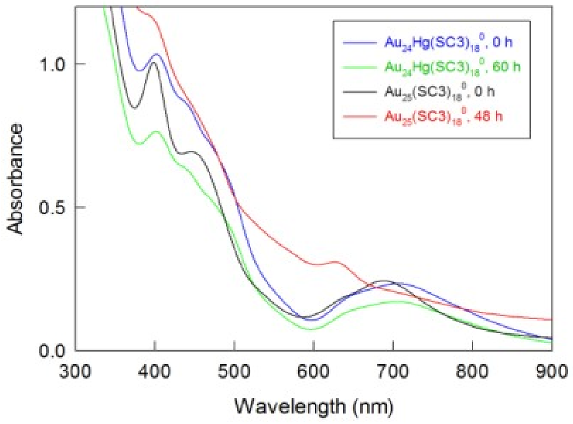

Figure 4.22 Comparison between the UV-vis absorption spectra of samples taken at different times (see legends) during the reaction of 30 mM $Au_{24}Hg(SC3)_{18}$ and 30 mM $Au_{25}(SC3)_{18}^0$. Toluene, 65 °C.

We tested a cluster protected by a longer alkanethiolate, that is, octanethiolate. The reaction still occurs (Figure 4.23), although with a smaller rate constant, $k = 6.6 \times 10^{-5}$ $M^{-1}s^{-1}$ (from analysis of the optical data). This shows that the length of the ligand does not hamper the fusion reaction and further points to the presence of a very fluid monolayer.[53] The very high quality of the optical spectrum of purified $Au_{38}(SC8)_{24}$, as well as those of the other two Au_{38} clusters, is worth noticing. The fusion reaction does not occur only with linear-chain alkanethiolate protected clusters. Figure 4.24 shows that this reaction also works with $Au_{25}(SC_2H_4Ph)_{18}^0$, which is an especially popular cluster. The estimated rate constant is 8.4×10^{-5} $M^{-1}s^{-1}$. By using $Au_{25}(SC3)_{18}^0$ we could check that the fusion occurs successfully also at room temperature, though on a much longer time scale (for this cluster, a few months). It is finally worth mentioning that in our preliminary experiments, we tested other low-polarity solvents, such as heptane, and found that the reaction proceeds equally well and is slightly faster. We selected toluene as the solvent of choice because $Au_{25}(SC3)_{18}^0$, which was expected to provide especially clear-cut NMR results, is not sufficiently soluble in alkanes. The same solubility issue also holds true for $Au_{25}(SC_2H_4Ph)_{18}^0$.

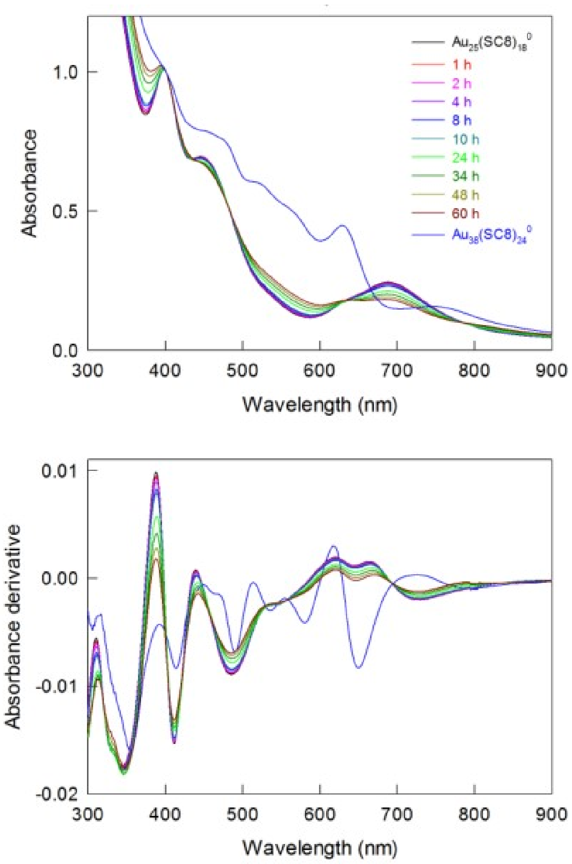

Figure 4.23 UV-vis absorption spectra of samples taken at different times (see legends) during the reaction of 30 mM $Au_{25}(SC8)_{18}^0$ at 65 °C in toluene. The lower graph shows the corresponding derivative plots. The black and the top blue curves show the spectra of $Au_{25}(SC8)_{18}^0$ and the purified product, respectively.

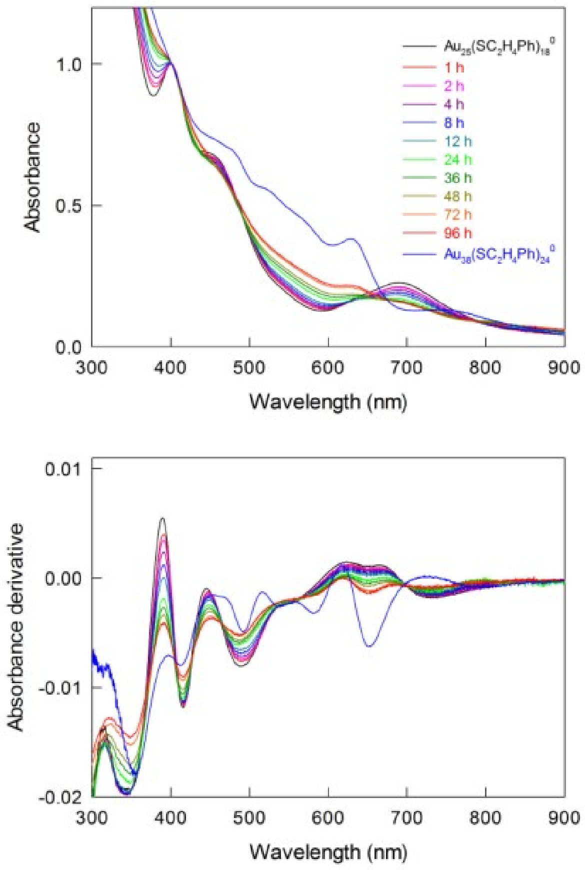

Figure 4.24 UV-vis absorption spectra of samples taken at different times (see legends) during the reaction of 30 mM $Au_{25}(SC_2H_4Ph)_{18}^0$ at 65 °C in toluene. The lower graph shows the corresponding derivative plots. The black and the top blue curves show the spectra of $Au_{25}(SC_2H_4Ph)_{18}^0$ and the purified product, respectively.

On the basis of the data, we propose that the reaction involves formation of a precursor complex in which significant van der Waals interactions between the ligands of the two interacting clusters act as the initial driving force. Previously, we found that this kind of interaction plays a key factor, together with intercluster Au−Au bonds, in the formation and stabilization of Au_{25} polymers in the solid state.[45,46] For this system, dispersion-corrected density functional theory indicated that the binding energy between two $Au_{25}(SC4)_{18}^0$ clusters in a dimeric state is indeed significantly large.[45] Au−Au bond formation between the two radicals $Au_{25}(SR)_{18}^0$ entails overlap between the two singly occupied molecular orbitals (SOMOs). It is thus conceivable that “sticky” van der Waals interactions may stabilize a dimeric precursor complex for a sufficiently long time to make the reaction between the two radicals possible also inside the solvent cage. As in the solid state, staple distortion and formation of an (initial) intercluster Au−Au bond would ensue. By studying electrochemically the distance effect on the electron-transfer rate across the monolayer of many $Au_{25}(SR)_{18}$ clusters, we showed that interactions between ligands are indeed very valuable to understand the dynamic structure of the monolayer.[53] van der Waals interactions are now being recognized as an important bonding factor in large Au nanoparticles and self-assembled monolayers.[73] As we pointed out earlier,[45,53,74] this is an even more important factor affecting the dynamics and properties of the monolayer capping small clusters. We thus speculate that the reaction kinetics is the result of a preequilibrium reaction in which a Au_{25} dimer is stabilized by the same mechanism (dispersion forces between ligands and intercluster Au−Au bond formation) described for this type of clusters in the solid state,[45] followed by a slow step entailing an irreversible bond reorganization. Interestingly, this reaction could also be seen as involving the formation of a superatomic molecule[75] from two open-shell superatoms.[76]

4.3 Conclusion

We have described a reaction in which the most stable and studied molecular cluster, $Au_{25}(SR)_{18}$, can be smoothly transformed into $Au_{38}(SR)_{24}$, another of the stable atomically precise clusters. Although transformations of clusters have been reported, that of $Au_{25}(SR)_{18}$ into $Au_{38}(SR)_{24}$ is peculiar in many senses: (i) it involves the two most studied molecular nanoclusters and truly features a benchmark case of fusion; (ii) it is the only case in which a solution-soluble, stable cluster is assembled directly by starting from the fundamental building block Au_{13}, a molecularly guided process that has been sought for many years;[5,25−31] (iii) as opposed to other transformations, this reaction does not require any co-reagent, whether the same or an exogenous thiol, or very high temperatures, or a different cluster;[11,12] (iv) this reaction is also very different from previously reported cases of transformations involving collision of different clusters in which, however, the number of metal atoms and ligands does not change; 12 (v) because $Au_{25}(SR)_{18}$ can be prepared in quite high yields, whereas the preparation of $Au_{38}(SR)_{24}$ is generally tedious and not as successful, this fusion reaction could be particularly useful to synthesize $Au_{38}(SR)_{24}$ capped by difficult to make or expensive thiols; and (vi) the very fact that this reaction of Au_{25} is so unexpected, whereas under identical conditions $Au_{38}(SR)_{24}$ is fully stable, may lead to revise some concepts of the relative stability of these clusters as well as trigger further work in this ever-expanding field of study.

4.4 Experimental Section

The clusters were prepared in the form of $Au_{25}(SR)_{18}^{-}$ anions and oxidized to $Au_{25}(SR)_{18}^{0}$ by column chromatography under aerobic conditions, as we already described.[45,49,50] The synthesis of $Au_{24}Hg(SC3)_{18}$ was carried out as described.[72] As to the fusion reactions, after a given amount of time, which depended on the ligand length, the reaction solution was cooled to room temperature and $Au_{38}(SR)_{24}$ was isolated by silica gel (Macherey-Nagel MN-Kieselgel 60 M, 230−400 mesh) column chromatography, under a nitrogen flux, and using hexane-toluene 5:1 as the eluent.

UV−vis absorption spectra of the clusters or cluster transformations were obtained in toluene with 2 mm cuvettes. The spectra were recorded with a CARY 5000 spectrophotometer. The spectra resolution was 0.5 nm.

The ESI mass-spectrometry (MS) measurements were carried out with a Q-Exactive hybrid quadrupole-Orbitrap high-resolution mass spectrometer (Thermo Fisher Scientific, Waltham, Massachusetts, USA). MS conditions were: electrospray ionization in positive mode, resolution of 70,000 (at m/z 200), target automatic gain control of 1×10^{6}, maximum injection time of 30 ms, scan range 2000−6000 a.m.u, capillary voltage of 4.5 kV, RF voltage of 100 V, capillary temperature of 100 °C, and auxiliary gas heater temperature of 350°C; nitrogen was used as sheath, auxiliary, and sweep gas at 20, 10, and 5 au, respectively.

The nanocluster samples (0.01 mg mL^{-1} in DCM) were infused by using a syringe pump at 10 μL min^{-1}. No cesium acetate, usually added to enhance ionization, was used. Calibration was performed with a standard solution purchased by Thermo Fisher Scientific (Pierce ESI positive Ion Calibration Solution). The software for analysis of MS data was Xcalibur 4.0 (Thermo Fisher Scientific).

^{1}H and ^{13}C NMR spectra were obtained on a Bruker Avance DMX-600 MHz spectrometer equipped with a 5 mm TX-1 inverse probe powered by field gradients along the x,y,z-axes and operating at 599.90 and 150.61 MHz, respectively. The probe temperature was controlled within ±0.1 °C through a Bruker BVT3000 temperature controller. Benzene-d_6 (100%, d_6) was purchased from Aldrich. The chemical shift values (δ) are given as ppm downfield from internal tetramethylsilane for both ^{1}H and ^{13}C nuclei. Integral values for the proton spectra were obtained by a prescan delay of 10 s to ensure a complete relaxation for all the resonances. The proton assignments were performed by TOCSY and NOESY. The ^{13}C chemical shift values were obtained from HMQC experiments.

The electrochemical experiments were carried out in DCM/0/1 M TBAH, under an Ar atmosphere in a glass cell thermostated at 25 °C. The working electrode was a 0.17 mm radius glassy carbon (GC) disk prepared and activated as already described.[77,78] The electrochemical area, 9.05×10^{-4} cm^2, was determined through measurements of the peak current for the oxidation of ferrocene (at low scan rates) in N,N-dimethylformamide/0.1 M n-Bu_4NClO_4, which is a medium where ferrocene has a diffusion coefficient of 1.13×10^{-5} cm^2 s^{-1}. The counter electrode was a Pt wire. An Ag wire, which was kept in a tube filled with the same electrolyte solution and separated from the main compartment by a Vycor frit, served as a quasi-reference electrode. Calibration of the latter was performed by addition of ferrocene at the end of the experiments; in the above solvent/electrolyte system, the ferricenium/ferrocene redox couple has E° = 0.460 V against the KCl saturated calomel electrode (SCE). All potential values are reported against SCE. We used a CHI 660c or a CH760d electrochemical workstation. To minimize the ohmic drop between the working and the reference electrodes, we used the positive feedback correction. For the DPV experiments, we used peak amplitude of 50 mV, pulse width of 0.05 s, 2 mV increments per cycle, and pulse period of 0.1 s. Cyclic voltammetry of 0.5 mM solutions of the clusters was used to determine their D values. The peak current (i p) measured at low scan rates (v) allowed determining the diffusion coefficient D by using the equation that relates $i_p / v^{1/2}$ to $D^{1/2}$.[79]

4.5 References

1. Tsukuda, T., Häkkinen, H. Eds. Protected Metal Clusters: From Fundamentals to Applications. *Frontiers of Nanoscience*; Elsevier: Amsterdam, 2015; Vol. 9.
2. Jin, R.; Zeng, C.; Zhou, M.; Chen, Y. Atomically Precise Colloidal Metal Nanoclusters and Nanoparticles: Fundamentals and Opportunities. *Chem. Rev.* **2016**, *116*, 10346-10413.
3. Chakraborty, I.; Pradeep, T. Atomically Precise Clusters of Noble Metals: Emerging Link between Atoms and Nanoparticles. *Chem. Rev.* **2017**, *117*, 8208-8271.
4. Murray, R. W. Nanoelectrochemistry: Metal Nanoparticles, Nanoelectrodes, and Nanopores. *Chem. Rev.* **2008**, *108*, 2688-2720.
5. Nishigaki, J.; Koyasu, K.; Tsukuda, T. Chemically Modified Gold Superatoms and Superatomic Molecules. *Chem. Rec.* **2014**, *14*, 897-909.
6. Knoppe, S.; Bürgi, T. Chirality in Thiolate-Protected Gold Clusters. *Acc. Chem. Res.* **2014**, *47*, 1318-1326.
7. Tian, S.; Li, Y.; Li, M.; Yuan, J.; Yang, J.; Wu, Z.; Jin, R. Erratum: Structural Isomerism in Gold Nanoparticles Revealed by X-Ray Crystallography. *Nat. Commun.* **2015**, *6*, 10012.
8. Tsukuda, T. Toward an Atomic-Level Understanding of Size-Specific Properties of Protected and Stabilized Gold Clusters. *Bull. Chem. Soc. Jpn.* **2012**, *85*, 151-168.
9. Qian, H.; Zhu, M.; Wu, Z.; Jin, R. Quantum Sized Gold Nanoclusters with Atomic Precision. *Acc. Chem. Res.* **2012**, *45*, 1470-1479.

10. Negishi, Y.; Kurashige, W.; Niihori, Y.; Nobusada, K. Toward the Creation of Stable, Functionalized Metal Clusters. *Phys. Chem. Chem. Phys.* **2013**, *15*, 18736-18751.
11. Zeng, C.; Chen, Y.; Das, A.; Jin, R. Transformation Chemistry of Gold Nanoclusters: From One Stable Size to Another. *J. Phys. Chem. Lett.* **2015**, *6*, 2976-2986.
12. Krishnadas, K. R.; Baksi, A.; Ghosh, A.; Natarajan, G.; Som, A.; Pradeep, T. Interparticle Reactions: An Emerging Direction in Nanomaterials Chemistry. *Acc. Chem. Res.* **2017**, *50*, 1988-1996.
13. Schaaff, T. G.; Whetten, R. L. Controlled Etching of Au:SR Cluster Compounds. *J. Phys. Chem. B* **1999**, *103*, 9394−9396.
14. Templeton, A. C.; Wuelfing, W. P.; Murray, R. W. Monolayer-Protected Cluster Molecules. *Acc. Chem. Res.* **2000**, *33*, 27-36.
15. Niihori, Y.; Hossain, S.; Sharma, S.; Kumar, B.; Kurashige, W.; Negishi, Y. Understanding and Practical Use of Ligand and Metal Exchange Reactions in Thiolate-Protected Metal Clusters to Synthesize Controlled Metal Clusters. *Chem. Rec.* **2017**, *17*, 473-484.
16. Nimmala, P. R.; Dass, A. $Au_{99}(SPh)_{42}$ Nanomolecules: Aromatic Thiolate Ligand Induced Conversion of $Au_{144}(SCH_2CH_2Ph)_{60}$. *J. Am. Chem. Soc.* **2014**, *136*, 17016-17023.
17. Nimmala, P. R.; Theivendran, S.; Barcaro, G.; Sementa, L.; Kumara, C.; Jupally, V. R.; Apra, E.; Stener, M.; Fortunelli, A.; Dass, A. Transformation of $Au_{144}(SCH_2CH_2Ph)_{60}$ to $Au_{133}(SPh\text{-}tBu)_{52}$ Nanomolecules: Theoretical and Experimental Study. *J. Phys. Chem. Lett.* **2015**, *6*, 2134-2139.
18. Zeng, C.; Liu, C.; Pei, Y.; Jin, R. Thiol Ligand-Induced Transformation of $Au_{38}(SC_2H_4Ph)_{24}$ to $Au_{36}(SPh\text{-}t\text{-}Bu)_{24}$. *ACS Nano* **2013**, *7*, 6138-6145.
19. Zeng, C.; Liu, C.; Chen, Y.; Rosi, N. L.; Jin, R. Gold−Thiolate Ring as a Protecting Motif in the $Au_{20}(SR)_{16}$ Nanocluster and Implications. *J. Am. Chem. Soc.* **2014**, *136*, 11922-11925.
20. Das, A.; Li, T.; Li, G.; Nobusada, K.; Zeng, C.; Rosi, N. L.; Jin, R. Crystal Structure and Electronic Properties of a Thiolate-Protected Au_{24} Nanocluster.

Nanoscale, **2014**, *6*, 6458-6462.

21. Zeng, C.; Li, T.; Das, A.; Rosi, N. L.; Jin, R. Chiral Structure of Thiolate-Protected 28-Gold-Atom Nanocluster Determined by X-Ray Crystallography. *J. Am. Chem. Soc.* **2013**, *135*, 10011-10013.
22. Dass, A.; Jones, T. C.; Theivendran, S.; Sementa, L.; Fortunelli, A. Core Size Interconversions of Au_{30}(S-tBu)$_{18}$ and Au_{36}(SPhX)$_{24}$. *J. Phys. Chem. C* **2017**, *121*, 14914-14919.
23. Higaki, T.; Liu, C.; Zhou, M.; Luo, T. Y.; Rosi, N. L.; Jin, R. Tailoring the Structure of 58-Electron Gold Nanoclusters: $Au_{103}S_2$(S-Nap)$_{41}$ and its Implications. *J. Am. Chem. Soc.* **2017**, *139*, 9994-10001.
24. Gan, Z.; Chen, J.; Wang, J.; Wang, C.; Li, M. B.; Yao, C.; Zhuang, S.; Xu, A.; Li, L.; Wu, Z. The Fourth Crystallographic Closest Packing Unveiled in the Gold Nanocluster Crystal. *Nat. Commun.* **2017**, *8*, 14739.
25. Nobusada, K.; Iwasa, T. Oligomeric Gold Clusters with Vertex-Sharing Bi- and Triicosahedral Structures. *J. Phys. Chem. C* **2007**, *111*, 14279-14282.
26. Jiang, D.-e.; Nobusada, K.; Luo, W. D.; Whetten, R. L. Thiolated Gold Nanowires: Metallic versus Semiconducting. *ACS Nano* **2009**, *3*, 2351-2357.
27. Das, A.; Li, T.; Nobusada, K.; Zeng, Q.; Rosi, N. L.; Jin, R. Total Structure and Optical Properties of a Phosphine/Thiolate-Protected Au_{24} Nanocluster. *J. Am. Chem. Soc.* **2012**, *134*, 20286-20289.
28. Goh, J.-Q.; Malola, S.; Häkkinen, H.; Akola, J. Role of the Central Gold Atom in Ligand-Protected Biicosahedral Au_{24} and Au_{25} Clusters. *J. Phys. Chem. C* **2013**, *117*, 22079-22086.
29. Malola, S.; Lehtovaara, L.; Häkkinen, H. A DFT Study of Linear Gold−Thiolate Superclusters Absorbing in the Therapeutic NIR Window. *J. Phys. Chem. Lett.* **2014**, *5*, 1329-1334.
30. Sheong, F. K.; Zhang, J. K.; Lin, Z. An $[Au_{13}]^{5+}$ Approach to the Study of Gold Nanoclusters. *Inorg. Chem.* **2016**, *55*, 11348-11353.
31. Xu, W. W.; Zeng, X. C.; Gao, Y. Au_{13}(8e): A Secondary Block for Describing a Special Group of Liganded Gold Clusters Containing Icosahedral Au_{13} Motifs. *Chem. Phys. Lett.* **2017**, *675*, 35-39.

32. Briant, C. E.; Theobald, B. R. C.; White, J. W.; Bell, L. K.; Mingos, D. M. P.; Welch, A. J. Synthesis and X-Ray Structural Characterization of the Centred Icosahedral Gold Cluster Compound $[Au_{13}(PMe_2Ph)_{10}Cl_2](PF_6)_3$; the Realization of a Theoretical Prediction. *J. Chem. Soc., Chem. Commun.* **1981**, 201-202.

33. Shichibu, Y.; Konishi, K. HCl-Induced Nuclearity Convergence in Diphosphine Protected Ultrasmall Gold Clusters: A Novel Synthetic Route to "Magic-Number" Au_{13} Cluster. *Small* **2010**, *6*, 1216-1220.

34. Richter, M.; Strähle, J. Synthesis and Structures of the Gold Cluster $[Au_{16}(AsPh_3)_8Cl_6]$. *Z. Anorg. Allg. Chem.* **2001**, *627*, 918-920.

35. Wan, X.; Tang, Q.; Yuan, S.; Jiang, D.; Wang, Q. M. Au_{19} Nanocluster Featuring a V-Shaped Alkynyl−Gold Motif. *J. Am. Chem. Soc.* **2015**, *137*, 652-655.

36. Wan, X.; Yuan, S.; Lin, Z.; Wang, Q. M. A Chiral Gold Nanocluster Au_{20} Protected by Tetradentate Phosphine Ligands. *Angew. Chem. Int. Ed.* **2014**, *53*, 2923-2926.

37. Heaven, M. W.; Dass, A.; White, P. S.; Holt, K. M.; Murray, R. W. Crystal Structure of the Gold Nanoparticle $[N(C_8H_{17})_4]$-$[Au_{25}(SCH_2CH_2Ph)_{18}]$. *J. Am. Chem. Soc.* **2008**, *130*, 3754-3755.

38. Zhu, M.; Aikens, C. M.; Hollander, F. J.; Schatz, G. C.; Jin, R. Correlating the Crystal Structure of a Thiol-Protected Au_{25} Cluster and Optical Properties. *J. Am. Chem. Soc.* **2008**, *130*, 5883-5885.

39. Shichibu, Y.; Negishi, Y.; Watanabe, T.; Chaki, N. K.; Kawaguchi, H.; Tsukuda, T. Biicosahedral Gold Clusters $[Au_{25}(PPh_3)_{10}(SC_nH_{2n+1})_5Cl_2]^{2+}$ (n = 2-18): A Stepping Stone to Cluster-Assembled Materials. *J. Phys. Chem. C* **2007**, *111*, 7845-7847.

40. Jin, R.; Liu, C.; Zhao, S.; Das, A.; Xing, H.; Gayathri, C.; Xing, Y.; Rosi, N. L.; Gil, R. R.; Jin, R. Tri-icosahedral Gold Nanocluster $[Au_{37}(PPh_3)_{10}(SC_2H_4Ph)_{10}X_2]^+$: Linear Assembly of Icosahedral Building Blocks. *ACS Nano*, **2015**, *9*, 8530-8536.

41. Song, Y.; Fu, F.; Zhang, J.; Chai, J.; Kang, X.; Li, P.; Li, S.; Zhou, H.; Zhu, M.

The Magic Au_{60} Nanocluster: A New Cluster-Assembled Material with Five Au_{13} Building Blocks. *Angew. Chem. Int. Ed.* **2015**, *54*, 8430-8434.

42. Qian, H.; Eckenhoff, T.; Zhu, Y.; Pintauer, T.; Jin, R. Total Structure Determination of Thiolate-Protected Au_{38} Nanoparticles. *J. Am. Chem. Soc.* **2010**, *132*, 8280-8281.
43. Liao, L.; Zhuang, S.; Yao, C.; Yan, N.; Chen, J.; Wang, C.; Xia, N.; Liu, X.; Li, M.-B.; Li, L.; Bao X.; Wu, Z. Structure of Chiral Au_{44}(2,4-DMBT)$_{26}$ Nanocluster with an 18-Electron Shell Closure. *J. Am. Chem. Soc.* **2016**, *138*, 10425-10428
44. Das, A.; Li, T.; Nobusada, K.; Zeng, Q.; Rosi, N. L.; Jin, R. Total Structure and Optical Properties of a Phosphine/Thiolate-Protected Au_{24} Nanocluster. *J. Am. Chem. Soc.* **2012**, *134*, 20286-20289.
45. De Nardi, M.; Antonello, S.; Jiang, D.; Pan, F.; Rissanen, K.; Ruzzi, M.; Venzo, A.; Zoleo, A.; Maran, F. Gold Nanowired: A Linear $(Au_{25})_n$ Polymer from Au_{25} Molecular Clusters. *ACS Nano*, **2014**, *8*, 8505-8512.
46. Antonello, S.; Dainese, T.; Pan, F.; Rissanen, K.; Maran, F. Electrocrystallization of Monolayer Protected Gold Clusters: Opening the Door to Quality, Quantity and New Structures. *J. Am. Chem. Soc.* **2017**, *139*, 4168-4174.
47. Parker, J. F.; Fields-Zinna, C. A.; Murray, R. W. The Story of a Monodisperse Gold Nanoparticle: $Au_{25}L_{18}$. *Acc. Chem. Res.* **2010**, *43*, 1289-1296.
48. Zhu, M.; Eckenhoff, W. T.; Pintauer, T.; Jin, R. Conversion of Anionic $[Au_{25}(SCH_2CH_2Ph)_{18}]^-$ Cluster to Charge Neutral Cluster via Air Oxidation. *J. Phys. Chem. C* **2008**, *112*, 14221-14224.
49. Dainese, T.; Antonello, S.; Gascón, J. A.; Pan, F.; Perera, N. V.; Ruzzi, M.; Venzo, A.; Zoleo, A.; Rissanen, K.; Maran, F. $Au_{25}(SEt)_{18}$, a Nearly Naked Thiolate-Protected Au_{25} Cluster: Structural Analysis by Single Crystal X-ray Crystallography and Electron Nuclear Double Resonance. *ACS Nano* **2014**, *8*, 3904-3912.
50. Agrachev, M.; Antonello, S.; Dainese, T.; Gascón, J. A.; Pan, F.; Rissanen, K.; Ruzzi, M.; Venzo, A.; Zoleo, A.; Maran, F. A Magnetic Look into the Protecting

Layer of Au_{25} Clusters. *Chem. Sci.* **2016**, *7*, 6910-6918.

51. Tofanelli, M. A.; Salorinne, K.; Ni, T. W.; Malola, S.; Newell, B.; Phillips, B.; Häkkinen, H.; Ackerson, C. J. Jahn-Teller Effects in $Au_{25}(SR)_{18}$. *Chem. Sci.* **2016**, *7*, 1882-1890.
52. Venzo, A.; Antonello, S.; Gascón, J. A.; Guryanov, I.; Leapman, R. D.; Perera, N. V.; Sousa, A.; Zamuner, M.; Zanella, A.; Maran, F. Effect of the Charge State ($z = -1, 0, +1$) on the Nuclear Magnetic Resonance of Monodisperse $Au_{25}[S(CH_2)_2Ph]_{18}^z$ Clusters. *Anal. Chem.* **2011**, *83*, 6355-6362.
53. Antonello, S.; Arrigoni, G.; Dainese, T.; De Nardi, M.; Parisio, G.; Perotti, L.; René, A.; Venzo, A.; Maran, F. Electron Transfer through 3D Monolayers on Au_{25} Clusters. *ACS Nano*, **2014**, *8*, 2788-2795.
54. Antonello, S.; Hesari, M.; Polo, F.; Maran, F. Electron Transfer Catalysis with Monolayer Protected Au_{25} Clusters. *Nanoscale*, **2012**, *4*, 5333-5342.
55. Agrachev, M.; Antonello, S.; Dainese, T.; Ruzzi, M.; Zoleo, A.; Aprà, E.; Govind, N.; Fortunelli, A.; Sementa, L.; Maran, F. Magnetic Ordering in Gold Nanoclusters. *ACS Omega* **2017**, *2*, 2607-2617.
56. Antonello, S.; Maran, F. Molecular Electrochemistry of Monolayer-Protected Clusters. *Curr. Opin. Electrochem.* **2017**, *2*, 18-25.
57. Yau, S. H.; Varnavski, O.; Goodson, T., III. An Ultrafast Look at Au Nanoclusters. *Acc. Chem. Res.* **2013**, *46*, 1506-1516.
58. Akola, J.; Walter, M.; Whetten, R. L.; Häkkinen, H.; Grönbeck, H. On the Structure of Thiolate-Protected Au_{25}. *Am. Chem. Soc.* **2008**, *130*, 3756-3757.
59. Antonello, S.; Perera, N. V.; Ruzzi, M.; Gascón, J. A.; Maran, F. Interplay of Charge State, Lability, and Magnetism in the Molecule-like $Au_{25}(SR)_{18}$ Cluster. *J. Am. Chem. Soc.* **2013**, *135*, 15585-15594.
60. Tlahuice-Flores, A.; Whetten, R. L.; Jose-Yacaman, M. Ligand Effects on the Structure and the Electronic Optical Properties of Anionic $Au_{25}(SR)_{18}$ Clusters. *J. Phys. Chem. C* **2013**, *117*, 20867-20875.
61. Fernando, A.; Weerawardene, K. L. D. M.; Karimova, N. V.; Aikens, C. M. Quantum Mechanical Studies of Large Metal, Metal Oxide, and Metal Chalcogenide Nanoparticles and Clusters. *Chem. Rev.* **2015**, *115*, 6112-6216.

62. Toikkanen, O.; Ruiz, V.; Ronnholm, G.; Kalkkinen, N.; Liljeroth, P.; Quinn, B. M. Synthesis and Stability of Monolayer-Protected Au_{38} Clusters. *J. Am. Chem. Soc.* **2008**, *130*, 11049-11055.

63. Qian, H.; Zhu, Y.; Jin, R. Size-Focusing Synthesis, Optical and Electrochemical Properties of Monodisperse $Au_{38}(SC2H4Ph)_{24}$ Nanoclusters. *ACS Nano* **2009**, *3*, 3795-3803.

64. Qian, H.; Zhu, M.; Gayathri, C.; Gil, R. R.; Jin, R. Chirality in Gold Nanoclusters Probed by NMR Spectroscopy. *ACS Nano* **2011**, *5*, 8935-8942.

65. Pelayo, J. J.; Whetten, R. L.; Garzón, I. L. Geometric Quantification of Chirality in Ligand-Protected Metal Clusters. *J. Phys. Chem. C* **2015**, *119*, 28666-28678.

66. Yao, Q.; Yuan, X.; Fung, V.; Yu, Y.; Leong, D. T.; Jiang, D.; Xie, J. Understanding Seed-Mediated Growth of Gold Nanoclusters at Molecular Level. *Nat. Commun.* **2017**, *8*, 927.

67. Xia, N.; Gan, Z.; Liao, L.; Zhuang, S.; Wu, Z. The Reactivity of Phenylethanethiolated Gold Nanoparticles with Acetic Acid. *Chem. Commun.* **2017**, *53*, 11646-11649.

68. Kim, M.; Tang, Q.; Kumar, A. V. N.; Kwak, K.; Choi, W.; Jiang, D.-E.; Lee, D. Dopant-Dependent Electronic Structures Observed for $M_2Au_{36}(SC_6H_{13})_{24}$ Clusters (M = Pt, Pd). *J. Phys. Chem. Lett.* **2018**, *9*, 982-989.

69. Antonello, S.; Dainese, T.; De Nardi, M.; Perotti, L.; Maran, F. Insight into the Interface between the Electrolytic Solution and the Gold Core in Molecular Au_{25} Clusters. *ChemElectroChem* **2016**, *3*, 1237-1244.

70. Antonello, S.; Dainese, T.; Maran, F. Exploring Collective Substituent Effects: Dependence of the Lifetime of Charged States of $Au_{25}(SC_nH_{2n+1})_{18}$ Nanoclusters on the Length of the Thiolate Ligands. *Electroanalysis* **2016**, *28*, 2771-2776.

71. Qian, H.; Liu, C.; Jin, R. Controlled Growth of Molecularly Pure $Au_{25}(SR)_{18}$ and $Au_{38}(SR)_{24}$ Nanoclusters from the Same Polydispersed Crude Product. *Sci. China: Chem.* **2012**, *55*, 2359-2365.

72. Liao, L.; Zhou, S.; Dai, Y.; Liu, L.; Yao, C.; Fu, C.; Yang, J.; Wu, Z. Mono-

Mercury Doping of Au_{25} and the HOMO/LUMO Energies Evaluation Employing Differential Pulse Voltammetry. *J. Am. Chem. Soc.* **2015**, *137*, 9511-9514.

73. Reimers, J. R.; Ford, M. J.; Marcuccio, S. M.; Ulstrup, J.; Hush, N. S. Competition of Van der Waals and Chemical Forces on Gold-Sulfur Surfaces and Nanoparticles. *Nature Rev.* **2017**, *1*, 0017.
74. Varnholt, B.; Guberman-Pfeffer, M. J.; Oulevey, P.; Antonello, S.; Dainese, T.; Gascón, J. A.; Bürgi, T.; Maran, F. Vibrational Coupling Modulation in n-Alkanethiolate Protected $Au_{25}(SR)_{18}^0$ Clusters. *J. Phys. Chem. C* **2016**, *120*, 25378-25386.
75. Walter, M.; Akola, J.; Lopez-Acevedo, O.; Jadzinsky, P. D.; Calero, G.; Ackerson, C. J.; Whetten, R. L.; Grönbeck, H.; Häkkinen, H. A Unified View of Ligand-Protected Gold Clusters as Superatom Complexes. *Proc. Natl. Acad. Sci. U. S. A.* **2008**, *105*, 9157-9162.
76. Cheng, L.; Ren, C.; Zhang, X.; Yang, J. New Insight into the Electronic Shell of $Au_{38}(SR)_{24}$: A Superatomic Molecule. *Nanoscale* **2013**, *5*, 1475-1478.
77. Antonello, S.; Musumeci, M.; Wayner, D. D. M.; Maran, F. Electroreduction of Dialkyl Peroxides. Activation−Driving Force Relationships and Bond Dissociation Free Energies. *J. Am. Chem. Soc.* **1997**, *119*, 9541-9549.
78. Meneses, A. B.; Antonello, S.; Arévalo, M.-C; Maran, F. Double-Layer Correction for Electron-Transfer Kinetics at Glassy Carbon and Mercury Electrodes in N,N-Dimethylformamide. *Electro-analysis* **2006**, *18*, 363-370.
79. Nicholson, R. S.; Shain, I. Theory of Stationary Electrode Polarography. Single Scan and Cyclic Methods Applied to Reversible, Irreversible, and Kinetic Systems. *Anal. Chem.* **1964**, *36*, 706-723.

4.6 Acknowledgements

I am particularly thankful to Dr. Alfonso Venzo for his contribution to the NMR measurements, Prof. Sara Bogialli (University of Padova) for the ESI mass spectrometry measurements, and Dr. Tiziano Dainese for his contribution to the synthetic work.

Chapter 5. Ligand Exchange-Place Reaction on $Au_{25}(SR)_{18}$

5.1 Introduction

One of the most promising field of application of metal NPs is represented by biomedicine. In general, nanosystems provides to researchers new tools to build up complex systems able to carry out fundamental functions at the interface with biosystems such as controlled, both in time and space, delivery of drugs, diagnosis, biomaterial engineering, stimuli-responsive systems.[1-3] In the last years, research in the field worked to overcome troubleshooting connected with the use of NPs in bio-environment as colloidal instability connected with aggregation and precipitation phenomena, short half-life in the bloodstream due to plasma proteins opsonization, non-specific targeting, and the toxicity issues.[4] One solution for, at least, part of these adverse issues come from a proper surface modification that could impart stealth behavior to the nanoparticles, proper solubility and stability, and, in general, biocompatibility. Smaller NPs that are able to pass through biological barriers resulted to be the more promising materials for biomedical applications. In particular, NPs made of gold represented one of the most useful nanostructured platforms in nanomedicine.[5-8] According to their dimension they can display both plasmonic or fluorescent behavior and according to their shape their absorption can be easily tuned along the visible and Near-IR electromagnetic spectrum. Moreover, the size, shape, charge and degree of hydrophobicity of NPs influence their ability to cross different biological barriers. Other than the shape and dimension of metal core, the functionalization of the NPs is also of great importance as well for imparting the desired biological response. Strategies for the modification of the organic layer usually employed for protecting the NP surface, have been developed to prepare Au NPs displaying a required set of such characteristics.

The use of a polymeric coating was often the preferred road followed for improve the stability of NPs in biological conditions. Polymers can be both adsorbed on or covalently bound to the surface of preformed NPs via grafting strategies.[9-12] In this context, poly(amino acids) are of particular interest because of their biocompatibility, easy functionalization, and intrinsic biological activity that could allow application in drug delivery, therapy, and diagnosis.[13-18] Covalent fixation leads to a higher stability of the nanosystem compared to methods based on non-covalent attachment.[19] They also allow for controlling the characteristics of the forming polymer, as well as the density and length of the surface-tethered polymer chains.[20] Different approaches have been employed to prepare Au NPs capped by water-soluble poly(amino acids). The direct formation of stable Au NPs can be achieved by the reduction of tetrachloroauric ions using amino acid homo- and heteropolymers[21-24] or taking advantage of the electrostatic interaction of preformed Au NPs with poly(amino acids).[25,26] Electrostatic or hydrophobic interactions between Au NPs capped by poly(amino acids) can lead to reversible assembly/disassembly and flocculation, as found for example for polylysine coated Au NPs.[27,28]

In a previous work carried out by Maran and co-workers[29] a novel grafting approach for the preparation of hybrid biocompatible star-like core–shell nanosystems consisting of the Au_{144} cluster capped by polylysine was proposed. This method works efficiently and could provide a versatile approach for grafting other poly(amino acids) from Au MPCs. Besides that, the final product provided unexpected optical features. In particular, the UV-vis absorption spectra revealed the presence of Surface Plasmon Resonance (SPR)-like band despite the ultrasmall size of the cluster core.[30,31] It is indeed well known that Au nanospheres with diameter larger than about 2 nm exhibit a SPR band at 520 nm and, as the size of the particles shrinks the SPR peak becomes damped, and eventually disappears.

At the light of the quite unexpected results obtained by the Maran group in the characterization of polylysine-grafted Au_{144} nanocluster, we decided to apply the same approach to synthesized analogous Au_{25} clusters. To pursue this aim, we proceeded first by introducing, by exchange reaction on $Au_{25}(C2Ph)_{18}$, ligands bearing amino groups and then carrying out a polymerization reaction with formation of polypeptides on the cluster surface. Optical and electrochemical characterization of the final product was finally performed with the purpose of investigating the possible birth and growth of a SPR-like band also for the smaller $Au_{25}(SR)_{18}$.

5.2 Results and Discussion

The first part of the work aimed at decorating the monolayer of $Au_{25}(SR)_{18}$ with polymerizable groups. To the purpose, ligands bearing an amino function should be inserted into the cluster monolayer. The chosen thiols (**1**) in shown below together with the corresponding ligands bearing a fluorenylmethyloxy-carbonyl (Fmoc) protecting group (**2**). This incoming ligand was designed to be sufficiently long to make the amino group protrude from the phenylethanethiol monolayer.

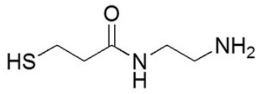

1

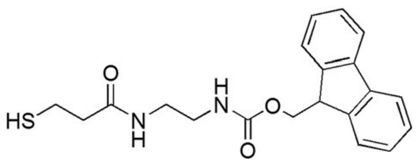

2

After the synthesis of the proper ligand **2**, described in the following, ligand exchange reactions on $Au_{25}(C2Ph)_{18}$ nanoclusters have been carried out. The extent of exchange was controlled by adjusting the relative concentrations of the cluster and exogenous ligand. The reaction was monitored by UV-vis absorption spectroscopy and MALDI-TOF mass spectroscopy. The Fmoc group was the removed and the resulting cluster allowed to react with a proper monomeric amino acid to induce the formation of a polypeptidic shell covalently bound to the cluster surface to give a product that was optically and electrochemically characterized.

5.2.1 Ligand and Monomers Synthesis

Synthesis of Incoming Ligand ***2****:* $HS\text{-}CH_2CH_2\text{-}CO\text{-}NH\text{-}CH_2CH_2\text{-}NHFmoc$

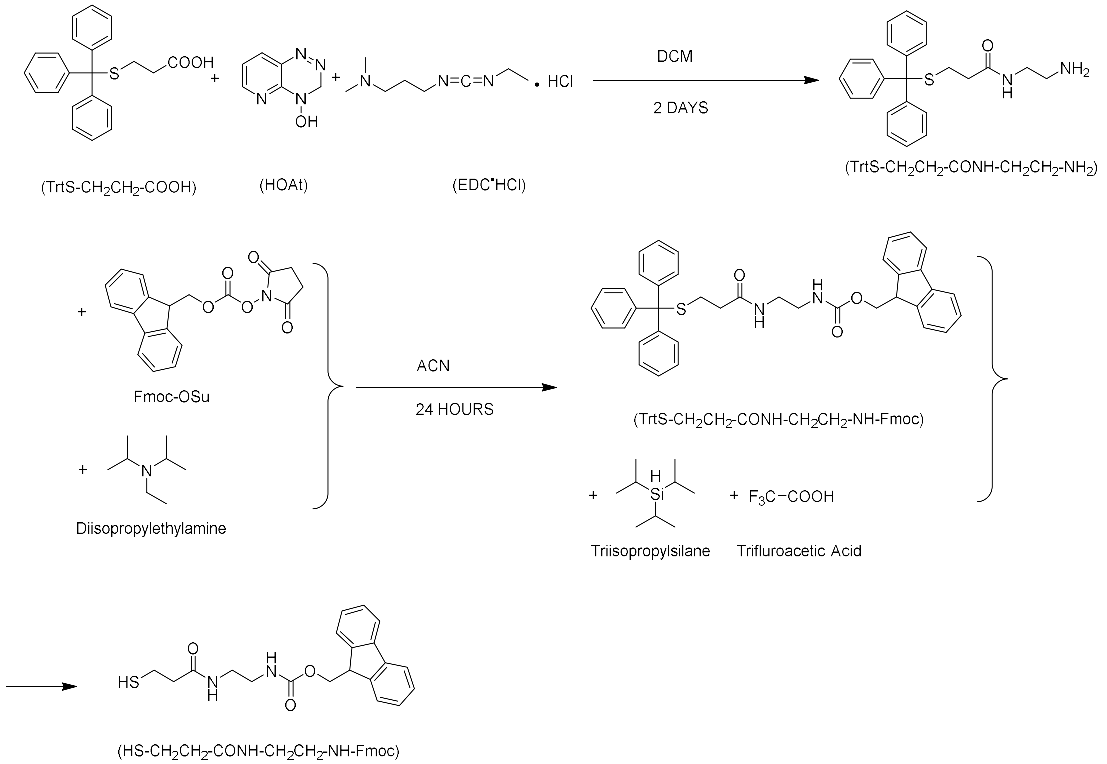

Scheme 5.1. The synthetic route of ligand **2**.

Synthesis of TrtS-$CH_2CH_2CONHCH_2CH_2NH_2$.

TrtS-CH_2CH_2COOH (500 mg, 1.43 mmol) and HOAt (234 mg, 1.71 mmol) (Tr = trytil) was dissolved in 10 ml of CH_2Cl_2 and EDC·HCl (330 mg, 1.71 mmol) was added. The reaction mixture was stirred for 2h, and then a solution of H_2N-CH_2CH_2-NH_2 (0.96 ml, 14.3 mmol) in 25 ml of CH_2Cl_2 was added dropwise during 1h. After 2 days the solvent was evaporated and the crude product was purified by silica gel chromatography column using CH_2Cl_2 and then the mixture CH_2Cl_2/MeOH (v: v = 1:5) as eluents.

Synthesis of TrtS-$CH_2CH_2CONHCH_2CH_2NHFmoc$.

TrtS-$CH_2CH_2CONHCH_2CH_2NH_2$ (1.3 g, 3.33 mmol) was dissolved in 20 ml of MeCN, a solution of Fmoc-OSu (1.12 g, 3.33 mmol) in 20 ml of acetonitrile and diisopropylethylamine (0.56 ml, 3.33 mmol) were added. The reaction mixture was stirred for 24 h and concentrated to 20 ml. The white precipitate was filtered, washed with 5 ml of acetonitrile cooled to 0 °C and dried. The organic solutions were collected, the solvent was evaporated, and the product was recrystallized from acetonitrile.

^{1}H NMR (200 MHz, $CDCl_3$): δ 7.55 (d, 2H, CHFmoc, J = 8 Hz), 7.51 (d, 2H, CHFmoc, J = 8 Hz), 7.20-7.50 (m, 19H; 15 H, Trt, 4H, Fmoc), 5.75 (s, 1H, NH), 5.20 (s, 1H, NH), 4.30 (d, 2H, CH_2Fmoc, J = 6 Hz), 4.15 (t, 1H, CHFmoc, J = 6 Hz), 3.26 (s, 4H, $2CH_2$), 2.50 (t, 2H, CH_2, J = 6 Hz), 2.10 (t, 2H, CH_2, J = 6 Hz).

Synthesis of HS-CH_2CH_2CO-$NHCH_2CH_2NHFmoc$.

TrtS-CH_2CH_2CO-$NHCH_2CH_2NHFmoc$ (0.3 g, 0.49 mmol) and 0.5 ml of triisopropylsilane (2.44 mmol) was dissolved in 8 ml of CH_2Cl_2. 1.5 ml of trifluoroacetic acid were added dropwise and the reaction mixture was stirred for 1 h. The solvent was evaporated, and 20 ml of diethyl ether were added to the white solid. The product was filtered, washed 6×20 ml of diethyl ether and dried.

^{1}H NMR (200 MHz, $CDCl_3$): δ 7.77 (d, 2H, CHFmoc, J = 8 Hz), 7.58 (d, 2H, CHFmoc, J = 8 Hz), 7.25-7.48 (m, 4H, Fmoc), 6.08 (s, 1H, NH), 5.19 (s, 1H, NH), 4,43 (d, 2H, CH_2Fmoc, J = 6 Hz), 4.21 (t, 1H, CHFmoc, J = 6 Hz), 3.37 (s, 4H, $2CH_2$), 2.78 (q, 2H, CH_2, J = 8 Hz), 2,46 (t, 2H, CH_2, J = 6 Hz), 1.57 (t, 1H, SH, J = 8 Hz).

Synthesis of Monomer: N-carboxyanhydride (NCA)

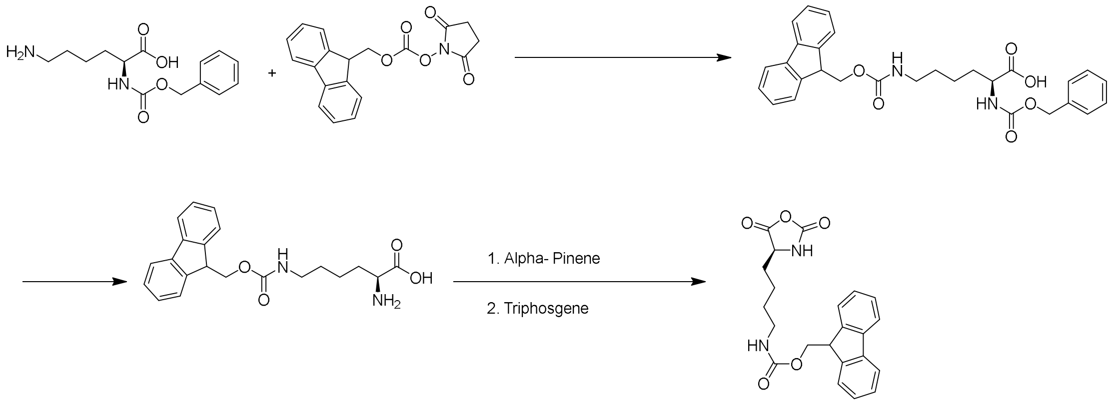

Scheme 5.2. The synthetic route of the monomer NCA.

Synthesis of Z-Lys(Fmoc)-OH.

Z-Lys-OH (5 g, 17.8 mmol) was suspended in 150 ml of water, and 7.75 ml (44.5 mmol) of triethylamine were added to get a clear solution. A solution of 7.2 g (21.4 mmol) of Fmoc-OSu in 100ml of MeCN was added dropwise during 6h. Then, the organic solvent was evaporated, the water solution was washed with diethyl ether (3 × 100 ml), and the pH was adjusted to 2 with 1M H_2SO_4. The product was extracted with ethyl acetate (3 × 100 ml), the solvent was dried over Na_2SO_4, and evaporated. The product was obtained as slightly yellow oil.

Synthesis of H-Lys(Fmoc)-OH.

Z-Lys(Fmoc)-OH (2.8 g, 5.57 mmol) was dissolved in 150 ml of MeOH and 0.5 g of Pd/C was added. The hydrogenation was continued until complete disappearance of starting material and formation of a white precipitate. The reaction mixture was concentrated to 50 ml, and 50 ml of water was added to dissolve the product. The catalyst was filtered off, the organic solvent was evaporated, and finally, H-Lys(Fmoc)-OH was recrystallized from water. The white crystals were filtered and dried in vacuo over P_2O_5.

^{1}H NMR (200 MHz, $CDCl_3$): δ 7.75 (d, 2H, CHFmoc, J = 8 Hz), 7.56 (d, 2H, CHFmoc, J = 8 Hz), 7.25-7.48 (m, 9H; 4H, Fmoc, 5H, Z), 5.64 (t, 1H, NH, J = 8 Hz), 5.09 (s, 2H, CH_2), 4.91 (d, 1H, NH), 4,43 (m, 3H; 2H, CH_2Fmoc; 1H, CH), 4.21 (t, 1H, CHFmoc, J = 6 Hz), 3.01-3.26 (m, 2H, CH_2), 1.65-1.85 (m, 2H, CH_2), 1.15-1.60 (m, 4H, CH_2).

Synthesis of N-carboxyanhydride (NCA).

H-Lys(Fmoc)-OH (5.00 g, 13.6 mmol), α-pinene (4.28 g, 31.4 mmol) and 60 ml ethyl acetate were weighed in a three-neck round bottom flask and heated up under reflux. Triphosgene (2.72 g, 9.17 mmol) was dissolved in 20 ml ethyl acetate and added slowly once the reflux started. The solution became clear and all solids disappeared after 3 h. 3/4 of the ethyl acetate was removed by distillation. 40 ml *n*-heptane was added, and the solution was heated to recrystallize. The NCA was recrystallized twice and subsequently washed with n-heptane, dried under vacuum, and stored in a refrigerator under P_2O_5.[32]

5.2.2 Cluster synthesis and Ligand Exchange Reaction

Synthesis of $Au_{25}(SC2Ph)_{18}^0$

$Au_{25}(SCH_2CH_2Ph)_{18}^0$, hereafter indicated as $Au_{25}(SC2Ph)_{18}^0$, was prepared as already described.[33,34]

500 mg (1.27 mmol) of $HAuCl_4 \cdot 3H_2O$ was dissolved in 40 ml of THF and then 833 mg of tetra-*n*-octylammonium bromide (1.52 mmol, 1.2 eq.) were added. The resulting red solution was stirred for 15 min at 20 °C. Stirring speed was set to 100 rpm and 1 ml (7.62 mmol, 6 eq.) of HSC_2Ph, dissolved in 10 ml of THF, was added dropwise over a period of ca. 3 min. The solution quickly became yellow and then, after ca. 45 min colorless. The stirring speed was raised to 600 rpm and a freshly prepared icy-cold aqueous solution (10 ml) of $NaBH_4$ (0.48 g, 12.7 mmol, 10 eq.) was quickly added to the mixture, which was kept at 20°C. The solution immediately became black, the typical color observed during the formation of large monolayer-protected clusters, and plenty of gas evolved. The reaction progress was monitored by UV-Vis absorption spectroscopy. After ca. two days, the reaction mixture was filtered on paper to remove black/dark grey residues insoluble in THF. The filtered solution had a dark-brown color with orange hues. THF was removed with a rotary evaporator to leave a reddish-brown oily solid covered by a colorless liquid. The solid was dissolved in toluene and washed with water (4 x 40 ml). Toluene was evaporated and the product was extracted with MeCN, leaving a black residue. MeCN was evaporated and the resulting orange-reddish oily solid was dissolved in Et_2O to yield a clear orange solution. Oxidation of the as prepared [$n\text{-}Oct_4N^+$] [$Au_{25}(SC2Ph)_{18}^-$] cluster to obtain the corresponding neutral, paramagnetic species $Au_{25}(SC2Ph)_{18}^0$ was performed by passage through a silica gel chromatography column, using DCM as eluent and under aerobic conditions. The orange solution of the anionic cluster in DCM was injected into the column and soon turned green while passing through the column. After evaporation of the so-treated DCM solution,

the oxidized clusters appear as a black-brownish powder. The clusters were further purified by washing them thrice with MeCN in which $Au_{25}(SC2Ph)_{18}^{0}$ is insoluble.

The MALDI-TOF spectrum of $Au_{25}(SC2Ph)_{18}^{0}$ shows a maximum m/z = 7394, in agreement with previous observations of pure samples of the same cluster. The sharpness and symmetry of the peak indicate a very high purity of the sample. Isotopic patterns are also consistent with the simulation results.

Ligand Exchange Reaction.

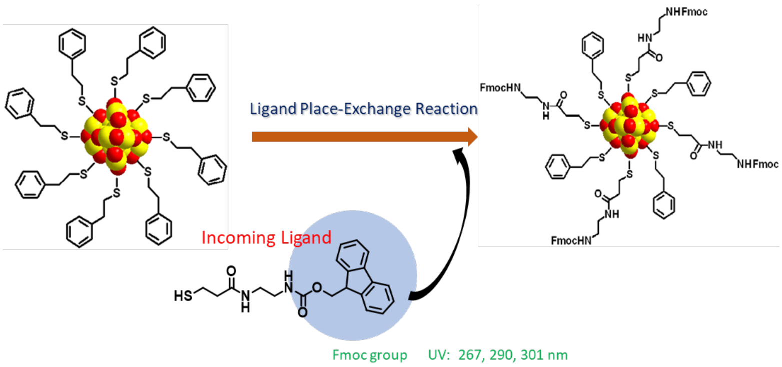

Scheme 5.3. Scheme for ligand exchange reaction.

To introduce into the Au_{25} monolayer structure groups suitable for initiating polymerization, we used the ligand place-exchange approach (Scheme 5.3).

Because $Au_{25}(SC2Ph)_{18}^{0}$ and incoming ligand have distinct different solubility, in order to select the appropriate reaction solvent, we tested the solubility of $Au_{25}(SC2Ph)_{18}^{0}$ and ligand **2** in different solvents which are shown in Table 5.1. The results clearly point to DCM as the most suitable solvent for the reaction since both the gold cluster and the ligand are highly soluble in that.

Table 5.1. Solubility of Incoming Ligand **2** and $Au_{25}(SC2Ph)_{18}^{0}$ in different common solvents.

Solvent	Ligand **2**	$Au_{25}(SR)_{18}^0$
Toluene	Insoluble	Soluble
Acetone	Insoluble	Soluble
DCM	Soluble	Soluble
MeCN	Soluble	Insoluble
Methanol	Insoluble	Insoluble
Ethanol	Insoluble	Insoluble
DMF*	Soluble	Soluble

*: The solubility of $Au_{25}(SC2Ph)_{18}^0$ in DMF evolves over the time as described in detail later.

The choice of DCM comported the need of carrying out some stability test for the cluster since many previous studies have shown that Au clusters may be oxidized or even destroyed due to their prolonged presence in DCM.[35,36] We then tested the stability of the $Au_{25}(SC2Ph)_{18}^0$ in this solvent by UV-vis absorption spectroscopy. Figure 5.1 shows that the optical behavior of the MPCs does not change significantly over time and it is stable for at least 77 hours in DCM (deoxygenated). Being the ligand exchange reaction usually completed in less than 24 h, we can conclude that the effect of DCM on $Au_{25}(SC2Ph)_{18}^0$ during the reaction evolution can be neglected.

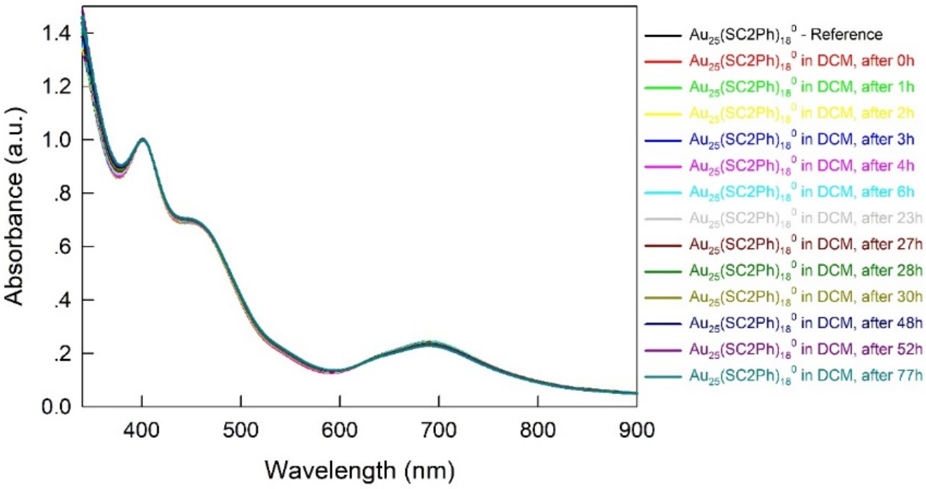

Figure 5.1. The changes of UV-vis absorption spectra of $Au_{25}(SC2Ph)_{18}^0$ in DCM under aerobic condition within 77 hours.

The exogenous ligand that we desire to insert in the native $Au_{25}(SC2Ph)_{18}$ monolayer is characterized by the presence of multiple amide groups that are known to be prone to form strong H-bonds with carbonyl groups. This could be the reason for the observed formation of a grayness insoluble precipitate in some of the experimental procedure. The amount of precipitate was observed to increase with the increase of the ligand/MPC molar ratio, probably because of the aggregation of the MPCs due to intercluster interactions. Although we chose Fmoc protective group to block the exposed amino group at the end of the chain when we designed and synthesized the incoming ligand, this was anyway not completely avoidable.

The experimental conditions of ligand exchange reaction were optimized in order to achieve different goals as to guarantee the integrity of the structure of Au_{25} nanocluster during the reaction, to exchange as many ligands as possible, to avoid the aggregation or precipitation of the Au_{25} MPCs after exchange.

The ligand exchange reaction was carried out, as said before, in DCM for no more than 24h by using different molar ratios of the thiol (**2**) and $Au_{25}(SC2Ph)_{18}^0$. Six different concentration ratios have been explored to obtain a stable MPC $Au_{25}(SC2Ph)_{18-x}(L)_x$ with the higher possible exchanged yield (Table 5.2). First, we kept the reaction at the same solvent volume, the same amounts of $Au_{25}(SC2Ph)_{18}^0$, and the same temperature (R.T.) to limit the number of variables, whereas, the amount of the exogenous ligand was changed from 2:1 to 50:1 respect the cluster concentration. We observed that a high concentration of the incoming ligands (as in entry 6 of Table 5.2) could eventually causes degradation the Au_{25} cluster, and/or formation of an insoluble precipitate (Figure 5.2). Eventually, we chose the condition n. 5 as the optimal condition.

Table 5.2. Different reaction conditions of ligand place-exchange reaction

Condition NO.	n [Au_{25}^{0}]: n (L)	Reaction Time (h)	UV	Maldi-TOF	Exchange Yield[b]
1	1: 2	24	[a]	1	---
2	1: 5	24	a	1	---
3	1: 8	24	a	1-2	24%
4	1: 10	24	a	1-3	---
5	1: 20	24	a	1-5	57%
6	1: 50	13	a	1-6	76%

a: UV spectroscopy shows the reaction product still hold typical peaks of $Au_{25}(SR)_{18}^{0}$ proving the intactness of $Au_{25}(SR)_{18}$ core; b: using Maldi-TOF calculation.

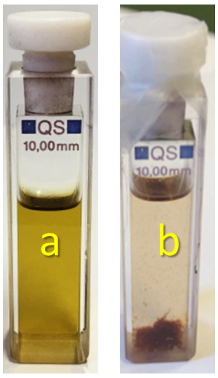

Figure 5.2. Appearance of sample solution of condition No.6 in DMF before (a) and after (b) 6h of reaction, clearly showing the formation of a precipitate.

As long as reaction conditions No. 5 concerns, the specific synthetic and purification procedure were as following:

10 mg (1.36×10^{-3} mmol) of $Au_{25}(SC2Ph)_{18}^{0}$ were dissolved in 3 mL of DCM, and a solution of 10 mg (0.0676 mmol, 20 eq.) of the incoming ligand (HS-CH_2CH_2-CONH-CH_2CH_2-NHFmoc) in 1 mL of DCM was added. The reaction mixture was stirred for 24 h and the solvent was rotary evaporated. The solid residue was washed with methanol (5 × 10 mL), and acetonitrile (5 × 10 mL). The

product was extracted with acetone to separate eventually the degrade clusters and other impurities.

The incorporation of **2** into the MPC monolayer leads to the desired product in high yield.

All the products were checked by UV-vis spectrometry to verify the presence of intact $Au_{25}(SR)_{18}$. The spectra obtained before and after exchange show the same fine features (peaks at 401 and 687 nm, shoulders at 455 nm) typical of $Au_{25}(SC2Ph)_{18}^0$ (Figure 5.3a), which is particularly evident in the derivative spectra (Figure 5.3b). The UV-vis spectra of the purified clusters confirm also the presence of the Fmoc-protected ligand in the MPC structure (Figure 5.3a), as proved by the presence of the characteristic bands (267, 290, and 301 nm) of the Fmoc group. Figure 5.4 nicely shows that increasing the relative concentration of the exogenous ligand in the reaction mixture leads to an increase of the height of Fmoc adsorption peaks respect to Au_{25} that is related to a larger average degree of substitution.

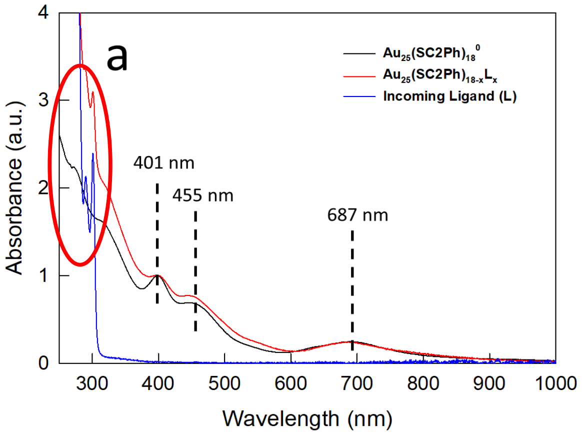

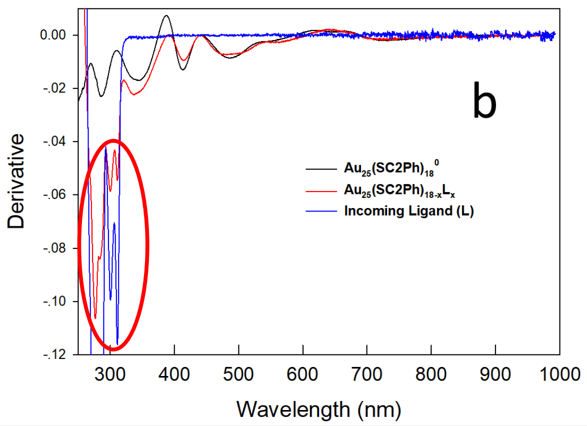

Figure 5.3. (a) UV-vis absorption and (b) corresponding derivative spectra for the relevant species (Condition NO. 5) before, during, and after MPC modification in DCM.

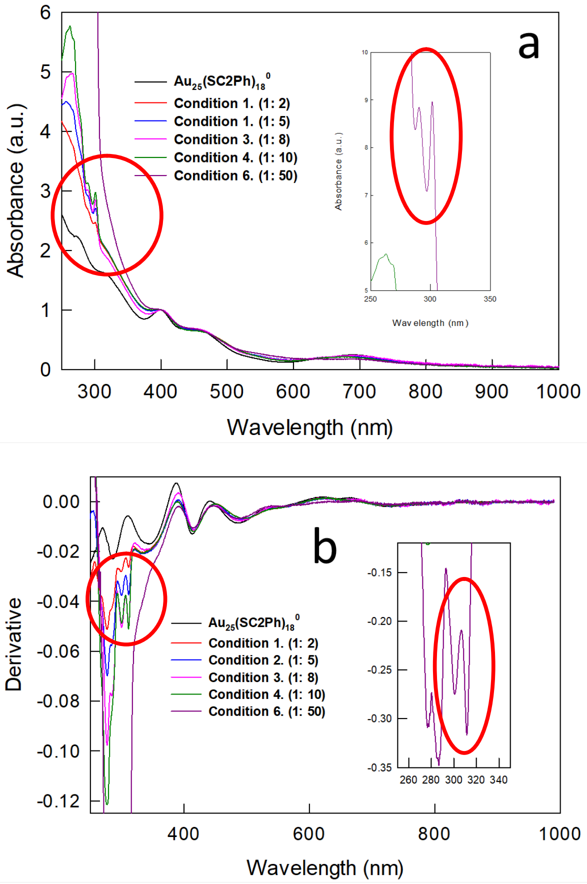

Figure 5.4. (a) UV-vis absorption and (b) corresponding derivative spectra for the relevant species (Condition NO. 1-4, 6) after MPC modification in DCM.

Electrochemical characterization of some of the exchange reaction products was also carried out. The DPV behavior (Figure 5.5) of the purified exchanged clusters confirms the presence of the Fmoc-protected ligand in the MPC monolayer thanks to the electroactivity of the fluorenyl function that is more pronounced for the cluster obtained with larger ligand/cluster ratio. At the same time, the fingerprint features (E°_{O1} = 0.139 eV and E°_{R1} = -0.188 eV) of Au_{25} are also present providing further evidence of the integrity of the cluster structure. Figure 5.5 shows the comparison of the electrochemical behaviors between the exchanged samples (Condition No. 3 and 5) and original Au_{25} under different synthetic conditions. The two centrals peaks of the modified cluster are slightly less separated (Figure 5.6) respect to phenylethanethiolate protected Au_{25} as expected due to the larger permittivity of the monolayer. It can be found that even after exchange, the samples still maintain the characteristic peaks of Au_{25}. Therefore, electrochemistry confirms what observed in the UV-vis spectra.

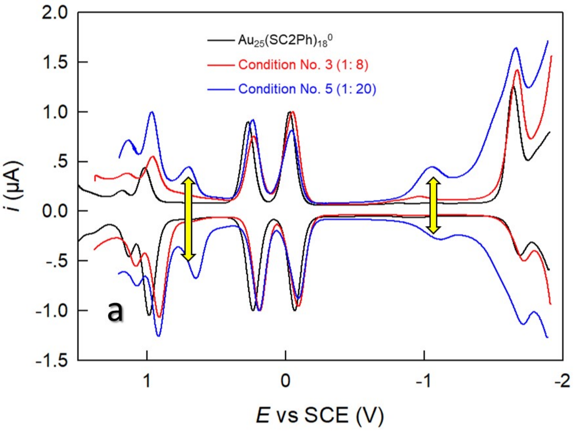

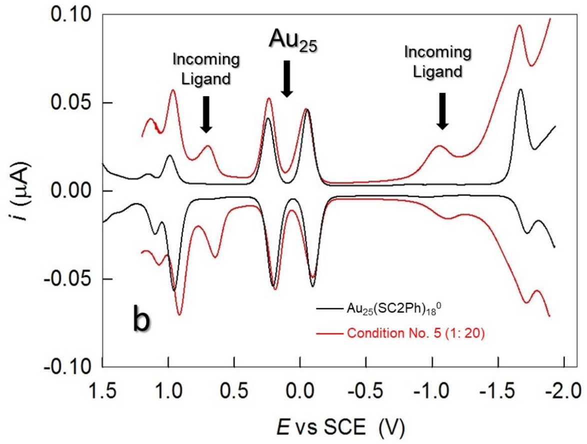

Figure 5.5. a. Comparison of DPV behaviors of $Au_{25}(SC2Ph)_{18}^0$ (black line) and the sample obtained from condition No. 3 (red line) and No.5 (blue line). b. DPV before" (black) and "after" (red) exchange in DCM.

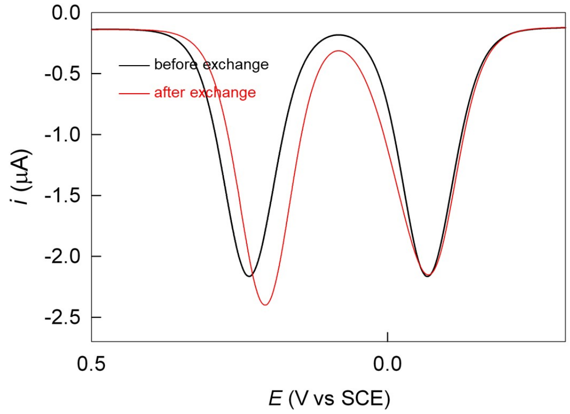

Figure 5.6. Comparison of DPV behaviors of the Au_{25} MPCs before (black) and after (red) exchange reaction in DCM. The curves were normalized at the potential of the first reduction peak (the right one).

Calculation of Exchange Yield: NMR and Mass Spectroscopy.

In order to understand how many ligands were exchanged into the cluster monolayer, MALDI-TOF mass spectrometry was employed. The mass spectra obtained after the exchange reaction (Figure 5.7) show different patterns of peaks for the different reaction conditions ascribable to a mixture of $Au_{25}(SR)_{18}$ clusters characterized by different substitution degrees. For example, the spectrum related to the sample obtained from condition No.4 (Figure 5.8) is characterized by an extent of exchange of about 24%, the larger fraction of the sample being the unsubstituted cluster, with a smaller quantity of monosubstituted and bisubstituted.

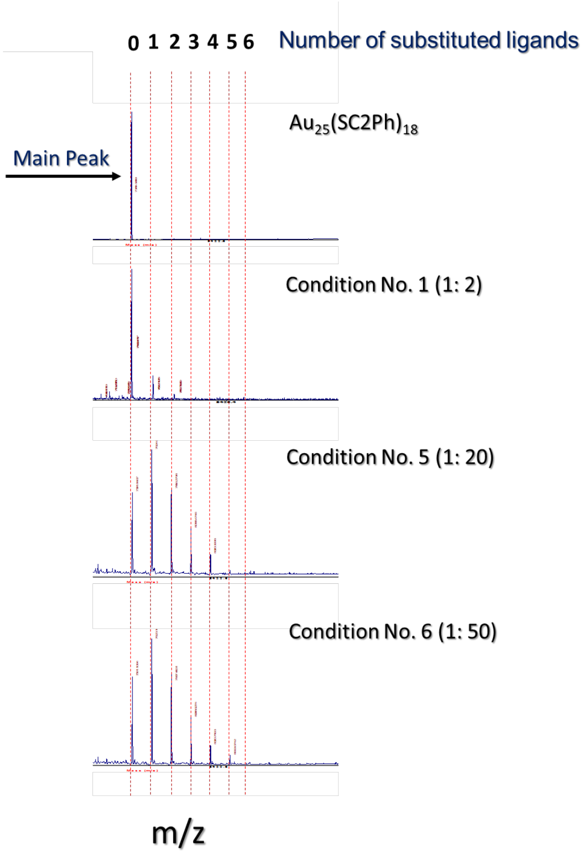

Figure 5.7. Maldi-TOF mass spectra monitoring the ligand exchange reaction.

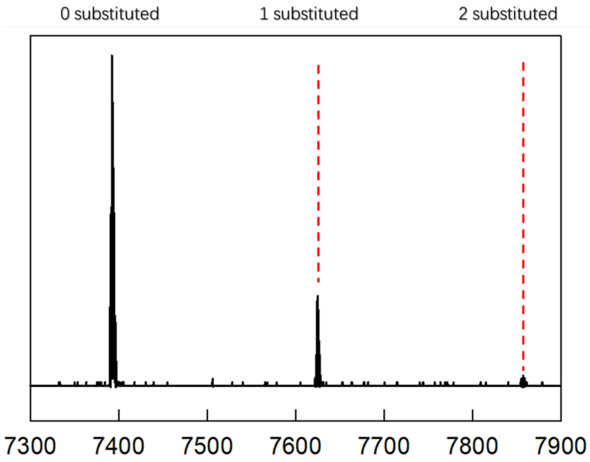

Figure 5.8. The exchange yield from MALDI-TOF spectrum was estimated from the relative intensity of the relevant peaks.

The average composition of the monolayers of the exchanged clusters was confirmed also by ^{1}H NMR spectroscopy after oxidatively decomposing the MPC with excess iodine followed by analysis of the molar ratio of the liberated ligands via quantitative comparison of the integrals of well-resolved peaks. NMR spectrum analysis (Figure 5.9) indicates that for the sample of condition No. 4, the extents of exchange are about 26% in very good agreement with MALDI determination. These results are also in line with previous exchanges on the same pristine cluster under comparable conditions.[36]

In general, the two techniques, NMR and MALDI-TOF spectroscopy, are profitably used to calculate the exchange rate of ligand exchange reaction, and the results of the two methods are basically consistent.

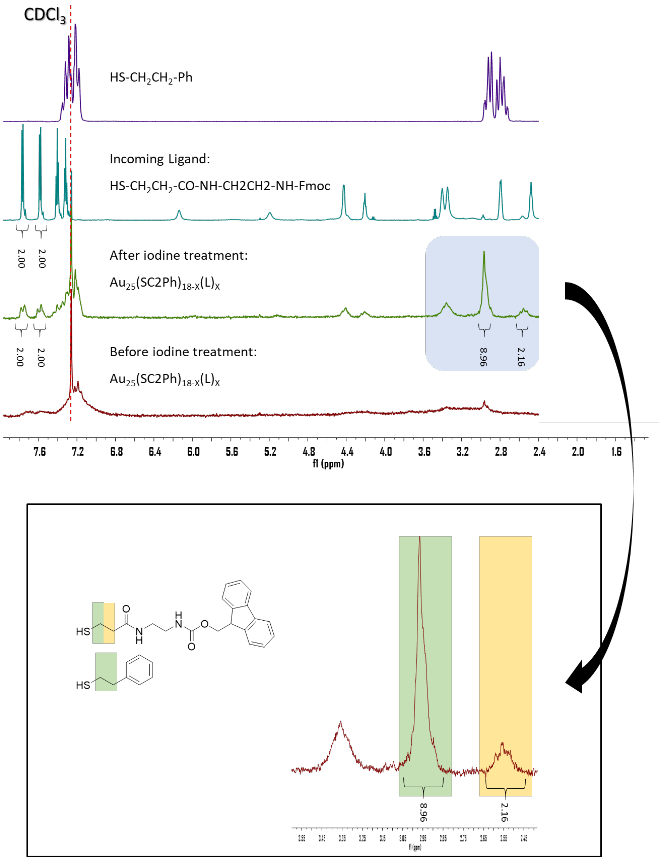

Figure 5.9. ^{1}H NMR spectra of (1) phenylethanethiol; (2) Incoming Ligand **2**; (3) The exchanged $Au_{25}(SC2Ph)_{18}$ (Condition No. 4); (4) The exchanged $Au_{25}(SC2Ph)_{18}$ (Condition No. 4) after decomposition with iodine. The inset highlights peak assignments. 200 MHz, $CDCl_3$, 25°C.

5.2.3 Ligand deprotection and polymerization

To obtain Au_{25} nanoclusters bearing free amino groups in the protective shell, the Fmoc groups were removed using piperidine as shown in Scheme 5.4.

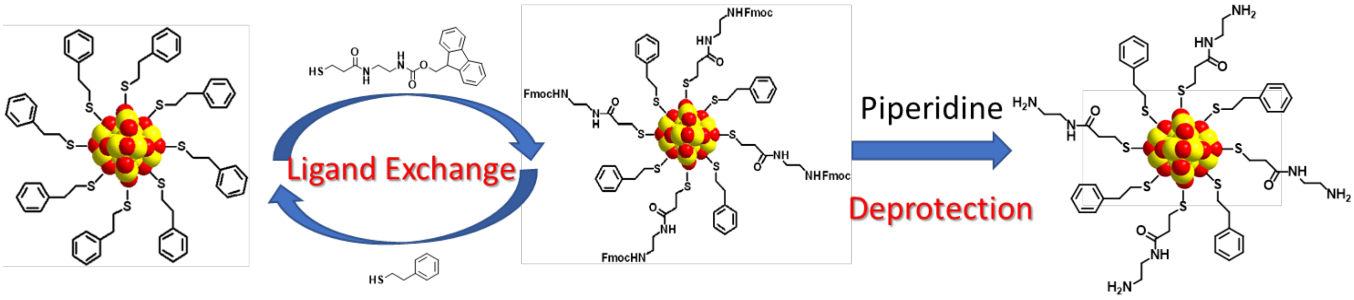

Scheme 5.4. Scheme for the preparation of the initiator for the N-carboxyanhydride polymerization.

The detailed procedure was as following: 10 mg Au_{25}-NHFmoc was dissolved in 2 ml DCM with vigorous stirring. Then, 50 μL piperidine was added into the solution dropwise. The reaction goes 10 minutes, and then is quenched by ether. The solid residue was washed with methanol (5 × 10 mL), and acetonitrile (5 × 10 mL). After deprotection, the UV-vis spectrum and its derivative maintain the same features as those of the pristine $Au_{25}(SC2Ph)_{18}$ cluster (Figure 5.10), losing the features related to fluorenyl function of the protecting group. The presence of the Au_{25} typical peaks indicates that the deprotection conditions do not affect the gold core.

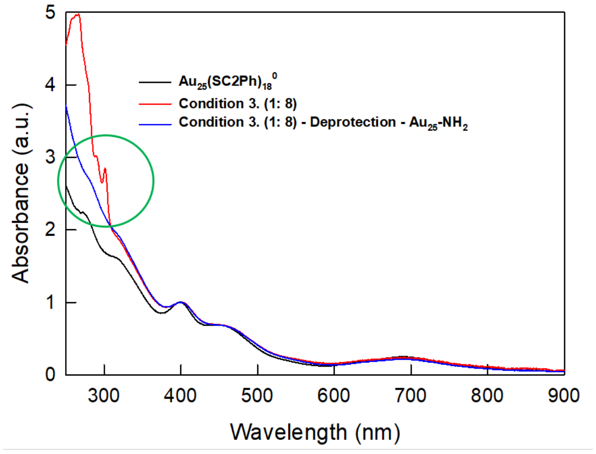

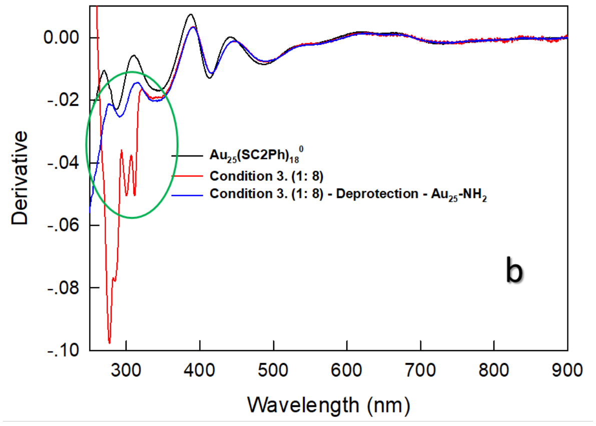

Figure 5.10. (a) UV-vis absorption and (b) corresponding derivative spectra for the relevant species before and after deprotection in DCM.

Since the following step, the polymerization reaction, is performed in DMF, it was necessary to check the stability of the gold clusters in DMF. Figure 5.11. shows that the cluster immediately changes from Au_{25}^0 to Au_{25}^- in DMF. The so-formed Au_{25}^- clusters are stable in DMF for more than 4 days.

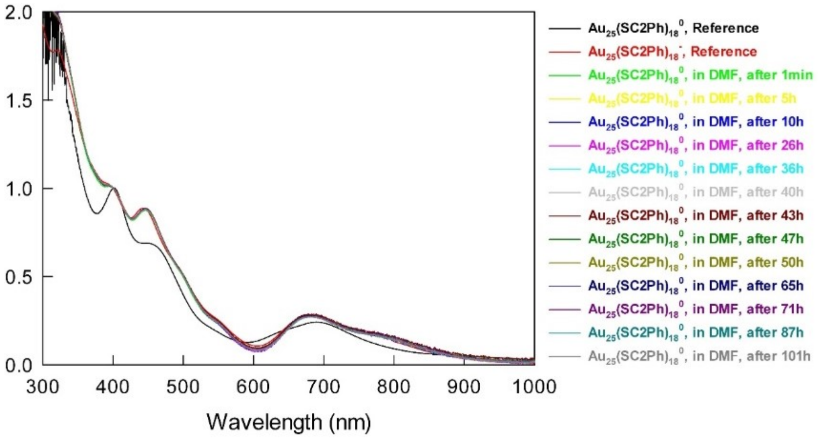

Figure 5.11. UV-vis spectra of $Au_{25}(SC2Ph)_{18}^0$ in DMF collected during 4 days.

The deprotected Au_{25}-NH_2 clusters were finally used as initiator for the ring opening polymerization of the monomer NCA (Scheme 5.5). The polymerization of NCA was carried out at room temperature and a monomer-to-initiator ratio of 50: 1 in DMF (deoxygenated). Polymerization was allowed to proceed for 3~4 days and was then stopped by the addition of diethyl ether. At low concentrations of initiator, the possible inclusion of other nanoclusters into the network of the forming polymer may be neglected. The resulting precipitate was washed several times with diethyl ether and methanol, to remove unreacted monomer and possible low molecular weight impurities. Polymerization was carried out using the sample obtained by condition No. 5.

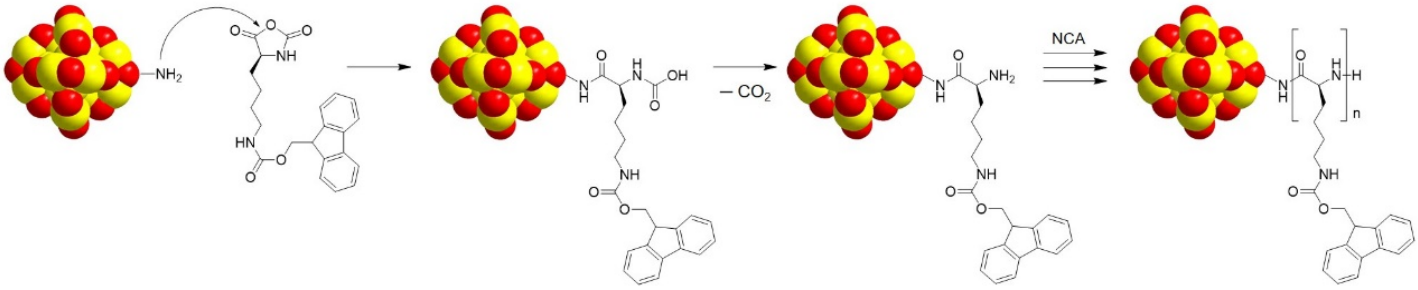

Scheme 5.4. NCA polymerization on the Au_{25}-NH_2 nanocluster.

To gain insights into the formation of the polylysine capped MPCs, the polymerization was followed by UV-vis absorption spectroscopy by periodically collecting samples that were then diluted and studied.

At the initial stages of the reaction, unlike $Au_{144}(SR)_{60}$ in which no changes in the spectra are observed.[29] Anyway, after 4 days, two clearly perceivable SPR-like bands appeared at ca. 500 and 815 nm (Figure 5.12).[30] As predicted by Gans theory in 1915[38], when the shape of Au NPs changes from spheres to rods, the SPR band split into two bands: a strong band in NIR region corresponding to electron oscillations along the long axis, referred to longitudinal band, and a weak band in the visible region at a wavelength similar to that of gold nanospheres, referred to transverse bands. While the transverse band is insensitive to the size changes, the longitudinal band is red shifted largely from the visible to near-infrared region with increasing aspect ratios (Length/Width).

Once again, as observed for Au_{144}, grafting of a polylysine peptide on the cluster periphery result in anomalous optical behavior also for Au_{25} nanoclusters.

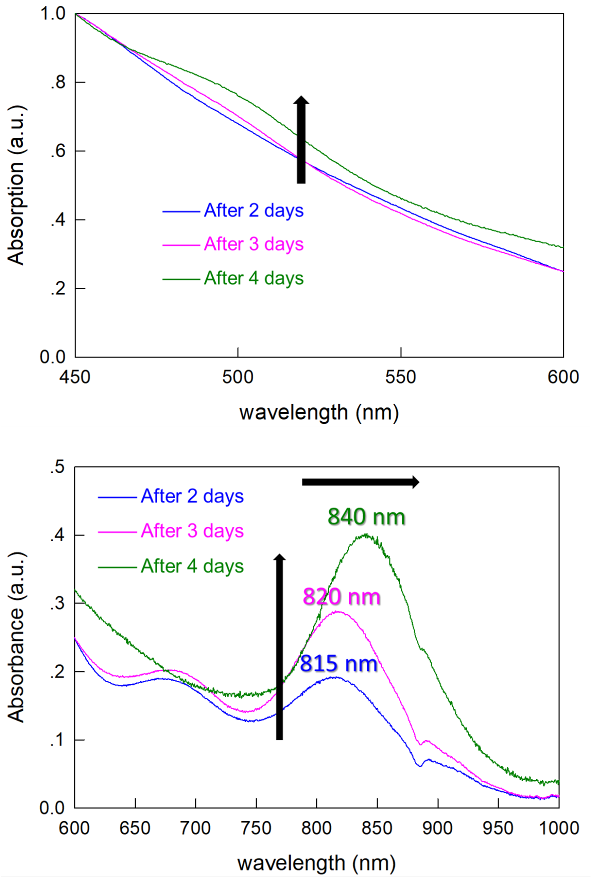

Figure 5.12. UV-vis spectra shows the evolution of the polymerization reaction of the polylysine capped Au_{25} in DMF.

DPV analysis of the product was carried out to gain some more information on the product nature and properties. The presence of two central peaks at almost the same potential of the Au_{25} original cluster support the thesis that the cluster core remains intact during the polymerization. Many additional peaks respect the starting material are detectable in the voltammetry that displays a very intriguing electroactivity that will need further investigation.

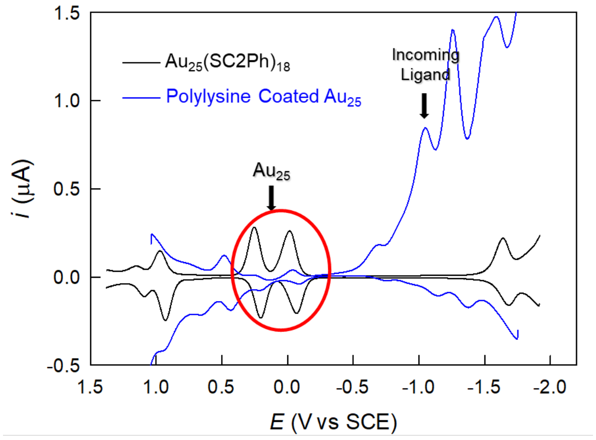

Figure 5.13. DPV of the polylysine capped Au_{25} in DMF.

Additional characterizations will be necessary to fully understand the origin of this phenomenon that appears to merge molecular and plasmon-like features together.

5.3 Conclusions

In this work an innovative method to prepare nanoclusters with a protecting layer made of a linear polylysine peptide has been explored. The method, previously used to covalently graft the polypeptide on the surface of an Au_{144} cluster, has been now tested on a smaller cluster, Au_{25} in order to investigate a more molecularly defined model system. Polymerization was performed directly on a Au_{25} nanocluster bearing free amino groups in the protective monolayer. For inserting a proper number of ligands, exchange reaction on $Au_{25}(C2Ph)_{18}$ were carried out exploring different experimental conditions. The exchange yield was demonstrated to depend on the initial Au_{25}/incoming ligand ratio and reaction time. As observed with Au_{144}, the optical properties of the polylysine modified Au_{25} were affected by the proceeding of the polymerization reaction. The UV-vis absorption spectra showed the appearance of two plasmon-like resonances that resemble the typical features of Au nanorods. Further investigation and characterizations of the polymerization product are necessary to understand the origin of this peculiar optical output anyway these preliminary results appear of interest for the preparation of very stable, functionalized nanosystems suitable for biomedicine applications, such as thermotherapy and bio-imaging. Regarding the method itself, it is simple, easily controllable, and could be conceivably extended to the preparation of core-shell nanosystems based on other mono- or co-poly(amino acids).

5.4 Experimental Section

The following solvents, salts, and reagents were commercially available and used as received.

Solvents: ethanol, methanol, toluene, dichloromethane, diethyl ether, petroleum ether, ethyl acetate, acetonitrile, dimethylformamide (Sigma-Aldrich).

Salts: potassium bisulfate, sodium bicarbonate, anhydrous sodium sulfate (Carlo Erba).

Reagents: 99.9+% hydrogen tetrachloroauratetrihydrate, tetra-n-octylamm-onium bromide, sodium borohydride, triisopropylsilane, trifluoroacetic acid, S-trityl-3-mercaptopropionic acid, ethylenediamine, triphosgene, α-pinene, triethylamine, 10% palladium on activated carbon, iodine (Sigma-Aldrich); 1- (3-dimethyl-aminopropyl) -3 -ethylcarbodiimide hydrochloride, 1- hydroxy -7 -aza -1, 2, 3-benzotriazole (GL Biochem), N-fluorenylmethyloxycarbonylsuc-cinimide, N, N-diisopropylethylamine, α-benzyloxycarbonyl lysine, piperidine (Iris Biotech). Flash chromatography was performed using silica gel 60M (0.04 - 0.063 mm, Macherey-Nagel) as stationary phase. Chloroform-d_3 (99.8%, Aldrich) was used as solvents for NMR spectroscopy. Analytical thin-layer chromatography (TLC) was carried out by using Macherey-Nagel TLC-cards (0.2 mm silica gel supported on plastic sheets). The spots were visualized first with UV light (λ = 254 nm) and then after exposure to iodine vapor and $KMnO_4$ aqueous solution. ^{1}H NMR spectra were recorded by using a Bruker model AC 200 and Avance-400 DRX spectrometers, operating at 200 MHz, respectively. Chemical shifts (δ) are given as parts per million (ppm) downfield from tetramethylsilane, which was added as the internal standard. Splitting patterns are abbreviated as follows: (s) singlet, (d) doublet, (t) triplet, (q) quartet, (m) multiplet. The proton assignments were carried out by standard chemical shift correlations. When possible, the monolayer composition was determined by decomposing the MPC with iodine. To this aim a crystal of iodine was added to the solution of Au MPC in NMR tube and the NMR spectrum was registered after formation of a black precipitate. The solution of the liberated ligands was analyzed through a comparison between the integrals of conveniently separated peaks, as illustrated in Figures 5.9.

UV-vis absorption spectroscopy

The UV-vis absorption spectra of the clusters were obtained in DCM with a Thermo Scientific Evolution 60S spectrophotometer. The spectra were recorded with a spectral resolution of 0.5 nm. The samples were at 0.2 mM concentration in 1 mm cuvettes.

MALDI-TOF mass spectrometry

Experiments were carried out with an Applied Biosystems 4800 MALDI-TOF/TOF spectrometer equipped with a Nd: YAG laser operating at 355 nm, with a laser firing rate of 200 Hz and an accelerating voltage of 25 kV. DCTB (trans-2-[3-(4-tert-butylphenyl)-2-methyl-2-propenylidene] malononitrile, Sigma -Aldrich, ≥98%) was used as the matrix. The instrument was calibrated with $Au_{25}(SC2Ph)_{25}$.[38] The clusters were dissolved in DCM containing DCTB to obtain 0.1 mM solutions with a 1:400 nanocluster/matrix ratio. A 5 µL solution was drop cast onto the sample plate and air-dried. All spectra were recorded using the reflector negative-ion mode.

Electrochemistry

The electrochemical experiments were carried out in DCM/0.1M TBAH, under an Ar atmosphere in a glass cell thermostated at 25°C. The working electrode was a 0.17 mm radius glassy carbon (GC) disk prepared and activated as already described.[40, 41] The electrochemical area, 9.05×10^{-4} cm^2, was determined through measurements of the peak current for the oxidation of ferrocene (at low scan rates) in N,N-dimethylformamide/0.1 M n-Bu_4NClO_4, which is a medium where ferrocene has a diffusion coefficient of 1.13×10^{-5} cm^2 s^{-1}.

The counter electrode was a Pt wire. An Ag wire, which was kept in a tube filled with the same electrolyte solution and separated from the main compartment by a Vycor frit, served as a quasi-reference electrode. Calibration of the latter was performed by addition of ferrocene at the end of the experiments; in the above solvent/electrolyte system, the ferricenium/ferrocene redox couple has E° = 0.460 V against the KCl saturated calomel electrode (SCE). All potential values are reported against SCE. We used a CHI 660c or a CH760d electrochemical workstation. To minimize the ohmic drop between the working and the reference electrodes, we used the positive feedback correction. For the DPV experiments, we used peak amplitude of 50 mV, pulse width of 0.05 s, 2 mV increments per cycle, and pulse period of 0.1 s. Cyclic voltammetry of 0.5 mM solutions of the clusters was used to determine their D values. The peak current (i_p) measured at low scan rates (v) allowed determining the diffusion coefficient D by using the equation that relates $i_p/v^{1/2}$ to $D^{1/2}$.[42]

5.5 References

1. Nguyen. K. T. and Zhao. Y. Engineered hybrid nanoparticles for on-demand diagnostics and therapeutics. *Acc. Chem. Res.* **2015**, *48*, 3016-3025.
2. Kemp. J. A.; Shim. M. S.; Heo. C. Y. and Kwon. Y. J. “Combo” nanomedicine: co-delivery of multi-modal therapeutics for efficient, targeted, and safe cancer therapy. *Adv. Drug Delivery Rev.* **2016**, *98*, 3-18.
3. Doane. T. L. and Burda. C. The unique role of nanoparticles in nanomedicine: imaging, drug delivery and therapy. *Chem. Soc. Rev.* **2012**, *41*, 2885-2911.
4. Sasidharan. A. and Monteiro-Riviere. N. A. Biomedical applications of gold nanomaterials: opportunities and challenges. *Wiley Interdiscip. Rev.: Nanomed. Nanobiotechnol.* **2015**, *7*, 779-796.
5. Dykmanand. L.; Khlebtsov. N. Gold nanoparticles in biomedical applications: recent advances and perspectives. *Chem. Soc. Rev.* **2012**, *41*, 2256-2282.
6. Saha. K.; Agasti. S. S.; Kim. C.; Li. X and Rotello. V. M. Gold nanoparticles in chemical and biological sensing. *Chem. Rev.* **2012**, *112*, 2739-2779.
7. Howes. P. D; Chandrawati. R. and Stevens. M. M. Colloidal nanoparticles as

advanced biological sensors. *Science*, **2014**, *346*, 1247390.

8. Abadeer. N. S. and Murphy. C. J. Recent progress in cancer thermal therapy using gold nanoparticles. *J. Phys. Chem. C* **2016**, *120*, 4691-4716.
9. Kang. Y. and Taton. T. A. Nanoparticles Core/Shell Gold Nanoparticles by Self-Assembly and Crosslinking of Micellar, Block-Copolymer Shells. *Angew. Chem. Int. Ed.* **2005**, *44*, 409-412
10. Chen. Y.; Cho. J.; Young. A. and Taton. T. A. Enhanced stability and bioconjugation of photo-cross-linked polystyrene-shell, Au-core nanoparticles. *Langmuir*, **2007**, *23*, 7491-7497.
11. Chen. H. Y.; Abraham. S.; Mendenhall. J.; Delamarre. S. C.; Smith. K.; Kim. I. and Batt. C. A. Encapsulation of single small gold nanoparticles by diblock copolymers. *ChemPhysChem*, **2008**, *9*, 388-392.
12. Rai. M.; Inglea. A. P.; Gupta. I. and Brandelli. A. Bioactivity of noble metal nanoparticles decorated with biopolymers and their application in drug delivery. *Int. J. Pharm.* **2015**, *496*, 159-172.
13. Lalatsa. A.; Schätzlein. A. G.; M. Mazza. M.; Le. T. B. H. and Uchegbu. I. F. Amphiphilic poly (L-amino acids)—new materials for drug delivery. *J. Controlled Release*, **2012**, *161*, 523-536.
14. Sulistio. A.; Lowenthal. J.; Blencowe. A.; Bongiovanni. M. N.; Ong. L.; Gras. S. L.; Zhang. X. and Qiao. G. G. Folic acid conjugated amino acid-based star polymers for active targeting of cancer cells. *Biomacromolecules*, **2011**, *12*, 3469-3477.
15. Xiao. H.; Qi. R.; Lui. S.; Hu. X.; Duan. T.; Zheng. Y.; Huang. Y. and Jing. X. Biodegradable polymer− cisplatin (IV) conjugate as a pro-drug of cisplatin (II). *Biomaterials*, **2011**, *32*, 7732-7739.
16. Park. S. -I.; Lee. E. -O.; Yang. H. -M.; Park. C. W. and Kim. J. -D. Polymer-hybridized liposomes of poly (amino acid) derivatives as transepidermal carriers. *Colloids Surf., B*, **2013**, *110*, 333-338.
17. Akagi. T.; Piyapakorn. P. and Akashi. M. Formation of unimer nanoparticles by controlling the self-association of hydrophobically modified poly(amino acid)s. *Langmuir*, **2012**, *28*, 5249-5256.

18. Suma. T.; Miyata. K.; Ishii. T.; Uchida. S.; Uchida. H.; Itaka. K.; Nishiyama. N. and Kataoka. K. Enhanced stability and gene silencing ability of siRNA-loaded polyion complexes formulated from polyaspartamide derivatives with a repetitive array of amino groups in the side chain. *Biomaterials*, **2012**, *33*, 2770-2779.
19. Li. D.; He. Q. and Li. J. Smart core/shell nanocomposites: intelligent polymers modified gold nanoparticles. *Adv. Colloid Interface Sci.* **2009**, *149*, 28-38.
20. von Werne. T. and Patten. T. E. Preparation of structurally well-defined polymer− nanoparticle hybrids with controlled/living radical polymerizations. *J. Am. Chem. Soc.* **1999**, *121*, 7409-7410.
21. Bao. Y.; Shen. G.; Liu. H. and Li. Y. Fabrication of gold nanoparticles through autoreduction of chloroaurate ions by thermo-and pH-responsive amino acid-based star-shaped copolymers. *Polymer*, **2013**, *54*, 652-660.
22. Bogdanov Jr. A. A.; Gupta. S.; Koshkina. N.; Corr. S. J.; Zhang. S.; Curley. S. A. and Han. G. Gold Nanoparticles Stabilized with MPEG-Grafted Poly(L-lysine): in Vitro and in Vivo Evaluation of a Potential Theranostic Agent. *Bioconjugate Chem.* **2015**, *26*, 39-50.
23. Gkikas. M.; Timonen. J.; Ruokolainen. J.; Alexandridis. P. and Iatrou. H. Facile aqueous synthesis and stabilization of nearly monodispersed gold nanospheres by poly(L‐proline). *J. Polym. Sci., Part A: Polym. Chem.* **2013**, *51*, 1448-1456.
24. Zhang. R.; Xu. S.; Luo. J.; Shi. D.; Liu. C and Liu. X. One-pot green synthesis of nanohybrid structures: gold nanoparticles in poly (γ-glutamic acid) copolymer nanoparticles. *RSC Adv.* **2014**, *4*, 25106-25113.
25. Perego. D.; Masciocchi. N.; Guagliardi. A.; Dominguez-Vera. J. M. and Gálvez. N. Poly (amino acid) functionalized maghemite and gold nanoparticles. *Nanotechnology*, **2013**, *24*, 075102.
26. Wang. C.; Tang. F.; Wang. X. and Li. L. Synthesis and application of biocompatible gold core poly-(L-Lysine) shell nanoparticles. *Colloids Surf., A*, **2016**, *506*, 425-430.
27. Murthy. V. S.; Cha. J. N.; Stucky. G. D. and Wong. M. S. Charge-Driven

Flocculation of Poly(L-lysine)Gold Nanoparticle Assemblies Leading to Hollow Microspheres. *J. Am. Chem. Soc.* **2004**, *126*, 5292-5299.

28. Guo. Y.; Ma. Y.; Xu. L.; Li. J. and Yang. W. Conformational Change Induced Reversible Assembly/ Disassembly of Poly-L-lysine-Functionalized Gold Nanoparticles. *J. Phys. Chem. C* **2007**, *111*, 9172-9176.
29. Guryanov. I.; Polo. F.; Ubyvovk. E. V.; Korzhikova-Vlakh. E.; Tennikova. T.; Rad. A. T.; Nieh. M. P. and Maran. F. Polylysine-grafted Au_{144} nanoclusters: birth and growth of a healthy surface-plasmon-resonance-like band, *Chem. Sci.* **2017**, ***8***, 3228-3238
30. Huang. X.; El-Sayed. M. A. Gold nanoparticles: Optical properties and implementationsin cancer diagnosis and photothermal therapy. *J. Adv. Res.* **2010**, *1*, 13-28.
31. Gans R. Form of ultramicroscopic particles of silver. *Ann. Phys.* **1915**, *47*, 270-284.
32. Habraken. G. J. M.; Peeters. M.; Dietz. C. H. J. T.; Oning. C. E. and Heise. A. How controlled and versatile is N-carboxy anhydride (NCA) polymerization at 0 °C? Effect of temperature on homo-, block- and graft (co)polymerization. *Polym. Chem.* **2010**, *1*, 514-524.
33. De Nardi, M.; Antonello, S.; Jiang, D.; Pan, F.; Rissanen, K.; Ruzzi, M.; Venzo, A.; Zoleo, A.; Maran, F. Gold Nanowired: A Linear $(Au_{25})_n$ Polymer from Au_{25} Molecular Clusters. *ACS Nano*, **2014**, *8*, 8505-8512.
34. Agrachev, M.; Antonello, S.; Dainese, T.; Gascón, J. A.; Pan, F.; Rissanen, K.; Ruzzi, M.; Venzo, A.; Zoleo, A.; Maran, F. A Magnetic Look into the Protecting Layer of Au_{25} Clusters. *Chem. Sci.* 2016, *7*, 6910−6918
35. Collins. C. B.; Tofanelli. M. A.; Crook. M. F.; Phillips. B. D.; Ackerson. C. J. Practical stability of $Au_{25}(SR)_{18}^{-1/0/+1}$, *RSC Adv.* **2017**, *7*, 45061-45065.
36. Zhu. M.; Eckenhoff. W. T.; Pintauer. T.; Jin. R. Conversion of Anionic $[Au_{25}(SCH_2CH_2Ph)_{18}]^-$ Cluster to Charge Neutral Cluster via Air Oxidation, *J. Phys. Chem. C* **2018**, *112*, 14221-14224.
37. Becucci. L.; Guidelli. R.; Polo. F. and Maran. F. Interaction of Mixed-Ligand Monolayer-Protected Au_{144} Clusters with Biomimetic Membranes as a

Function of the Transmembrane Potential. *Langmuir*, **2014**, *30*, 8141-8151.

38. Gans. R. Form of ultramicroscopic particles of silver. *Ann. Phys.* **1915**, *47*, 270-284.
39. Venzo. A.; Antonello. S.; Gascón. J. A.; Guryanov. I.; Leapman. R. D.; Perera. N. V.; Sousa. A.; Zamuner. M.; Zanella. A. and Maran. F. Effect of the Charge State (z = −1, 0, +1) on the Nuclear Magnetic Resonance of Monodisperse $Au_{25}[S(CH_2)_2Ph]_{18}^z$ Clusters. *Anal. Chem.*, **2011**, *83*, 6355-6362.
40. Antonello, S.; Musumeci, M.; Wayner, D. D. M.; Maran, F. Electroreduction of Dialkyl Peroxides. Activation−Driving Force Relationships and Bond Dissociation Free Energies. *J. Am. Chem. Soc.* **1997**, *119*, 9541-9549.
41. Meneses, A. B.; Antonello, S.; Arévalo, M.-C; Maran, F. Double-Layer Correction for Electron-Transfer Kinetics at Glassy Carbon and Mercury Electrodes in N, N-Dimethylformamide. *Electroanalysis*, **2006**, *18*, 363-370.
42. Nicholson, R. S.; Shain, I. Theory of Stationary Electrode Polarography. Single Scan and Cyclic Methods Applied to Reversible, Irreversible, and Kinetic Systems. *Anal. Chem.* **1964**, *36*, 706-723.